Universidad
Carlos III de Madrid
www.uc3m.es

TESIS DOCTORAL

NUMERICAL AND EXPERIMENTAL INVESTIGATIONS ON PSEUDO-2D GAS FLUIDIZED BEDS

Autor:
Fernando Hernández Jiménez

Director de Tesis:
Antonio Acosta Iborra

DEPARTAMENTO DE INGENIERÍA TÉRMICA Y DE FLUIDOS

Leganés, Madrid, Octubre de 2013.

Universidad
Carlos III de Madrid
www.uc3m.es

TESIS DOCTORAL

NUMERICAL AND EXPERIMENTAL INVESTIGATIONS ON PSEUDO-2D GAS FLUIDIZED BEDS

Autor: Fernando Hernández Jiménez

Director de Tesis: Antonio Acosta Iborra

Firma del Tribunal Calificador,

Firma

Presidente:

Vocal:

Secretario:

Calificación: _____

Leganés, Madrid, 4 de Octubre de 2013

No amount of experimentation can ever prove me right; a single experiment can prove me wrong.
Albert Einstein.

When you play the game of thrones you win or you die, there is no middle ground.
Cersei Lannister in "A Song of Ice and Fire", a book written by George R.R. Martin.

Contents

List of Figures

List of Tables

Preface

This PhD Thesis has been performed in the University Carlos III of Madrid, School of Engineering, in the Department of Thermal and Fluid Engineering, under the supervision of Dr. Antonio Acosta Iborra. The thesis was initiated in Autumn 2009 and lasted until Summer 2013.

The author deeply appreciates the funding support by the Spanish Government (Project DPI2009 - 10518) and the Autonomous Community of Madrid (Project S2009 / ENE - 1660), which has been of great help during the PhD.

During the realisation of the PhD, a collaboration framework with the "Laboratory of Energy Science and Engineering" from ETH Zürich, headed by Prof. Christoph R. Müller, was established by means of three different research stays performed in June-July of 2010, November of 2011 and November of 2012.

All the results presented in this dissertation have been obtained by the author unless otherwise specified.

Fernando Hernández Jiménez
Department of Thermal and Fluid Engineering,
University Carlos III of Madrid.
October 2013.

Acknowledgments

During the last few years, the ISE research group has welcomed the pleasant visits of several researchers during different conferences related to the main research lines of our group. I would like to thank all of them for their visits, which have been a great resource of ideas for this thesis: Filip Johnsson, *Chalmers University of Technology*, Bo Leckner, *Chalmers University of Technology*, Ruud van Ommen, *Delf University of Technology*, David Pallarès, *Chalmers University of Technology* and Allan Hayhurst, *University of Cambridge*.

I would like to give special thanks to the personnel of the Laboratory of Energy Science and Engineering research group of the ETH Zürich. In particular to Christoph R. Müller and James R. Third for their help, ideas, support and patience during my stays in 2010, 2011 and 2012.

Agradecimientos

Una vez terminada la tesis, es decir, escrita, revisada, corregida, revisada otra vez, etc, llega la hora de agradecer, y la verdad que son muchas las personas que me vienen a la cabeza, pero nos centraremos en las importantes.

El primero, sin lugar a dudas, es mi director de tesis, Antonio Acosta. Tengo que agradecerle por toda la paciencia que ha tenido conmigo y por el esfuerzo que también le ha supuesto a él la realización de esta tesis. Espero que Edu no me deje en muy mal lugar.

Dentro del departamento, a todo el mundo con el que he compartido un rato de café o de sobremesa para hacer de todo esto un lugar mucho más ameno. A Ulpiano por engañarme para hacer la tesis, a Domingo por enseñarme a meter golazos, a Merche por enseñarme a ser pragmático, a la generación anterior (Celia, Sergio, Antonio Soria...) por enseñame que lo malo no es la tesis sino lo que viene después, al resto de gente del grupo ISE, y al grupo de Mecánica de fluidos por compartir algo más que departamento. A Iterate FC... A los técnicos de laboratorio por haber construido el lecho con el que he podido realizar la parte experimental de la tesis.

Mención especial por aguantarme se merecen Javi Sánchez, por haber sido el que más tiempo me ha sufrido como compañero de despacho, y Luismi, con el que he estado más tiempo que con mi madre desde que empezamos la carrera allá por 2003.

A Christoph y James (seguro que Gabriela estará encanta de traducir esta parte), por haberme acogido tan generosamente en sus casas y en su grupo durante mis estancias en Suiza.

A todos mis amigos y personas queridas que han estado ahí durante estos últimos años, los que aún siguen y los que se han quedado atrás.

A mis padres, a mi hermano, y a toda mi familia por hacerme saber que siempre estarán ahí.

A Reyes, por su cariño, paciencia y compañia en éste último año y medio de (sana) locura. Gracias.

Resumen

El presente documento se divide en siete capítulos que estudian, tanto numérica como experimentalmente, lechos fluidizados de pequeño espesor, es decir, lechos fluidizados pseudo bidimensionales (2D). Este tipo de sistemas son cruciales para entender la dinámica de los sistemas gas-partícula. A este respecto, lechos pseudo-2D, típicamente tienen una pared transparente para poder tener acceso óptico al interior del sistema, y poseen un reducido espesor para asegurar que la visualización es representativa de todo el sistema. Además, hay que tener en cuenta que las paredes delantera y trasera restringen el movimiento de los sólidos, siendo el comportamiento del flujo distinto comparado con sistemas tridimensionales (3D). Por lo tanto, es vital interpretar correctamente los resultados (tanto experimentales como numéricos) de este tipo de lechos pseudo-2D para poder entender la física de la fluidización y poder escalar los resultados a otros tipos de lechos.

Tras una breve introducción en el Capítulo 1, en el segundo capítulo de la presente tesis se realiza una comparación entre los resultados obtenidos mediante una simulación empleando el modelo de dos fluidos y los resultados experimentales en un lecho 2D. Gracias a las técnicas de medida no intrusiva de Análsis Digital de Imágenes (DIA) y Velocimetría por Imágen de Partículas (PIV), el comportamiento de burbujas, así como el movimiento de los sólidos, se obtienen en todo el lecho en las mismas condiciones que las simulaciones numéricas. Los resultados muestran una buena similitud en cuanto al comportamiento de burbujas, pero no en cuanto a la velocidad media de la fase partículas, siendo sobreestimada por los resultados simulados para los dos modelos de arrastre estudiados (Gidaspow y Syamlal-O'Brien). Esto se puede atribuir a la ausencia de las paredes delantera y trasera en la simulación, que es resuelta en un dominio 2D puro, que considera solamente las paredes laterales. Por lo tanto, a partir de las observaciones experimentales realizadas en combinación con los resultados numéricos, se demuestra que para lechos de espesor delgado, el efecto de ambas paredes en el movimiento de las partículas puede ser muy significativo.

La fuente de las discrepancias encontradas en el Capítulo 2 entre los resultados experimentales y simulados se puede atribuir a diversos factores. Para estudiar cuales

de estos factores tienen un impacto mayor en las simulaciones, el Capítulo 3 estudia el movimiento de las partículas alrededor de burbujas, usando datos obtenidos con simulaciones que emplean el modelo de dos fluidos. Los resultados de la simulación son verificados con modelos contrastados de la literatura. En particular, se utiliza el modelo de flujo potencial de Davidson (Davidson and Harrison, 1963) para burbujas 2D. Para ello, el capítulo estudia el movimiento de la fase sólida alrededor de burbujas aisladas y para burbujas en erupción. Los resultados procedentes de la simulación muestran una gran similitud con los del modelo de flujo potencial para ambos tipos de burbujas, y también con resultados experimentales para burbujas en erupción (Müller et al., 2007).

Además, otra manera de validar las simulaciones respecto al comportamiento de burbujas es estudiar el comportamiento de la fase gas en el lecho. Ésto se realiza en el Capítulo 4, dónde se estudia el intercambio de gas debido a la advección entre la fase burbujas y fase densa en un lecho burbujeante. De nuevo, los resultados para burbujas aisladas concuerdan perfectamente con el modelo de flujo potencial de Davidson (Davidson and Harrison, 1963). Este resultado motiva el estudio llevado a cabo en la segunda parte del capítulo, que se basa en caracterizar el intercambio de gas cuando el lecho trabaja en regimen burbujeante. Se propone un nuevo modelo para burbujas 2D que interactúan ente ellas, que tiene en cuenta la dependencia de este intercambio de gas con el tamaño de burbuja y la velocidad del gas. Esto lleva a la deducción de una expresión analítica simple para el intercambio de gas. Dicha expresión no es función unicamente de la velocidad de mínima fluidización sino que depende además de la velocidad superficial del gas y de un parámetro que tiene en cuenta el paso de gas a través de la fase densa (throughflow).

Una vez visto que el comportamiento de burbujas en lechos pseudo-2D concuerda muy bien con resultados puramente 2D, los siguientes dos capítulos de la tesis estudian el efecto de las paredes delantera y trasera del lecho. Este estudio se lleva a cabo numéricamente en el Capítulo 5 y experimentalmente en el Capítulo 6. El Capítulo 5 presenta simulaciones 3D de lechos pseudo-2D considerando condiciones de contorno típicas para la interacción partícula pared. Además, el capítulo emplea el modelo Euleriano-Lagrangiano de simulación discreta de partículas (DEM), como herramienta alternativa numérica. Los resultados demuestran que el uso de la condición de contorno clásica de deslizamiento parcial no es adecuado para reproducir el comportamiento del lecho pseudo-2D. Ello se corrobora con simulaciones DEM en la primera parte de este capítulo. Por consiguiente, en la segunda parte del capítulo, una nueva condición de contorno de deslizamiento parcial para la fase partícula se desarrolla empleando simulaciones DEM, y se compara con la condición de contorno clásica de Johnson y

Jackson (Johnson and Jackson, 1987), la cual se emplea comunmente en el modelo de dos fluidos para simular lechos fluidizados. El coeficiente de deslizamiento parcial de la nueva condición de contorno es negativo para valores bajos de concentración de sólidos. Esta tendencia es opuesta a la del coeficiente de deslizamiento de la condición de contorno clásica de Johnson y Jackson. Cuando la nueva condición de contorno desarrolada en el capítulo se implementa en el modelo de dos fluidos, muestra resultados más favorables para un lecho fluido pseudo-2D que la condición de contorno clásica.

Por último en el Capítulo 6, se realiza una cuantificación experimental de las fuerzas de fricción sobre las partículas originada por la interacción con paredes delantera y trasera en un lecho fluido pseudo-2D. El capítulo propone la obtención de dicha fuerza de fricción por medio del enlace entre la señal de presión con la distribucin de los sólidos obtenida utilizando DIA. Mediante un simple balance de fuerzas en el lecho, esta fuerza de fricción puede ser estimada como función de la caída de presión dentro del lecho, el propio peso del lecho, y tanto la velocidad como la aceleración del centro de masas del lecho. La fuerza de fricción resultante es proporcional a la velocidad de los sólidos multiplicada por un coefficiente de interacción partícula-pared, lo cuál es coherente con la naturaleza fluida de la fase densa en un lecho fluido. De acuerdo con los resultados obtenidos, este coeficiente depende del tamaño de partícula, se ve poco afectado por la velocidad superficial, y es prácticamente insensible a la relación de aspecto del lecho. Se demuestra además, que la contribución de estas fuerzas de fricción en las fluctuaciones de presión del lecho no pueden ser despreciadas.

En resumen, la tesis revela, numérica y experimentalmente, que los efectos producidos por las paredes del lecho en las partículas no pueden ser despreciados y afectan el movimiento de la fase densa así como a las fluctuaciones de presión del lecho. Sin embargo, el comportamiento de burbujas parece estar poco afectado por la presencia de las paredes. Por lo tanto, para poder extrapolar correctamente los resultados experimentales de un lecho pseudo-2D, o para validar los códigos numéricos con las observaciones en este tipo de lechos, es esencial acudir a modelos de especficos de interacción partícula pared que sean capaces de describir el efecto combinado de todas las paredes del lecho en estos sistemas de espesor delgado.

Abstract

This dissertation is divided into seven chapters that study, numerically and experimentally, fluidized beds of small thickness, i.e., pseudo two−dimensional (2D) gas fluidized beds. These types of fluidized beds are crucial for the understanding of the dynamics of gas−particle systems. In this regard, pseudo−2D fluidized bed systems typically have a transparent wall, to allow optical access to the system, and the volume of the bed possesses a small thickness to ensure that the visualisation is representative of the whole system. Additionally, the front and the rear walls restrict the motion of the solids, leading to different flow behaviour compared to fully three-dimensional (3D) systems. Therefore, a correct interpretation of the observations and numerical simulations of pseudo−2D beds is crucial for the understanding of the fluidization physics and the scale-up of the results to other types of beds.

After a brief introduction in Chapter 1, the second chapter of the present thesis addresses a comparison between two-fluid model simulations, and the experimental results of a 2D gas-solid fluidized bed are presented. Thanks to the non-intrusive Digital Image Analysis (DIA) and Particle Image Velocimetry (PIV) experimental techniques, the real bubble behaviour and solids motions are obtained in the whole bed in the same conditions as the numerical simulations. The results show that, despite the good agreement found in the bubble behaviour, the mean particle velocity predicted by the simulations systematically over-predicts the experimental results for two different well-known drag models (Gidaspow and Syamlal-O'Brien). This is attributed to the absence of the front and rear walls in the two-fluid model, which was computed in a pure 2D domain, where only the left and right walls are present. Therefore, the experimental observations in combination with the numerical simulations indicate that for thin-bed thicknesses, the effects of the front and the rear wall on the particle motion may be significant.

The exact source of the discrepancies found in Chapter 2 between the experiment and simulation results can be attributed to several factors. To study which of these factors has a crucial impact on the simulations, the motion of particles around bubbles from two-fluid model simulations are studied in Chapter 3. The simulation results

are verified with reliable models found in the literature. In particular, the classical potential flow theory by Davidson and Harrison (1963) for 2D bubbles is used for this verification. To do this, the motion of solids around isolated and erupting bubbles is studied in the chapter. The simulation results show a strong agreement with the potential flow model by Davidson and Harrison (1963) for isolated and erupting bubbles and with the experimental results for erupting bubbles of (Müller et al., 2007).

Furthermore, another way to verify the validity of the simulations in terms of the bubble behaviour is to study the behaviour of the gas phase in the bed. This is accomplished in Chapter 4, where the gas interchange due to advection between the bubble and emulsion phases in a bubbling bed was studied. Again, the results for the isolated bubbles agree with the classical potential flow theory by Davidson and Harrison (1963). This motivates the study performed in the second part of the chapter, which is to characterise the gas interchange coefficient when the fluidized bed is operated in a bubbling regime. A new model is proposed for 2D interacting bubbles, that considers the dependence of the gas interchange on both the bubble size and the gas velocity under bubbling regime conditions. This findings leads to a deduction of a simple analytical expression for the gas interchange. This novel expression is not only a function of the minimum fluidization velocity but also depends on the superficial velocity of the bed and the throughflow parameter.

Having seen that the bubble behaviour in pseudo−2D beds agrees well with the pure 2D results, the next two chapters of the dissertations aim at studying the effects of the front and rear walls of the bed. This is performed numerically in Chapter 5 and experimentally in Chapter 6. Fully 3D simulations of pseudo-2D beds considering the classical particle-wall boundary conditions are presented in Chapter 5. Additionally, the Eulerian-Lagrangian discrete element method (DEM) is used in this chapter as an alternative numerical technique. It is proved that the usage of the classical partial-slip boundary condition is unsuccessful to reproduce the expected behaviour of the pseudo-2D bed. This is corroborated by the DEM simulations in the first part of the chapter. Therefore, in the second part, a novel partial-slip boundary condition for the solid phase is developed using DEM simulations and is compared with the classical Johnson and Jackson boundary condition (Johnson and Jackson, 1987) commonly employed in two-fluid model simulations. The partial-slip coefficient of the new boundary condition is found to be negative at low values of solids concentrations in contrast to the Johnson and Jackson boundary condition. The new boundary condition is implemented in a two-fluid model and shows more favourable results for pseudo-2D beds.

Finally, an experimental quantification of the frictional forces between the solid phase and the front and rear walls in a pseudo−2D gas fluidized bed is performed for

the first time in Chapter 6. This is performed by coupling the pressure signal with the solids distribution obtained from DIA. Using a simple force balance in the bed, this frictional force can be estimated as a function of the measured pressure drop in the bed, the bed weight and the velocity and acceleration of the centre of mass of the bed. The resulting frictional force is proportional to the solids velocity times a particle-wall interaction coefficient, which is in harmony with the fluid-like nature of the dense phase in a fluidized bed. This coefficient is found to be very sensitive to the particle diameter, less affected by the superficial gas velocity and weakly affected by the bed aspect ratio. It is demonstrated that the contribution of the frictional forces on the fluctuations of the pressure drop in the bed cannot be neglected.

In summary, the present thesis reveals, numerically and experimentally, that the effects exerted by the bed walls on the particles are not negligible and can affect the motion of the dense phase as well as the pressure fluctuations in the bed. However, the effect of the walls seems to weakly affect the bubble behaviour. Hence, to correctly extrapolate the experimental results from pseudo-2D beds to other systems, or to validate numerical codes with the pseudo-2D observations, it is essential to resort to specific particle-wall interaction models capable of describing the combined effects of all the bed walls in these types of beds of small thickness.

Chapter 1

General Introduction

1.1 Motivation

Fluidization is the operation by which solids particles are transformed into a fluid-like state through suspension in a gas or liquid. This method has some unusual characteristics that fluidization engineering takes advantage of (Kunii and Levenspiel, 1991).

One of the most popular fluidization techniques is the gas fluidization of beds, which which is an operation widely used in industry; fluid-catalytic cracking (FCC), gasification and combustion of coal, biomass or wastes, drying, freezing acceleration, Fischer-Tropsch synthesis or coating of tablets in the pharmaceutical industry are just a few examples.

Gas fluidized beds are specially indicated when solid-gas reactions occur. This complex reacting multiphase flow is often difficult to model because of the very different length scales that are present; therefore, fundamental investigations are needed before reliable models can be developed for the design and control of fluidized beds, for example the quantitative relation of dispersion to the granular and the Reynolds stresses (Gidaspow et al., 2004).

1.1.1 The gas fluidization of granular media

A gas-fluidized bed consists of a bed of particles contained in a column and supported by a distributor. The distributor is typically a plate with orifices where air passes through. The distributor can alternatively be made of a porous material that allows a fluid to pass. At very low gas flow rates, the particles are stationary as the fluid percolates through the voids of the bed. In this condition, the bed is referred to as a 'fixed bed'. As the gas flow is increased, the particles start to move and collide with each other around their equilibrium position, resulting in an increased spacing between

the single particles. This system is termed an 'expanded bed' (Kunii and Levenspiel, 1991; Davidson and Harrison, 1963).

If the flow rate is further increased to a point at which the flow rate of the gas is high enough for the pressure drop across the bed to become equal to the weight of the bed per unit area of the column, the bed reaches minimum fluidization conditions, and the particles are completely supported by the gas flow. The superficial velocity of the gas required for this state is the minimum fluidization velocity U_{mf}. Equating the pressure drop of the air across the bed (i.e., from the distributor to the upper part above the bed surface) at minimum fluidization conditions, ΔP_{bed}, with the weight per unit area of all the particles gives:

$$\Delta P_{bed} = (1 - \epsilon_{mf})(\rho_s - \rho_g)gL_{mf} \tag{1.1}$$

where L_{mf}, ρ_g, ρ_s and ϵ_{mf} are, respectively, the height of the bed, the densities of the gas and the particles and the voidage of the bed (i.e., gas volume fraction) at the minimum fluidization conditions.

For most gas-solid systems of large particles, voids containing only gas (hereafter 'bubbles') are formed in the bed after the superficial velocity exceeds U_{mf}, thus $U_{mf} = U_{mb}$, where U_{mb} is the superficial velocity at which bubbles are first found. Because the particles are fluidized, they behave as a fluid and the bubbles freely migrates upwards. This movement is very similar to the bubbles of gaseous substances in liquids. Outside the bubbles, the particles are still fluidized close to each other, forming what is called the 'dense phase' (Davidson and Harrison, 1963).

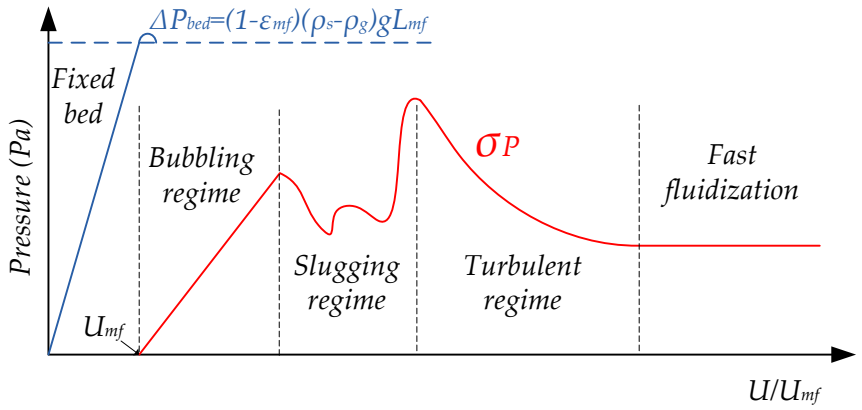

Figure 1.1: Illustration of the evolution of the mean value and the standard deviation of the pressure drop in the bed versus the normalised superficial gas velocity.

Figure 1.1 shows an illustration of the evolution of the mean pressure drop and its standard deviation in the bed versus the superficial gas velocity (Kunii and Levenspiel,

1991; Makkawi and Wright, 2002).

Different flow regimes can be found in fluidization when the gas flow is increased. If the bubbles are smaller than the bed horizontal dimension, their shape is mostly unperturbed by the walls. This fluidization regime is called the freely bubbling regime. If a bed is deep enough, the bubble diameter will approach the diameter of the bed. This flow regime is referred to as slugging. This thesis is focused on the behaviour of fluidized beds in the bubbling regime, which are mainly operated using group B particles according to Geldart's classification (Geldart, 1973). In the beds of Geldart B solids, bubbles form as soon as the velocity exceeds U_{mf}; small bubbles are formed at the distributor and grow and coalesce as they rise through the bed. Particles within the Geldart group D classification have also been used in this dissertation. The main difference of group D particles is that they spout easily if the bed is operated under high superficial gas velocities so that the bubble size approaches the bed diameter.

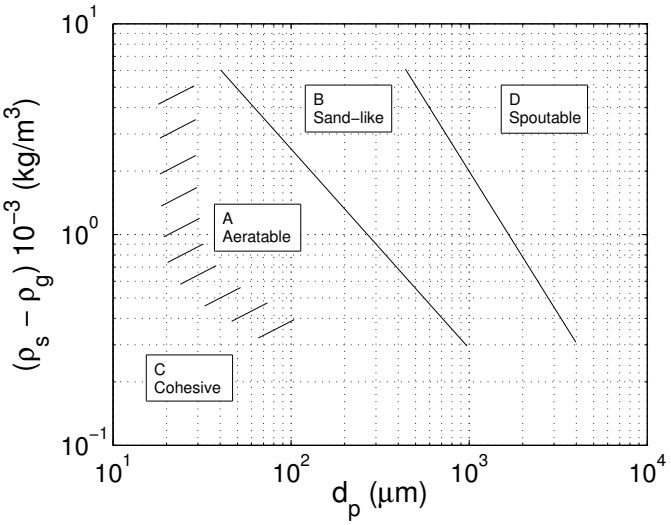

Figure 1.2: Diagram of the Geldart classification of particles (Geldart, 1973).

In beds of small particles, the motion of the bubbles becomes more vigorous when the velocity of fluidization is increased. This is accompanied by increasing pressure fluctuations up to a critical velocity, U_c, when the pressure fluctuations reach a maximum value. This maximum in pressure fluctuations marks the transition between bubbling and so-called turbulent fluidized beds. Instead of clearly defined bubbles, voids of distorted shapes and vigorous motion are observed in a turbulent fluidized bed. The particles form clusters and strands and the distinction between the particulate phase and the void phase becomes much less marked than in the bubbling regime.

At even higher fluidization velocities, a pneumatic transport regime can be observed, in which particles are swept out of the bed vessel. The velocity of the fluidizing gas for

this regime must reach approximately 20 times the settling velocity for small particles (Kunii and Levenspiel, 1991; Makkawi and Wright, 2002). Instead of the dense phase in a bubbling bed, the particles are now widely dispersed, so particle-particle interactions can be neglected.

Another operational variant of a fluidized bed is the spouted bed. The bottom of a spouted bed is usually conical with a large orifice at the bottom. Gas of high velocity is injected through the orifice and forms a permanent spout, which penetrates through the entire bed. Particles are entrained by the gas in the spout, and at the top of the bed, the entrained particles fall back to the surface of the spouted bed giving the entire bed a fountain-like appearance. The particles in the annulus around the spout move slowly downwards. Sometimes spouted beds show both spouting and bubbling characteristics; these are called spouted fluidized beds.

Figure 1.3 exemplifies the different fluidization regimes described above.

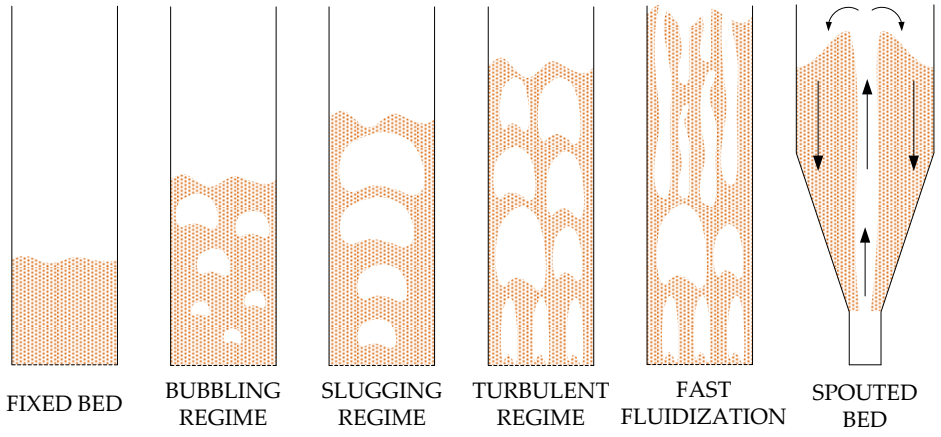

Figure 1.3: Examples of the different fluidization regimes.

1.1.2 The characterisation of gas fluidized beds

As commented previously, gas fluidized beds are widely used in industry. Despite this, the theoretical understanding of two-phase granular systems is still rather poor. This lack of understanding is mainly a result of very complex flow structures in such systems, which evolve over time. Furthermore, very different length scales are encountered in such systems, and a full empirical or mathematical description of the interactions amongst phenomena occurring at different length and time scales is extremely difficult. Indeed, prediction of the stochastic behaviour of granular systems at any of the time or length scales is still a formidable challenge that has attracted much attention from the physics community in recent years (Kunii and Levenspiel, 1991; Grace and Taghipour,

2004).

Pseudo-2D gas fluidized beds have been of great help in the understanding of two-phase granular system. these types of systems must have a transparent wall to allow optical access to the interior of the bed and possess a small thickness to ensure that the visualisation is representative of the whole system. Additionally, 2D simulations requires less computational cost than fully 3D systems. However, pseudo-2D gas fluidized beds cannot be directly simulated in a pure 2D domain, the presence of the front and rear walls on the system strongly affect the behaviour of the bed. Therefore, it is important to estimate and consider this effect.

A correct characterisation of gas fluidized beds is essential for the improvement of their current applications and also for the development of new applications. Experimental and numerical techniques are very powerful tools for the characterisation of fluidized beds. These techniques are described in the following sections.

1.1.3 Experimental techniques

Three non-intrusive experimental techniques have been used in this thesis, Digital Image Analysis (DIA), Particle Image Velocimetry (PIV), and pressure signal analysis. These techniques are well-known in the field of fluidized beds, and a brief description of them is presented below.

Digital Image Analysis (DIA)

The DIA technique can be applied to images acquired with a CCD digital camera over an optically accessible part of the bed. The opacity of the solids restricts the analysis to two-dimensions, excepting the bed surface or inside the bubbles. Two main objectives are usually pursued with DIA:

- A clear identification of the two phases of the fluidized bed: the bubble phase free of particles where the porosity ϵ is equal to 1, and the dense phase free of bubbles where the porosity approaches the minimum fluidization conditions $\epsilon = \epsilon_{mf}$.
- The bubbles can be characterised based in their equivalent diameter, centroid position, bubble centroid velocity, etcetera.

The digital images can be acquired in grey scale with values ranging from 0 to 255. A threshold transformation is necessary for the identification of the two phases explained above. The original image is transformed into a black and white image where the pixels with values equal to 0 represent the bubble phase and the pixels of the dense phase take a value equal to 1 (Otsu, 1979). It is with the black and white image that

the bubble properties are typically calculated.

Particle image velocimetry (PIV)

The PIV technique has been used to characterise the dense phase velocity (Raffel et al., 2007; Sveen, 1998-2007). PIV uses two consecutive frames to measure the displacement of the particles, Δx or Δy, and therefore to calculate the velocity using the time delay between the two frames, Δt.

$$u(x,t) = \frac{\Delta x(x,t)}{\Delta t} \tag{1.2}$$

$$v(x,t) = \frac{\Delta y(y,t)}{\Delta t} \tag{1.3}$$

Typically, the PIV technique is applied to a single phase flow field seeded with particles small enough to follow the flow motion exactly (Raffel et al., 2007). The particles are illuminated by a light sheet generated by a laser. The domain (images of the particles in a two-dimensional plane) is divided into smaller sections called interrogation windows, whose size is fixed or can be reduced along consecutive steps. The light is generated in two pulses, and the displacement of the tracer particles between the two light pulses is determined using statistical methods, such as the cross-correlation function, for each window.

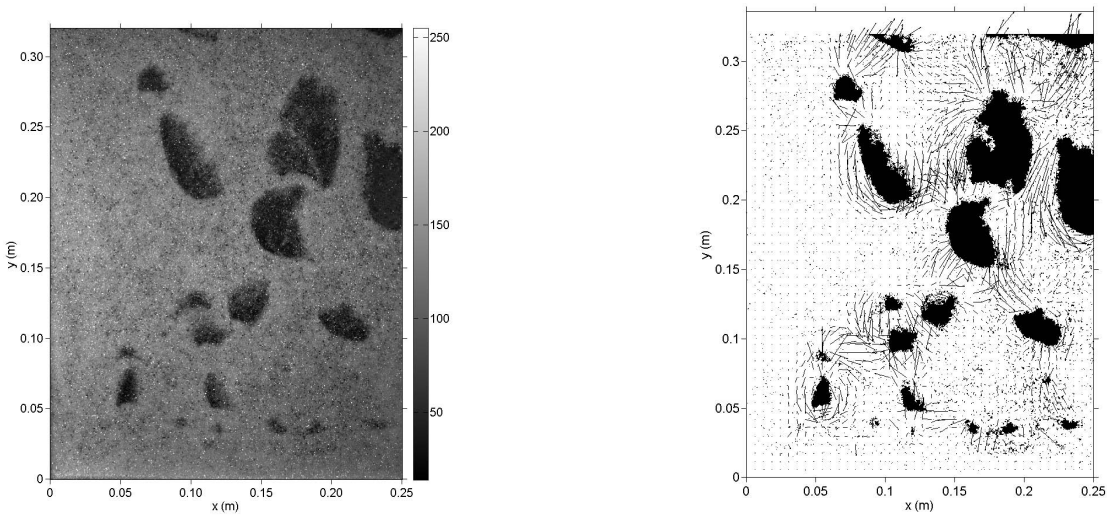

(a) (b)

Figure 1.4: DIA and PIV processing (a) raw particle image; (b) bubble mask and PIV velocity vectors for the solids phase.

PIV can be applied in pseudo-2D fluidized beds because of the transparent wall

that allows optical access to the interior of the bed. In this case, the bed is continuously illuminated, and the images are recorded at frequencies approximately 200 Hz. Typically, the window size is in between 16 to 64 pixels, with an overlap of 0.5. The velocity can be calculated by dividing the displacement by the lapse of time between the two images; therefore, the velocity vectors were obtained every 8 pixels.

PIV has been widely used in fluidized beds, see for example Almendros-Ibáñez et al. (2006); Almendros-Ibáñez et al. (2010); Busciglio et al. (2008); Müller et al. (2007); Laverman et al. (2008); Sánchez-Delgado et al. (2010, 2013); Santana et al., (2005); Vun et al. (2010).

Figure 1.4 shows an example of an acquired raw image (a) as well as the threshold transformation explained in the DIA together with the PIV velocity vectors calculated between two consecutive frames for the solids phase (b).

Pressure signal analysis

Time and frequency signal analysis of the gas pressure measured in the bed or in its plenum is extensively used in research and industry to characterise or monitorise the dynamics of fluidized bed systems. Many studies have been conducted in this field, and currently, the pressure signal is routinely employed to obtain a large amount of information concerning the dynamics of a fluidized bed, e.g., Johnsson et al. (2000); van Ommen et al. (2011).

Most pressure transducers use the change in conductivity of a material under stretch or strain to measure the pressure. These pressure transducers are connected to the bed by a probe and to the computer by an acquisition card to save or to visualise the digital signal. An amplifier module may be needed depending on the pressure transducer used. The pressure signal can be utilised to distinguish the fluidization regime or to determine the minimum fluidization conditions.

Apart from the techniques described above, there are other measurements techniques (Wether , 1999) that are currently used in fluidized bed research such as:

- Capacitance probes. These probes are based on the measurement of the dielectric constant of the space between the two plates. They have been used extensively in fluidized bed research and have provided valuable insights into solid concentrations and bubble dynamics. As a disadvantage, distortions in the electric field can lead to difficulties in obtaining measurements (Sharma et al., 2000).

- Fibre optic probes. The light that is scattered and reflected by the particles is received by the sensor fibres. It is possible to calculate the velocity of particles or

bubbles by cross-correlating the measurements of two spatially separated optical probes. However, a reliable calibration of the optical probe can be difficult due to the complexity of the light dispersion patterns (Sobrino et al., 2009a,b).

- Laser Doppler Anemometry (LDA). This technique is based on a laser passing a cell that transforms it into two lasers of different frequency to detect the direction and velocity of the particle movement. LDA can only provide point measurements of velocities. Spatially resolved velocity measurements require movement of the probe leading to non-instantaneous spatial measurements (Mathiesen et al., 2000).

- X-Ray tomography. A tomographic technique based on the attenuation of X-rays. The attenuation is a function of the chemical composition of the bed material, the concentration and the thickness of the layer of particles through which the beam penetrates. The spatial and temporal resolution of this technique is currently not very high (van Ommen and Mudde, 2008).

- Acetone Planar Laser Induced fluorescence. In this technique, acetone is excited and recorded with a high-resolution camera to study the gas flow and mixing patterns. Only a reduced area of the bed can be studied due to the limited size of the laser sheet (Müller et al., 2009; Solimene et al., 2006).

- Electrical Capacitance Tomography (ETC). Tomography is a technique based on the measurement of electrical capacitance. The measured capacitance is a function of the void fraction of the fluidized material. The main challenge in ECT is the reconstruction of high-resolution images based on a limited number of measurements, because the number of sensor elements is typically small (van Ommen and Mudde, 2008).

- Magnetic Resonance Imaging (MRI). Magnetic Resonance detects nuclei with non-zero spin quantum number. Applying magnetic gradients enables spatially resolved measurements to be made. However, the size of the area to be measured is very limited (Köhl et al., 2013; Müller et al., 2008).

- Gas concentration infrared measurements. This promising technique is based on digital image analysis of images acquired with an infrared and a visual high-speed camera to obtain the local concentration of a gas non-transparent to radiation (CO_2). Calibration can be a difficult considering that only the dilute region should be taken into account to measure the gas concentration (Dang et al., 2013).

1.1.4 Numerical modelling

Numerical modelling of fluidized beds is one of the methodologies most commonly used in this study to achieve a better understanding of the behaviour of these systems. Numerical modelling of fluidized beds has advance significantly over the last decades due to the significant enhancement and development of computational systems.

Four main approaches can be found in literature for the simulation of fluidized beds depending on the level of detail and resolution required (Grace and Taghipour, 2004; Van der Hoef et al., 2005). The most detailed approach is the direct simulation of the fluid flow surrounding solid particles and the interaction between them. For such approaches, lattice Boltzmann methods are normally used (see, for example, Deen et al. (2012); Ladd and Verberg (2001); Kriebitzch et al. (2013); Reddy et al. (2013); Third and Müller (2013)), although classical finite volume schemes are also possible. The direct simulation of gas-fluidized beds demands large computational resources, surpassing the current hardware capabilities unless a relatively small number of particles are to be simulated.

A second approach in the simulation of fluidized beds is by direct particle or discrete element modelling, which is based on a Lagrangian simulation of each particle trajectory coupled with the Eulerian simulation of the bulk gas flow. The solid-gas interaction is computed through semi-empirical closure models to reduce the level of detail required in the solution of the gas phase (Deen et al., 2007; Müller et al., 2008). Although very promising, this Lagrangian-Eulerian approach is still computationally intensive.

The level of resolution in particle motion can be reduced by computing only the bulk velocity behaviour of particles and not their individual trajectories. This is the essence of a third approach known as Eulerian-Eulerian, or CFD, two-fluid modelling of fluidized beds. In the Euler-Euler approach, the gas phase and the particles or solids phase are treated as two interpenetrating and continuum media in an Eulerian framework using the conservation equation of fluids, (Gidaspow, 1994; Kuipers et al., 1992; Van Wachem and Almstedt, 2003). As in the case of the Lagrangian-Eulerian approach, the two-fluid simulation of fluidized beds requires the use of closure models for the gas-solids interaction. However, the lack of detailed description of the motion of the particles in the two-fluid simulation necessitates the inclusion of sophisticated particle-particle interaction models, which are normally based on empirical and theoretical relations linked to the kinetic theory of gases through the concept of granular temperature (Gidaspow, 1994).

A fourth approach can be followed using bubble discrete models and phenomenological methods, in which only the most relevant macroscopic characteristics of the

bed are reproduced, e.g., gross bubble behaviour and general motion of the emulsion phase (see, for example, Bokkers et al. (2006); Briongos et al. (2011)). Because this approach is based on simplified models and phenomenological correlations, it is the less computationally intensive and, therefore, it is especially suitable for the simulation and optimisation of large scale fluidized beds supporting chemical reactions such as combustion or gasification.

Figure 1.5 shows examples of the different modelling strategies of fluidized beds described above.

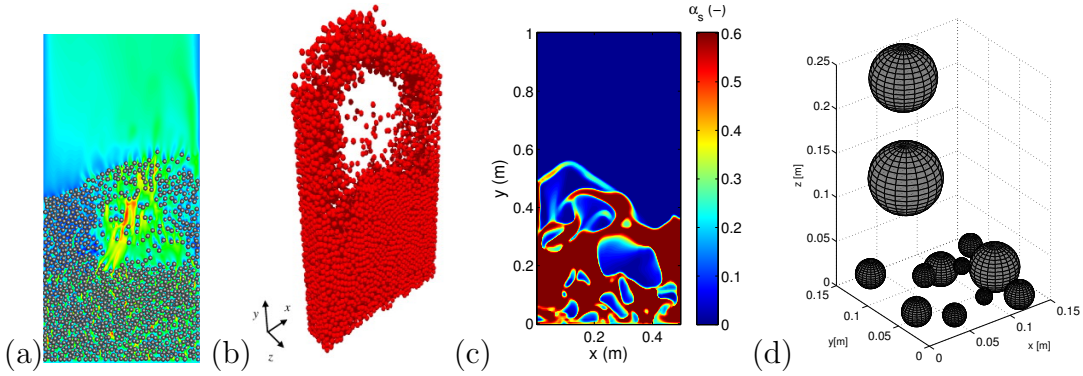

Figure 1.5: Different approaches in numerical modelling of fluidized beds. a) DNS (Third and Müller, 2013), b) DEM (Müller et al., 2008), c) two-fluid model, d) DBM (Briongos et al., 2011).

The Eulerian-Eulerian two-fluid approach is by far the method most common method encountered in the current simulations of fluidized beds. This is perhaps due to its compromise between computational cost, level of detail provided and potential of applicability. As a consequence, there is an increasing need of verification (confirming the accuracy of the computational aspects of the model) and validation (objective consideration of computational and numerical error (Grace and Taghipour, 2004), as well as a comparison of the model predictions and experimental data over broad ranges of conditions) of the closure models utilised in the two-fluid simulation of gas fluidized beds in different operative conditions and applications (see, for instance, Peirano et al. (2001); McKeen and Pugsley (2003); Patil et al. (2005); Taghipour et al. (2005); Li et al. (2010); Busciglio et al. (2009); Hernández-Jiménez et al. (2011a,b); Acosta-Iborra et al. (2011, 2012)). However, as some authors have noted (Grace and Taghipour, 2004), this verification and validation should be interpreted and extrapolated with caution due to the complex nature of fluidized beds. Great care is required to verify the computational aspects of the model and to plan and execute proper experimental validation tests, covering a wide range of conditions, especially where deviations are compared with computational and experimental errors.

1.2 Scope of the thesis

In the previous section, the importance of pseudo-2D gas fluidized beds for the understanding of two-phase granular systems was stated. In addition, complete information of what occurs in pseudo-2D beds can be achieved by numerical simulations. The validation of the numerical codes to be used for the design and scale-up of fluidized bed systems requires comparison with real experimental data. These data are usually obtained from pseudo-2D fluidized beds. This motivates the following key objectives of the present dissertation.

- The study of the capabilities of the two-fluid model to reproduce the behaviour of experimental pseudo-2D beds. As explained before, pseudo-2D beds are a common configuration for the analysis of granular systems, because they easily allow the visualization of the interior of the bed.

- The use of two-fluid model simulations to provide useful information that is difficult to measure in experimental facilities. This includes, for example, bubble eruption phenomena or the evaluation of the gas interchange through bubbles.

- The improvement of the predictive capabilities of two-fluid models for the case of pseudo-2D fluidized beds. In particular, because particle-wall interactions play an important role in these types of systems, an alternative boundary condition is developed using the micro-scale information obtained using DEM simulations.

- The experimental estimation and relative quantification of the frictional forces induced by the walls in pseudo-2D beds. The final aim of this objective is to determine whether the front and rear walls have an important impact on the measurements of pseudo-2D beds. In addition, the coefficient of friction, experimentally determined, can be relevant for the simulation models.

1.3 Methodology of the thesis

The methodology followed in the present thesis is based on the combination of numerical simulations with experimental evidence. In the dissertation, this is achieved in two ways. First, the experimental results can aid the practical validation of some particular aspect of the numerical simulations. Second, the simulations can be used more reliably to obtain detailed information about a certain aspect. Experimental measurement in granular media can be a difficult task. The common techniques have been previously explained, and each of them presents some type of disadvantage, such as the cost of the

facility, the spatial or temporal resolution, calibration and applicability only to experimental facilities. Therefore, using numerical simulations can be a good complementary tool for understanding fluidized bed systems.

Concerning the experimental methodology, direct DIA and PIV experimental data have been used in this work. The data were collected by Dr Sánchez Delgado, specifically used for the results presented in Chapter 2, and Dr Christoph R. Müller (ETH Zürich, Laboratory of Energy Science and Engineering), complementary data for the results presented in Chapter 3. The first experimental campaign was conducted at the University Carlos III of Madrid, whereas the second used published experimental data from experiments at the University of Cambridge. Experimental measurements found in the literature were used as well, for example, Laverman et al. (2008), for a system operated under similar conditions, to check the reliability of the measurements. Another different pseudo-2D beds was constructed at the University Carlos III to perform the experimental measurements presented in Chapter 6, which were performed by the present author.

Regarding the methodology followed for the numerical simulations, two-fluid model simulations were mainly used in this work. The work performed in the thesis initially used the software ANSYS Fluent (v 6.3.26), but continued with the software MFIX (Multiphase Flow with Interphase eXchages) because the latter is more specialised for the simulation of gas-solid systems. Additionally, the open source nature of MFIX helped to achieve a better understanding and control of the two-fluid model equations actually used, as well as to give the opportunity to modify the source code.

DEM simulation data were also used in this work. These data has been gently yielded by Dr Christoph R. Müller and Dr James R. Third from ETH Zürich, Laboratory of Energy Science and Engineering and were used for the results presented in Chapter 5 to compare with the two-fluid model as well as for the newly developed boundary condition.

The simulations were performed in desktop computers, workstation "IPY" (16 CPUs) (University Carlos III of Madrid) and cluster "POLLY" (132 CPUs) (ETH Zürich).

Except for the DIA and PIV experimental techniques employed in the Chapters 2 and 3, all the post-processing scripts were developed by the author using MATLAB® and Fortran programming languages.

1.4 Outline of the thesis

The dissertation is structured according to the chronological order of the studies performed.

In the first part of this dissertation (Chapter 2), a thorough comparison between the two-fluid model simulations and the experimental results of a pseudo-2D gas-solid fluidized bed is performed. Thanks to the experimental information extracted from DIA and PIV, the bubble behaviour and the motion of solids, respectively, can be obtained and compared with the simulation predictions. The results show that, despite the agreement found in the bubble behaviour, the mean particle velocity predicted by pure 2D simulations over-predicts the experimental results. This is attributed to the absence of the front and rear walls in the two-fluid model 2D simulations. The comparison of Chapter 2 demonstrates that for thin bed thicknesses, the effect of the front and the rear wall on the particle motion can be significant and should not be neglected.

To achieve a better understanding of the discrepancies encountered between the simulation and the experimental data in Chapter 2, the following chapters concentrate on the individual aspects, such as the motion of particles around isolated bubbles or the particle-wall interactions.

Chapter 3 of the dissertation studies the motion of solids around isolated and erupting bubbles using two-fluid model simulations and compares the results with several models found in the literature. The simulation results are in very good agreement with the potential flow model proposed by Davidson (Davidson and Harrison, 1963) and with experimental results for erupting bubbles.

Chapter 4 aims at characterising the gas interchange due to advection between the bubble and emulsion phases in a bubbling bed by means of two-fluid model simulations. The first part of this analysis is focused on the behaviour of the air through isolated bubbles rising in the bed; the results are again compared with the classical potential flow theory of Davidson (Davidson and Harrison, 1963). The isolated bubbles show nearly perfect agreement with the potential flow theory. Subsequently, the work analyses the gas interchange in a fluidized bed operated in the bubbling regime, motivated by the good agreement found for isolated bubbles. In this part, the potential flow theory for isolated bubbles is no longer valid. Therefore, to model the dependence of the gas interchange on the bubble size and superficial velocity, an analytical expression for the gas interchange is deduced.

Continuing the work of Chapter 2, where significant discrepancies between the two-fluid model simulations and the experimental data were found, Chapter 5 introduces a DEM model. The first part of this chapter studies the differences and similarities

of both the DEM and two-fluid model simulations of a pseudo-2D fluidized bed. The effects of the inter-particle and particle-wall coefficients of friction and the coefficient of restitution are studied, the coefficient of friction being the most influential parameter. In the second part of Chapter 5, a new partial-slip boundary condition for the solid phase in pseudo-2D fludized beds is developed using information of the micro-scale bed dynamics from the DEM simulation data, where the spatial resolution is higher. The new boundary condition is compared with the Johnson and Jackson boundary condition (Johnson and Jackson, 1987), which is commonly employed in two-fluid model simulations. The new boundary condition was implemented in a two-fluid model and shows more favourable results for pseudo-2D beds.

In Chapter 6, the pressure signal in a pseudo-2D bed is processed in combination with the solids distribution obtained from DIA to give an estimation of the frictional forces between the solids and the front and rear walls of the bed. As indicated previously, these forces are presumably responsible for the inability of pure 2D simulations to reproduce real pseudo-2D beds. Using a force balance, the resulting wall frictional forces can be estimated as a function of the pressure drop in the bed, the bed weight, as well as the velocity and acceleration of the centre of mass of the bed. The chapter concludes with an evaluation of the contribution of the frictional forces on the pressure fluctuation of the bed.

Finally, the conclusions obtained from this doctoral thesis are summarised in Chapter 7.

The flow chart in Figure 1.6 shows the evolution through the different chapters.

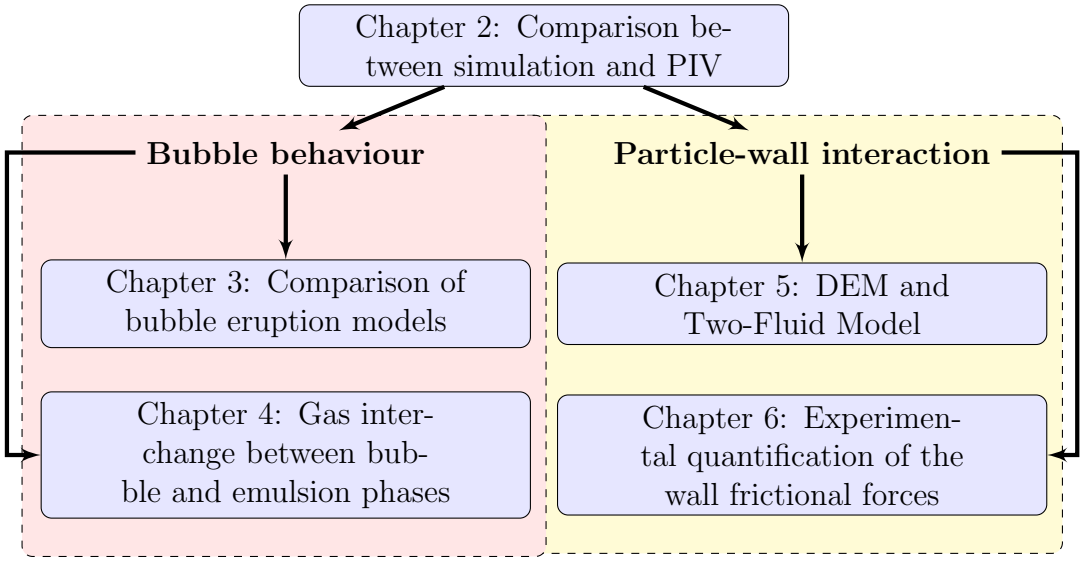

Figure 1.6: Flow chart showing the outline of the thesis.

As a result of the work in this thesis, the following papers have been published or

submitted for publication.

- The work from Chapter 2 resulted in the following publication: Comparison between two-fluid model simulations and particle image analysis & velocimetry (PIV) results for a two-dimensional gas-solid fluidized bed. *Chemical Engineering Science* 66, 3753-3772, 2011. F. Hernández-Jiménez, S. Sánchez-Delgado, A. Gómez-García, A. Acosta-Iborra.

- The work from Chapter 3 resulted in the following publication: Comparison of bubble eruption models with two-fluid simulations in a 2D gas-fluidized bed. *Chemical Engineering Journal* 171, 328-339, 2011. F. Hernández-Jiménez, J.R. Third, A. Acosta-Iborra, C.R. Müller.

- The work from Chapter 4 resulted in the following publication: Gas interchange between bubble and emulsion phases in a 2D fluidized bed as revealed by two-fluid model simulations. *Chemical Engineering Journal* 215-216, 479-490. 2013. F. Hernández-Jiménez, A. Gómez-García. D. Santana, A. Acosta-Iborra.

- The work from Chapter 6 resulted in the following work: Experimental quantification of the particle-wall frictional forces in pseudo-2D gas fluidized beds. *Submitted for publication.* F. Hernández-Jiménez, J. Sánchez-Prieto. A. Soria-Verdugo, A. Acosta-Iborra.

The following conference presentations are also an outcome of the thesis.

- The first part of Chapter 5 resulted in: Critical evaluation of Euler-Euler and Euler-Lagrangian modelling strategies in a 2D gas fluidized bed. *Proceedings of CFB10 Conference*, 432-93, 2011. F. Hernández-Jiménez, J.R. Third, A. Acosta-Iborra, C.R. Müller.

- The work from Chapter 4 was initially motivated by: Characterization of the gas interchange between bubble and emulsion using two-fluid model simulations. *Proceedings of 21FBC Conference*, 56, 2012. F. Hernández-Jiménez, A. Gómez-García, D. Santana, A. Acosta-Iborra.

- The second part of Chapter 5 resulted in: Euler-Euler and Euler-Lagrangian evaluation of a pseudo 2D gas fluidized bed: an estimation of the wall boundary condition from DEM. *Proceedings of FLUIDIZATION XIV Conference*, 161, 2013. F. Hernández-Jiménez, J.R. Third, A. Acosta-Iborra, C.R. Müller.

- The work from Chapter 6 was initially motivated by: Linking of the pressure oscillations in a pseudo two-dimensional bed with the spatiotemporal distribution of particles. *Proceedings of FLUIDIZATION XIV Conference*, 180, 2013. F. Hernández-Jiménez, J. Sánchez-Prieto, A. Soria-Verdugo, Acosta-Iborra.

Further work has also been published in the following refereed journals or conference presentations:

- Experimental and computational study on the bubble behavior in a 3D fluidized bed with a vertical-axis, rotating distributor. *Proceedings of FLUIDIZATION XIII*, 50, 2010. A. Acosta-Iborra, C. Sobrino, F. Hernández-Jiménez, M. de Vega.

- Experimental and computational study on the bubble behavior in a 3-D fluidized bed. *Chemical Engineering Science* 66, 3499-3512, 2011. A. Acosta-Iborra, C. Sobrino, F. Hernández-Jiménez, M. de Vega.

- A novel methodology for simulating vibrated fluidized beds using two-fluid models. *Chemical Engineering Journal* 198-199, 261-274, 2012. A. Acosta-Iborra, F. Hernández-Jiménez, M. de Vega, J. Villa-Briongos.

Chapter 2

Comparison between two-fluid model simulations and experimental DIA-PIV results of a pseudo-2D bubbling gas-fluidized bed

Contents

2.1 Abstract

This chapter compares simulation and experimental results of the hydrodynamics of a two-dimensional, bubbling air-fluidized bed. The simulation in this study has been conducted using an Eulerian-Eulerian two-fluid approach based on two different and well-known closure models for the gas-particle interaction: the drag models due to Gidaspow and Syamlal - O'Brien. The experimental results have been obtained by means of Digital Image Analysis (DIA) and Particle Image Velocimetry (PIV) techniques applied on a real bubbling fluidized bed of 0.005 m thickness to ensure the two-dimensional behaviour. In this work, several results have been obtained from both simulation and experiments and mutually compared. Previous studies in literature devoted to the comparison between two-fluid models and experiments are usually focused on bubble behaviour (i.e. bubble velocity and diameter) and dense-phase distribution. However, the present work examines and compares not only the bubble hydrodynamics and dense-phase probability within the bed, but also the time-averaged dense-phase velocity, the air troughflow and the instantaneous interaction between bubbles and dense-phase.

Besides, quantitative comparison of the time-averaged dense-phase probability as well as the velocity profiles at various distances from the distributor has been performed by means of the definition of a discrepancy factor, which accounts for the quadratic difference between simulation and experiments The resulting comparison shows and acceptable resemblance between simulation and experiments for dense-phase probability, and good agreement for bubble diameter and velocity in two-dimensional beds, which is in harmony with other previous studies. However, regarding the time-averaged velocity of the dense-phase, the present study clearly reveals that simulation and experiments only agree qualitatively in the two-dimensional bed tested, the vertical component of the simulated dense-phase velocity being nearly an order of magnitude larger than the one obtained from the PIV experiments. This discrepancy increases with the height above the distributor of the two-dimensional bed, and it is even larger for the horizontal component of the time-averaged dense-phase velocity. In other words, the results presented in this work indicate that the fine agreement commonly encountered between simulated and real beds on bubble hydrodynamics is not a sufficient condition to ensure that the dense-phase velocity obtained with two-fluid models is similar to that from experimental measurements on two-dimensional beds.

2.2 Introduction

The majority of the works comparing two-fluid models and experiment results are primarily focused on the behaviour of bubbles, bed expansion, pressure signals and time-averaged solids or gas volume fractions. The literature on this topic is abundant; from the earlier works of Boemer et al. (1998); Van Wachem et al. (1998), to the more recent studies comprising image analysis (Busciglio et al., 2009), particle drag optimization procedures (Vejahati et al., 2009), and time-averaged volume fraction (Deza et al., 2009; Min et al., 2010). Particularly, the works of Deza et al. (2009) and Min et al. (2010) show a reasonable agreement between 2D and 3D simulations and X-ray imaging experiments of cylindrical fluidized beds of 9.5 cm and 15.2 cm respectively. It is worth noticing that, in concordance with the two-phase theory of gas fluidized beds (Davidson and Harrison, 1963), the velocity and growth of bubbles in a gas fluidized bed primarily depends on the emulsion equivalent density (related to void fraction) and the excess of gas, being less relevant other factors such as the size of the bed and the dense phase motion (Kunii and Levenspiel, 1991). Besides, several studies demonstrate that the simplified two-phase theory describes fairly well the behaviour of bubbles in three- and two-dimensional beds (see for example Darton et al. (1977); Shen et al. (2004)).

However, it seems necessary to extend the classical bubble behaviour validation to other macroscopic characteristics such as the mean particle motion. The mean particle motion is a key factor in the motion and mixing of small and large particles (e.g. biomass) in bubbling fluidized beds (Kunii and Levenspiel, 1991). With the development of CCD cameras and Particle Image Velocimetry (PIV) or other velocimetry techniques, there are several studies showing experimental information on particle velocity in very thin, fluidized beds, whose behaviour can be considered two- or quasi-two dimensional (e.g. Bokkers et al. (2004); Liu et al. (2005); Santana et al., (2005); Almendros-Ibáñez et al. (2006); Laverman et al. (2008); Sánchez-Delgado et al. (2010). At this regard, reported mean particle velocities are clearly smaller than the characteristic bubble velocity in two-dimensional beds working with Geldart B particles and superficial velocity around 2 times the minimum fluidization velocity . For example, tracking the individual particle trajectories in a quasi two-dimensional bed of 0.022 m thickness, Jung et al. (2005), measured the time-averaged vertical velocity of particles far from the lateral walls, obtaining an ascending vertical velocity of value around 0.12 m/s. Using PIV in a two-dimensional bed of 0.015 m thickness, Laverman et al. (2008), obtained peak velocities over 0.075 m/s and 0.11 m/s for, respectively, the upward and downward mean flow of particles at a vertical distance of 0.15 m from

the distributor. These values are for beds of relatively small lateral width (i.e. 0.15 m) at 0.14 to 0.15 m height over the distributor, being the particle velocities smaller if the bed width is increased (Laverman et al., 2008). It seems, however, that the vertical velocity of particles in three-dimensional beds (Lin et al., 1985) can be larger than in two-dimensional beds, especially for superficial velocities of more than 3 times.

Inspection of open literature reveals that, only recently, a reduced number of works make a comparison between the mean particle motion of experiments and two-fluid model simulations. Jung and Gidaspow (2006), and also Dan et al. (2010), presented simulation results of a gas fluidized bed with 0.022 m thickness and 0.15 m width. Among other results, they compared the simulated time-averaged particle velocity with previous experiments of a similar bed (Jung et al., 2005). The comparison was performed at a height of 0.14 m from the distributor in the central part of the bed plane (i.e. far from the lateral walls), and the level of agreement shown was excellent. Lindborg et al. (2007), made a qualitative comparison of the velocity vector fields of two-dimensional simulations and three-dimensional measurements taken from Lin et al. (1985). This was equally done by Hosseini et al. (2010), incorporating also in the comparison the velocity vectors from Laverman et al. (2008). These results evidence a clear resemblance in the particle recirculation patterns obtained in simulation and experiments, but it appears that the simulations over-predict the modulus of the particle velocity vectors for small superficial velocities ($U/U_{mf} = 1.65$ in Lindborg et al. (2007)), and that the prediction of the vertical position of the recirculation centre is not completely satisfactory (Hosseini et al., 2010). Ahuja and Patwardhan (2008), for $U/U_{mf} = 5.6$, as well as Wang and Liu (2010), this last study using FCC particles, compared their two-dimensional simulation results with three-dimensional experiments and found acceptable agreement in the radial profiles of velocity. Li et al. (2010) compared the experimental results from the work done by Laverman et al. (2008) in a pseudo 2D fluidized bed with 2D and 3D simulations using the drag model of Gidaspow. Their results, accounting for a bed column of 1.5 cm thickness and 30 cm width, indicate that there is a great discrepancy with the experimental particle velocities when the system is modelled as a pure 2D plane due to the lack of interaction with the frontal and rear walls. Note that these works use for the quantitative comparison experimental results from three-dimensional beds or are restricted to a small portion of a quasi two-dimensional bed.

Despite the available experimental techniques, none of the above described studies on simulation verification and validation have performed a systematic quantitative comparison of two-fluid models and PIV results in the whole plane of a two-dimensional bed combining reduced thickness (less than 0.01 m), relatively large width, and a small

superficial velocity ($U/U_{mf} \leq 2$). Such comparison would be interesting since it could be used, not only as a verification tool for the two-fluid model employed, but also as a complementary source of information in the interpretation of PIV data.

The present chapter performs a comparison between Eulerian-Eulerian two-fluid simulation and experimental results of a two-dimensional gas-solid fluidized bed working in the bubbling regime. In particular, thanks to the use of non-intrusive techniques based on digital image analysis (DIA), the time-averaged distribution, size and velocity of bubbles taken from experiments in a quasi two-dimensional bed are compared with the simulation results of the same bed computed with several implementations of two-fluid models. Furthermore, this comparison is extended to the particle phase velocity outside bubbles, which, in the case of the experiments, is obtained after applying particle image velocimetry (PIV) techniques. The simulation comprises two different closures: Gidaspow (Gidaspow, 1994) and Syamlal - O'Brien (Syamlal and O'Brien, 1987) drag models. All the closure models are used in standard form to reveal their original behaviour, and no adjustment of coefficient is then performed. The final aim of this multiple comparison is to show whether the level of similarity between simulation and experiments encountered in bubble kinetics is also present, or not, in particle phase velocity. Unexpectedly, the results obtained in the present work seem to indicate that, despite the reasonable agreement reached in bubble size and velocity, any of the Eulerian-Eulerian two-fluid models tested overpredicts the mean particle velocity by nearly an order of magnitude compared to the experimental PIV results.

2.3 Experimental facility and data acquisition

The experimental facility used for the comparison of the computational data is a two-dimensional cold fluidized bed of dimensions 0.5 x 2 x 0.005 m (width W, height h, and thickness, Z) (Sánchez-Delgado et al., 2010). Figure 2.1 shows a schematics of the facility. The fluidized bed was filled with ballotini glass particles of Geldart-B, 2500 kg/m^3 density, and 0.6-0.8 mm diameter. That means that in the tested bed there are less than 9 particles in the bed thickness direction, which ensures the 2-D dimensionality of the bed (Nedderman and Laohakul, 1980). The fixed bed height was $h_1 = 0.3$ m, and the superficial velocity at minimum fluidization conditions, U_{mf}, was 0.35 m/s. A very small fraction of the particles (less than 1%) were black instead of transparent in order to enhance the tracking of the solids phase by improving the peak detection in the PIV correlation matrix. Therefore, in principle, 3-D effects such as velocity components and gradients along the thickness direction are not going to appear and are not needed to be included in the simulation. The air distributor consists of

a perforated plate with 50 holes of 0.001 m diameter spaced 0.01 m apart. The front wall was made of glass and the rear wall was made in aluminium, covered by a black card to increase the contrast in the images. The superficial gas velocity (U_0 = 0.62 m/s) was fixed to 1.75 times U_{mf}.

Two 650 watts spotlights were used to get a uniform illumination of the bed. A high speed video camera, Redlake Motion pro X3, took images of the front view of the fluidized bed at 125 frames per second. In order to increase the spatial resolution of the images for bubble probability and, specially, dense phase velocity, only half of the bed was recorded: from one lateral wall of the fluidized bed to the central vertical line of the bed. Figure 2a shows an example of the particle images taken from one half on the bed in which the dark regions are the ascending bubbles. From the statistical point of view, the rest of the fluidized bed was symmetrical in behaviour to the recorded portion. In this way, the dimensions of the images taken were 0.25 x 0.32 m ($w1$ x $h1$ in 2.1) corresponding to (992 x 1270 pixels). On the other hand, for bubbles properties such as equivalent diameter and velocity, it is not needed a great resolution, so bubbles data can be obtained from images taken from the entire bed.

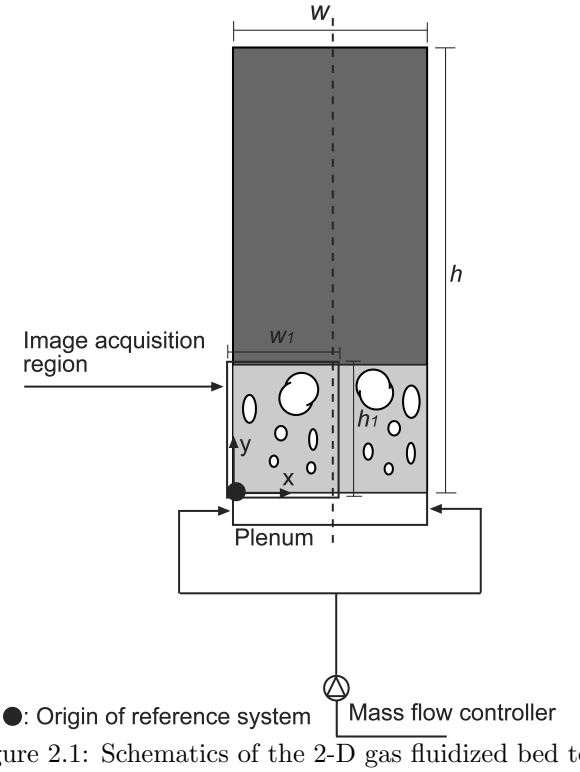

Figure 2.1: Schematics of the 2-D gas fluidized bed tested

The images from this experimental set-up were processed by means of DIA techniques to obtain the instantaneous bubble size as well as the bubble velocity (i.e. velocity vectors) within the two-dimensional domain. Particularly, size and centroid position were extracted from the images after performing a threshold that separated

gas from dense phase (see Otsu (1979)). Therefore, each pixel of each image was classified as bubble ($C = 0$) or dense phase ($C = 1$). This is represented in 2.2b as black and white areas respectively. The images were summed and rescaled with the total number of images processed, producing a time-averaged image that represents the proportion of time that a point is occupied by solid, $\overline{C}(x, y) = \sum_{i=1}^{N} C_i(x, y)/N$, where N is the number of images, therefore, the proportion of time that a point is occupied by bubbles is defined as $\overline{B} = 1 - \overline{C}$. $\overline{B}$ and $\overline{C}$ may be respectively interpreted as the bubble and dense phase probability.

Regarding the dense phase velocity, it was calculated by means of a particle image velocimetry (PIV) technique applied to the images. The particular implementation of the technique is also explained in Sánchez-Delgado et al. (2010), and is based on the correlation of consecutive-in-time images using the multigrid PIV code MATPIV (Sveen, 1998-2007). Interrogation windows of 16 x 16 pixels with 0.5 overlap were typically used in this PIV analysis performed to compute the velocity field of the dense phase. Following the procedure of Laverman et al. (2008) in order to correct the influence of particle raining from the roof of bubbles, the time-averaged velocity was calculated as:

$$V(x, y) = \sum_{i=1}^{N} C_i(x, y) v_{s,i}(x, y) / \sum_{i=1}^{N} C_i(x, y) \tag{2.1}$$

Since C is null inside bubbles, it is only necessary to obtain the particle velocities outside them. Note that bubbles are regions relatively free of particles and the PIV results there may not be reliable. Therefore, mean velocities were calculated from PIV results outside bubbles after applying a mask that rejects dense phase velocity inside bubbles. This is indicated in 2.2b, which contains an example of the instantaneous velocity vector field of the dense phase. For illustrative purposes the number of vectors per unit area has been reduced in this figure. According to the standard theory of PIV measurement (Raffel et al., 2007), the estimation of each velocity vector can be affected by bias and subpixel errors. In a uniformly illuminated bed, bias errors are principally generated by velocity gradients whose scale is smaller than the interrogation window. In the present work the bias error has been reduced thanks to the use of multigrid PIV techniques that employ very small interrogation windows at the final PIV processing stage. The size of these windows is 16 x 16 pixels (about 8 mm size), which is shorter than the principal velocity scales of the problem. Peak-locking and background noise are the main source of subpixel error in a two-dimensional velocity field. As the concentration of particles in the dense phase is high, the background noise and the peak-locking are not expected to have a relevant impact in the accuracy of

the results (Raffel et al., 2007). All these effects, together with the unsteady character of the bed, contribute to the uncertainty of the time-averaged results. One way to quantify an upper bound for the overall uncertainty of the time-averaged results is to evaluate the standard deviation of the average from a series of independing data blocks (Laverman et al., 2008). In the present study, data blocks containing each one over 1000 image pairs were used and compared with a long-term average. Following this procedure, the upper bounds of the uncertainty for the time-average vertical velocity, horizontal velocity and dense-phase probability are 4.84%, 11% and 1% respectively. The larger uncertainties are typically obtained near the bed surface.

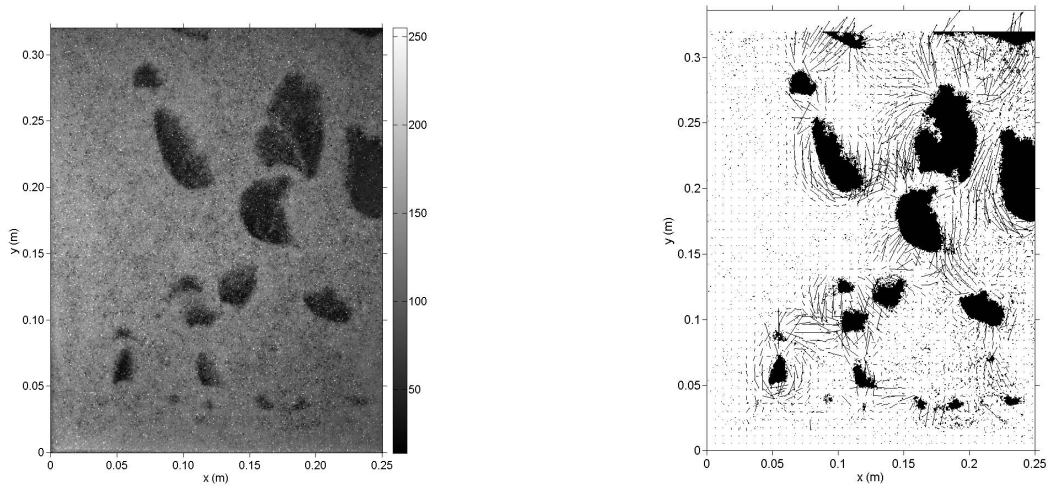

(a) (b)

Figure 2.2: Processing of experimental results: (a) instantaneous particle image of half portion of the bubbling fluidized bed; (b) bubble mask and PIV velocity vectors for dense phase.

2.4 Computational Model

The numerical simulation, performed by solving the conservation equations of mass and momentum and granular temperature using FLUENT 6.3.26 CFD software (Fluent, 2006). A multifluid Eulerian model was applied, where gas and solids (i.e. particles) are treated as two interpenetrating phases. The kinetic theory of granular flow, which deals with the conservation of the stochastic fluctuation of solids kinetic energy, was used for the closure of the solids stress terms. Two drag models were employed to solve the interaction between both phases: Gidaspow drag function (Gidaspow, 1994) and Syamlal - O'Brien drag function (Syamlal and O'Brien, 1987; Syamlal et al., 1993). Gidaspow drag model was selected due to the robustness in convergence that it showed during the simulation campaign of the present study. Previous studies (Taghipour et

al., 2005) have shown little differences between Gidaspow and Syamlal - O'Brien model, nevertheless, simulations with this two drag models have been carried out in order to compare them. The governing equations as well as the closure expressions for both drag models can be found in Appendix A.

A second order scheme was used to discretized the convective derivatives: Second order implicit for time advance formulation, Phase Coupled SIMPLE for pressure-velocity coupling, Second Order Upwind for Momentum and Granular Temperature, QUICK for volume fraction. The 2D computational domain was discretized using 20301 nodes in a structured but inhomogeneous mesh of rectangular cells. The mesh size has been chosen on the basis of a sensitivity analysis on the mesh density shown on the following section. A time step of 5e-4 seconds, with 75 iterations per time step, was chosen in order to ensure the convergence of the problem for the Gidaspow drag model. The Syamlal - O'Brien drag function was solved with the same time step, but 100 iterations per time step were needed in order to ensure its convergence. Further details of the solution procedure can be found in Appendix A The restitution coefficient implemented was 0.9, which is an acceptable value reported in the literature for glass particles (Syamlal and O'Brien, 1987). Note also that this value includes the effects of energy dissipation due to the particles inelastic deformation and frictional losses (Goldschmidt et al., 2001).

A laminar regime for the gas phase and the walls were modelled employing the standard no-slip boundary condition for both phases. This condition ensures that particle velocity profiles are in good agreement with the experimental results (see next section). A simple pressure boundary condition was imposed at the top of the freeboard (outlet vent with null lost coefficient). The inlet gas velocity was modelled with a uniform profile, which can be considered similar to that appearing in porous plate distributors and a first approximation for perforated plate distributors. The initial solids volume fraction chosen for the simulation starting was $\alpha_s = 0.6$, and the selected maximum packing limit is $\alpha_{s,max} = 0.63$. The particle diameter selected corresponds to the averaged diameter of particles used in the experimental set-up section. More information on the geometrical and operative conditions of the simulated fluidized bed can be encountered in Table 2.1.

Figure 2.3 illustrates the computational domain employed in the present study, which involves only the two-dimensional fluidized bed, that is to say, without considering the plenum and the distributor, and its dimensions correspond to the experimental facility (0.5 x 0.2 m). As Figure 2.3 shows, the rectangular grid concentrates toward the inlet in order to improve the spatial resolution in the bubble formation region. Note that, due to the stochastic nature of the bubble distribution in the fluidized bed, the

Table 2.1: Main simulation parameters.

Parameters	**Values**
Particle density, ρ_s	2500 kg/m^3
Gas density, ρ_g	1.225 kg/m^3
Particle diameter, d_s	700 μm
Restitution coefficient, e_{ss}	0.90
Initial solids volume fraction, α_s	0.6
Bed width, W	0.5 m
Bed height, h	2 m
Static bed height, h_1	0.3 m
Drag function, K_{gs}	Gidaspow, Syamlal - O'Brien
Wall boundary condition	No-slip
Inlet boundary condition	Velocity inlet
Outlet boundary condition	Pressure outlet
Regime	Laminar
Time step	5e-4 s

computational domain covers all the bed volume and not only the half plane used for the experimental data acquisition. In this figure the computational mesh is presented with its boundary condition together with a snapshot of the solids volume fraction obtained after simulating a time period of 20 seconds.

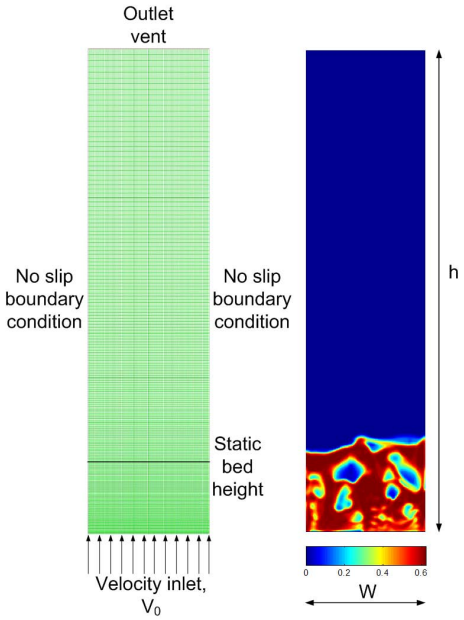

Figure 2.3: Computational domain with the boundary conditions used in the simulations (left) and a snapshot of solids volume fraction in the bed after 20 seconds of simulation (right).

2.5 Results comparison

The post-processed data from the simulation have been compared with the experimental data. The time used for averaging the experimental data was 26 seconds, excluding the transient fluidization start, with a frame rate of 125 Hz which gives a total number of 3271 images. For the calculation of the time-averaged quantities 35 seconds were simulated. The first 5 seconds of the simulation start-up were removed in order to eliminate the initial transient behaviour of the bed. By this way, the actual time period employed for the evaluation of the time-average quantities in the simulation was 30 seconds, which is comparable to the time period used in the experiments. In the simulation, data was exported every 5e-3 real-time seconds, which gives 6000 frames to post-process. The difference between the number of frames used in the simulation and the experiments should not affect the results because the bed is under statistically steady conditions. The main results of this comparison are described in the following subsections.

It has to be said, that in order to be consistent with the technique employed in the experiments, where raining particles inside bubbles are not taken into account (as done in Laverman et al. (2008)), the same technique has been developed with the simulation results. On each frame on either simulation or experiment, the velocity obtained is imposed to be null inside bubbles. The choice of the threshold value for the solids volume fraction in the simulation campaign will be discussed in section 2.5.2.

2.5.1 Sensitivity of results on mesh density

The influence of the number of nodes on the results has been studied for the reference case described in Table 2.1. This sensitivity of the results on the mesh density can be considered as indicative of the level of discretization error in the simulation. Figure 2.4 contains some examples of time-averaged results for the reference case (Table 2.1) using a refined mesh of 80601 nodes and a coarse mesh of 10431 nodes, compared with the simulation results for the mesh of the previous sections (20301). Each result has been normalized with the simulation output of the case using a mesh of 20301 nodes. In the figure, the VOF mean value variable corresponds to the time-averaged of the mean dense phase volume fraction over the whole bed plane. Also in Figure 2.4 the recirculation centre height refers to the mean height of the two main recirculations of solids in the bed, and the bubble probability is the discrepancy in bubble probability over the whole bed (see following section).

Although some differences between the case of 20301 nodes and the case of 80601 can be find in Figure 2.4, these differences constitute less than 10% of the resultant

values. In contrast, a mesh of 10431 nodes leads to larger differences in the parameters shown in Figure 2.4. The time of computation and the effort required for the image analysis of the refined mesh was more than 4 times that of the mesh for 20301. Thus, a mesh with 80601 nodes yields little changes in the results compared to a mesh of 20301 nodes but much more computational effort.

In addition, the average solids volume fraction in a middle point of the bed ($x = 0.25$ m, $y = 0.25$ m) has been calculated after 30 seconds of simulation for the three tested meshes. Also the computational cost (time to complete each computation) is included for a simulated time of 30 seconds. Taking into account all the results on the grid sensitivity, it seems that the mesh with 20301 provides simulation results very similar to the refined mesh (80601 nodes) while requiring a quarter of computational effort. Therefore, this justifies the use of the mesh with 20301 nodes as the default option in the present work.

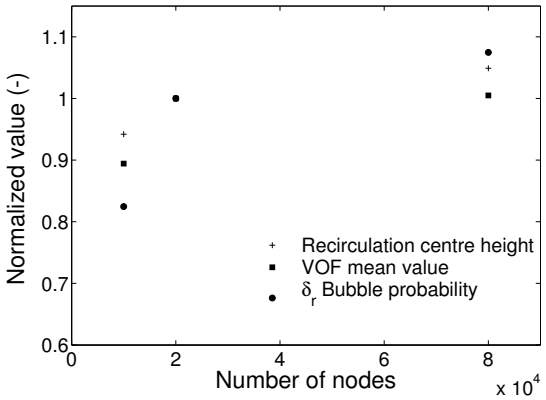

Figure 2.4: Sensitivity of time-averaged results on the mesh density.

Table 2.2: Sensitivity results on the mesh density.

Mesh (number of nodes)	**min δx (m)**	**min δy (m)**	**Average solids volume fraction**	**Computational cost (h)**
10431 (57x183)	0.0089	0.0039	0.4853	∼100
20301 (101x201)	0.005	0.0028	0.5019	∼200
80601 (201x401)	0.0025	0.0014	0.5095	∼800

2.5.2 Bubble probability and time-averaged particle velocity

Figures 2.5a and 2.5b compares the bubble probability maps from the experimental measurements and the simulation using the parameters of Table 2.1. In the construction of the probability maps, the simulation results were processed in the same way as described for the particle image, that is, assuming a value of 0 at the points of the

simulated fluidized bed that are inside a bubble and a value 1 otherwise. Note that this methodology eliminates the continuous transition of particle void fraction that connects the interior to the exterior of the bubbles in the simulated results. A threshold value of 0.3 in particle volume fraction was used to separate the interior from the exterior of a bubble.

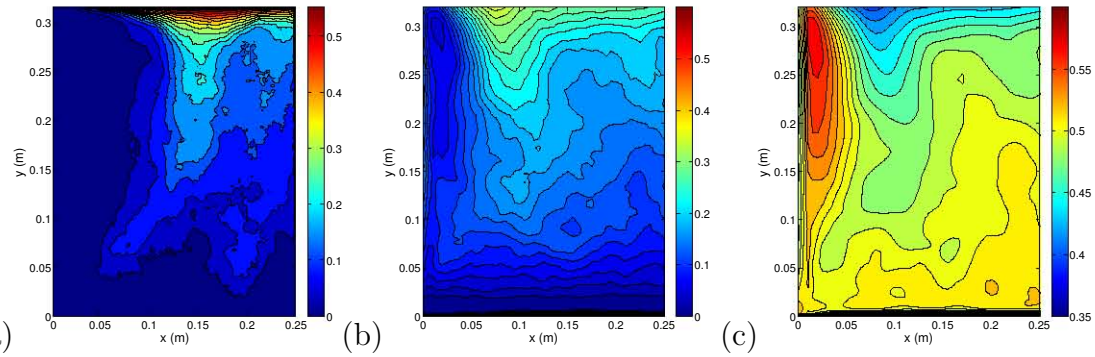

Figure 2.5: Bubble probability, $\overline{B}$, maps calculated from the experimental results (a), simulation results using Gidaspow drag model (b). A map of mean volume fraction of particles, $\overline{\alpha_s}$, is also included (c).

The lowest values in bubble probability, for both numerical and experimental results, appear at the bottom of the bed and near the walls. This indicates, as expected, that bubbles are less frequent near the lateral walls of the bed and smaller in size near the distributor. Paying attention to the bubble channelling, it can be observed that the highest bubble probability is near the free surface and also in a vertically aligned region in the bed created by the tendency of bubbles to ascend through the same path (i.e. bubble channel). The bubble channelling is less intense in the computed than in the experimental bed. This indicates that the simulation model of Table 2.1 provides a better distribution of bubble than the experiment. This can be attributed to the effect of the distributor, a uniform velocity profile was selected for the simulation whereas the experiment used a perforated plate with a certain number of orifices. In the experiment, the bubble generation is limited to the position of the orifices but in the simulation it is homogeneous along the width of the distributor.

One interesting question is whether the bubble probability maps obtained are equivalent or not to the mean void fraction concentration maps. Or, otherwise, it would be useful to know if dense phase probability maps (i.e. one minus the bubble probability) may be used to estimate the mean volume fraction of particles in a bubbling fluidized bed. Since the maps of both dense phase probability and mean volume fraction of particle are directly available from the numerical results, the simulation can be used to give an answer to this question. For this purpose, the mean volume fraction of particles, Figure 2.5c, has been calculated from the simulation described in Table 2.1.

From the comparison of Figures 2.5b and 2.5c it is clear that the bubble probability distribution pattern and the mean volume fraction of particles are very similar.

A more detailed comparison of bubble and dense phase probability results has been done at different bed heights: close to the distributor, $y = 0.05$ m, at the half of the bed, $y = 0.15$ m, $y = 0.25$ m, and at a region close to the freeboard, $y = 0.30$ m. In particular, Figures 2.6a and 2.6c compares the experimental and simulation profiles of bubble probability and mean dense phase vertical velocity, $\overline{V_y}$, for a horizontal cut at 0.25 m from the distributor. Apart from the drag model of Gidaspow (Gidaspow, 1994) used as reference case, Table 2.1, a complementary simulation is also included in Figure 2.6b relying on the same operating parameters as the reference case but using the Syamlal - O'Brien drag model (Syamlal and O'Brien, 1987). In experimental as well as numerical results, the bubble probability increases towards the centre of the bed due to the mentioned channelling of bubbles (i.e. $x = 0.25$ m in Figure 2.5a). However, the channelling region is wider in the numerical results due to a better distribution of bubbles in the computed bed. This effect is present in both models, but seems to be more pronounced in the simulation with the Syamlal - O'Brien drag model. Interestingly, all the simulations show an increment in bubble probability near the wall that is not observed in experiments. This indicates that the bubbles in the numerical simulation are more prone to attach to the wall than in the experiments. This can be explain with the effect of the distributor. In the experiment, the orifices close to the lateral walls are limited to generate bubbles towards the centre of the bed, whereas in the simulation this limitation is less pronounced because the uniform velocity profile imposed at the bottom of the bed.

A comparison of time-averaged vertical velocities of solids particles, $\overline{V_y}$, is shown in Figure 2.6c, where it can be seen that although the trends are similar, the magnitude of the numerical velocities are higher, especially when using the drag model from Syamlal - O'Brien. This fact indicates that the simulated bubbles impel upwardly the dense phase in a more effective way than the actual bubbles in the experimental bed. As a result, sharper gradients of descending appear near the wall in the simulation results compared to the PIV measurements. Due to the wide bubble path shown by the simulation, the time-averaged downward velocity has a peak value closer to the wall than the experiments. As the experimental time-averaged particle velocity is very small compared to the simulated one, the PIV velocity profiles are nearly flat in Figure 2.6c. Particularly, for the downwardly moving mean flow of particles (close to the wall) the minimum velocity is of order 0.02 m/s, whereas far from the walls the peak of ascending velocity is 0.015 m/s. Note that these very reduced values of particle velocity are also observed in the work of Laverman et al. (2008). For illustrative purposes, experimental

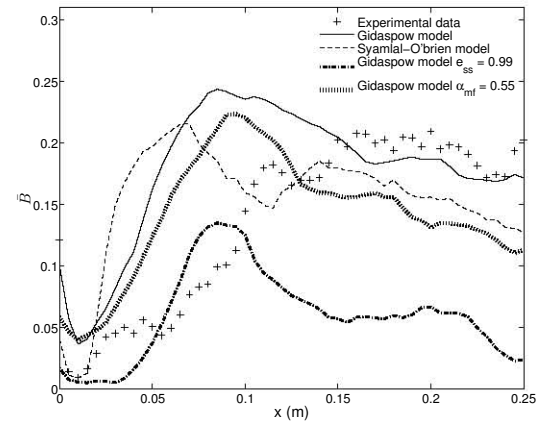

(a)

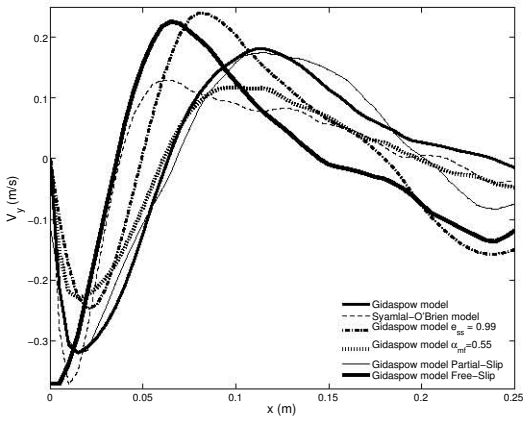

(b)

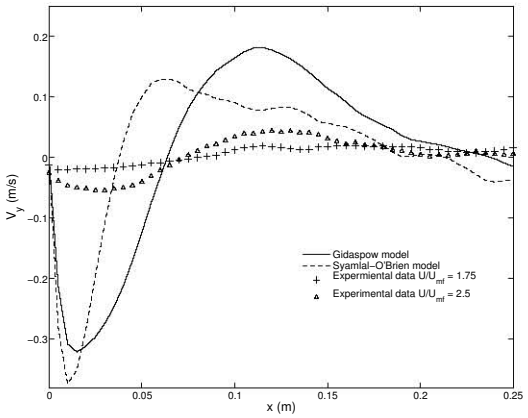

(c)

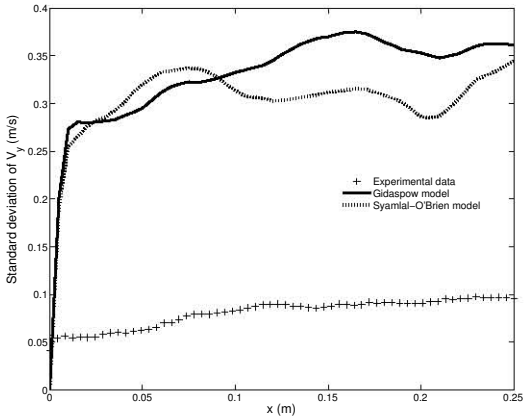

(d)

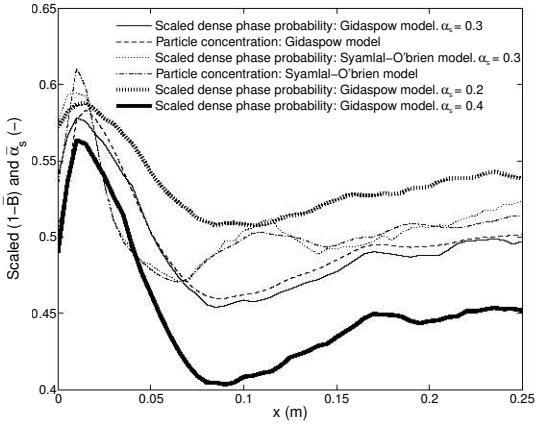

(e)

Figure 2.6: Comparison of simulation and experimental profiles at y = 0.25 m for $\overline{B}$ (a), and time-averaged velocity of dense phase (b) and (c), and its standard deviation (d). Also, included the comparison of scaled dense phase probability, $\overline{C}\alpha_{s,mf}$, and mean solids volume fraction, $\overline{\alpha}_s$, calculated from the simulation (e).

results for $U/U_{mf} = 2.5$ are also included in Figure 2.6c. These experimental results demonstrate that after increasing the superficial gas velocity from $U = 1.75U_{mf}$ to $2.5U_{mf}$, the magnitude of time-averaged particle velocity remains very small compared to the simulation.

The largest velocity gradients and the velocity peak closest to the wall are found in Figure 2.6b for the Syamlal - O'Brien model. Therefore, in view of Figure 2.6a-b, of the two drag models tested in the present two-dimensional configuration of fluidized bed, the drag model of Gidaspow seems to yield the closest qualitative results to the experimental profiles of bubble probability and dense phase velocity. However, the discrepancies in magnitude between the time-averaged particle velocity of the simulation using Gidaspow drag model and the experimental results for the two-dimensional bed of Table 2.1 are still enormous. When the simulation is performed increasing the restitution coefficient to $e_{ss} = 0.99$, the time-averaged velocity is reduced up to a 70% from the $e_{ss} = 0.9$, as Figure 2.6b indicates, but the particle velocity overestimation continues to be very appreciable and the simulated profiles of bubble probability clearly separates from the experiments for x $>$ 0.1 m (Figure 2.6a). The time-averaged velocity of particles is also diminished by reducing the initial solids volume fraction of the simulation to an arbitrary small value $\alpha_s = 0.55$, instead of the more realistic bed parameter $\alpha_s = 0.6$, and maintaining the rest of operative conditions of Table 2.1. As in the case of increasing the coefficient of restitution, the price to be paid with the diminishing of α_s is the reduction of the simulated bubble probability near the bed centre ($x = 0.25$ m). Furthermore, it seems that increasing e_{ss} or α_s, also eliminates the qualitative agreement between the velocity profiles. This is shown in Figure 2.6b, in which the velocity profiles for the simulation using Gidaspow drag model with $e_{ss} = 0.99$ or $\alpha_s = 0.55$ are characterised by a downflow motion of particles at $x = 0.25$ m that is more intense than the obtained for original parameters $e_{ss} = 0.9$ and $\alpha_s = 0.6$.

Figure 2.6b also illustrates that the no-slip boundary condition imposed in the simulation for the solids phase is as approximately verified in the experimental results. However, the region in which descending particles are slowed down by the lateral walls is larger in the experiments than in the simulation, suggesting that perhaps other effects such as frontal and posterior walls friction are influencing the measured bed in this region. Profiles for two different lateral boundary conditions have been included, i.e. free-slip (specularity coefficient = 0) and partial-slip (specularity coefficient = 0.6), in order to ensure that the overestimation of the solids velocity is not a consequence of the lateral walls boundary condition. As it can be seen, the three conditions give velocities in the same order of magnitude and generate the same bed behaviour. Taking this into account, the effects of the lateral walls boundary condition will not be longer

discussed in this paper.

Figure 2.6d shows the standard deviation of the solids phase velocity shown in Figure 2.6b, comprising the experimental results, as well as the simulation results using Gidaspow and Syamlal - O'Brien drag models. The standard deviations have been obtained in each point time-averaging the squared difference of the instantaneous vertical velocity and its mean value. The standard deviation of the velocity follows the same trend than the time-averaged values. Note that the simulation gives values an order of magnitude higher than the experiments. Obviously close to the wall, the standard deviation calculated from the simulation tends to zero as no-slip conditions were selected. Nevertheless, this happens for a small region near the wall that do not affects the rest of the bed. In the experimental results this decrement of the standard deviation of the velocity is also appreciated but not with the same intensity.

As mentioned previously, in order to compare dense phase probability with mean particle concentration, it is necessary to rescale one of the variables. In Figure 2.6e, the horizontal profile of the dense phase probability has been rescaled, by multiplying it by 0.6, and depicted together with the mean particle concentration from simulations that use Gidaspow and Syamlal - O'Brien drag models. Clearly, the dense phase probability is practically equal to the mean volume fraction of particles. This is probably due to the nearly uniformity of the void fraction in the dense phase outside bubbles. In consequence, Figure 2.6e encourages the use of the scaled dense phase probability as a good approximation to the mean volume fraction of particles in bubbling fluidized beds.

In addition, Figure 2.6e illustrates the scaled dense phase probability for different bubble detection thresholds. This representation clearly shows that using 0.3 as threshold ensures that the simulated dense phase probability $(1 - \overline{B})$ is analogous to the simulated time-averaged dense phase, $\overline{\alpha}_s$. The results indicate that the boundary of the bubble placed with threshold $\alpha_s = 0.3$ perfectly balances de gradients of solids volume fraction towards the interior of the bubble and towards the exterior.

The root mean squared discrepancy along a horizontal line in the bed, δ, can be used in order to obtain a numerical quantification of the differences between simulation and experiments in two-dimensional beds:

$$\delta = \sqrt{\frac{1}{N}\sum_{i=1}^{N}(X_{exp_i} - X_{sim_i})^2} \tag{2.2}$$

where X corresponds to the variable which is going to be compared and N is the number of data values (i.e. points along the selected horizontal line) involved in the

calculation of the mean square discrepancy.

Thus, the relative discrepancy of the simulation in reproducing the experimental data is calculated after dividing δ by the root mean square value of the measured variable:

$$\delta_r = \frac{\delta}{\sqrt{\frac{1}{N}\sum_{i=1}^{N} X_{exp_i}^2}} \tag{2.3}$$

Table 2.3: Discrepancy of measurements from simulation results using Gidaspow drag function.

Variable	**y = 0.05 m**		**y = 0.15 m**	
	δ	$\delta_r[\%]$	δ	$\delta_r[\%]$
$\overline{C}$	0.0591	6.15	0.0399	4.52
$\overline{B}$	0.0591	138.18	0.0399	32.33
$\overline{V_y}$	0.0119 m/s	136.59	0.0554 m/s	657.43
$\overline{V_x}$	0.0173 m/s	439.35	0.0554 m/s	1088.33
Variable	**y = 0.25 m**		**y = 0.3 m**	
	δ	$\delta_r[\%]$	δ	$\delta_r[\%]$
$\overline{C}$	0.0707	8.17	0.1287	15.21
$\overline{B}$	0.0707	46.36	0.1287	70.91
$\overline{V_y}$	0.1166 m/s	944.34	0.0993 m/s	748.77
$\overline{V_x}$	0.0374 m/s	1355.25	0.0592 m/s	2334.65

Table 2.4: Discrepancy of measurements from simulation results using Syamlal - O'Brien drag function.

Variable	**y = 0.05 m**		**y = 0.15 m**	
	δ	$\delta_r[\%]$	δ	$\delta_r[\%]$
$\overline{C}$	0.0429	4.46	0.0270	3.06
$\overline{B}$	0.0429	106.73	0.0270	21.85
$\overline{V_y}$	0.0733 m/s	840.50	0.1281 m/s	1520.19
$\overline{V_x}$	0.0802 m/s	2039.98	0.0159 m/s	312.15
Variable	**y = 0.25 m**		**y = 0.3 m**	
	δ	$\delta_r[\%]$	δ	$\delta_r[\%]$
$\overline{C}$	0.0721	8.31	0.1188	13.93
$\overline{B}$	0.0721	47.33	0.11188	69.63
$\overline{V_y}$	0.1015 m/s	821.79	0.0980 m/s	739.09
$\overline{V_x}$	0.0805 m/s	2918.38	0.0630 m/s	2481.40

Tables 2.3 and 2.4 summarize the discrepancies encountered between the experimental measurements of the two-dimensional bed and the simulation with Gidaspow

and Syamlal - O'Brien drag models. Four different heights have been selected. For the two drag models tested, the tabulated results show that the absolute discrepancy, δ, in dense phase and bubble probability increase with y for $y \geq 0.05$ m. The relative discrepancy in bubble probability is an order of magnitude superior ($\leq 138\%$) than in dense phase probability ($\leq 15\%$) on account of the reduced root mean square value of bubble probability, especially near the distributor. The relative discrepancy in dense phase velocities is by far larger than in bubble probability, reaching a maximum of 1323% and 2389% for vertical and horizontal velocities respectively. The lowest absolute discrepancies δ in velocity are typically encountered near the distributor, probability while the largest discrepancies are placed at the centre of the bed height (i.e. $\overline{V_y}$) or near the bed surface ($\overline{V_x}$ for Gidaspow drag model). As the root mean square value of $\overline{V_y}$ increases rapidly with the distance to the distributor, there is a decrease in the relative value of discrepancy, δ_r, for the two drag models. Observe that the relative discrepancy for horizontal velocity $\overline{V_x}$ is usually larger than for $\overline{V_y}$.

As Tables 2.3 and 2.4 shows, Syamlal - O'Brien drag model produces a slightly smaller discrepancy of the simulated bubble or dense phase probability compared to Gidaspow model. However, regarding the time-averaged dense phase velocity, it is the Gidaspow model which yields the smaller discrepancies, especially near the distributor. For brevity reasons, only the simulations for this drag model will be shown in the remaining sections.

Table 2.5 contains the discrepancies between the mean volume fraction of particles and the scaled dense phase probability, where both magnitudes have been obtained from simulations. The tabulated results corroborate that the mean volume fraction of particles can be estimated with the scaled dense phase probability, being the estimation discrepancy 3% near the surface of the bed and around 10% close to the distributor (i.e. $y = 0.05$ m).

Table 2.5: Discrepancy between the mean volume fraction of particles and the scaled dense phase probability.

$\overline{\alpha}_s$ **vs** $\overline{C}\alpha_{s,mf}$	**y = 0.05 m**		**y = 0.15 m**		**y = 0.25 m**		**y = 0.3 m**	
	δ	δ_r[%]	δ	δ_r[%]	δ	δ_r[%]	δ	δ_r[%]
Gidaspow	0.0372	10.38	0.005	1.40	0.0081	2.30	0.0110	3.35
Syamlal - O'Brien	0.0320	8.57	0.0099	2.65	0.0082	2.29	0.0097	2.92

2.5.3 Recirculation regions and flow of solids in the time-averaged bed

The causes of the discrepancies between simulations and experiments encountered in the previous section can be surveyed by comparing the recirculation of particles within the bed. Figure 2.7 shows the time averaged velocity field for the simulation in Table 2.1 and for the PIV results from experiments. To enhance visualization not all the vectors has been displayed in Figure 2.7. It can be observed that the velocities in the upflow and downflow of particles are remarkable larger in the simulation, Figure 2.7a, than in the actual fluidized bed, Figure 2.7b. Another clear difference is the location of the mean recirculation centres. To visualize more easily the position of the recirculation centres, Figure 2.8 presents the streamlines (see Appendix B). Note that those streamlines are calculated connecting the tangent direction of each time-averaged vector field presented in Figure 2.7. Although not very rigorously, these streamlines may be interpreted as indicative of the time-averaged pathlines of the bed particles. Appendix B details the method used for the computation of the streamlines. It should be noted that the streamlines have been obtained assuming the dense phase as an incompressible and two-dimensional fluid. The incompressibility of the dense phase outside bubbles is a well grounded assumption (Davidson and Harrison, 1963). Of course the bubbles have a perturbation effect on the incompressibility of the dense phase that is transmitted to the time-averaged velocity field. Time-averaging the Equation A.1, the incompressibility condition (i.e. $\nabla \cdot \vec{v_s} = 0$) surfaces up since, for the fluidization regime studied here, the gradients of the time-averaged volume fraction of particles are small (except near the bed surface, see Figure 2.5) and the coupled oscillation of particle velocity and volume fraction is confined only to the bubble perimeter and bed surface.

Recalling that the half of the bed was studied, Figure 2.8 indicates the existence of two main recirculation regions in the bed (i.e. one per half area studied) whose centre position is placed in the simulation nearer to the wall and to the distributor than in the results from the experiments. The location of the recirculation centre is shown in Table 2.6. This concentrates the experimental streamlines towards the centre line of symmetry (y = 0.25 m in Figure 2.8b) in contrast to the ascending streamlines from the simulation, which are closer to the wall (Figure 2.8a). Therefore, in order to preserve the descending flow of particles (streamlines near the wall at y = 0 m), the simulation results are characterized by a larger downward velocity than the corresponding experimental data. According to Table 2.6, the descending flow of particles has a peak velocity whose modulus, $max|\overline{V_x}|$ and $max|\overline{V_y}|$, are an order of magnitude larger in the simulation than in the experiments. Not only is the

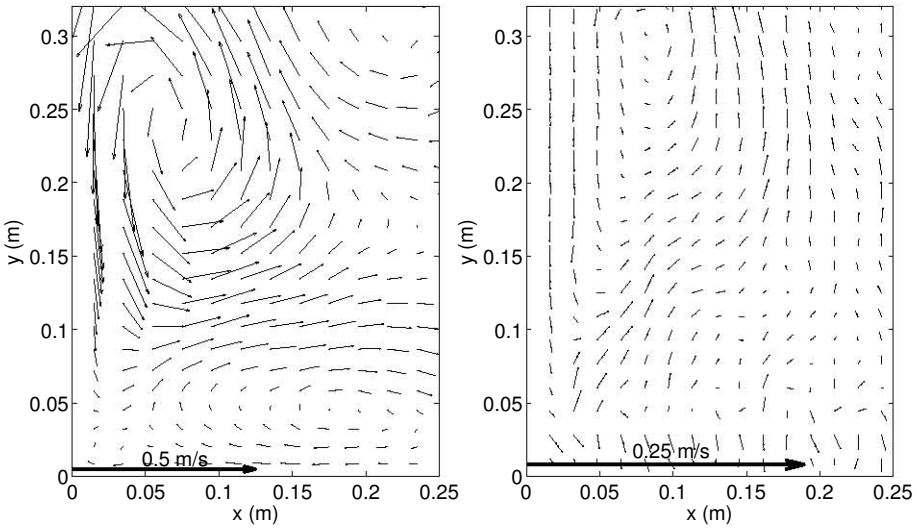

(a) (b)

Figure 2.7: Time-averaged velocity vectors of dense phase ($\vec{V}$) calculated from simulation (a) and experiments (b). Both figures have the same vector scale.

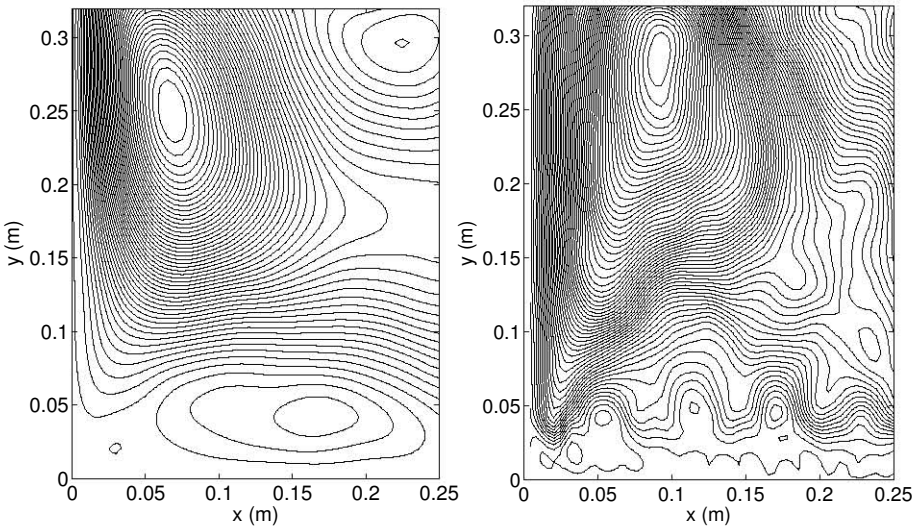

(a) (b)

Figure 2.8: Streamlines of the time-averaged velocity of dense phase calculated from simulation (a) and experiments (b).

displacement of the recirculation region the cause of the large values of δ in Tables 2.3 and 2.4. The time-averaged particle mass flow can be calculated as the integral along a horizontal line connecting the two main recirculation centres of a bed:

$$\dot{m} = \int \overline{V_y} \alpha_s \rho_s Z dx \tag{2.4}$$

The results are presented in Table 2.6 and evidence that the transport of particles is 10 times larger in the simulation compared to the experiment. As the superficial gas

velocity is equal in both cases, one plausible explanation is that the ultimate origin of the discrepancies between simulations and experiments is due to an over-predicted net drag force on the ascending dense phase in the two-fluid models employed in the present study.

Table 2.6: Comparison of time-averaged results for the dense flow in the bed.

Variable	**Simulation**	**Experiment**
x_{RC}	0.0650 m	0.0927 m
y_{RC}	0.2379 m	0.2863 m
$max\|\overline{V_x}\|$	0.2664 m/s	0.0212 m/s
$max\|\overline{V_y}\|$	0.3281 m/s	0.0264 m/s
$\dot{m}$	35.98 kg/s	3.02 kg/s

Figures 2.8a and 2.8b also shed light into the high discrepancies in time-averaged velocity of particles encountered near the distributor. In the numerical results of Figure 2.8a it appears another minor recirculation zone close to the distributor. It seems that in the experiments there is also small intensity recirculations located nearby the distributor but smaller than in the simulation. However, the nature of the minor recirculations near the distributor in the experiments seems to be probably produced by the three-dimensionality of particle flow near the distributor and jet effect produced by the orifices of the distributor. The three-dimensional character of the particle flow near the distributor is caused by the bubbles, whose size in that region is smaller or comparable to the thickness of the bed. Also, those minor recirculations can be attributed to the coalescence of the jets of several consecutive orifices of the distributor. Of course, the two-dimensional simulations cannot reproduce these small recirculations. Without a doubt, this contributes to the large discrepancies for $\overline{V_x}$ and $\overline{V_y}$ observed in Tables 2.3 and 2.4 at $y = 0.05$ m.

2.5.4 Bubble diameter and velocity

After processing the results from the two-phase code, the bubble data can be compared with the experimental data and with theoretical models. The procedure to capture the simulated bubbles is based on a threshold value. Contours of solids volume fraction equal 0.3 are obtained on each frame, and bubble centroid and bubble equivalent diameter are obtained at this point using the contour and avoiding bubbles with a diameter lower than 0.01 m. Bubble velocity is obtained associating bubbles on time step t with the time step $t + 1$, taking into account the size of the bubble and its height. This can be done because the time step used to analyse the data is small enough to track any bubble properly (Busciglio et al., 2009). The procedure followed by the calculation

of bubble diameter and velocity using the simulation results is exactly the same than using the experimental results once the bubble contour is defined.

The theoretical model used in the present study is the adaptation of the Darton's model (Darton et al., 1977) to two-dimensional beds (Shen et al., 2004), in which the diameter of a bubble subjected to coalescence is modelled as:

$$D_b = \left(\frac{5.4543}{\lambda}\right)^{2/3} \left[(U_0 - U_{mf})\left(y + \frac{\lambda A_0}{2.1419Z}\right)\right]^{2/3} g^{-1/3} \tag{2.5}$$

$$U_b = \phi\sqrt{gD_b} \tag{2.6}$$

where ϕ is a parameter that takes several values depending on the literature. Davidson and Harrison (1963) gave a value for equal to 0.71 for three-dimensional beds. Later Shen et al. (2004) proposed a value between 0.8 and 1 applicable to two-dimensional beds. Also in Equation 2.5, A_0 is the total area of the distributor divided by the number of orifices, Z is the thickness of the bed, U_0 is the superficial velocity of the gas, U_{mf} is minimum fluidization velocity, y is the vertical distance from the distributor to the bubble centroid, and λ is a constant obtained from experiments which for the studied fluidized bed takes a value around 9.86 (Almendros-Ibáñez et al., 2006).

Figure 2.9 shows the relation between the mean (time-average) and standard deviation of the equivalent bubble diameter (Caicedo et al., 2003) versus the vertical distance from the distributor to the bubble centroid, y, and Figure 2.10 depicts the dependence of the mean and standard deviation of bubble velocity on the equivalent bubble diameter. The simulation and the experimental data compared in these figures are represented by average values (Figures 2.9a and 2.10a) and their standard deviation (Figures 2.9b and 2.10b). In particular, for the construction of the average data in Figures 2.9a and 2.10a, the arithmetical mean is calculated with the bubbles whose centroid is placed within a thin interval surrounding each value selected in the horizontal axis. The standard deviation of the instantaneous values of the bubble diameter and velocity in Figures 2.9b and 2.10b characterize the dispersion from the mean values.

As Figure 2.9 illustrates, the Gidaspow's drag model yields the bubble growth with height in terms of both mean and standard deviation values, that most closely resembles the experimental data. In particular, the mean bubble diameter of the simulation with this drag model is slightly smaller but in acceptable agreement with the theoretical model of Shen et al. (2004), Equation 2.5, except at distances greater than the static height of the bed surface, y = 0.3 m, where the theoretical model is not applicable. This level of similarity between model and simulation for mean bubble diameter profile along the bed height is also observed in other previous publications

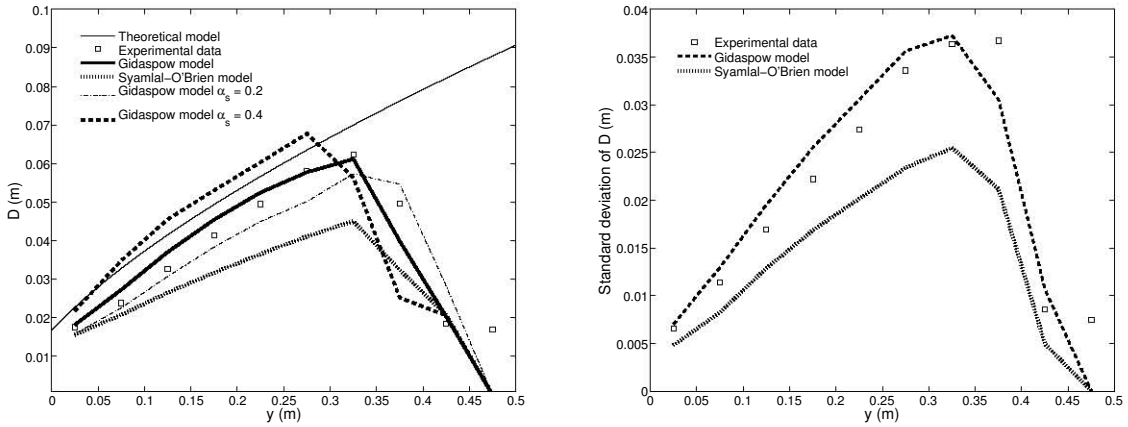

(a) (b)

Figure 2.9: Mean bubble diameter as a function of height from the distributor, y, obtained from simulation and experimental data (a) and its standard deviation (b).

(see, for instance, Van Wachem et al. (1998); Patil et al. (2005)) The experimental data of bubble diameter are inside the simulation data dispersion shown in Figure 2.9b. The standard deviation of the simulated bubble diameter is remarkable close to the experimental one. However, the experimental data do not fit the theoretical model as closely as the numerical results. The apparently more randomly behaviour of the experimental results due to the lower number of bubbles taken from the images may be the reason of this discrepancy. It is symptomatic that both experiments and simulation predict larger bubble diameter in a similar degree near the bed surface, indicating that Equation 2.5 could be adjusted and extended to this complex region of the bed. However, more experimental data would be advisable to support this improvement.

Figure 2.9a also indicates that the drag model of Syamlal - O'Brien tends to slightly underestimate the bubble growth from experiments and from the model of Shen et al. (2004), when applied to the operative conditions studied in the present work. However, according to Figure 2.10a, but this is not as clear for the standard deviation for the bubble velocity shown in Figure 2.10b, the drag model of Syamlal - O'Brien confers for relatively small bubbles, 0.04 m, the velocity dependence on bubble diameter most fitted to the classical dependence of Davidson and Harrison (1963), Equation 2.6 for $\phi = 0.71$. This seems to be facilitated by an underprediction of bubble velocity at low heights. The simulation based on Gidaspow drag model leads to the closest results to the experimental data in Figure 2.10a. As a general trend, it can be said that the theoretical model for isolated bubbles due to Equation 2.6 with $\phi = 0.71$, overpredicts the bubble velocity of the present experiments in the range of medium sized and large bub-

bles. Notice that the model of bubble growth used in this study assumes that bubbles are not close to the eruption stage, but large bubbles in Figure 2.10a presumably are placed near the bed surface as Figure 2.9a shows. This would explain the systematic deviation of the simulation results when 0.09 m.

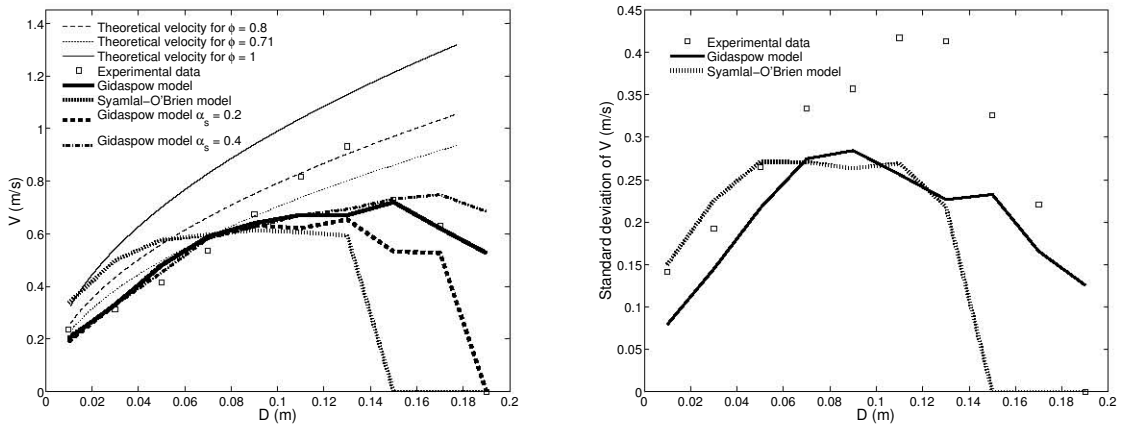

(a) (b)

Figure 2.10: Vertical mean bubble velocity as a function of bubble equivalent diameter obtained from simulation and experimental data (a) and its standard deviation (b).

In Figures 2.9a and 2.10a results obtained for different bubble threshold, 0.2 and 0.4 are also included. The bubble diameter varies accordingly with this value. Obviously, larger bubbles are obtained when this value is 0.4 and smaller bubbles when the value is 0.2, but both results are in accordance with the theoretical model. Paying attention to the bubble velocity, no differences can be seen in the range where data are reliable, this range covers bubble diameters up to 0.07 m placed up to 0.3 m above the distributor, which is the static bed height. In general, the value of 0.3 for bubble threshold provides the results most similar to experiments and the theoretical model.

2.5.5 Air throughflow

The distribution mechanisms of the air flow in the studied fluidized bed can be analysed to explain the encountered differences in dense phase velocities between the experiments and the simulation. As presented in Shen et al. (2004), three are the main distribution channels of air in the bed: the transport of air contained in bubbles, the air percolating between particles (i.e. minimum fluidization air), and the air throughflow. The air throughflow is the excess of air that ascends bypassing pairs or groups of consecutive bubbles. It is calculated here using the conservation of mass balance of Shen et al. (2004), illustrated also in Figure 2.11.

$$U_0 = U_{th} + (1 - \delta_b)U_{mf} + \delta_b U_b \tag{2.7}$$

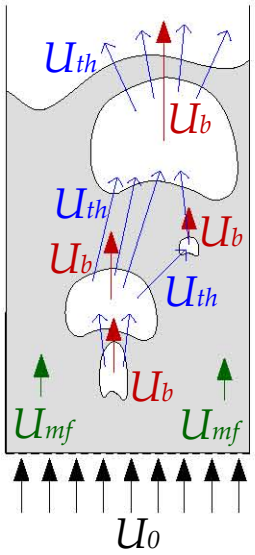

Figure 2.11: Schematic illustration of the gas velocities in Equation 2.7 in a 2D bed.

where U_{th} is the throughflow velocity, that is, the air throughflow per unit of distributor area, U_0 is the superficial air velocity, U_{mf} is the minimum fluidization velocity, and U_b is the mean ascending velocity of the bubbles weighted with their frontal area:

$$U_b = \frac{\sum_{i=1}^{N} A_{b,i} v_{b,i}}{\sum_{i=1}^{N} A_{b,i}} \tag{2.8}$$

being v_b and A_b the ascending velocity and the frontal area (.i.e. area on the images or simulation plane) of a bubble, and N_b is the number of bubbles present in the studied region of the bed of frontal area A_f. In Equation 2.7 δ_b is the fraction of the studied region that is occupied by bubbles:

$$\delta_b = \frac{\sum_{i=1}^{N} A_{b,i}}{A_f} \tag{2.9}$$

In Equation 2.7, $\delta_b U_b$ represents the visible bubble flow, U_{vis}, which can be defined as the visible gas flow (i.e. gas transported by a bubble) that is crossing a horizontal surface at a certain height above the distributor, extended along the bed height, as sketched in Figure 2.12. The explanation of the previous simplification is described as follows.

$$U_{vis} = \frac{1}{ZW}\frac{1}{y_{fb}} \int_{y=0}^{y=y_{fb}} v_b A_{b,T} dy \tag{2.10}$$

where $A_{b,T}$ refers to the transversal area of the bubble which can be calculated as

$A_{b,T} = l_b Z$, where l_b is the width of the bubble at a certain height, so l_b depends on y.

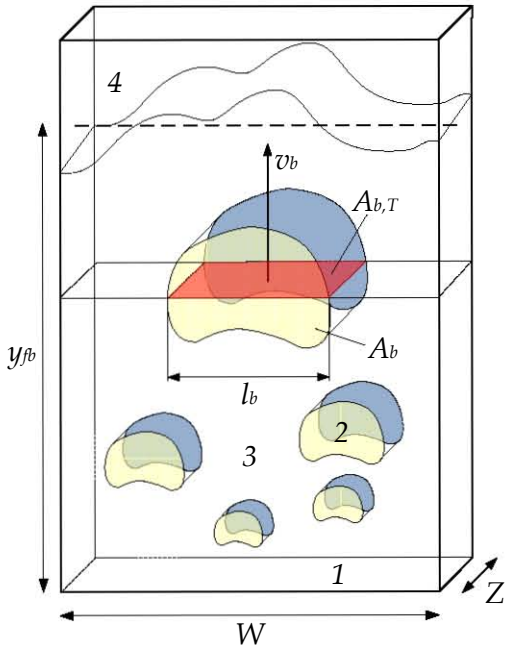

Figure 2.12: Illustration of the calculation of the visible bubble flow in a pseudo-2D bed. 1. Distributor, 2. Bubbles, 3. Dense phase, 4. Freeboard.

$$U_{vis} = \frac{1}{ZWy_{fb}} \int_{y=0}^{y=y_{fb}} v_b l_b(y) Z dy \tag{2.11}$$

In this expression, $\int_{y=0}^{y=y_{fb}} l_b(y) dy$ is equal to the frontal area of the bubbles, A_b, and it can be applied to all the bubbles in a certain time step.

$$U_{vis} = \frac{1}{ZWy_{fb}} \sum_{i=1}^{N_b} v_{b,i} A_{b,i} Z = \frac{1}{y_{fb} W} \sum_{i=1}^{N_b} v_{b,i} A_{b,i} \tag{2.12}$$

Therefore, multiplying and dividing by the frontal area of the bubbles.

$$U_{vis} = \sum_{i=1}^{N_b} \frac{v_{b,i} A_{b,i}}{y_{fb} W} = \frac{\sum_{i=1}^{N_b} v_{b,i} A_{b,i}}{\sum_{i=1}^{N_b} A_{b,i}} \frac{\sum_{i=1}^{N_b} A_{b,i}}{y_{fb} W} \tag{2.13}$$

Substituting $y_{fb}W$ as the frontal area of the bed, A_f, the visible bubble flow, U_{vis}, can be calculated as the product of the mean ascending velocity of the bubbles, U_b, and the fraction of the bed occupied by bubbles, δ_b, both of them defined in Equations 2.8 and 2.9.

$$U_{vis} = \frac{\sum_{i=1}^{N_b} A_{b,i} v_{b,i}}{\sum_{i=1}^{N_b} A_{b,i}} \frac{\sum_{i=1}^{N_b} A_{b,i}}{A_f} = U_b \delta_b \tag{2.14}$$

Using Equation 2.7 the throughflow velocity has been calculated for the total sam-

pling area of the bed, $A_f = w_1 h_1$, and time-averaged. Table 2.7 compares de simulation and experimental results. For the simulation, the reference case described in Table 2.1 has been selected, taking the same fluidization velocity than in the experiments, $U_{mf} = 0.35$ m/s.

Table 2.7: Simulation and experimental results for the visible flow and throughflow in the bed and bed expansion.

Variable	Simulation	Experiment
δ_b	0.122	0.118
U_{vis}	0.0579 m/s	0.0410 m/s
U_{th}	0.2466 m/s	0.02629 m/s
$\overline{y}_{fb}$	0.3771 m	0.3391 m

According to the results of Table 2.7, the fractional area of the bed occupied by bubbles is only 3% larger in the simulation than in the experiments. The visible bubble flow per distributor area is an order of magnitude smaller than the other terms of Equation 2.7, including the throughflow velocity U_{th}. This agrees with the results presented by Shen et al. (2004). Besides, the visible bubble flow obtained from the simulation is more than 40% larger, and the throughflow is 6.6% smaller, than in the results from the experiments. This has important consequences in the analysis of the results: there is a slight underestimation of the throughflow velocity in the simulation compensated by an increase in visible flow. As the visible bubble flow is six or more times smaller than the throughflow, the slight underestimation of U_{th} generates an important increase, in relative terms, in U_{vis} and also in U_b provided δ_b remains nearly unchanged. Thus, using the weighted average of Equation 2.8, the simulation performed is characterised by a larger U_{vis}, which enhances the transport of dense phase compared to the experiments. However, this 40% increment of U_{vis} seems by itself unable to generate in most of the simulated bed a vertical flow of dense phase between 4 to more than 9 times superior than in experiments, as show in Table 1.

Therefore, other relevant causes in addition to the overprediction of U_{th}, may be behind the large values of the discrepancy δ_r in Table 2.1. One hypothesis is that some fraction of the air throughflow of Table 2.7 in the experimental fluidized bed is actually bypassing the dense phase, ascending just close to the wall surfaces, where the void fraction is large since the packing of particles close to the wall is not as efficient as in the bulk of the bed. If this attached-to-wall air flow is significant, it can reduce the throughflow crossing the bulk of the dense phase and, as a consequence, reduce the drag forces between gas and dense phase and hence decrement particle velocities in the experiments. Provided that in a real two-dimensional fluidized bed the ratio surface-area to volume is high (but not in the simulated bed), this may be a hypothesis that

should not be disregarded. Another hypothesis is that the drag models between air and particles, lead to an overprediction of net forces on dense phase even if the throughflow velocity crossing the bulk of the bed is similar in simulation and experiments. Finally, due to the complex nonlinear nature of the bed hydrodynamics, it is also possible that the models accounting for frictional forces between particles may not reproduce the effective viscosity of the dense phase in regions involved in the transport of particles, such as the bubble wake. A dimensionless parameter can be defined for the visible bubble flow rate, as done by Hilligardt and Werther (1986).

$$\Psi = \frac{U_{vis}}{U_0 - U_{mf}} \tag{2.15}$$

This parameter indicates the fraction of the excess of flow actually carried by bubbles. The simulation and experimental results for Ψ are plotted on Figure 2.13 together with two models. One of the models for Ψ has been taken from Hilligardt and Werther (1986).

$$\begin{aligned} \Psi = 0.26 \quad \text{for} \quad y \leq 0.275 \text{ m} \\ \Psi = 0.35 \left(\frac{y}{W}\right) 0.5 \quad \text{for} \quad y \geq 0.275 \text{ m} \end{aligned} \tag{2.16}$$

where y is the distance above de distributor and is the width of the bed. The other model used is from Johnsson et al. (1991):

$$\Psi = f2 \left(y + 4\sqrt{A_0}\right) 0.4 \tag{2.17}$$

where:

$$f2 = (0.26 + 0.7\exp(-3.3 d_s 10^3))(0.15 + (U_0 - U_{mf}))^{-0.33} \tag{2.18}$$

where d_s is the particle diameter and A_0 is the area of the distributor per orifice.

As expected, the fraction of visible flow Ψ is higher in the simulation than in the experimental results, since Equation 2.16 is proportional to U_{vis}. Apart from the differences between the experimental and the simulation results, the model from Hilligardt and Werther (1986), gives a value of Ψ constant for the range of vertical position studied (i.e. from the bottom of the bed till the static bed height), and does not follow the growth experienced by the simulation and the experimental data. This can be explained by the fact that the model from Hilligardt and Werther (1986), was developed for a three-dimensional fluidized bed. Besides, Equaton 2.17 has been selected for Geldart-D particles since the model for Geldart B leads to $\Psi = 0.65$. On the other hand, the model of Johnsson et al. (1991), provides a growth of the fraction of visible flow that seems to be more representative of the two-dimensional bed studied.

Nevertheless, Equation 2.17 does not tend to zero close to the distributor in contrast to the simulation and the experimental results presented in Figure 2.13.

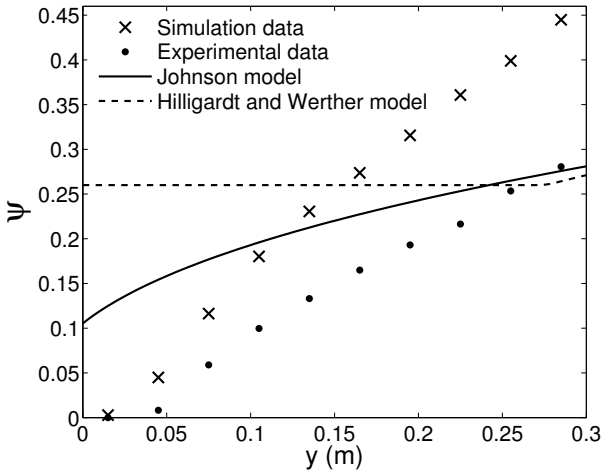

Figure 2.13: Fraction of visible bubble flow.

The last part of this section compares the bed expansion obtained from the two-fluid simulation (Gidaspow model) and the experimental data. Results on this regard are included on Table 2.7. The bed expansion has been calculated with the mean y-coordinate of the freeboard (i.e. transversally averaged height of the bed surface), $\overline{y}_{fb}$, which has been time-averaged over the same number of snapshots utilized for the calculation of bubble diameter and velocity in the previous section. The resulting time-averaged mean y-coordinate of the freeboard is 0.3771 m and 0.3391 m for the simulation and experimental results, respectively. As the visible flow in the simulation results is higher than in the experiments, more bubbles appear in the simulation and, therefore, the bed expansion has to be higher than in the real bed tested.

2.5.6 Instantaneous interaction between bubble and dense phase

A comparison of the instantaneous behaviour of dense phase surrounding bubbles can be valuable in order to explain the differences encountered between the simulation and experimental results. Figure 2.14 shows the relative vectors of two coalescent bubbles for the simulation and experimental results superimposed to the instantaneous dense phase concentration maps and the images of particles, respectively.

Both simulation and experiments reveal the same physical interaction between bubbles and dense phase: downward motion of particles at the sides of the bubble, high particle velocity in the wake of the leading bubble, and deformation of the trailing bubble in the wake of the leading one.

Table 2.8 compares some hydrodynamics values of the two bubbles depicted in

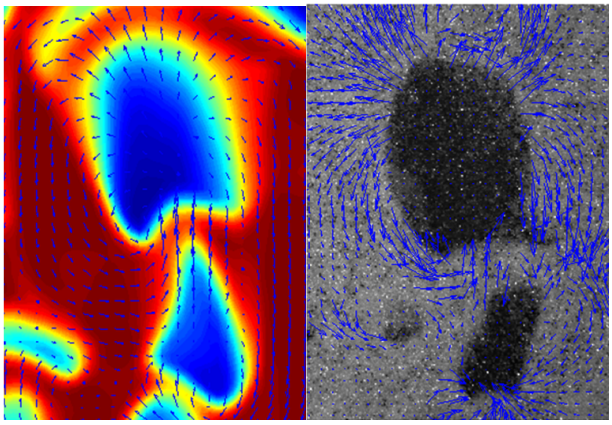

(a) (b)

Figure 2.14: Dense phase velocity vectors surrounding a pair of coalescent bubbles taken from the bed simulation (a), and from the experiments (b). The simulation and experimental results are respectively shown superimposed to their particle volume fraction map and image of particles.

Figure 2.14. Obviously, it was not possible to capture two identical pairs of coalescent bubbles in the experiments and the simulation. In fact the pair of bubbles from the simulation is nearly two times bigger than the pair selected from the experimental images.

Table 2.8: Hydrodynamics related to two coalescent bubbles.

Parameter	**Simulation**	**Experiment**
Leading bubble diameter	0.0984 m	0.0585 m
Leading bubble ascending velocity	0.9238 m/s	0.4125 m/s
Leading bubble gas velocity	3.4633 m/s	–
Coalescing bubble diameter	0.0639 m/s	0.0310 m/s
Coalescing bubble ascending velocity	0.6000 m/s	0.4687 m/s
Coalescing bubble diameter gas velocity	3.3772 m/s	–
Downflow velocity	0.4012 m/s	0.1260 m/s
Wake velocity	1.201 m/s	0.2016 m/s

Figure 2.15a depicts the streamlines of the dense phase velocity of the two coalescent bubbles obtained from experiments, Figure 2.14b. In Figure 2.15a, the image of particles of this part of the bed has been superimposed to the streamlines, being the bubbles the dark areas of the image. Also, the streamlines for the dense phase velocity of the bubbles in Figure 2.14a, have been calculated for the simulation results and presented in Figure 2.15b. In order to compare the simulation and experimental results in the same conditions, in Figures 2.15a and 2.15b, the streamline calculation procedure described in Appendix B fills the interior of the bubbles with null dense phase velocity, since no information in PIV is obtained there. As explained in the Appendix B, the method of streamline calculation ensures soft-curvature streamlines inside regions of

unknown particle velocity. The actual streamlines of the falling particles inside bubbles is also expected to follow soft trajectories (i.e. parabolic trajectories). To verify this assumption, Figure 2.15c presents the streamlines of the same simulated bubbles of Figure 2.15b but now using all the velocity information of dense phase, that is, including the velocities inside bubbles. Note that no significant differences between Figures 2.15b and 2.15c appear. Thus, it is assumed that the streamlines of Figure 2.15a are weakly affected by the computing artefacts related to the lack of experimental velocity data inside bubbles.

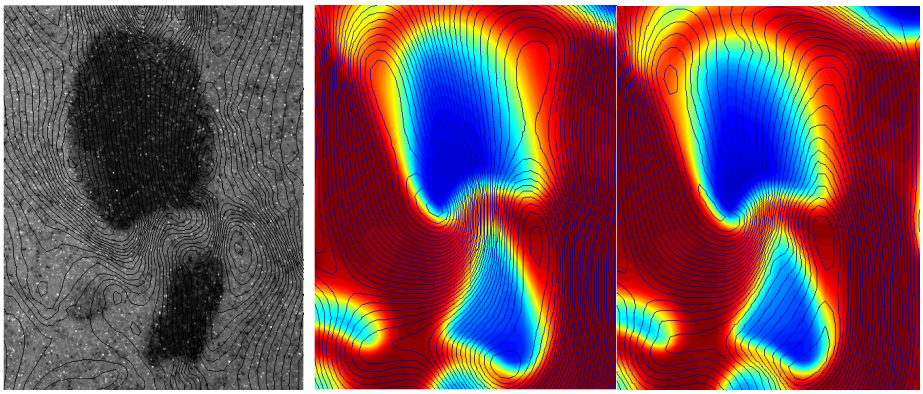

(a) (b) (c)

Figure 2.15: Dense phase streamlines surrounding a pair of coalescent bubbles taken from the bed experiments (a), and the simulation (b). Also included the simulation results with the streamlines incorporating the dense phase velocities inside bubbles (c). The simulation and experimental results are respectively shown superimposed to their particle volume fraction map and image of particles.

Those pair of bubbles have been compared with the theoretical model developed by Toei and Matsumo (1967) for vertically aligned bubbles, that correlates its dimensionless position $H^* = H/H_{0,min}$ versus its dimensionless time $T = (v_{b,L}t)/H_{0,min}$, where H corresponds with the location of the top of each bubble, $H_{0,min}$ is the distance between the top of the leading bubble and the bottom of its wake, $v_{b,L}$ is the vertical velocity of the leading bubble, and t is the time.

For the simulation results presented in Table 2.8, the dimensionless position takes values of $H^*_L = 3.05$ and $H^*_{Tr} = 1.65$ for the leading bubble and the trailing one, respectively, that lead to an increment of dimensionless position $\Delta H^* = H^*_L - H^*_{Tr} \approx 1.4$. This value $H^*_L = 3.05$ corresponds to a dimensionless time $T \approx 1.5$ and with $\Delta H^*_{model} \approx 1.25$ according to the experimental correlation plot shown in Toei and Matsumo (1967). Regarding the experimental results of Table 2.8, the dimensionless positions are $H^*_L = 3.43$ and $H^*_{Tr} = 2.12$, that is $\Delta H^* = 1.31$. Using $H^*_L = 3.43$ in the correlation of Toei and Matsumo (1967), a dimensionless time of $T \approx 1.8$ and an increment of dimensionless position $\Delta H^*_{model} \approx 1.13$ is obtained. Therefore, the experimental result for ΔH^* is 16% greater than the corresponding model prediction

ΔH^*_{model}. Similarly, the numerical result for ΔH^* is 12% superior than ΔH^*_{model}. That means that both simulation and experimental results experience the same level of agreement with the bubble coalescence model presented by Toei and Matsumo (1967). As $1 \leq T \leq 2.5$ in for the simulation and experimental results, the coalescent bubbles of Table 8 are not out of the range of interaction and coalescence of vertically aligned bubbles shown in Toei and Matsumo (1967).

The same analysis has been done for a simulated and experimental bubble as much isolated as the chaotic behaviour of the bed admit. The main hydrodynamics parameters of the selected semi-isolated bubbles are included in Table 2.9, and Fig2.16 presents their streamlines calculated in the same way than in Figure 2.14. In general, the streamlines from both simulation (Figure 2.16b) and experiments (Figure 2.16a) are qualitatively similar, and negligible differences appear between the simulation results for the streamlines calculated without and with the particle velocities in the bubbles (Figure 2.16c).

The velocity coefficient ϕ in Table 2.9 has been calculated with the instantaneous values of bubble diameter and velocity. Although the experimental and the simulation values obtained for ϕ are of the same order, the experimental results in Table 2.9 present a value clearly far from the well known range $\phi = 0.71 - 1$. However, the instantaneous values of ϕ are not necessarily representative of mean bubble conditions, and can be merely attributed to the stochastic behaviour of bubbling beds.

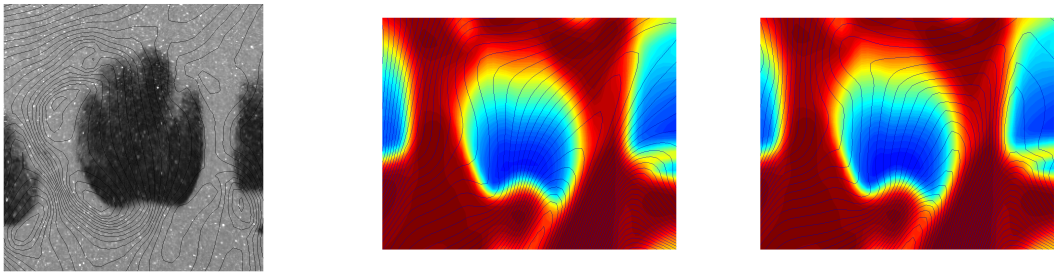

(a) (b) (c)

Figure 2.16: Dense phase streamlines surrounding a bubble taken from experiments (a), and simulation (b). Also included the simulation results with the streamlines incorporating the dense phase velocities inside bubbles (c). The simulation and experimental results are respectively shown superimposed to their particle volume fraction map and image of particles.

The bubble gas velocities presented in Tables 2.8 and 2.9 correspond to the vertical velocity of the air at the centre of each bubble. Obviously, the gas velocity cannot be obtained from the experimental results because only the dense phase velocity is measured. It can be verified that the gas inside the bubble is much faster than the bubble rising velocity. The difference between the bubble gas velocity and the bubble

Table 2.9: Hydrodynamics parameters of semi-isolated bubbles.

Parameter	Simulation	Experiment
Bubble diameter	0.0893 m	0.0680 m
Bubble ascending velocity	0.6111 m/s	0.2658 m/s
Bubble gas velocity	1.7127 m/s	–
Particles downflow velocity	0.4025 m/s	0.1739 m/s
Wake velocity	0.5647 m/s	0.2450 m/s
$\phi = \frac{v_b}{\sqrt{gD_{eq}}}$	0.653	0.326

velocity constitutes the throughflow, reaching in this particular bubble a value around 1.1 m/s, that is 2.9 times the minimum fluidization velocity U_{mf}. That figure of throughflow is closer to the predictions of the Davidson theory for three-dimensional bubbles ($3U_{mf}$) than for two-dimensional ones ($2U_{mf}$) (Davidson and Harrison, 1963). For the case of coalescent bubbles, Table 2.8, the throughflow velocity elevates to 2.54 m/s and 2.78 m/s for the rear and trailing bubble. The throughflow of air is the responsible of the acceleration of particles between coalescent bubbles. As Table 2.8 shows, the particle velocity between the coalescent bubbles (i.e. wake of the leading bubble) is nearly 6 times superior in the simulation than in the PIV experiments, but the diameter of the simulated bubbles selected in Table 2.8 is less than twice that of the experiments. Note also that the downflow velocity of particles at both sides of the leading bubble (Table 2.8) in the case of the simulation is less than 3.2 times intense than in the experiments.

Assuming that the solids velocity is proportional to the coalescent bubbles velocity and their level of approximation (proportional to T), the air between the coalescent bubbles selected from the simulation in Table 2.8 would be more efficient in driving particles than in the coalescent bubbles selected from experiments. An overprediction of the air drag due to models tested can be an important cause of the large particle velocity encountered between simulated bubbles compared to PIV measurements, since the drag force of air is the main factor participating in the raising forces on a particle. From Table 2.9, it is also noticeable that the wake velocity as well as the particle downflow velocity of the simulated bubble is around 2.3 times larger than the experimentally measured bubble. However, the velocity of the simulated bubble is also 2.3 larger than the experimental one, which explains the reason of that difference in the wake velocity of the semi-isolated bubbles selected in Table 2.9.

Other types of bubbles morphologies (splitting, erupting and wall-attached bubbles) may be analyzed but have not been included here for brevity reasons.

2.6 Summary and Conclusions

Two major types of information have been analysed in the present study aimed to the comparison of Eulerian-Eulerian two-fluid simulation and experimental results in a two-dimensional gas-solid fluidized bed: bubble hydrodynamics, and dense-phase (i.e. particle-phase) velocity. In particular, in contrast to previous comparison studies usually focused on bubble behaviour and dense-phase distribution, the present work examines and compares not only the bubble hydrodynamics and dense-phase probability within the bed, but also the time-averaged dense-phase velocity, the air troughflow and the instantaneous interaction between bubbles and dense-phase.

To increase generality of results, the two-fluid simulations presented in this work were conducted using two different and well-known closure models for the gas-particle interaction. For verifying the simulation results, an experimental bed of 0.005 m thickness was measured here to ensure the two-dimensionality of the bed dynamics. The experimental data from this bed concerning bubble behaviour and dense-phase distribution were obtained in the present work through non-intrusive techniques based on the digital analysis of a long temporal sequence of images. In harmony with previous studies present in literature, the two-fluid models tested here were able to qualitatively predict the bubble growth and velocity as well as the bubble probability distribution within the bed. Furthermore, an acceptable level of quantitative agreement between two-fluid simulation and experiments is confirmed in this study regarding bubble diameter and velocity in a two-dimensional bed. The similitude encountered between the simulated and experimental standard deviations of bubble diameter and velocity are also noticeable. The results of the present work reveals that, of the two drag models tested, the model of Gidaspow (Gidaspow, 1994) provides the best approach to the experiments and to simplified models based on the two-phase theory of fluidized beds. Exception of this is the bubble probability profiles in the studied two-dimensional bed, which seem to be best predicted using the Syamlal - O'Brien drag model (Syamlal and O'Brien, 1987). Interestingly, both drags models, Gidaspow and Syamlal - O'Brien, provide in this work a better bubble distribution (i.e. more homogeneous bubble probability maps) than the experimental bed.

Thanks to the simulation results, the present work clearly proves that the dense-phase probability can be used as a good approximation of time-averaged particle volume fraction in a bubbling bed. In the simulations, since the transition of bubble phase too dense phase is not as sharp as in experiments, a bubble detection threshold equal to the arithmetic mean between the maximum and minimum particle concentration is recommended. This important fact, which seems to be obviated by other previ-

ous publications, indicate that simple digital image techniques can be used to obtain satisfactory estimations of time-averaged particle concentration in a two-dimensional bed.

The most important result of the present chapter is probably the quantitative comparison between simulations and experiments performed for the time-averaged dense-phase velocity in the whole plane of the two-dimensional bed. Regarding the experimental velocity of the dense-phase, it was extracted in this work from the images of the real bed thanks to the application of a multigrid particle image velocimetry (PIV) technique. The resulting experimental velocities of particles obtained in this work are coherent with other PIV measurements of bubbling beds of small thickness reported in literature. The comparison of time-averaged velocity of dense-phase from simulation and experiments was done here through the use of horizontal profiles of velocity as well as the definition of a discrepancy factor, which allows a quantitative comparison of dense-phase velocities not conducted before in bubbling fluidized beds studies.

Additionally, a global analysis of the dense-phase velocity field from both simulation and experiment data was done in the present study with the aid of streamlines maps calculated using an original and robust method developed ad-hoc that can be applicable to simulation and noisy experimental data. Surprisingly, and despite the above described similarities in bubble diameter and velocity, the results of the present work indicate that the time-averaged velocities of the particle-phase in the simulated bed are nearly one order of magnitude larger than the velocities obtained from PIV experiments. Therefore, the fine agreement in bubble behaviour found between simulation and experiments does not ensure the same level of agreement in dense-phase velocities in the framework of two-dimensional beds. This significance result, not reported previously in literature, occurs for the two well-known drag models tested, indicating that in Eulerian-Eulerian two-fluid simulations the behaviour of bubble velocity and diameter is relatively uncoupled from, or insensitive to, the resulting dense-phase velocity. Since the superficial air velocities in the simulation and in the experimental bed have been set to similar values in this study, three principal causes of such a high discrepancy can be postulated: (1) the possible overestimative nature of the particle drag models in reproducing the net forces of the gas on a particle in a two-dimensional regime; (2) the effects of particle-wall friction that may be present at the frontal and back wall of a real quasi-two dimensional bed, and (3) the influence of the higher porosity near the wall in a real fluidized bed, which may bypass a significant fraction of the air near the walls of a two dimensional bed and be the cause of the reduced values of bubble visible flow (the driver mechanism of particles) found in the experiments of this work compared to the performed simulations. Further research involving perhaps different

experiments and operative conditions are needed to discriminate the relative influence of the postulated causes of the discrepancy in dense-phase velocity.

Nomenclature

A_0	total area of the distributor divided by the number of orifices, (m^2)
A_b	frontal area of the bubbles, (m^2)
$A_{b,T}$	transversal area of the bubbles, (m^2)
A_f	total sampling area of the bed, (m^2)
$\overline{C}$	proportion of time that a point is occupied by solids (-)
$\overline{B}$	proportion of time that a point is occupied by bubbles (-)
d_i	diameter, (m)
D_b	bubble diameter, (m)
e_{ss}	restitution coefficient, (−)
K_{gs}	gas/solid momentum exchange, (−)
$\vec{g}$	aceleration due to gravity, (9.8 m/s^2)
$k_{\Theta,s}$	diffusion coefficient for granular energy, (kg/s m)
H^*	dimensionless position for coalescence bubbles, (−)
H	location of the top of a bubble, (m)
$H_{0,min}$	distance between the top of a leading bubble and its wake, (m)
h	bed height, (m)
h_1	fixed bed height, (m)
l_b	width of the bubble at a certain height, (m)
$\dot{m}$	particle mass flow rate, (kg/s)
N	number of images, (−)
N_b	number of bubbles, (−)
v_b	bubble vertical velocity, (m/s)
v_i	velocity, (m/s)
$\vec{v_i}$	velocity vector, (m/s)
$\vec{V}$	mean particle velocity, (m/s)
V_x	horizontal particle velocity, (m/s)
V_y	vertical particle velocity, (m/s)
t	time, (s)
T	dimensionless time (−)
H	vertical location of the bubble top, (m)
U_0	superficial velocity, (m/s)
U_{th}	through flow velocity, (m/s)

U_{vis}	visible flow, (m/s)
U_b	mean vertical bubble velocity, (m/s)
W	bed width, (m)
1_1	width of the sampling area, (m)
x	horizontal position, (m)
y	vertical position, (m)
y_{fb}	freeboard height, (m)
Z	bed thickness, (m)

Greek letters

α_i	volume fraction, $(-)$
δ	root mean square discrepancy $(-)$
δ_b	fractional area occupied by bubbles $(-)$
δ_r	relative discrepancy $(-)$
δ_x	minimum cell size in horizontal direction (m)
δ_y	minimum cell size in vertical direction (m)
Θ_i	granular temperature, (m^2/s^2)
λ	bubble growth coefficient $(-)$
μ_i	shear viscosity, (kg/s m)
ρ_i	density, (kg/m^3)
$\overline{\overline{\tau_i}}$	stress tensor, (Pa)
ϕ	bubble velocity coefficient $(-)$
Ψ	fraction of visible flow $(-)$

Subscripts

g	gas
i	general index
s	solids
mf	minimum fluidization
L	leading bubble
RC	recirculation centre
Tr	trailing bubble

Bibliography

Ahuja, G.H., Patwardhan, A.W., CFD and experimental studies hold-up distribution and circulation patterns in gas-solid fluidized beds *Chem. Eng. J.*, 143 (2008), pp. 147-160

Almendros-Ibáez, J.A., Sobrino, C., de Vega, M., Santana, D., A new model for ejected particle velocity from erupting bubbles in 2-D fluidized beds *Chem. Eng. Sci.*, 61 (2006), pp. 5981-5990

Boemer, A., Qi, H., Renz, U., Verification of Eulerian simulation of spontaneous bubble formation in a fluidized bed *Chem. Eng. Sci.*, 53 (1998), pp. 1835-1846

Bokkers, G.A.,Laverman, J.A., van Sint Annaland, M., Kuipers, J.A.M., Modelling of large-scale dense gas-solid bubbling fluidised beds using a novel discrete bubble model *Chem. Eng. Sci.*, 61 (2006), pp. 5590-5602

Bokkers, G.A., van Sint Annaland, M., Kuipers, J.A.M., Mixing and segregation in a bidisperse gas-solid fluidised bed: a numerical and experimental study *Powder Technol.*, 140 (2004), pp. 176-186

Busciglio, A., Vella, G., Micale, G., Rizzuti, L., Analysis of the bubbling behaviour of 2D gas-solid fluidized beds. Part II. Comparison between experiments and numerical simulations via Digital Image Analysis Technique *Chem. Eng. J.*, 148 (2009), pp. 145-163

Caicedo, G.R., Prieto Marqus, J.J., Garca Ruz, M., Guardiola Soler,J. A study on the behaviour of bubbles of a 2D gas-solid fluidized bed using digital image analysis *Chem. Eng. and Proc.*, 42 (2003), pp. 9-14

Dan, S., Jianzhi, W., Huilin, L., Yunhua, Z., Juhui, C., Gidaspow, D., Ming, C., Numerical simulation of gas-particle flow with a second-order moment method in bubbling fluidized beds *Powder Technol.*, 199 (2010), pp. 213-225

Darton, R.C., LaNauze R.D., Davidson, J.F., Harrison, D., Bubble growth due to coalescence in fluidized beds *Trans. of the I. Chem. Eng.* , 55 (1977), pp. 274-280

Davidson, J. R., Harrison, D., Fluidized Particles Cambridge University Press (1963)

Davidson, J. R., Harrison, D., Fluidization Academic Press, New York (1971)

Deza , M., Franka, N. P., Heindel, T. J., Battaglia, F., CFD modelling and X-ray imaging of biomass in a fluidized bed *J. of Fluids Eng.* (2009), p. 131

Fluent, 2006. Fluent 6.3 Documentation. FLUENT Inc. http://fluent.com/.

Gidaspow, D. Multiphase Flow and Fluidization: Continuum and Kinetic Theory Descriptions Academic Press, San Diego (1994)

Goldschmidt, M. J. V., Kuipers, J. A., van Swaaij, W. P. M., Hydrodynamic modelling of dense gas-fluidised beds using the kinetic theory of granular flow: effect of coefficient of restitution on bed dynamics *Chem. Eng. Sci.*, 56 (2001), pp. 571-578

Grace, J.R., Taghipour, F., Verification and validation of CFD models and dynamic similarity for fluidized beds *Powder Technol.*, 139 (2004), pp. 99-110

Hilligardt, K., Werther, J., Local bubble gas hold-up and expansion of gas/solid fluidized beds *German Chem. Eng.*, 9 (1986), pp. 215-221

Hosseini, S.H., Ahmadi, G., Rahimi, R., Zivdar, M., Esfahany, M.N., CFD studies of solids hold-up distribution and circulation patterns in gas-solid fluidized beds *Powder Technol.*, 200 (2010), pp. 202-215

Johnsson, F., Andersson, S., Leckner, B., Expansion of a freely bubbling fluidized bed *Powder Technol.*, 68 (1991), pp. 117-123

Jung, J., Gidaspow, D., Gamwo, I.K., Measurement of two kinds of granular temperatures, stresses and dispersion in bubbling beds *Ind. Chem. Eng. R.*, 44 (2005), pp. 1329-1341

Jung, J., Gidaspow, D., Bubble computation, granular temperatures, and Reynolds Stresses *Chem. Eng. Communications*, 193 (2006), pp. 946-975

Kunii, D., Levenspiel, O., 1991. Fluidization Engineering. Butterworth-Heinemann Series in Chemical Engineering.

Laverman, J.A., Roghair, I., van Sint Annaland, M., Kuipers, H., Investigation into the hydrodynamics of gas-solid fluidized beds using particle image velocimetry coupled with digital image analysis *Can J. Chem. Eng.*, 86 (2008), pp. 523-535

Li, T., Grace, J., Bi, X. Study of wall boundary condition in numerical simulations of bubbling fluidized beds *Powder Technol.*, 203 (2010), pp. 447-457

Lin, J.S., Chen, M.M., Chao, B.T., A novel radioactive particle tracking facility for measurement of solids motion in gas fluidized beds *AIChE J.*, 31 (1985), pp. 465-473

Lindborg, H., Lysberg, M., Jakobsen, H.A., Practical validation of the two-fluid model applied to dense gas-solid flows in fluidized beds *Chem. Eng. Sci.*, 62 (2007), pp. 5854-5869

Liu, Z., Zheng, Y., Jia, L., Zhang, Q., Study of bubble induced flow structure using PIV *Chem. Eng. Sci.*, 60 (2005), pp. 3537-3552

Min, J., Drake, J. B., Heindel, T. J., Fox, R. O., Experimental validation of CFD simulations of a lab-scale fluidized-bed reactor with and without side-gas infection *AIChE J.*, 56 (2010), pp. 1434-1446

Nedderman, R.M., Laohakul, C. The thickness of the shear zone of flowing granular materials *Powder Technol.*, 25 (1980), pp. 91-100

Otsu, N. A threshold selection method from gray-level histograms IEEE Transactions on Systems, Man, and Cybernetics, 9 (1979), pp. 62-66

Patil, D.J., van Sint Annaland, M., Kuipers, J.A.M., Critical comparison of hydrodynamic models for gas-solid fluidized beds-Part I: bubbling gas-solid fluidized beds operated with a jet *Chem. Eng. Sci.*, 60 (2005), pp. 57-72

Raffel, M., Willert, C., Kompenhans, J. Particle Image Velocimetry, A Practical Guide Springer, Berlin (2007)

Sánchez-Delgado, S., Marugan-Cruz, C., Acosta-Iborra, A., Santana, D., Dense-phase velocity fluctuation in a 2-D fluidized bed *Powder Technol.*, 200 (2010), pp. 37-45

Santana, D., Nauri, S., Acosta, A., Garca, N., Macas-Machn, A., Initial particle velocity spatial distribution from 2-D erupting bubbles in fluidized bed *Powder Technol.*, 150 (2005), pp. 1-8

Shen, L., Johnsson, F., Leckner, B., Digital image analysis of hydrodynamics two-dimensional bubbling fluidized beds *Chem. Eng. Sci.*, 59 (2004), pp. 2607-2617

Sveen J.K., 1998-2007. MATPIV. http://www.math.uio.no/jks/matpiv/.

Syamlal, M., O'Brien, T.J., 1987. Derivation of a drag coefficient from velocity-voidage correlation. U.S. Department of Energy, Office of Fossil; Energy, National Energy Technology Laboratory, Morgantown, WV. Unpublished Report. Syamlal and O'Brien, 1989

Syamlal, M., Rogers, W., O'Brien T.J., 1993. MFIX Documentation: Vol. 1, Theory Guide. National Technical Information Service, Springfield, VA. DOE/METC-9411004, NTIS/DE9400087.

Taghipour, F., Ellis, N., Wong, C., Experimental and computational study of gas-solid fluidized bed hydrodynamics *Chem. Eng. Sci.*, 60 (2005), pp. 6857-6867

Toei, R., Matsumo, R., The Coalescence of Bubbles in the Gas-Solid Fluidized Bed Kyoto University, Japan (1967)

Van Wachem, B.G.M., Schouten, J.C., Krishna, R., van den Bleek, C.M., *Computers Chem. Eng.*, 22 (1998), pp. S299-S306

Vejahati, F., Mahinpey, N., Ellis, N., Nikoo, M.B., CFD simulation of gas-solid bubbling fluidized bed: a new method for adjusting drag law *Can. J. Chem. Eng.*, 87 (2009), pp. 19-30

Wang., J., Liu, Y., EMMS-based Eulerian simulation on the hydrodynamics of a bubbling fluidized bed with FCC particles *Powder Technol.*, 197 (2010), pp. 241-246

Chapter 3

Comparison of bubble eruption models with two-fluid simulations in a 2D gas-fluidized bed

Contents

3.1 Abstract

Two-fluid simulations of gas-solid fluidized beds are performed in this chapter with a threefold aim: (1) explore the capabilities of two-fluid modelling to reproduce realistically bubble eruption patterns in two-dimensional fluidized beds; (2) compare the

results obtained from the two-fluid simulations with particle ejection models; and (3) provide information about the mutual interaction of the gas and particle flows during bubble eruption. To fulfil these aims, results from two-fluid simulations concerning the vertical and horizontal velocities of particles in bubble domes, prior to and during bubble eruption, are reported and compared with previously published experimental data taken from a bed of comparable geometry and operating conditions. The comparison shows excellent quantitative agreement. Particle ejection velocities estimated through semi-empirical and theoretical models proposed in the literature are compared with the particle behaviour in the bubble dome obtained from the two-fluid simulations. The results obtained here indicate that the theory based on the potential flow around a cylinder provides a more accurate prediction for the particle velocities in erupting bubbles than semi-empirical relations. For the data reported here it has been found that the velocity of particles in the bubble dome forms an angle with the vertical direction that is twice the angle formed by the radial direction. This observation is contrary to standard models of 2D bubbles, which assume that the particles are ejected radially outwards from the dome.

3.2 Introduction

One aspect worthy of further study in fluidized bed systems, is the behaviour at the top of the bed, that is, bubble eruption and collapse, and the associated ejection, elutriation or entrainment of particles. An understanding of the underlying physics of these processes is not only important from an academic point of view but is also of industrial relevance. The rate of particle elutriation affects the operation of a fluidized bed reactor, and the height of particle entrainment is an important design parameter. It has been suggested that particles are ejected into the freeboard either from the roof (Do et al., 1972; Saxena and Mathur, 1984) or the wake of a bubble (George and Grace, 1978). Pemberton and Davidson (Pemberton and Davidson, 1986) emphasised the importance of the effect of the walls on the ejection mechanism, finding that in a two-dimensional (2D) bed, ejection from the roof of the bubble dominated, whereas in a three-dimensional (3D) bed ejection from the wake of the bubble was favoured for sufficiently high gas velocities. The pattern in which bubbles erupt can also influence whether particles are ejected from the wake or the roof of a bubble, and the maximum height reached by the ejected particles (Levy et al., 1983; Hatano and Ishida, 1981). Hatano and Ishida (Hatano and Ishida, 1981) divided the patterns of bubbles bursting at the top of a fluidized bed into four categories: (1) isolated bubbles, (2) successively rising bubbles, (3) coalescing bubbles, and (4) successively coalescing bubbles. In the

case of the eruption of an isolated bubble, particles are ejected from the roof of the bubble, whereas particles are ejected from the wake of the leading bubble in the case of coalescing bubbles (Levy et al., 1983; Hatano and Ishida, 1981).

Experimental studies using Particle Image Velocimetry (PIV), are used to investigate the eruption of solids in fluidized beds. Santana *et al.* (Santana et al., 2005) studied the mechanism of solids ejection in a bubbling fluidized bed of 5 mm thickness filled with sand particles of 0.3 mm mean diameter and fluidized with air at superficial velocity of $U = 2.8 \times U_{\mathrm{mf}}$. They found good agreement between their measurements and the empirical model proposed by Fung and Hamdullahpur (Fung and Hamdullahpur, 1994). Using the same bed, Almendros-Ibáñez *et al.* (Almendros-Ibáñez et al., 2006) continued this work for a range of fluidization velocities (i.e. from 2 to 4 times U_{mf}) and modified the Fung and Hamdullahpur model by taking into account the bubble velocity, the bubble growth, and the bubble rise direction. Later, Müller *et al.* (Müller et al., 2007) extended the work of Santana *et al.* (Santana et al., 2005) by studying the vorticity of the particulate phase surrounding a bubble and applying the potential flow theory (Pemberton and Davidson, 1986) to predict the particle velocities in the dome of the bubble. For that study, Müller *et al.* (Müller et al., 2007) employed a bed of 10 mm thickness filled with either sand or aluminium oxide particles with mean diameters of approximately 0.6 mm and 0.5 mm, respectively. Superficial velocities covering a range from 1.2 to 1.96 times U_{mf} were studied. Although the potential flow theory was originally developed for isolated bubbles ascending in a fluidized bed, the results reported in (Pemberton and Davidson, 1986) showed that potential flow theory can also be used to predict the particle velocity in the dome of an erupting bubble.

Although there are differences between laboratory controlled 2D beds and real 3D beds, general theories describing the bubble behaviour before eruption in 2D situations have proved to be extensible to 3D domains by merely adding a third dimension in the resulting models. This is, for example, the case of potential flow theory (Davidson, 1963). Furthermore, the mechanism of particle ejection in 3D beds in which the superficial gas velocity is less than 10 or 15 times U_{mf} is very similar to the mechanism that dominants in 2D beds, i.e. particles are ejected predominantly from the roof of bursting bubbles (Pemberton and Davidson, 1986). Therefore, it is believed that studies performed in 2D beds are a valuable tool for assessing and developing bubble eruption models. However, it should be stressed that other phenomena in 2D fluidized bed studies may not easily transferred to 3D beds.

The discrepancies found between experiments and simulation regarding the mean solids velocity in Chapter 2 may be caused by several factors. In order to rule out some of this factors the motion of particles around bubbles using two-fluid model simulations

is studied.

The present chapter reports two-fluid simulations of a 2D bed filled with particles group B of Geldart's classification and fluidized with air. The main objective of this study is to test the ability of such simulations to reproduce realistically the particle velocity during bubble eruption, as well as to compare the results with (i) experimental data and (ii) existing semi-empirical and theoretical models for particle ejection. In the first part of the work, the particle velocities around an isolated bubble in the centre of the simulated bed are compared with results derived from the potential flow theory, which is commonly accepted as a good representation of the particle velocity around bubbles far from walls or from other bubbles (Kunii and Levenspel, 1991). The effect of a second, smaller bubble on the simulated velocity profile around a bubble is also studied. In the second part of the work, the velocity profiles of particles in the dome of an erupting bubble are analysed and compared with experimental PIV data together with the velocity profiles predicted by the particle ejection models of Fung and Hamdullahpur (Fung and Hamdullahpur, 1994), Almedros-Ibáñez *et al.* (Almendros-Ibáñez et al., 2006), and Müller *et al.* (Müller et al., 2007). Such a comprehensive comparison has not been reported in the literature before and allows a critical evaluation of various particle ejection models. Additionally, once the capabilities of the two-fluid model have been verified in the framework of isolated and erupting bubbles, the relationship between the instantaneous gas and particle velocities in the bubble dome is investigated using results from the two-fluid simulation. Such coupled information regarding the two phases (gas and solids) is difficult to obtain experimentally, which confers an added value to the simulation results.

3.3 Simulated system

In this work the bubble dynamics were studied in two fluidized beds. Table 3.1 summarises the most important parameters for these two systems. Case 2 was chosen to match the experimental system reported by Müller *et al.* (Müller et al., 2007). For both systems the gas inlet velocity was set to be $U = 1.25 \times U_{\mathrm{mf}}$ such that the bed operates in a bubbling regime with only a small number of bubbles present. This ensures the existence of isolated bubbles within the centre of the bed, which are required for this study. Figure 3.1 shows contours of solids volume fraction for a snapshot of simulation case 1. A Cartesian coordinate system is employed in this work, with the x and y axes aligned along the horizontal and vertical directions respectively.

Table 3.1: Simulation parameters

Parameter	Case 1	Case 2
Particle density (kg/m^3)	1000	2600
Gas density (kg/m^3)	1.2	1.2
Gas viscosity (Pa s)	1.8e-5	1.8e-5
Particle diameter (mm)	1.2	0.6
Minimun fluidization velocity (m/s)	0.3	0.225
Bed width (m)	0.2	0.2
Bed height (m)	0.5	0.5
Static bed height (m)	0.27	0.27
Initial voidage (-)	0.4	0.4
Superficial gas velocity (m/s)	0.375	0.283
Restitution coeffcient (-)	0.9	0.9
Angle of internal friction (°)	30	30

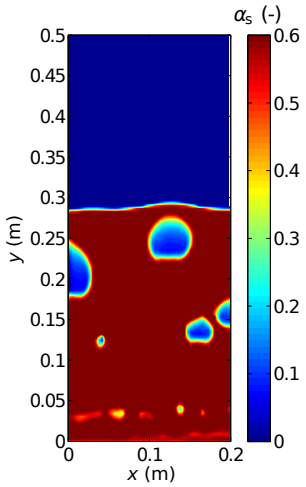

Figure 3.1: Snapshot of the particle volume fraction in the 2D fluidized bed simulated (case 1).

3.4 Two-fluid model

3.4.1 General equations

The two-fluid model, based on the conservation equations of mass, momentum and granular temperature, was solved using the MFIX code (Multiphase Flow with Interphase eXchanges) (Syamlal et al., 1993; Benyahia et al., 2007). The kinetic theory of granular flow, which characterized the stochastic fluctuations of the solids kinetic energy, was used for the closure of the solids stress terms. The governing equations as well as the closure models can be found in appendix A.

A second order accurate scheme was used to discretise the convective derivatives. For simulation case 1, the 2D computational domain was discretised using square cells

of 3.6 mm length in a mesh of 7645 nodes. Thus, the cell size was 3 times the particle diameter. For simulation case 2, square cells of 2.5 mm length were chosen due to the smaller particle size used in this case, resulting in a mesh of 15288 nodes. The initial time step was set to 0.5×10^{-5} s to ensure convergence of the equation system during the first seconds of the simulation. A uniform and steady velocity profile was chosen at the inlet boundary and a fixed pressure boundary condition was chosen at the top of the freeboard. The lateral walls were modelled as no-slip walls for both phases. It is felt that the lateral boundary condition does not have a strong influence on the motion of an isolated bubble in the centre of the bed. The initial solids volume fraction was set to 0.6.

The solids volume fraction and solids velocity were recorded every 0.005 s to provide the temporal resolution required to study bubble eruption events. In order to study bubble motion, it is necessary to distinguish between bubbles and the emulsion phase. This is done by setting a cutoff value for the solids volume fraction equal to $\alpha_s = 0.3$, as reported by Hernández-Jiménez et al. (2011a), which is the arithmetic mean of the maximum and minimum solids volume fractions in the simulated bed. Any region in which the solids volume fraction is less than 0.3 is defined to be a bubble.

The drag force correlation used in this study is the extension of the Hill and Koch drag law (Hill et al., 2001a,b), proposed by Benyahia *et al.* (Benyahia et al., 2006). Details about the drag force can be found in Appendix A.

3.5 Theoretical models for particle ejection

The bubble eruption results obtained from the simulations are compared to three bubble eruption models: (*i*) potential flow theory (Müller et al., 2007), (*ii*) the Fung and Hamdullahpur model (Fung and Hamdullahpur, 1994), and (*iii*) the Almendros-Ibáñez model (Almendros-Ibáñez et al., 2006).

Pemberton and Davidson (Pemberton and Davidson, 1986) used the potential flow theory to predict the particle flow in the dome formed by an erupting bubble. Müller *et al.* (Müller et al., 2007) extended this theory to predict the velocity of particles at the top of the dome formed by an erupting bubble. The velocity potential, Φ, is governed by Laplace's equation:

$$\nabla^2 \Phi = 0 \tag{3.1}$$

For a 2D system, the velocities in the x and y directions are given by:

$$U = \frac{\partial \Phi}{\partial x} \tag{3.2}$$

$$V = \frac{\partial \Phi}{\partial y} \tag{3.3}$$

As a first approximation, the bubble in a 2D bed is assumed to be of cylindrical shape with a radius R and velocity U_b. The velocity vector of the bubble centroid forms an angle θ_b with the positive vertical direction (Almendros-Ibáñez et al., 2009). In this work the angle θ_b shall be termed the direction of bubble rise. The velocity potential around a cylinder is given by (Davidson, 1963) as:

$$\Phi_{xy} = -U_b \left(\frac{R^2}{x^2 + y^2} \right) (y \cos(\theta_b) + x \sin(\theta_b)) \tag{3.4}$$

Here the coordinate pair (x, y) describe the distance from the centre of the cylinder in the horizontal and vertical directions. Using equations (3.2) and (3.3) the velocities in the x and y directions are given by:

$$U = \left(\frac{U_b R^2}{x^2 + y^2} \right) \left(\frac{2x(y \cos(\theta_b) + x \sin(\theta_b))}{x^2 + y^2} - \sin(\theta_b) \right) \tag{3.5}$$

$$V = \left(\frac{U_b R^2}{x^2 + y^2} \right) \left(\frac{2y(y \cos(\theta_b) + x \sin(\theta_b))}{x^2 + y^2} - \cos(\theta_b) \right) \tag{3.6}$$

If the bubble ascends in vertical direction, $\theta_b = 0$, and the expressions (3.4), (3.5) and (3.6) can be simplified to give:

$$\Phi_{xy} = -U_b y \left(\frac{R^2}{x^2 + y^2} \right) \tag{3.7}$$

$$U = 2U_b xy \left(\frac{R}{x^2 + y^2} \right)^2 \tag{3.8}$$

$$V = U_b \left(y^2 - x^2 \right) \left(\frac{R}{x^2 + y^2} \right)^2 \tag{3.9}$$

Turning now to bubble eruption models, Fung and Hamdullahpur (Fung and Hamdullahpur, 1994) assumed a linear decrease of the particle velocity with the eruption angle, θ:

$$\frac{\vec{V}}{V_{\max}} = \left(1 - \frac{|\theta|}{\theta_{\max}} \right) \vec{e}_r \tag{3.10}$$

where $V_{\max}$ is the maximum vertical velocity of the particles in the dome of the bubble,

$\vec{V}$ is the particle velocity vector, $\theta_{\max}$ is the maximum value of the eruption angle and $\vec{e_r}$ is the unit vector in the radial direction relative to the centroid of the bubble. The eruption angle, θ, is the angle that defines the position of any point in the bubble dome, and can cover a range from -90° to 90°. The eruption angle is defined to be 0° at the top of the bubble, as indicated in figure 3.2.

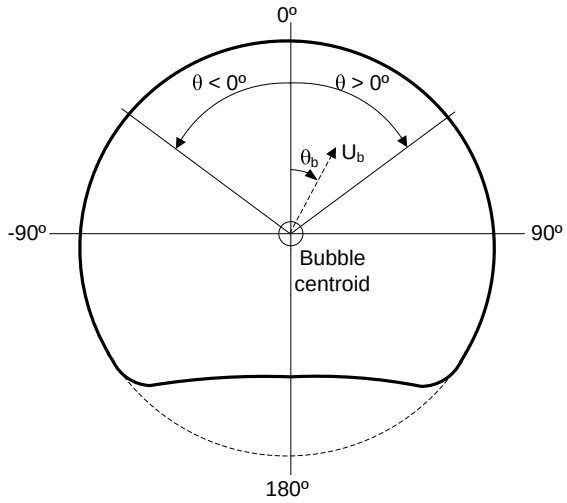

Figure 3.2: Sketch of a bubble showing the definition of the eruption angle, θ, and the direction of bubble rise, θ_b.

Almendros-Ibáñez *et al.* (Almendros-Ibáñez et al., 2006) modified the model of Fung and Hamdullahpur (Fung and Hamdullahpur, 1994) by including the bubble velocity, the bubble growth, and the direction of bubble rise. They described the particle velocity using the expression

$$\vec{V}(\theta) = \vec{U}_{p,b}(\theta) + \vec{U}_{p,gr}(\theta) \tag{3.11}$$

where $\vec{V}$ is the particle velocity and the added subscripts b and gr indicate the contributions from the velocity of the centroid of the bubble and the bubble growth, respectively. These terms were expressed as:

$$\vec{U}_{p,b}(\theta) = \begin{Bmatrix} U_b \left(\frac{\theta-\theta_{\min}}{\theta_b-\theta_{\min}}\right) \vec{e_r} \ , & \theta < 0 \\ U_b \left(\frac{\theta-\theta_{\max}}{\theta_b-\theta_{\max}}\right) \vec{e_r} \ , & \theta \geq 0 \end{Bmatrix} \tag{3.12}$$

$$\vec{U}_{p,gr}(\theta) = \begin{Bmatrix} U_{gr}(2 - \sin(\theta_b)|\sin(\theta_b)|) \left(1 - \frac{\theta-\theta_{\min}}{\theta_b-\theta_{\min}}\right) \vec{e_r} \ , & \theta < 0 \\ U_{gr}(2 + \sin(\theta_b)|\sin(\theta_b)|) \left(1 - \frac{\theta-\theta_{\max}}{\theta_b-\theta_{\max}}\right) \vec{e_r} \ , & \theta \geq 0 \end{Bmatrix} \tag{3.13}$$

where θ is the eruption angle and θ_b is the angle between the bubble rise velocity vector and the vertical direction. As equations (3.12) and (3.13) are applicable for non-symmetrical domes, the positive and negative limits of the eruption angle, $\theta_{\max}$

and $\theta_{\min}$ respectively, can have different values. The bubble velocity in this model is calculated at the instant when the bubble breaks through the dome. This instant is difficult to define in the two-fluid model due to the continuous character of the simulated solids-phase. In the present work the process of bubble eruption starts when the vertical velocities of the particles within the bubble dome begin to decrease. For the cases considered here, θ_b is very close to 0°, i.e. the ascent of the bubbles is almost vertical. In equation (3.13), the bubble growth velocity can be defined as follows:

$$U_{gr} = \frac{1}{2}\frac{\partial D_{eq}}{\partial t} \tag{3.14}$$

The model described by equations (3.11) to (3.14) states that the maximum particle velocity at the dome of an erupting bubble is equal to the bubble velocity. However, this leads to an overestimation of the maximum particle velocities when compared to the results of the two-fluid simulation because the particle velocities in the bubble dome are smaller than the velocity of the centroid of the bubble. Thus, a modification of the particle ejection model of Almendros-Ibáñez *et al.* (Almendros-Ibáñez et al., 2006) is suggested. Instead of using the velocity of the bubble centroid in equation (3.12), the velocity U_b shall be obtained from the simulation results for the bubble dome at the position $\theta = 0°$, as is the case for $V_{\max}$ in equation (3.10). This leads to:

$$\vec{U}_{p,b}(\theta) = \begin{cases} V_{\max}\left(\frac{\theta-\theta_{\min}}{\theta_b-\theta_{\min}}\right) & , \quad \theta < 0 \\ V_{\max}\left(\frac{\theta-\theta_{\max}}{\theta_b-\theta_{\max}}\right) & , \quad \theta \geq 0 \end{cases} \tag{3.15}$$

It is important to note that the models of Fung and Hamdullahpur (Fung and Hamdullahpur, 1994) and Almendros-Ibáñez *et al.* (Almendros-Ibáñez et al., 2006) assume that particles are ejected in the radial direction. However, this is not the case in the potential flow model described by equation (3.7).

In order to compare the results of the two-fluid simulations with the models described above, the velocity of bubbles within the simulations must be obtained. In this work the bubble velocity is estimated based on the displacement of the centre of mass of the bubble calculated over ten time steps. The diameter of the bubble is assumed to be the diameter of a circle with an area equal to that of the bubble, $D_{eq} = \sqrt{4A/\pi}$.

3.6 Results and discussion

3.6.1 Isolated bubbles

The first part of the results focuses on comparing particle velocities extracted from the two-fluid model for an isolated bubble in the middle of the bed with the velocity predicted by the potential flow theory, equation (3.7). Here, an arbitrarily selected bubble is analysed for each of the two cases summarised in Table 3.1. During the course of this work several bubbles have been analysed for each simulation case. Similar behaviour was observed for all of the bubbles studied. Therefore, it is felt that the bubbles presented here are representative of the bubbles that have been analysed.

The bubble studied for simulation case 1 has an equivalent diameter of $D_{eq} = 3.3 \times 10^{-2}$ m and a rise velocity of $U_b = 0.369$ m/s. The direction of bubble rise is approximately $\theta_b = 0°$. The bubble is as isolated as possible, with no other bubbles in its surroundings and as far as possible from the freeboard and the side walls. Figure 3.3 shows three snapshots of the isolated bubble consisting of contour maps of the solids volume fraction, the solids velocity, and the vorticity, following the analysis performed in (Müller et al., 2007). Arrows representing the solids velocity vectors have been superimposed on the velocity and vorticity maps. For clarity only every second vector has been plotted. For 2D systems, the vorticity of the particulate phase is given by:

$$\omega = \left(\frac{\partial V}{\partial x} - \frac{\partial U}{\partial y} \right) \tag{3.16}$$

where the partial derivatives are calculated from the simulation data using a second order central difference scheme involving a 3×3 matrix of mesh nodes. Information about the vorticity of a fluidized bed is highly relevant because most models and correlations are based on potential flow theory and can, therefore, be compromised if ω is not close to zero in the emulsion phase.

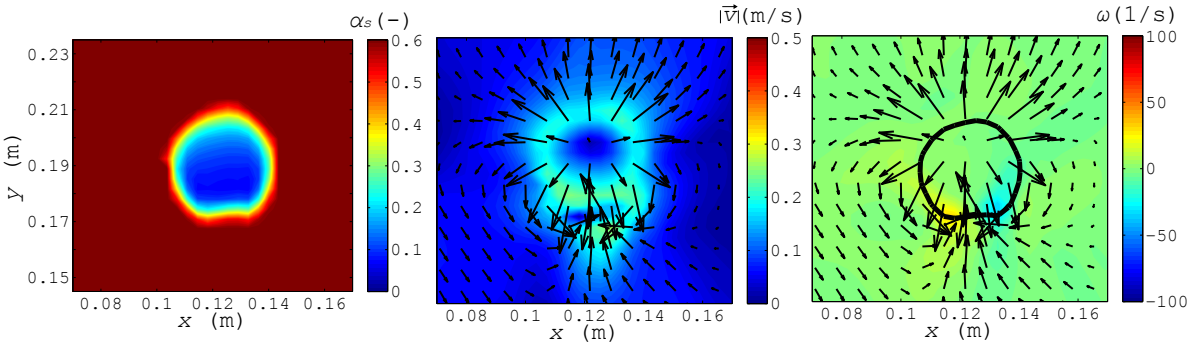

Figure 3.3: Bubble contours for case 1: solids volume fraction (-), solids velocity (m/s) and vorticity (1/s). $U_b = 0.369$ m/s.

The maps of solids fraction and velocity in figure 3.3 suggest qualitative agreement with the potential flow theory: The bubble is nearly circular, the highest solids velocities are located at the sides of the bubble, and the bubble wake is restricted to a small region in the lower part of the bubble. Both the velocity vectors and vorticity in the wake of the bubble indicate that the largest vorticity is confined to the bubble wake and that the vorticity rapidly decreases outside of this region. Figure 3.4 plots the simulation results for the vertical and horizontal velocities of the solid phase at points around a circle surrounding the contour defining the bubble (i.e. the contour defined by $\alpha_s = 0.3$ in figure 3.3). For comparison purposed, the solid phase velocities predicted by potential flow theory around a cylinder of radius $R = D_{eq}/2$ are also shown in figure 3.4. The horizontal axis in figure 3.4 is the angle θ of each point around the circle. As in the case of the particle ejection models described in the previous section, θ starts at the bubble top and increases in the clockwise direction. The results shown in figure 3.4 for both the horizontal and vertical velocities show good quantitative agreement around the whole bubble perimeter, particularly at the bubble top defined by $-90° < \theta < 90°$. Even in the bubble wake, where the deviation of the bubble shape from a circle is expected to be greatest, the agreement of both the shape and magnitude of the velocity profiles is remarkable.

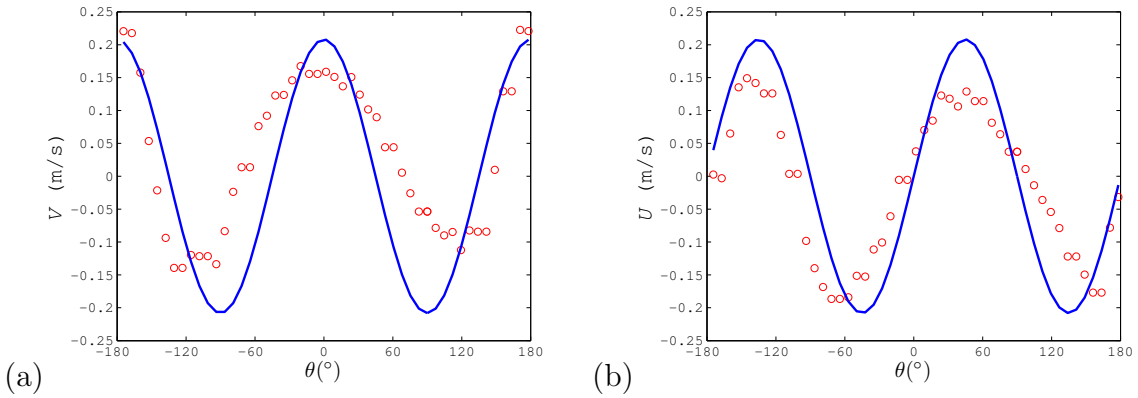

(a) (b)

Figure 3.4: Particle velocity for case 1: (a) Vertical velocity (m/s), (b) Horizontal velocity (m/s). Solid line, potential flow theory; red circle, two-fluid model. $U_b = 0.369$ m/s.

The bubble analysed for case 2 has a similar size and velocity to the bubble considered above. Specifically, the bubble has an equivalent diameter of $D_{eq} = 3.5 \times 10^{-2}$ m and a rise velocity of $U_b = 0.327$ m/s. The direction of bubble rise is approximately $\theta_b = 0°$. Figure 3.5 shows contour maps of the solids volume fraction, the velocity of the solids and the vorticity of the solid phase for this bubble. These data indicate that this bubble is not isolated and that there is a second, smaller bubble to the right of it. This smaller bubble interacts with the larger bubble and disturbs the flow pattern

around it.

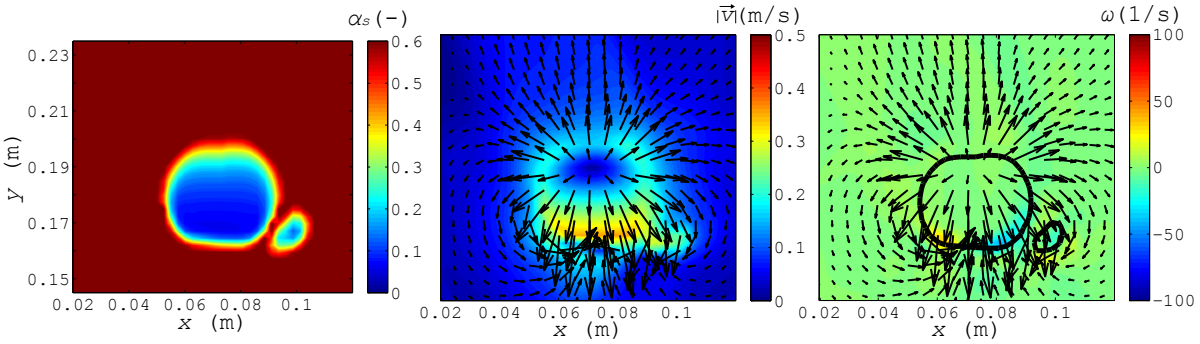

Figure 3.5: Bubble contours for case 2: solids volume fraction (-), solids velocity (m/s) and vorticity (1/s). $U_b = 0.327$ m/s.

Figure 3.6 shows the horizontal and vertical velocities of the solid phase at points on a circle surrounding the large bubble show in figure 3.5. For comparison, the velocities predicted by potential flow theory are also plotted. The simulated velocities circumscribing the selected bubble show good agreement with the predictions from potential flow theory. It is interesting to note that the influence of the small bubble on the velocities of the solid phase encircling the large bubble is restricted to a small region close to the location of the small bubble. This suggests that the potential flow theory may be a robust model for predicting the flow pattern around bubbles and may be able to provide useful information in non-ideal cases, such as case 2.

Comparing the velocity profiles shown in figures 3.4 and 3.6, it is evident that both cases share a similar, small deviation from the potential flow model. In the upper half of the bubble, the region of positive vertical velocity obtained from the simulation is broader than that predicted by potential flow theory (i.e. from $\theta = -45°$ to $45°$). In the lower half of the bubble, however, the region of positive vertical velocity is smaller

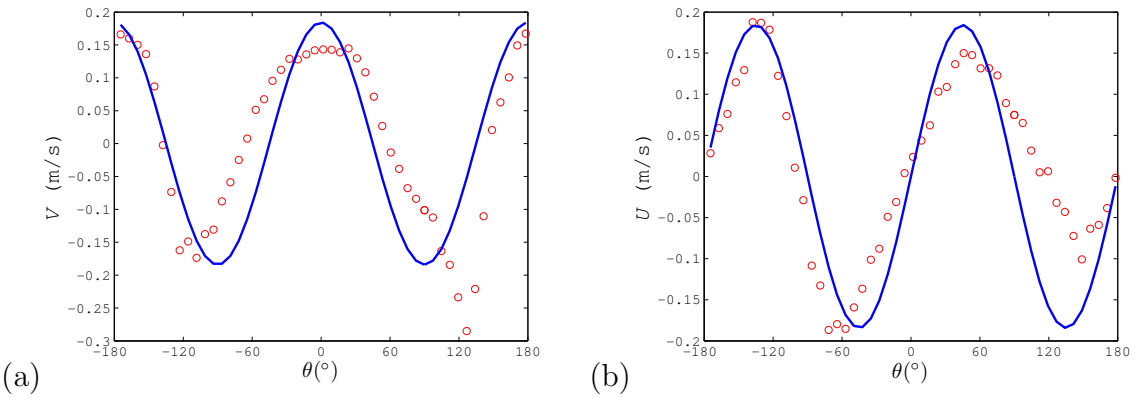

(a) (b)

Figure 3.6: Particle velocity for case 2: (a) Vertical velocity (m/s), (b) Horizontal velocity (m/s). Solid line, potential flow theory; red circle, two-fluid model. $U_b = 0.327$ m/s.

than predicted by the potential flow profiles. This phenomena may be explained by recognising that the bubble is not a perfect circle and, thus, the centre of mass of the bubble used for the calculation of θ in the velocity profiles is placed slightly above the real centre of the circle that encloses both the bubble and its wake. However, identifying the circle that encloses the bubble and its wake is a somewhat subjective operation. For this reason, the bubbles in this work shall be represented by a circle centred at the centre of mass of the bubble.

3.6.2 Bubble eruption

In this section results obtained from the two-fluid model simulations for the vertical and horizontal velocities of particles in the dome (i.e. the roof) of erupting bubbles are compared with predictions from the particle ejection models described previously. Following the methodology used above in the study of isolated bubbles, one bubble is selected at random for each of the simulation cases summarised in Table 3.1. Again, the bubbles analysed here are felt to be representative of the bubbles that have been analysed for each of the two simulation cases.

To allow the evolution of the particle motion during bubble eruption to be analysed, particle velocities have been obtained at various stages of the bubble eruption process. In this work bubble eruption is defined as beginning when the vertical velocities of the particles within the bubble dome begin to decrease. In the results presented here, time, t, is defined to be 0 at this point. Based on this definition, it is expected that, for $t \geq 0$, the particles within the bubble dome will have been ejected from the bulk of the bed and that the interactions between these particles will be greatly reduced. Consequently, these particles are assumed to follow approximately parabolic trajectories for $t \geq 0$.

Figure 3.7 shows contour maps of the solids volume fraction, solids velocity and solids vorticity for an erupting bubble from simulation case 1. Arrows indicating the solids velocity vectors have been superimposed on the velocity and vorticity plots. The first time depicted in figure 3.7 is $t = -25$ ms, that is, 25 ms before the bubble starts to erupt.At this time the top of the bubble is approximately $D_{eq}/2$ below the free surface of the bed. At $t = -25$ ms the bubble has an an equivalent diameter of $D_{eq} = 4.7 \times 10^{-2}$ m, a rise velocity of $U_b = 0.424$ m/s, and a velocity due to bubble growth of $U_g = 5.9 \times 10^{-2}$ m/s. The direction of bubble rise is approximately $\theta_b = 0°$. The velocity vectors shown in figure 3.7 indicate that between $t = 25$ ms and $t = 50$ ms, the particles within the bubble dome begin to fall back towards the bed (i.e. $V < 0$), showing that the bubble dome is starting to collapse. For $t = 75$ ms, the solids volume fraction within the dome of the bubble is very low, which can be interpreted as rupture of the bubble dome.

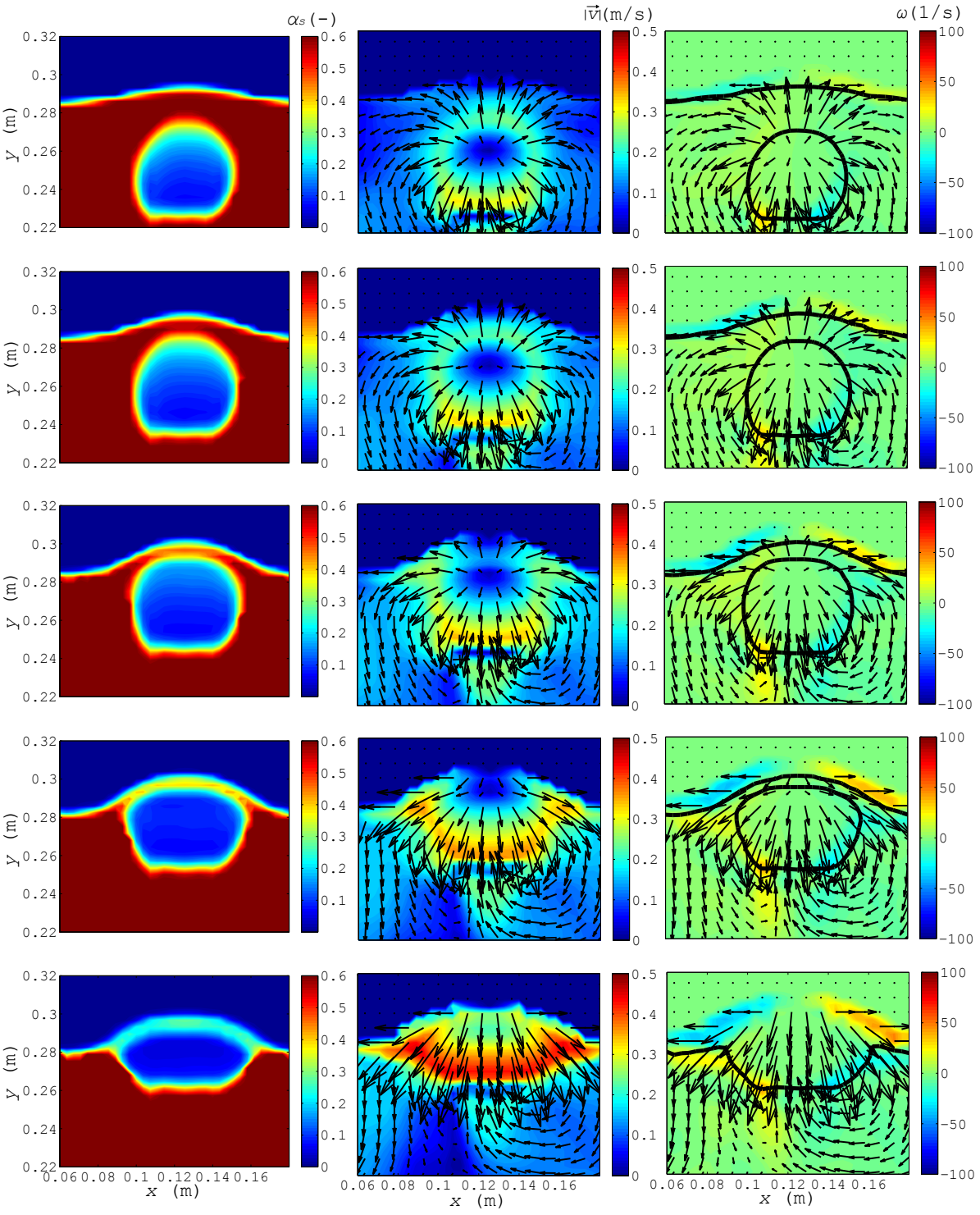

Figure 3.7: Erupting Bubble contours for case 1: rows correspond to different time instants, from $t = -25$ ms (Upper row) to $t = 75$ ms (lower row), every 25 ms, and columns correspond, from left to right, to solids volume fraction (-), solids velocity (m/s), and vorticity (1/s). $U_b = 0.424$ m/s and $U_g = 5.9 \times 10^{-2}$ m/s.

The vorticity maps presented in figure 3.7 show that, at $t = -25$ ms, the vorticity around the bubble is close to zero, except in its wake. This is consistent with the observations made for the isolated bubbles analysed above. Interestingly, once the bubble begins to erupt, this region of high vorticity appears to remain in an approximately constant position throughout the collapse of the bubble dome.

Figures 3.8 and 3.9 compare the velocities of particles within the dome of the bubble shown in figure 3.7, with velocities predicted by a range of bubble eruption models. The velocity profiles are plotted against the eruption angle, θ, and are shown for times of $t = -25$, 0 and 25 ms. The results show that the best agreement between the ejection models and the simulation results occurs at $t = 0$. At this value of t, all of the bubble eruption models are in good agreement with the simulation data obtained for the vertical velocities near the centre of the bubble dome (i.e. $-20° \leq \theta \leq 20°$). Considering both the vertical and horizontal velocities, the potential flow model appears to show the best agreement with the simulation data at $t = 0$. The Fung and Hamdullahpur model (Fung and Hamdullahpur, 1994) is plotted in figures 3.8 and 3.9 for two different values for the maximum angle of eruption $\theta_{\max}$: 50° and 90°. These two values demonstrate the effect of varying $\theta_{\max}$ in the Fung and Hamdullahpur model (Fung and Hamdullahpur, 1994). It is clear from figure 3.8 that, near to the top of the bubble, $\theta_{\max} = 90°$ predicts the simulation results more accurately. However, for $\mid \theta \mid > 20°$, $\theta_{\max} = 50°$ gives a more accurate prediction of the particle velocities. Nevertheless, the model from Fung and Hamdullahpur (Fung and Hamdullahpur, 1994) cannot predict the rounded shape of the velocity profile for either of the values of $\theta_{\max}$ studied.

In figures 3.8 and 3.9 the model from Almendros-Ibáñez *et al.* (Almendros-Ibáñez et al., 2006) is presented in the modified form given by equation (3.15). The values of $\theta_{\max}$ and $\theta_{\min}$ required by this model were obtained from the bubble contours shown in figure 3.7. Close to the top of the bubble there is good agreement between this model and the simulated vertical velocities of the particles. However, this model over-predicts the vertical velocities of the particles for larger magnitudes of the eruption angle (i.e. $\mid \theta \mid > 20°$). For example, at $\mid \theta \mid = 40°$ figure 3.8 shows that the two-fluid simulation yields a vertical velocity of particles around 50 % smaller than the velocity derived from the modified model of Almendros-Ibáñez *et al.* (Almendros-Ibáñez et al., 2006). This finding is in agreement with the relative error shown by Almendros-Ibáñez *et al.* (Almendros-Ibáñez et al., 2006) for their model for $\theta > 50°$ in bubbles whose mass centres are below the bed surface (i.e. case (a) and (b) in (Almendros-Ibáñez et al., 2006)). However, the relative errors reported in Almendros-Ibáñez *et al.* (Almendros-Ibáñez et al., 2006) were smaller in magnitude that those in figure

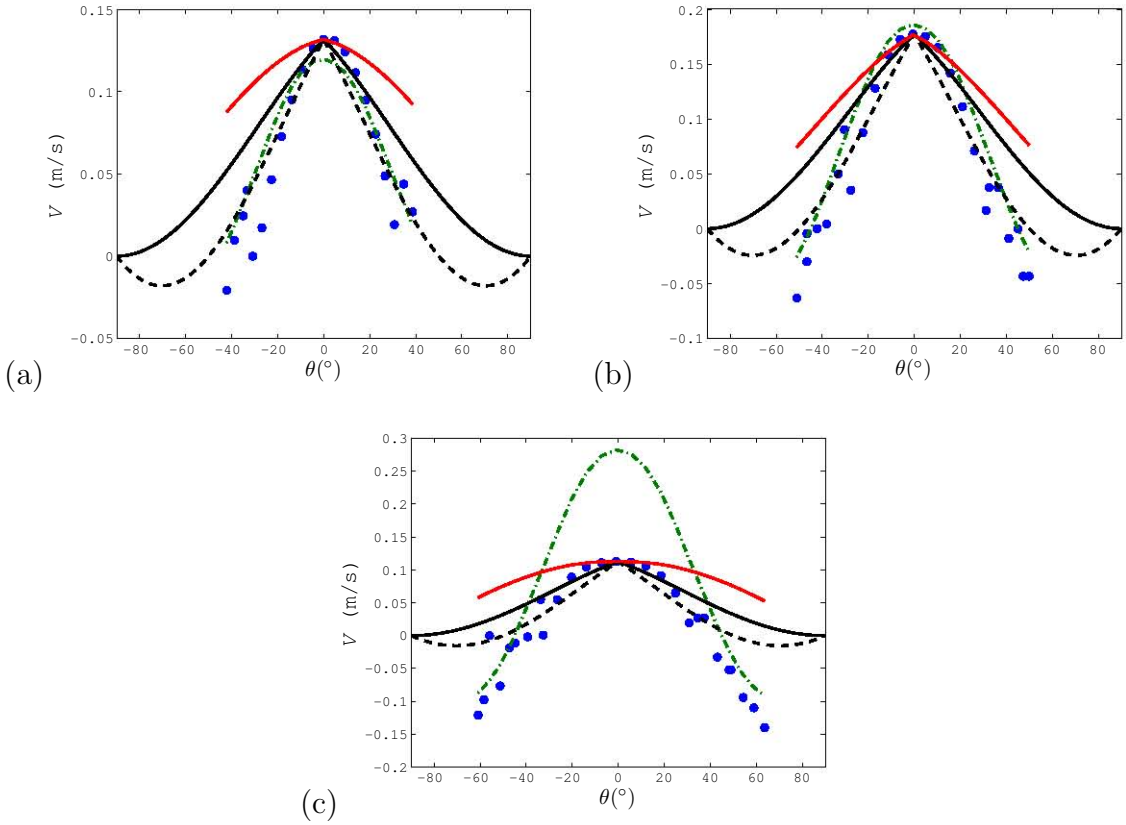

Figure 3.8: Particle dome vertical velocity V for case 1 shown in Figure 3.7: (a) $t = -25$ ms, (b) $t = 0$, (c) $t = 25$ ms. Blue filled circle, two-fluid model; green dash-dot line, potential flow theory; red solid line, modified Almendros-Ibañez model; black solid line, Fung and Hamdullahpur model 90°; dash black line, Fung and Hamdullahpur model 50°. $U_b = 0.424$ m/s and $U_g = 5.9 \times 10^{-2}$ m/s.

3.8, which may be attributed to the greater fluidization velocity and more vigorous bubbling regime studied in (Almendros-Ibáñez et al., 2006). In this regard, due to bubble coalescence and deformation, higher particle velocities during bubble eruption can be expected if the superficial velocity of air injected into the bed is increased (Fung and Hamdullahpur, 1994). It should be noted that, like the Fung and Hamdullahpur model (Fung and Hamdullahpur, 1994), the velocity profiles predicted by the model of Almendros-Ibáñez *et al.* (Almendros-Ibáñez et al., 2006), can be modified by varying the values of $\theta_{\max}$ and $\theta_{\min}$.

For the horizontal component of the particle velocity, U, figure 3.9 demonstrates that, of the models considered here, only potential flow theory is able to provide results that are comparable with the two-fluid simulation. The model of Fung and Hamdullahpur (Fung and Hamdullahpur, 1994) and the modified Almendros-Ibáñez *et al.* (Almendros-Ibáñez et al., 2006) model predict qualitatively the variation of U with θ, but the magnitude of the velocities predicted by these models is significantly smaller than the simulation results. At large magnitudes of the eruption angle, the model of

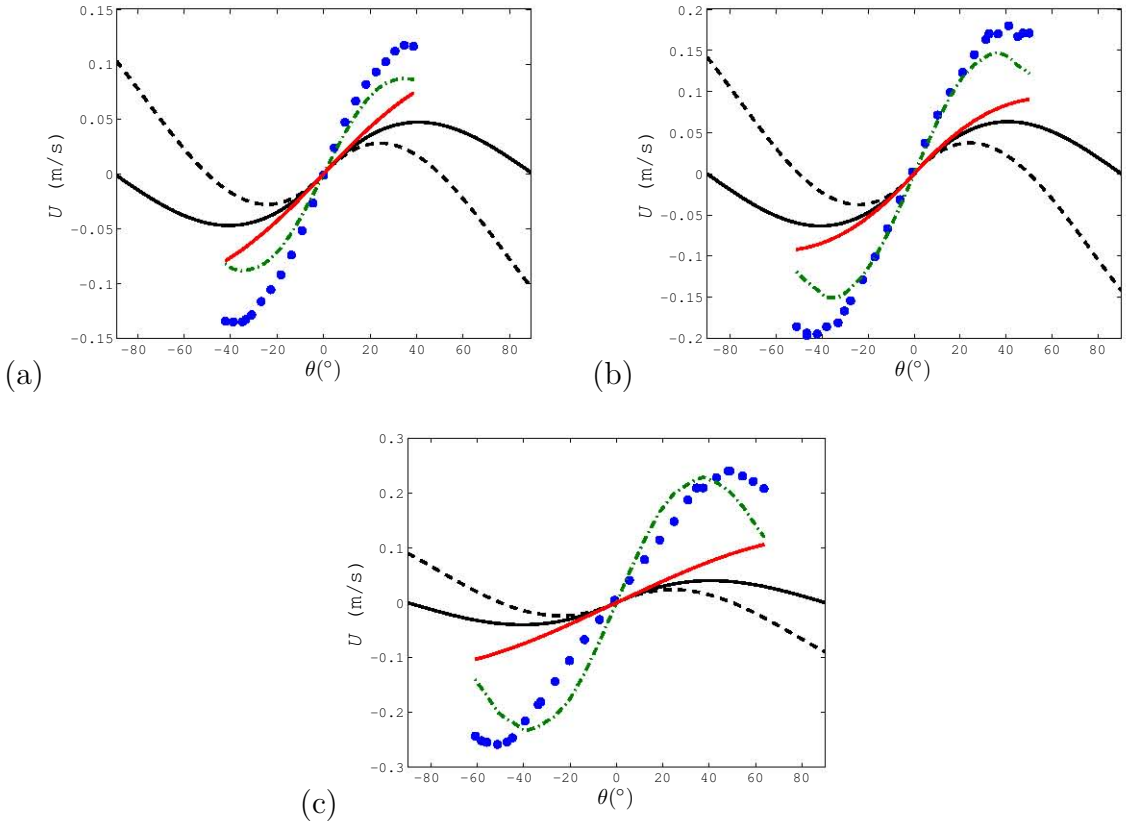

Figure 3.9: Particle dome horizontal velocity U for case 1 shown in Figure 3.7: (a) $t = -25$ ms, (b) $t = 0$, (c) $t = 25$ ms. Blue filled circle, two-fluid model; green dash-dot line, potential flow theory; red solid line, modified Almendros-Ibañez model; black solid line, Fung and Hamdullahpur model 90°; dash black line, Fung and Hamdullahpur model 50°. $U_b = 0.424$ m/s and $U_g = 5.9 \times 10^{-2}$ m/s.

Almendros-Ibáñez *et al.* (Almendros-Ibáñez et al., 2006) predicts larger values for the horizontal velocity than the model of Fung and Hamdullahpur (Fung and Hamdullahpur, 1994) because the bubble growth effect in equation (3.13) are most pronounced in these regions. However, the inclusion of these effects does not appear to be sufficient to account for the large horizontal velocities encountered in the simulation.

For $t = 25$ ms, figures 3.8 and 3.9 indicate that potential flow is no longer able to predict the velocity of the ejected particles. This can be explained by considering that for $t > 0$, particles are ejected from the bubble with the result that the dome starts to deviate from the liquid-like behaviour, a requirement for the potential flow theory to hold. Furthermore, the bubble grows laterally more than vertically during bubble eruption, which reduces the particle velocity at the bubble dome compared to the predictions obtained from potential flow theory.

For simulation case 2, an erupting bubble of equivalent diameter $D_{eq} = 6.0 \times 10^{-2}$ m, rise velocity $U_b = 0.484$ m/s, and a velocity due to its growth of $U_g = 8.0 \times 10^{-2}$ m/s, has been selected. Figure 3.10 shows contour maps of the solids volume fraction, solids

velocity and vorticity of the solids for this bubble. Arrows indicating the velocity vectors have been superimposed onto the velocity and vorticity plots. For the sake of clarity, only the results for $t = 0$ are shown. Similar to the isolated bubbles analysed in case 2, the erupting bubble shown in figure 3.10 has a small satellite bubble, this time to the left of the main bubble. Neither the velocity vectors nor the vorticity field appear to be perturbed by the small bubble except in a region very close to it. The largest values of the vorticity are encountered in the wake of the main bubble and in the region between the two bubbles.

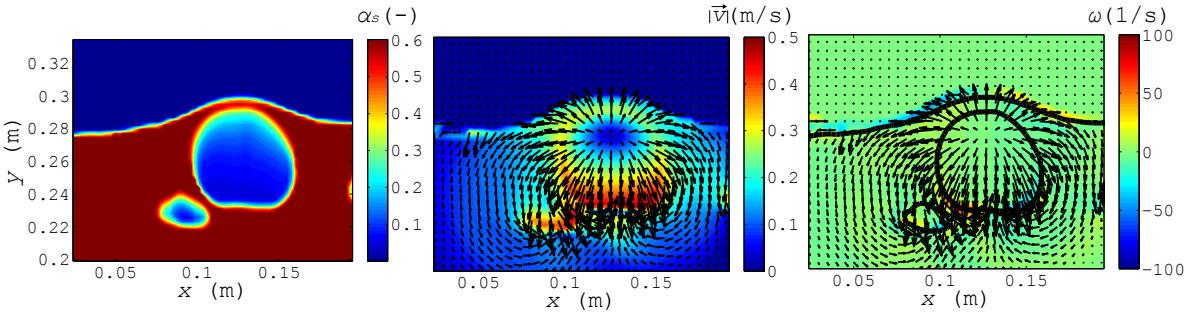

Figure 3.10: Erupting Bubble contours for case 2: solids volume fraction (-), solids velocity (m/s), and vorticity (1/s). $U_b = 0.484$ m/s and $U_g = 8.0 \times 10^{-2}$ m/s.

In contrast to the erupting bubble analysed for case 1, the bubble shown in figure 3.10 does not rise vertically, but at an angle of $\theta_b \approx -13°$ from the vertical direction. This small deviation of θ_b from zero has an impact on the velocity profiles of the particles in the bubble dome, as illustrated in figure 3.11 which shows the vertical and horizontal velocities of the solids at time $t = 0$. In particular, the two-fluid simulation results shown in figure 3.11a indicate that the vertical component of the particle velocity is larger on the left side of the dome than on the right side. It is thought that this asymmetry arises from the deformation of the bubble dome caused by the non-zero value of θ_b (Almendros-Ibáñez et al., 2006).

Of the models considered here, potential flow theory gives the most accurate predictions for the vertical and horizontal velocity profiles for case 2. This is in agreement with the findings for case 1. At the sides of the bubble, i.e. $\theta < -20°$ and $\theta > 20°$, there is excellent agreement between the vertical velocities predicted by the potential flow theory and the two-fluid simulation data in figure 3.11. The potential flow theory considered here accounts for a non-zero value of θ_b. However, the potential flow theory over-predicts the vertical velocities at the top of the bubble dome by approximately 15 %. The model from Almendros-Ibáñez *et al.* (Almendros-Ibáñez et al., 2006) also compensates for bubbles whose centroid does not rise in a perfectly vertical direction. This model gives an excellent prediction for the vertical velocities close to $\theta = \theta_b$ but

over-predicts the vertical velocity at large values of θ.

The model of Fung and Hamdullahpur (Fung and Hamdullahpur, 1994) does not account for the direction of bubble rise. As a result, the agreement between the vertical velocities predicted by this model and the simulation data is not only poor for large θ, as was noted for case 1, but also for $\theta = \theta_b$. The distortion of the horizontal velocity profile due to the non-zero value of θ_b is less pronounced than the deformation of the vertical velocity profile, as shown in figure 3.11. Therefore, as in case 1, the potential flow model provides the best predictions of U at $t = 0$.

The data presented in figure 3.11 indicate that the small bubble on the left of the bubble selected in case 2 does not have a noticeable impact on the profiles of the particle velocities in the bubble dome. Excluding the deformation induced by the non-zero value of θ_b, the velocity profiles for case 2 at $t = -25$ and 25 ms are similar to those shown in figures 3.8 and 3.9. For brevity, these data are not shown here.

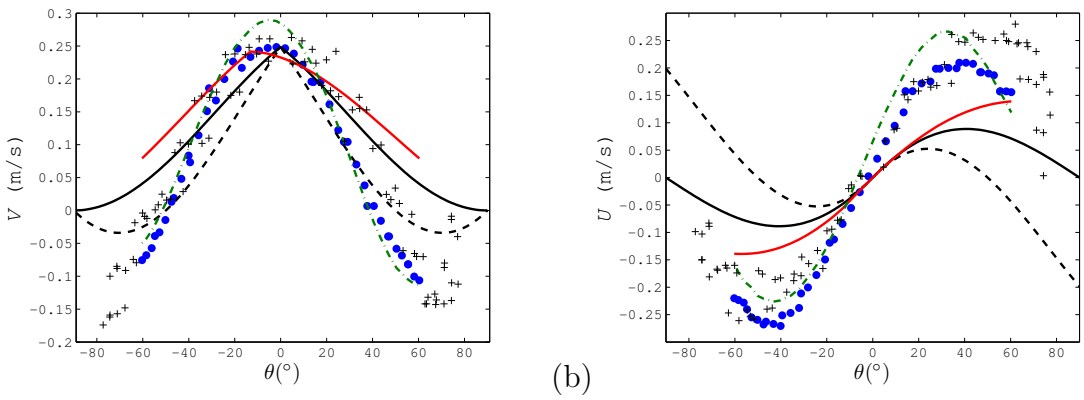

(a) (b)

Figure 3.11: Particle dome velocity for case 2 shown in Figure 3.10: (a) Vertical velocity V, (b) Horizontal velocity U. Blue filled circle, two-fluid model; green dash-dot line, potential flow theory; red solid line, modified Almendros-Ibañez model; black solid line, Fung and Hamdullahpur model 90°; dash black line, Fung and Hamdullahpur model 50°; +, experimental data (Müller et al., 2007). $U_b = 0.484$ m/s and $U_g = 8.0 \times 10^{-2}$ m/s.

The simulation parameters of case 2 where chosen to match the experiments reported by Müller *et al.* (Müller et al., 2007), who measured particle velocities in the domes of bubbles using PIV. In their study, Müller *et al.* (Müller et al., 2007) found that potential flow theory gave a better prediction for the velocity of particles in the dome of an erupting bubble than the correlation proposed by Fung and Hamdullahpur (Fung and Hamdullahpur, 1994). To allow a comparison to be made between the two-fluid simulations reported here and the experimental data reported by Müller *et al.* (Müller et al., 2007), a set of measurements of the vertical and horizontal particle velocity taken from (Müller et al., 2007) has been included in figure 3.11. These data were obtained for a bubble of equivalent diameter $D_{eq} = 6.4 \times 10^{-2}$ m and velocity

$U_b = 0.3$ m/s, which are both similar to the erupting bubble studied for simulation case 2. It should be noted that, compared to the current work, Müller *et al.* (Müller et al., 2007) used different definitions for the eruption angle, θ, and for $t = 0$. In that work, the data presented in figure 3.11 corresponds to $t' = 32$ ms, which is equivalent to $t = 0$ for the definition of time used here. Similarly, the data have been reprocessed employing the definition of θ used in this paper. Figure 3.11 indicates that, although there is more scatter in the experimental data, there is good agreement between the experimental results reported by Müller *et al.* (Müller et al., 2007) and the two-fluid simulations reported here.

3.6.3 Gas and particle flow direction in an erupting bubble

The good agreement between the PIV results reported by Müller *et al.* (Müller et al., 2007) and the simulations reported here suggests that the two-fluid simulation reproduces realistically the solids velocity during bubble eruption. Therefore, qualitative results from the two-fluid simulations regarding the gas velocities can be used with a certain level of confidence, although no direct validation with experimental data is possible due to the lack of published experimental data. Despite the fact that gas velocities have been measured in the freeboard close to erupting bubbles, e.g. (Vun et al., 2010; Hartung et al., 2008; Müller et al., 2009), the existing experimental techniques do not allow a direct measurement of the gas velocity through the particles in the bubble dome. The lack of experimental measurements of the simultaneous particle and gas velocities in a two-dimensional erupting bubble means that, at present, such coupled information is only available from numerical "experiments".

Figure 3.12 compares the angles that the simulated gas and solids velocities form, relative to the positive vertical direction. The angle, β, is given by:

$$\beta = \text{atan}\left(\frac{U}{V}\right) \tag{3.17}$$

In figure 3.12, the angles formed by the gas, β_g, and particle velocities, β_p, are shown for times $t = 0, 25$ and 50 ms. These data were obtained for simulation case 1 but analogous results can also be obtained using data from simulation case 2. The results obtained from the experimental PIV data (Müller et al., 2007) plotted in figure 3.11 are also included here to verify the simulation results. Note that the results for $t = -25$ ms, that is, prior to particle ejection, are similar to those for $t = 0$ and are not included for clarity.

It is clear from figure 3.12 that, except at the top of the bubble dome, the gas and particles in the dome of erupting bubbles move in different directions. In particular,

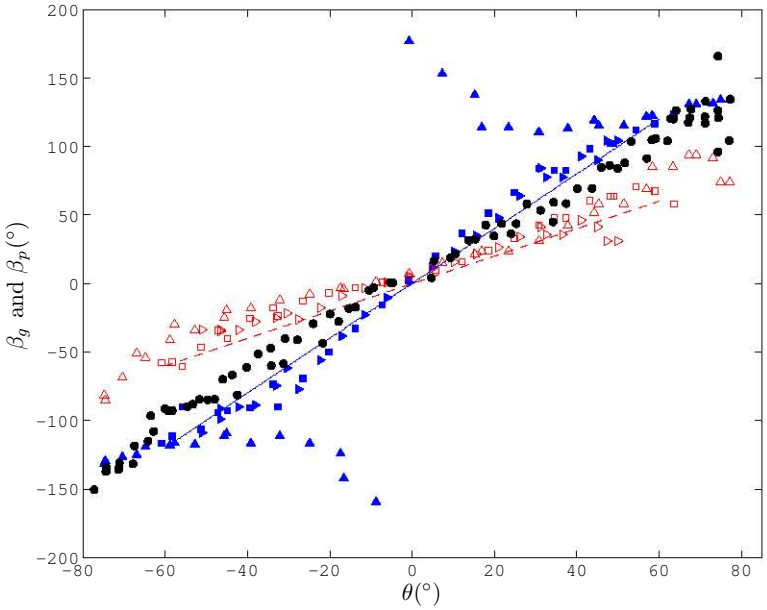

Figure 3.12: Gas and particle velocity angles, β_g and β_p, in the dome of an erupting bubble at several time instants for simulation case 1. Also included the prediction $\beta_{p,pot} \approx 2\theta$ from the potential flow theory. Filled blue points, solids velocity; empty red symbols, gas velocity; blue solid line, 2θ; red dash line, θ; filled black circles, experimental data (Müller et al., 2007). $\triangleright$, $t = 0$ ms; $\square$, $t = 25$ ms; $\triangle$, $t = 50$ ms.

the β_g points on figure 3.12 lie on a straight line of slope unity given by the equation $\beta_g = \theta$. This indicates that the gas moves radially outwards form the centre of the erupting bubble, taking the shortest possible path out of the bubble. In contrast, the magnitude of the angle between the velocity of the particles and the vertical direction is always greater than would be expected for purely radial flow, i.e. $\beta_p = \theta$.

It was demonstrated above that potential flow is able to predict the velocities of particles within the dome of an erupting bubble at $t = 0$. Therefore, by substituting the velocities predicted by potential flow theory into equation (3.17), the following expression can be derived for the value of β_p predicted by potential flow theory:

$$\beta_{p,pot} = \operatorname{atan}\left(2\frac{\tan(\theta)}{1-\tan^2(\theta)}\right) \approx 2\theta \tag{3.18}$$

where $\theta = \operatorname{atan}(x/y)$.

The line $\beta_p = 2\theta$ has been included on figure 3.12 and shows that the particle velocity angle β_p obtained from the two-fluid simulation is in good agreement with the angle estimated by potential flow theory around a cylinder. In addition, the particle velocity angle β_p has been calculated with equation (3.17) using the PIV data that was shown in figure 3.11. As the simulation data, the experimental results indicate

that β_p is closer to 2θ than to θ. This means that the particle velocity angle relative to the vertical direction is twice the radial direction angle, i.e. $\beta_p \approx 2\theta$. The success of potential flow theory in predicting β_p is more than remarkable taking into account that the approximation given by equation (3.18) holds even in the last instant before the bubble collapse, $t = 25$ ms. For $t = 50$ ms the bubble has already collapsed and the potential theory around a cylinder is not able to reproduce the particle velocity direction, although the gas phase continues expanding radially.

3.7 Conclusions

The motion of particles around bubbles in 2D fluidized beds has been simulated using a two-fluid model. For isolated bubbles that are far from the freeboard, the simulated particle motion around bubbles is found to be described well by potential flow theory, a finding which is in agreement with experimental evidence (Davidson, 1963). For erupting bubbles good agreement is found between the simulated velocity profiles and the PIV data reported by Müller *et al.* (Müller et al., 2007). Of the models for bubble eruption that have been tested here, the predictions of the potential flow theory shows the best agreement with results from PIV experiments and two-fluid simulations.

Both the simulation and experimental data indicate that particles are ejected from the dome of erupting bubbles at an angle of 2θ relative to the vertical direction, where θ is the angle that a radial line, connecting the bubble centroid to a position in the bubble dome, makes with the vertical. This observation is consistent with particle motion in the bubble dome being governed by potential flow theory, but is contrary to the standard models of a 2D bubble (e.g. (Fung and Hamdullahpur, 1994) and related models), which assume that the particles are ejected radially outwards from the dome.

Nomenclature

A	bubble area (m^2)
D_{eq}	bubble equivalent diameter (m)
K_{gs}	gas-solid momentum exchange (-)
R	bubble equivalent radius (m)
U_b	bubble velocity (m/s)
U_{gr}	bubble growth velocity (m/s)
$U_{p,b}$	particle velocity related to bubble velocity (m/s)
$U_{p,g}$	particle velocity related to bubble growth (m/s)
U	particle horizontal velocity (m/s)

V	particle vertical velocity (m/s)
$\vec{V}$	particle velocity (m/s)
g	gravity vector (m/s^2)
$\vec{v_g}$	gas velocity (m/s)
$\vec{v_s}$	solids velocity (m/s)
x	horizontal coordinate (m)
y	vertical coordinate (m)

Greek letters

α_s	solids volume fraction (-)
α_g	voidage (-)
β	Velocity vector angle in the dome(°)
ρ_s	solids density (kg/m^3)
ρ_g	gas density (kg/m^3)
ω	vorticity (1/s)
θ	eruption angle (°)
θ_b	direction of bubble rise (°)
$\theta_{\max}$	maximun eruption angle (°)
$\theta_{\min}$	minimun eruption angle (°)
Φ	velocity potential flow (m^2/s)

Bibliography

Almendros-Ibáñez, J.A., Sobrino, C., de Vega, M.,Santana, D. A new model for ejected particle velocity from erupting bubbles in 2-D fluidized beds. *Chem. Eng. Sci* 61 (2006) 5981-5990.

Almendros-Ibáñez, J.A., Pallarés, D., Johnsson, F., Santana, D. Novel approach to characterize fluidized bed dynamics combining particle image velocimetry and finite element method. *Ind. Eng. Chem. Res* 48 (2009) 5010-5023.

Benyahia, S., Syamlal, M., O'Brien, T.J. Extension of Hill-Koch-Ladd drag correlation over all ranges of Reynolds number and solids volume fraction. *Powder Technol.* 162 (2006) 166-174.

Benyahia, S., Syamlal, M., O'Brien, T.J. Summary of MFIX equations 2005-4, 2007.

Harrison, D., Davidson, J.F. Fluidised Particles, Cambridge University Press, Cambridge, 1963.

Do, H.T., Grace, J.R., Clift, R. Particle ejection and entrainment from fluidized beds. *Powder Technol.* 6 (1972) 195.

Fung, A.S., Hamdullahpur, F.A. A gas and particle flow model in the freeboard of a fluidized bed based on bubble coalescence. *Powder Technol.* 74 (1994) 121.

George, S.E., Grace, J.R. Entrainment of particles from aggregative fluidized beds. *AIChE Symp. Ser.* 74 (1978) 67.

Hartung, G., Müller, C.R., Hult, J., Kaminski, C.F, Dennis, J.S. Laser diagnostic investigation of the bubble eruption patterns in the free board of fluidized beds. Part 1: Optimized Acetone PLIF measurements, *Industrial & Engineering Chemistry Research* 47, 5686-5697, 2008.

Hatano, H., Ishida, M. The entrainment of solids particles from a gas-solid fluidized bed. *J. Chem. Eng. Jpn.* 14 (1981) 306.

Hernández-Jiménez, F., Sánchez-Delgado, S., Gómez-García, A., Acosta-Iborra, A. Comparison between two-fluid model simulations and particle image analysis & velocimetry (PIV) results for a two-dimensional gas-solid fluidized bed. *Chem. Eng. Sci.* 66 (2011) 3753-3772.

Hill, R.J., Koch, D.L., Lad, A.J.C. The first effects of fluid inertia on flows in ordered and random arrays of spheres. *J. Fluid Mech.* 448 (2001) 213-241.

Hill, R.J., Koch, D.L., Lad, A.J.C. Moderate Reynolds number flows in ordered and random arrays of spheres. *J. Fluid Mech.* 448 (2001) 243-278.

Kunii, D., Levenspiel, O. Fluidization Engineering: Butterworth-Heinemann: Newton, MA, 1991.

Levy, E.K., Caram, H.S., Dille, J.C.,Edelstein, S. Mechanism for solid ejections from gas-solid fluidized beds. *AIChE J.* 29 (1983) 383.

Müller, C.R., Davidson, J.F., Dennis, J.S., Hayhurst, A.N. A study of the motion and eruption of a bubble at the surface of a two-dimensional fluidized bed using particle image velocimetry (PIV). *Ind. Eng. Chem. Res* 46 (2007) 1642-1652.

Müller, C.R., Hartung, G., Davidson, J.F., Hult, J., Kaminski, C.F., Dennis, J.S. Laser diagnostic investigation of the bubble eruption patterns in the free board of

fluidized beds. Part 2: Simultaneous acetone PLIF and stereoscopic PIV measurements, *AIChE Journal* 55, 1369-1382, 2009.

Pemberton, S.T., Davidson, J.F. Elutriation from fluidized beds - I. Particle ejection from the dense phase into the freeboard. *Chem. Eng. Sci.* 41 (1986) 243.

Santana, D., Nauri, S., Acosta, A., Garca, N., Macas-Machn, A., Initial particle velocity spatial distribution from 2-D erupting bubbles in fluidized bed. *Powder Technol.* 150 (2005) 1-8.

Saxena, S.C., Mathur, A. On the origin of solids projected from the surface of a gas-fluidized beds. *Chem. Eng. Sci.* 39 (1984) 917.

Syamlal, M., Rogers, W., O'Brien, T.J. MFIX Documentation: Theory guide , U.S. department of Energy (DOE), Morgantown Energy Technology Center, Morgantown, West Virginia, 1993.

Vun, S., Naser, J., Witt, P.J., Yang, W. Measurements and numerical predictions of gas vortices formed by single bubble eruptions in the freeboard of a fluidised bed. *Chem. Eng. Sci.* 65 (2010) 5808-5820.

Chapter 4

Gas interchange between bubble and emulsion phases in a 2D fluidized bed as revealed by two-fluid model simulations

Contents

4.1 Abstract

Using two-fluid model simulations, the present chapter aims at characterizing the interchange due to gas advection between the emulsion phase and bubbles in fully bubbling beds of Geldart group B particles that are fluidized with air. In the studied beds the bubbles are slow, which means that the advection transport of gas through the bubble boundary is the main mechanism of gas interchange. In an initial verification step, the pressure distribution and the gas interchange coefficient for isolated bubbles obtained in the two-fuid simulation are compared with the classical potential flow theory of fuidized beds, providing concordant results. In a second step, the work analyzes the gas interchange in fully bubbling beds and the effects of the superficial velocity, bed height, and particle diameter on the interchange coefficient and the crossflow ratio. The results indicate that both the interchange coefficient and the crossflow ratio in bubbling beds are about two times those predicted by the potential theory of isolated bubbles. A corrected model for the gas interchange is proposed based on the introduction of the gas throughflow into the classical potential flow theory. As a consequence, the gas interchange coefficient in the corrected model is a function of the superficial gas velocity instead of the minimum fluidization velocity.

4.2 Introduction

Especially crucial for the understanding and control of fluidized bed combustors, gasifiers, and other reactors, is the characterisation of the gas interchange between the emulsion of particles (i.e. the dense phase) and large voids (i.e. bubbles) in the bed. Simultaneous measurement of both the gas and the particle velocities in real beds entails serious difficulties that have not been satisfactorily solved at present. Thus, detailed numerical modelling of the bubbling process constitutes a valuable tool that can provide complete information of the gas dynamics within the fluidized bed.

Experimental works available in the literature studying the gas interchange reflect the mentioned difficulties in the measurement of the gas phase transport in such systems. Most of these works are strongly influenced by the potential flow theory developed in the early 1960's by Davidson & Harrison (Davidson & Harrison, 1963) to

calculate the volume of gas going in and out of an isolated bubble.

Experimental investigations on the gas interchange can be classified into two categories: single bubbles and freely bubbling beds. In both categories the experimental technique employed is usually the analysis of the variation of a tracer concentration with time (Sit & Grace, 1978, 1981; Chiba and Kobayashi, 1970; Solimene et al., 2006; Wu & Agarwal, 2003). For example, Sit & Grace (Sit & Grace, 1978, 1981) measured the concentration of ozone in a two-dimensional bed and estimated the overall mass transfer coefficient in pairs of coalescence bubbles that were consecutively injected. Wu & Agarwal (Wu & Agarwal, 2003) studied the effect of the temperature on the mass transfer coefficient using single bubbles containing Argon. They found a decrease in the mass transfer coefficient with the temperature. Patil *et al.* (Patil et al., 2003) characterized numerically and experimentally the gas dispersion in a single bubble rising in a fluidized bed. Their simulation showed similar results to the model by Davidson & Harrison (Davidson & Harrison, 1963). More recently, Solimene *et al.* (Solimene et al., 2006) employed a novel technique based on zirconia oxygen sensors to study the nitrogen mixing in a bubble injected in an air fluidized bed, and Pavlin *et al.* (Pavlin et al., 2007) measured the gas interchange in a three dimensional (3D) fluidized bed by means of nuclear magnetic resonance. Lately, Dang et al. (2013) developed a new infrared technique to measure the gas concentration in the dilute region of a pseudo-2D bed, showing results for isolated bubbles in very good agreement with the Davidson model (Davidson & Harrison, 1963). Though these new experimental methods can advance the understanding of the gas transport in a bed, they are still unable to provide a full characterization of the gas interchange between the emulsion phase and the bubbles. Information from experiments can be complemented with predictions given by numerical simulations.

The work started in Chapter 3 to discriminate the factors that are the source of the discrepancies found in Chapter 2, is continued here. Another way of verifying the validity of the simulation results concerning the bubble behaviour is the analysis of the gas phase.

The aim of the present chapter is to study the gas interchange due to advection between the bubble and emulsion phases in bubbling beds of Geldart B particles. This is done by means of two-fluid model simulations in a 2D domain. In the studied beds the bubbles are slow, which means that the advection transport of gas through the bubble boundary is the main mechanism of gas interchange. The first part of the analysis is focused on the behaviour of the air through isolated bubbles rising in the bed. This includes the evaluation of the gas pressure distribution and the gas interchange coefficient. The results are compared with the classical potential flow

theory by Davidson & Harrison (Davidson & Harrison, 1963). The analysed isolated bubbles show, qualitatively and quantitatively, a good agreement with the theory.

Subsequently, the work analyses the gas interchange in a fluidized bed operated in the bubbling regime, that is, a bed containing multiple interacting bubbles. In addition to the gas interchange coefficient, the crossflow ratio of the bubbles is also evaluated. Both the interchange coefficient and the crossflow ratio in a bubbling bed are characterized in this work as a function of the bubble size, the distance to the distributor, the superficial gas velocity, and the particle size.

The results indicate that, when the bed is operated under bubbling regime, the potential flow theory for isolated bubbles is no longer valid. Therefore, in order to model the dependence of the gas interchange on the bubble size and superficial velocity, an analytical expression for the gas interchange in multiple interacting 2D bubbles is deduced and compared with the simulation results.

4.3 Simulated systems

Two different fluidized bed configurations are studied in this work. Table 4.1 summarizes the general parameters of these two configurations. Configuration 1 was chosen to match the experimental system and the simulations reported by Patil *et al.* (Patil et al., 2003). Their system was operated under minimum fluidization velocity and an isolated bubble was injected near the distributor. Patil *et al.* (Patil et al., 2003) analyzed the consistence of the simulation with the well known potential flow model of Davidson (Davidson & Harrison, 1963) as well as with the experimental data. Configuration 2 is a bed arbitrarily selected to carry out the simulations of isolated bubbles as well as multiple interacting bubbles.

Table 4.1: Simulation configurations

Parameter	**Configuration 1**	**Configuration 2**
Gas density (kg/m^3), ρ_g	1.2	1.2
Gas viscosity (Pa s), μ_g	1.8e-5	1.8e-5
Bed width (m), W	0.3	0.5
Bed walls height (m), H	1	1
Initial voidage (-), $\alpha_{g,i}$	0.4	0.4
Restitution coefficient (-), e	0.95	0.9
Angle of internal friction (°)	30	30

In all the configurations, air properties at ambient conditions ($T = 20°C$ and $P = 1$ atm) are used for the gas of fluidization and the injection of bubbles. As shown in Table 4.2, Configuration 1 and 2 were used in case 1-a and case 1-b, respectively, for

the simulation of isolated bubbles injected in a bed fluidized with air at minimum fluidization conditions $U = U_{mf}$. Cases 2-a to 2-h in Table 4.3 refer to Configuration 2 in fully bubbling conditions $U \geq 1.5U_{mf}$. Case 2-a will be taken as the base case for the characterization of the gas interchange in bubbling fluidized beds. Two different types of Geldart B particles were used in the simulations. The first type has a particle diameter of $d_p = 0.46$mm, density of $\rho_s = 2660$ kg/m^3 and a resulting minimum fluidization velocity of $U_{mf} = 0.19$ m/s (Patil et al., 2003). The second type of particles used in this work has a diameter of $d_p = 0.7$ mm, density of $\rho_s = 2500$ kg/m^3 and minimum fluidization velocity $U_{mf} = 0.35$ m/s.

Table 4.2: Isolated bubble cases

Case	U/U_{mf}	Static bed height (m), H_0	Particle density (kg/m^3), ρ_s	Particle diameter (mm), d_p	Configuration
1-a	1	0.4	2660	0.46	1
1-b	1	0.5	2500	0.7	2

Table 4.3: Bubbling regime cases

Case	U/U_{mf}	Static bed height (m), H_0	Particle density (kg/m^3), ρ_s	Particle diameter (mm), d_p	Configuration
2-a	2.25	0.3	2500	0.7	2
2-b	1.5	0.3	2500	0.7	2
2-c	2.5	0.3	2500	0.7	2
2-d	2.75	0.3	2500	0.7	2
2-e	3	0.3	2500	0.7	2
2-f	2.25	0.15	2500	0.7	2
2-g	2.25	0.5	2500	0.7	2
2-h	2.25	0.3	2660	0.46	2

Fig. 4.1 shows two example snapshots of the solids volume fraction corresponding to the simulation of an isolated bubble using Configuration 1 (case 1-a), and a bubbling bed employing Configuration 2 (case 2-a). A Cartesian coordinate system is used in this work, with the x and y axes aligned along the horizontal and vertical directions respectively.

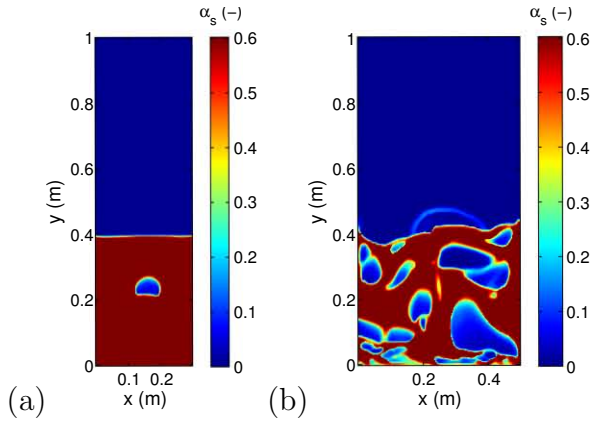

Figure 4.1: Snapshot of solids volume fraction for: a) case 1-a, and b) case 2-a.

4.4 Theory

4.4.1 Two-fluid model

The two-fluid model is based on the conservation equations of mass, momentum and granular temperature, which were solved here using the MFIX code (Multiphase Flow with Interphase eXchanges) (Syamlal et al., 1993; Benyahia et al., 2007). The kinetic theory of granular flow, which characterizes the stochastic fluctuations of the solids kinetic energy, was used for the closure of the solids pressure and stress terms. The governing equations as well as the closure models can be found in appendix A.

Regarding the numerical solution of the governing equations, a second order accurate scheme was used to discretize the convective derivatives. For case 1-a, the 2D computational domain was discretised using square cells of 5 mm length, in a mesh of 12000 nodes. For the case 1-b the cells were rectangular with 5 mm length in the x direction and 5.5 mm in the y direction, resulting in a mesh of 18000 nodes. In all the cases, the time step was automatically adapted to ensure convergence of the equation system and the initial time step was set to 0.5×10^{-5} s at the startup of the simulation. A uniform and steady gas velocity profile was selected for the inlet boundary representing the distributor at the bottom of the bed. A fixed pressure boundary condition was chosen for the top of the freeboard. The lateral walls of the bed were modeled as no-slip walls for the gas phase. The Johnson & Jackson partial slip boundary condition were chosen for the solids phase at the walls (Johnson & Jackson, 1987). The initial solids volume fraction of the bed was set to 0.6.

For the analysis of isolated bubbles in cases 1-a and 1-b, the superficial velocity of the gas that enters the bed was equated to U_{mf}. A void region of square section was set at the bottom of the bed as initial condition. The rest of the emulsion phase was

initially at $\alpha_{g,i}$ in Table 1. After a few time steps the bubble is formed and tracked over time until it reaches the bed surface. The bubbles tested experienced only a small growth along its ascending path. Several simulations starting with different areas of the initial void region were created to produce bubbles of different diameters. For the simulation of the bubbling beds in cases 2-a to 2-h, no injection was needed since bubbles were produced naturally from the fluidization air.

The drag force correlation used in this study for all the simulations is the one proposed by Gidaspow (Gidaspow, 1994). Details about the drag force can be found in Appendix A.

4.4.2 Gas interchange parameters

In a gas fluidized bed the gas interchange between the bubble and emulsion phases is commonly characterized through the interchange coefficient and the crossflow ratio (Kunii & Levenspiel, 1991). The interchange coefficient refers to the volumetric flow rate of gas going from a bubble to the emulsion or from the emulsion to a bubble, $\dot{V}_{be}$, and is expressed per unit volume of the bubble, V_b:

$$K_{be} = \frac{\dot{V}_{be}}{V_b} \tag{4.1}$$

For slow moving bubbles, the integral for the gas flow going from the emulsion phase to a bubble can be considered similar to the integral for the gas flowing from the bubble to the emulsion phase, since bubble coalescence and growth are relatively slow phenomena compared to the gas velocity. In the studied beds the bubbles have a slow rise velocity, which means that the advection transport of gas through the bubble boundary is the main mechanism of gas interchange. For particles smaller than the ones studied in the present work, the bubbles may not be slow and the diffusion of species may play an important role in the gas interchange.

The classical potential flow theory for fluidized beds (Davidson & Harrison, 1963) dictates that 2D isolated bubbles, far from the walls and the bed surface, have an incoming volumetric gas flow rate that is $\dot{V}_{be} = 2D_b U_{mf} Z$, with Z as an arbitrary thickness associated to the 2D bed, so that:

$$K_{D\&H,2D} = \frac{8U_{mf}}{\pi D_b} \tag{4.2}$$

Figure 4.2 shows a sketch of a bubble and the volume of gas going from the emulsion to the bubble, and from the bubble to the emulsion phase. The bubble velocity in the figure is defined using the displacement of the bubble centroid.

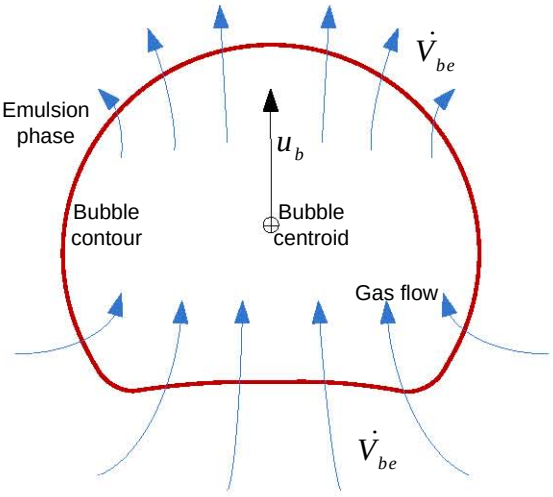

Figure 4.2: Sketch of a bubble and the volume of gas going in and out of it.

The crossflow ratio accounts for the number of times the bubble gas is replaced as the bubble rises through a characteristic distance, L_c, in the bed:

$$X_{L_c} = \frac{K_{be} L_c}{v_b} \tag{4.3}$$

Here, the characteristic distance can be taken as either the bubble diameter or the vertical distance from the bubble centroid to the average level of the bed surface under bubbling conditions. In Eq. 4.3 $v_{b,b}$ is the bubble rise velocity, which can be estimated for bubbling beds as (Kunii & Levenspiel, 1991):

$$v_{b,b} = c_1(U - U_{mf}) + c_2\sqrt{gD_b} \tag{4.4}$$

where c_1 and c_2 are constants that depend on the bed system.

A theoretical value of the crossflow ratio for an isolated bubble can be calculated from the potential flow theory by substituting $K_{D\&H,2D}$ into K_{be}:

$$X_{D\&H,2D} = \frac{8U_{mf}L_c}{\pi v_{b,i} D_b} \tag{4.5}$$

where $v_{b,i}$ is the bubble velocity of an isolated bubble rising in a fluidized bed (Davidson & Harrison, 1963).

$$v_{b,i} = \phi\sqrt{gD_b} \tag{4.6}$$

As first approximation, this expression for isolated bubbles can also be used for bubbling beds (Darton et al., 1977). The value of the coefficient ϕ is normally comprised within the interval 0.6 and 1 (Kunii & Levenspiel, 1991).

4.4.3 Data processing technique

To characterize the bubble behaviour and calculate the gas interchange, the data from the two-fluid simulation were sampled every 5×10^{-3} s over 30 seconds of physical time. Each instantaneous sample constitutes a frame. To construct mean quantities, the first 5 seconds at the start-up of the simulation were eliminated from the sampling data set.

In order to study bubble motion, it is necessary to distinguish between the bubble and emulsion phases. This is done by setting in a cutoff value equal to $\alpha_s = 0.3$ for the instantaneous solids volume fraction, as reported by Hernández-Jiménez et al. (2011a), which is the arithmetic mean of the maximum and minimum solids volume fractions in the simulated bed. The contour given by the cutoff value defines the bubble interphase or boundary. Any region in which the solids volume fraction is less than 0.3 is assigned to be a bubble. The bubble centroid is the geometrical center of the bubble area delimited by this contour, and the bubble diameter is obtained from a circle having the same area as the bubble. The bubble velocity is calculated tracking the bubble centroid along consecutive simulation time steps. Over 70000 bubbles are extracted for each case to create the time average results.

Once a bubble is defined, the volume of gas going from the bubble to the emulsion phase (or viceversa) can be calculated. This is done by computing the bubble velocity using two successives frames. Then, the gas flow can be obtained with the gas velocity that is entering or leaving the bubble through its boundary, in a reference system that moves with the bubble:

$$\dot{V}_{be} = \int_{\Omega_b} \alpha_g(\vec{v_g} - \vec{v_b})\vec{n}dl = \int_{\Omega_b} \alpha_g[-(u_g - u_b)dy + (v_g - v_b)dx] \tag{4.7}$$

where u_g and v_g are the horizontal and vertical components of the gas velocity, respectively, u_b and v_b are the horizontal and vertical components of bubble velocity, respectively, Ω_b is the bubble contour line, $\vec{n}$ is the normal vector to the bubble contour, going from inside to outside the bubble, and dl is the differential length of the bubble contour, so $\vec{n}dl = (-dx, +dy)$. To integrate Eq. 4.7 numerically, the bubble contour Ω_b is divided into small sections $\Omega_{b,k}$. The integral accounting for all the sections $\Omega_{b,k}$ is the net gas flow through the bubble interphase or boundary, which is null if the bubble growth is much less than the gas interchange (a valid assumption for slow bubbles). Therefore, Eq. 4.7 must be separated in two contributions, one is the gas going from the emulsion to the bubble ($\dot{V}_{be} > 0$) and the other is the gas going from the bubble to the emulsion ($\dot{V}_{be} < 0$). Thus, for a given bubble, results for all the contour sections, $\Omega_{b,k}$, with positive contributions of the incoming flow, $\dot{V}_{be,k} > 0$, are

added (note that these sections may happen to be anywhere at the bubble contour and are not necessarily placed one after the other). The same is done for all the sections through which the flow leaves the bubble, $\dot{V}_{be,k} < 0$. The gas interchange calculated with the incoming flow of a bubble (i.e. summation of each $\dot{V}_{be,k}$ that has positive value) is practically identical to the one derived from the outgoing flow (summation of each $\dot{V}_{be,k}$ that has negative value).

Note that the volume of gas going in and out of the bubble, can be calculated using in Eq. 4.7 the local velocity of the bubble boundary instead of the bubble centroid velocity (u_b, v_b). By this way the effect of the bubble deformation and growth on the gas interchange coefficient can be captured. This boundary velocity can be estimated with the length of a line that perpendicularly leaves the bubble contour from a point at a given frame, and intersects the contour of the bubble at the following frame. Dividing the length of this line by the time step between the two frames, gives an estimation of the local velocity of the bubble interphase. The boundary velocity, which may not be equal to the solids velocity, is used to evaluate the gas flow that is actually crossing the bubble boundary, that is, the gas velocity relative to the local velocity of the bubble interphase. Therefore, since the gas flow crossing the boundary must be computed with the gas velocity component perpendicular to the bubble boundary, the component of the bubble interphase velocity to be used must be also in perpendicular direction to the bubble boundary. Hence, this boundary velocity is not strictly the bubble centroid velocity, though it can be demonstrated that these two velocities lead to consistent results, that is, they produce similar values of the gas interchange through a non-growing bubble if the time step used in the calculation of the boundary velocity is small. For size- or shape-varying bubbles, the use of the local velocity of the bubble boundary provides a more accurate value for the volume of gas crossing the bubble, but the computational cost is dramatically increased. For the isolated bubble and the bubbling regime cases studied in the present work, several tests were done using the boundary velocity of the bubble (for the isolated bubble and for the bubbling regime cases), and results similar to those using the centroid velocity of the bubble were obtained. This outcome should be expected since the observed bubble displacement and deformation is relatively slow compared to the interstitial gas velocity. Therefore, from hereafter it is implicit that all the results presented were calculated using the bubble centroid velocity (u_b, v_b) in Eq. 4.7, as the associated computational cost is lower.

4.5 Results for isolated bubbles

4.5.1 Pressure distribution

The first part of the analysis is devoted to a practical validation of the simulated gas behaviour through isolated bubbles. For this purpose, the gas pressure recovery and distribution for an isolated rising bubble is studied using cases 1-a and 1-b of Table 4.2. Fig. 4.3 shows the pressure signal for an acquisition point placed at the middle of the bed at a height above the distributor $y = 0.2475$ m. This point is crossed by a rising isolated bubble producing a variation of the local pressure of the gas over time shown in Fig. 4.3a. The temporal evolution of the pressure experiences a rapid fall, indicating that the bubble crosses the acquisition point at a time between 0.4 to 0.5 seconds after having been injected. The pressure is recovered once the bubble has crossed the acquisition point.

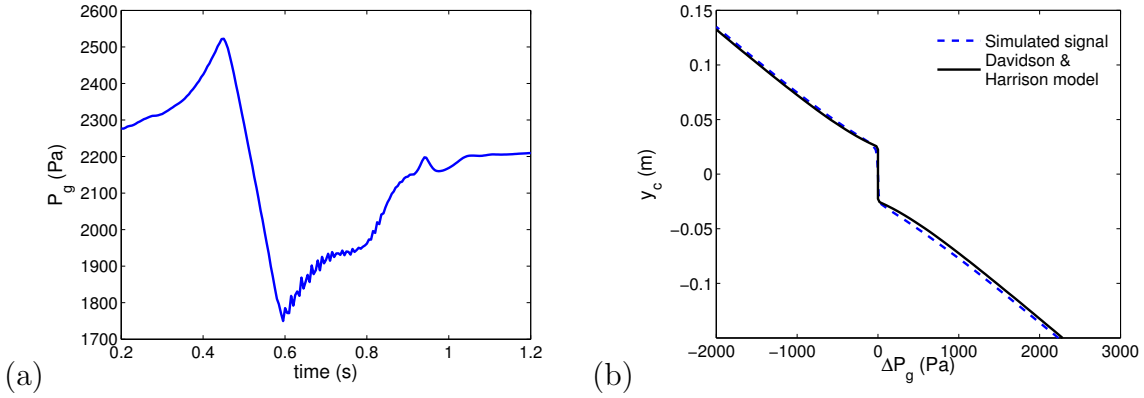

Figure 4.3: a) Simulated gas pressure signal versus time at a height of $y = 0.2475$ m perturbed by a bubble, and b) gas pressure distribution along the radial coordinate with the theoretical model by Davidson & Harrison. Case 1-a.

The pressure distribution obtained from the simulation in the vicinity of a rising 2D bubble (case 1-a) is included in Fig. 4.3b. In this figure the vertical axis y_c is the vertical coordinate relative to the bubble centroid while ΔP_g is the gas pressure, also relative to the pressure at the bubble centroid. As Fig. 4.3b shows, the presence of the bubble perturbs the linear decay given by the solids column weight (i.e. $-y_c \rho_d g$) creating an overpressure over the bubble and a pressure depression at the bubble wake. To verify the validity of this simulation outcome the pressure distribution from the potential flow model for a cylindrical void (Davidson & Harrison, 1963) is plotted in Fig. 4.3b:

$$\frac{\Delta P_g}{\rho_d} = \left\{ \begin{array}{c} -g\left(y_c - \frac{a^2}{y_c}\right) \ , \ |y_c| \geq a \\ 0 \ , \ |y_c| < a \end{array} \right\} \tag{4.8}$$

where a is the radius of the bubble and $\rho_d = \alpha_g \rho_g + (1 - \alpha_g)\rho_s$ is the bulk density of the emulsion phase. As can be observed, the pressure distribution in the vicinity of an isolated bubble in the simulation fits fairly well the theoretical potential flow model.

4.5.2 Gas interchange

Once the pressure perturbation produced by an isolated bubble has been verified, the gas interchange between isolated bubbles and the emulsion phase can be studied and compared with the potential flow model by Davidson & Harrison (Davidson & Harrison, 1963). To fulfil this goal, several isolated bubbles in cases 1-a and 1-b were simulated.

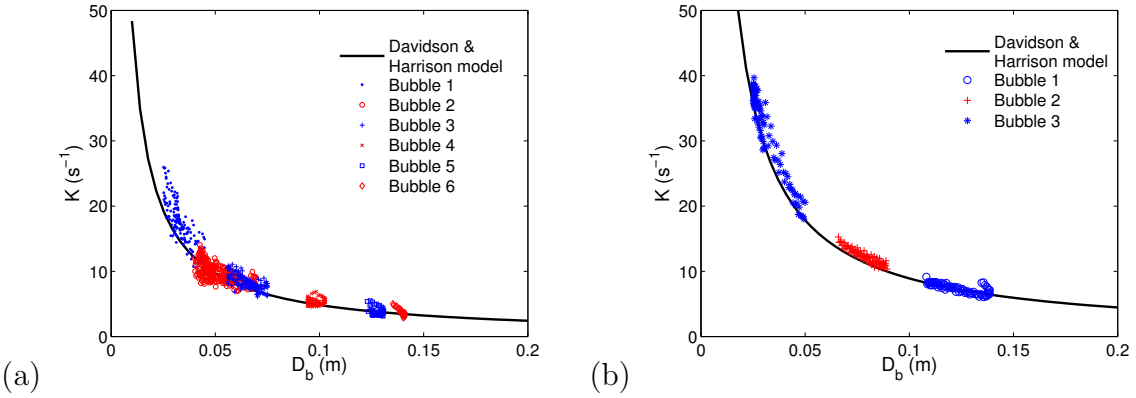

Figure 4.4: Interchange coefficient versus the bubble diameter for several isolated bubbles and comparison with the model by Davidson & Harrison, a) particles with $d_p = 0.46$ mm (case 1-a); b) particles with $d_p = 0.7$ mm (case 1-b).

Fig. 4.4 shows the gas interchange coefficient obtained from the two-fluid model simulations for several isolated bubbles injected in a bed of particles with diameter $d_p = 0.46$ mm (Fig. 4.4a) and $d_p = 0.7$ mm (Fig. 4.4b). Each bubble produces a set of scatter points corresponding to the evolution of the instantaneous interchange coefficient from the formation of the bubble until the eruption at the bed surface. Bigger bubbles are formed farther from the distributor, requiring less time to erupt and, therefore, fewer data points in the figure are obtained in that case. In Fig. 4.4 the interchange coefficient calculated from the potential flow model proposed by Davidson & Harrison (Davidson & Harrison, 1963) is included. As can be seen, all the bubbles are in very good agreement with the potential flow model, Eq. 4.2. Excellent agreement between simulated isolated bubbles and the potential flow theory was also reported by

Patit *et al.* (Patil et al., 2003) in a bed similar to the one used in Fig. 4.4a (case 1-a).

Notice that the gas interchange is calculated through the contour of the simulated bubbles, which is not necessarily circular but, instead, kidney-shaped or circular with a bottom indentation. In contrast, the potential flow theory from Davidson & Harrison (Davidson & Harrison, 1963) simplifies the bubble shape to a perfect circle (in two-dimensions). However, Collins (Collins, 1965) demonstrated that the distortion of the bubble contour introduced by the bottom indentation of a two-dimensional bubble has little effect on the gas flow field. This probably explains why the simulation results (pressure profile and gas interchange) for kidney- or indented-circle-shaped isolated bubbles are very close to the results estimated using the Davidson & Harrison model (Davidson & Harrison, 1963).

The results of this section indicate that the two-fluid simulation can reproduce realistically the gas flow and pressure distribution through isolated bubbles in accordance to the potential flow theory. Besides, previous works have shown that the solid motion in the vicinity of bubbles obtained from two-fluid simulations also follows the theoretical velocity given by the potential flow model (Hernández-Jiménez et al., 2011b).

4.6 Results for fully bubbling beds

4.6.1 General bubble behaviour

Before analyzing the gas interchange in fully bubbling beds, this part of the analysis concentrates on the general behaviour of bubbles in the simulated bed in case 2-a. Fig. 4.5 shows the mean bubble diameter D_b and the vertical bubble velocity v_b, as a function of the height above the distributor, y, and the bubble diameter, D_b. Fig. 4.5b also includes two models for the bubble velocity. One model is given by Eq. 4.6 using the typical value $\phi = 0.7$. The other model is Eq. 4.4 whose coefficients need to be fitted to the simulated data and results in $c_1 = 0.48$ and $c_2 = 0.53$.

Fig. 4.5 depicts the typical behaviour of bubbles that takes place in a 2D bubbling bed. The black solid curve in Fig. 4.5 is the mean of the bubble data set, calculated for each interval of the horizontal axis of the plots, and the vertical errorbars refer to plus/minus one standard deviation of the data. The cross points correspond to the median of the data. It can be observed that both median and mean values give very similar results in Fig. 4.5. The bubble diameter increases monotonically with the height above the distributor until the static bed height is reached (Fig. 4.5a). As expected, the bubble velocity shown in Fig. 4.5b increases with the bubble diameter. These results on the bubble behaviour are in harmony with experimental measurements, as previously

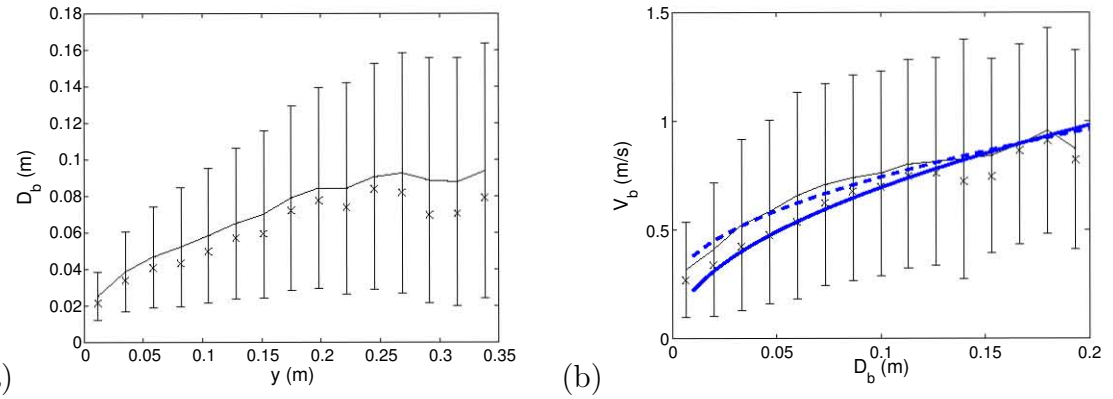

Figure 4.5: a) Bubble diameter versus height above the distributor and b) bubble velocity versus bubble diameter. Case 2-a. Black solid line: mean and standard deviation values, ×: median values. Blue solid line: $v_b = 0.7\sqrt{gD_b}$. Blue dashed line: $v_b = 0.48(U - U_{mf}) + 0.53\sqrt{gD_b}$.

reported (Busciglio et al., 2009; Li et al., 2010; Hernández-Jiménez et al., 2011a). Note that Fig. 4.5b indicates that the mean bubble velocity is slow. This is so since the bubble velocity remains below the gas interstitial velocity ($U_{mf}/\alpha_{gmf} \approx 0.87m/s$). Only large bubbles seem to have mean velocity greater than the interstitial velocity (Fig. 4.5b).

4.6.2 Mean interchange coefficient and crossflow ratio

The mean interchange coefficient and the crossflow ratio are studied in this section. As shown in section 4.2, the simulations are able to predict the gas interchange of isolated bubbles according to the theoretical model by Davidson & Harrison (Davidson & Harrison, 1963). However, this theoretical model of potential flow was developed for isolated bubbles and does not consider the perturbation arising from the interaction between two or more bubbles. Consequently, a new model is developed here in order to incorporate this interaction between bubbles in the estimation of the gas interchange.

When slow bubbles are close to each other, the excess gas passes through bubbles as a low resistance shortcut to the freeboard (Kunii & Levenspiel, 1991). The larger the superficial velocity in the bed, the greater the number of bubbles and the more intense the gas flow through the bubbles, the so called throughflow, which plays an important role in bubbling fluidized beds and should be taken into account. The throughflow velocity U_{th} can be estimated as the excess of gas velocity $(U - U_{mf})$ that is not transported by the visible flow of bubbles and concentrates preferentially in the bubble path regions. The effect of the throughflow on the gas interchange was first studied by Sit and Grace (Sit & Grace, 1981). They measured the interphase mass transfer for a pair of coalescencing bubbles, and estimated a rough enhancement factor based on the

percentage of the bubbles coalescing in a freely bubbling bed.

In the present work a different approach from that of Sit and Grace (Sit & Grace, 1981) is followed. It will be assumed that the presence of multiple interacting bubbles in a bed increases the gas velocity in the vicinity of each bubble. An effective way of considering this effect is to use a corrected velocity U^* in the Harrison & Davidson's interchange coefficient, Eq. 4.2, in place of the minimum fluidization velocity U_{mf}. The corrected velocity U^* comprises the throughflow velocity as well as the minimum fluidization velocity:

$$U^* = U_{mf} + U_{th} = U_{mf} + \delta(1 - \Psi)(U - U_{mf}) \tag{4.9}$$

Where δ is the throughflow concentration parameter, which is just the inverse fraction of the bed where the gas velocity modulus (i.e. magnitude) is higher than the interstitial minimum fluidization velocity U_{mf}/α_g. The estimation of δ in the 2D simulated bed can be done as follows. Fig. 4.6 shows a snapshot of the bed containing the bubble and surface contours. The area in black color, A_1, corresponds to the regions of the bed (taken only those below the bed surface) where the gas velocity is smaller than U_{mf}/α_g, and the area in white color, A_2, is the area where the gas velocity is greater than U_{mf}/α_g. The instantaneous value of the throughflow concentration parameter is then $\delta_k = (A_1 + A_2)/A_2$, and the time average value of δ_k, covering all the simulation time, provides δ. For the base case (case 2-a), the simulation results give $\delta = 1.30$.

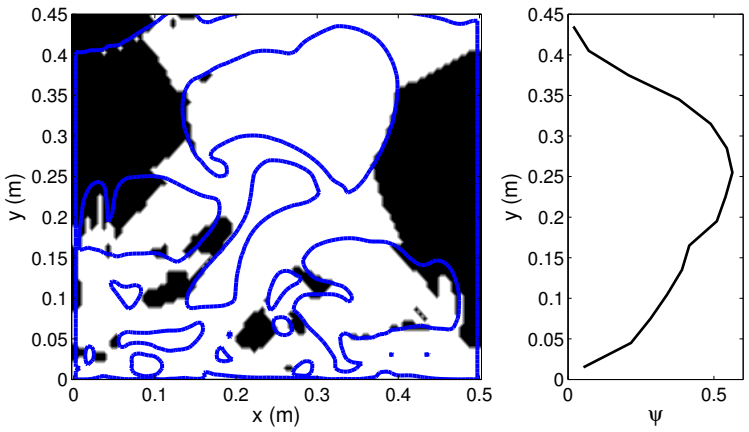

Figure 4.6: Snapshot of the bed with black areas as the region with a gas velocity below the interstitial gas velocity, and time-averaged coefficient Ψ as a function of the height. Case 2-a.

Ψ in Eq. 4.9 is the fraction of the visible flow over the excess flow, i.e. visible flow over that predicted by the two-phase theory. The visible flow can be calculated for each time instant as the apparent volumetric flow rate that is transported by the bubbles crossing a given sampling horizontal section in the bed.

$$\Psi = \sum_{i \in bubbles} \frac{\vec{v}_{b,i} \pi D_{b,i}^2 / 4}{(U - U_{mf}) W H} \tag{4.10}$$

The time average profile of Ψ is presented in Fig. 4.6 as a function of the distance of the sampling horizontal section to the bed distributor, y. The mean of Ψ along y in Fig. 4.6 gives $\Psi = 0.394$ for case 2-a.

Therefore, introducing U^* from Eq. 4.9 in Eq. 4.2 leads to the following correction of the interchange coefficient:

$$K_{corrected,2D} = \frac{8U^*}{\pi D_b} = \frac{\zeta U}{D_b} \tag{4.11}$$

where $\zeta = (8/\pi)\left[\delta(1-\Psi) + (U_{mf}/U)(1-\delta-\delta\Psi)\right]$. Using the values for δ and Ψ calculated before for case 2-a, it is easy to see that $\zeta = 2.246$. For the sake of simplicity and compactness, ζ can be approximated to $9/4$. Thus:

$$K_{corrected,2D} \approx \frac{9U}{4D_b} \tag{4.12}$$

The mean interchange coefficient K_{be} is presented in Fig. 4.7 and has been calculated making the average of the individual interchange coefficient of the simulated bubbles within each interval of vertical distance to the distributor (horizontal axis in Fig. 4.7a) or bubble diameter (fig. 4.7b). In Fig. 4.7a the median and the interquartile ranges are plotted, with circles denoting the mean values. In Fig. 4.7b, the mean and standard deviation are depicted as a continuous line plus the errorbars, and the median as cross points. As can be observed in Fig. 4.7b, both mean and median values give similar values when plotted versus the mean bubble diameter. Therefore, only the mean value of the interchange coefficient will be provided from now on when plotted versus the bubble diameter. Fig. 4.7b also shows the gas interchange coefficient calculated with the model by Davidson & Harrison (Davidson & Harrison, 1963), Eq. 4.2, and with the corrected model, Eq. 4.12. Of the two models, the corrected model is the one that best predicts the simulation results for the gas interchange.

According to Fig. 4.7a, the gas interchange per unit volume decreases when the distance to the distributor increases. This happens because the bubble diameter grows with the height, Fig. 4.5a, while the gas interchange decreases with the bubble diameter, Fig. 4.7b. The fact that the interchange coefficient decreases with the bubble diameter in Fig. 4.7b evidences that the gas flow interchanged between dense and bubble phases grows less rapidly than the bubble volume when the bubble diameter increases. In fact, according to the classical potential flow theory, i.e. $K_{D\&H,2D}$ in Eq. 4.2, the interchange coefficient is inversely proportional to the bubble diameter.

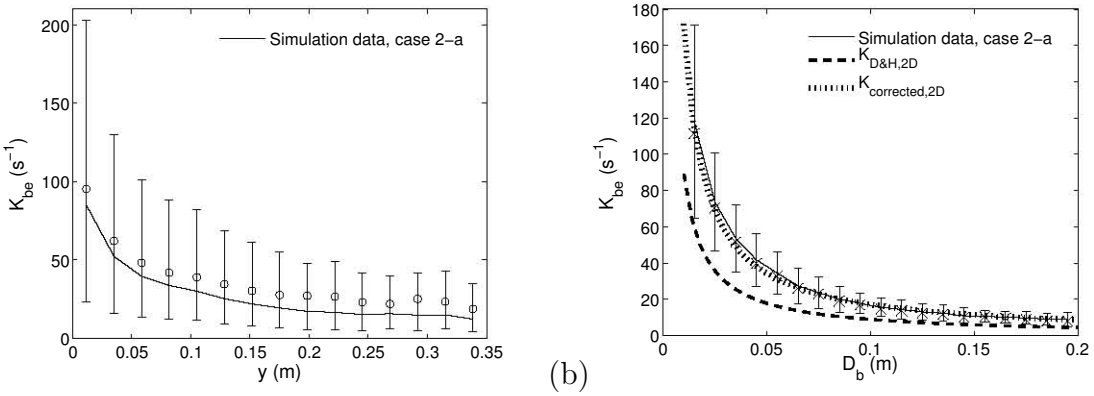

(a) (b)

Figure 4.7: Gas interchange coefficient a) versus the height, solid line: median values and interquartile ranges, ∘: mean values; and b) versus the bubble diameter together with the theoretical model by Davidson & Harrison and the corrected model, Eq 4.12, solid line: mean and standard deviation values, ×: median values. Case 2-a.

However, it is clear from Fig. 4.7b that $K_{D\&H,2D}$ is 50% smaller than the interchange coefficient from the two-fluid simulations. This is due to the fact that the potential flow theory applies to isolated bubbles that are very far from other bubbles.

The value of the coefficient ζ can be also adjusted by fitting Eq. 4.11 to the two-fluid simulation results shown in Fig. 4.7b. Performing this fitting by regression, the value $\zeta = 2.272$ is obtained, which is close to the previously deduced value $\zeta = 9/4$.

The expression for the corrected interchange coefficient $K_{corrected,2D}$, Eq. 4.12, can be used to define a corrected crossflow ratio:

$$X_{corrected,2D} = \frac{K_{corrected,2D} L_c}{v_b} = \frac{9 U L_c}{4 v_b D_b} \tag{4.13}$$

where v_b is the bubble velocity that can be calculated using either the correlation for isolated bubbles, $v_{b,i}$ (Equation 4.6), or the correlation for bubbling beds, $v_{b,b}$ (Equation 4.4).

Fig. 4.8 shows the crossflow ratio as a function of the distance above the distributor and as a function of the bubble diameter. In this figure the crossflow ratio has been calculated from the simulation using the median of the individual crossflow ratios of the bubbles captured within each abscissa interval of distance to the distributor, Fig. 4.8a, and of bubble diameter, Fig. 4.8b.

In Fig. 4.8a, X_{fb} denotes the crossflow ratio computed with the charateristic length, L_c, equal to the distance from the bubble centroid to the surface of the bed. This crossflow ratio represents the maximum number of times the gas contained in a bubble can be renewed until the bubble reaches the bed surface. When the characteristic length, L_c, is equal to the bubble diameter, D_b, the crossflow ratio is denoted with X_{Db}

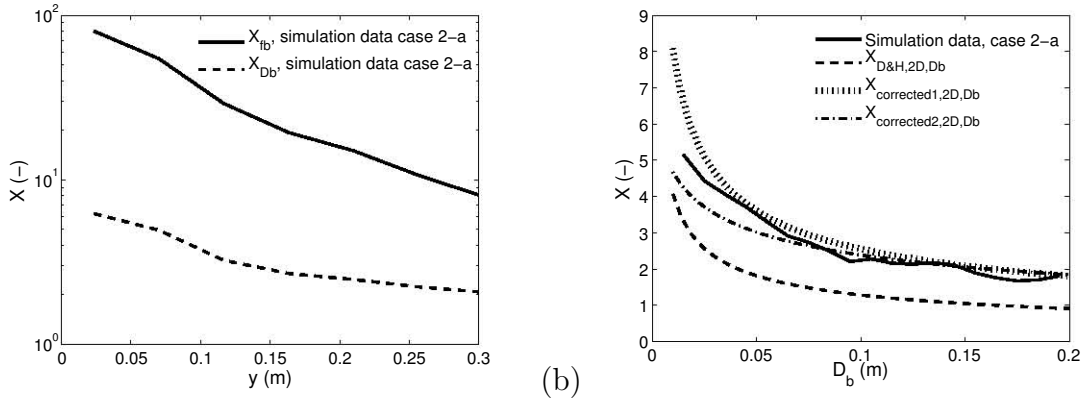

Figure 4.8: Crossflow ratio a) versus the height (using $L_c = fb$ and $L_c = D_b$); and b) versus the bubble diameter (using $L_c = D_b$) together with the theoretical model by Davidson & Harrison and the corrected model. Case 2-a.

and can be interpreted as an approximation of the number of times the bubble gas is renewed between successive bubble coalescences, whose frequency is of order U_b/D_b in a bed densely populated with bubbles such as the one studied here (Darton et al., 1977).

According to the above definition, X_{fb} is typically greater than X_{Db}, as Fig. 4.8 demonstrates, and the two crossflow ratios decrease with the distance to the distributor and the bubble diameter. Interestingly, K_{be} in Fig. 4.7a and X_{Db} in Fig. 4.8a, seem to tend to an asymptotic value when the distance to the distributor is increased ($y/H_0 > 1/3$).

The crossflow ratio X_{Db} obtained from the two-fluid simulation of the bubbling bed is shown in Fig. 4.8b together with the predictions given by the potential flow model, $X_{D\&H,2D}$ in Eq. 4.5 for $L_c = D_b$, and the corrected crossflow ratio proposed in this work, $X_{corrected,2D}$ for the two approximations concerning the bubble velocity in Eq. 4.13. One approximation takes the bubble velocity from Eq. 4.6 (isolated bubble) with $\phi = 0.7$ to calculate the crossflow ratio, $X_{corrected1,2D}$. The aim of this approximation is to obtain a model as simple as possible. The other approximation uses Eq. 4.4 (bubbling regime) with c_1 and c_2 fitted from the simulation case 2-a (see Fig. 4.5b) to calculate $X_{corrected2,2D}$. As in the case of the interchange coefficient in Fig. 4.7b, the potential flow model $X_{D\&H,2D}$ underpredicts the simulated crossflow ratio in Fig. 4.8b, while the corrected model $X_{corrected,2D}$ better fits the simulation data. In particular, the corrected model using the bubble velocity $v_{b,b}$, $X_{corrected2,2D}$, gives the closest results to the simulated crossflow ratio. Nevertheless, the corrected crossflow ratio, $X_{corrected1,2D}$, can be used as well for simplicity without making an excesive error.

4.6.3 Superficial gas velocity effect

This section investigates the effect of the superficial gas velocity on the interchange coefficient. In Fig. 4.9a the mean gas interchange coefficient obtained in the simulation data, has been normalized with the analytical model proposed, $K_{corrected,2D}$, given by Eq. 4.12. The simulations represent bubbling beds with 5 different superficial velocities ranging from $U/U_{mf} = 1.5$ to 3 (i.e. from $U = 0.525$ m/s to 1.05 m/s) and the same settled bed height $H_0 = 0.3$ m (cases 2-a to 2-e).

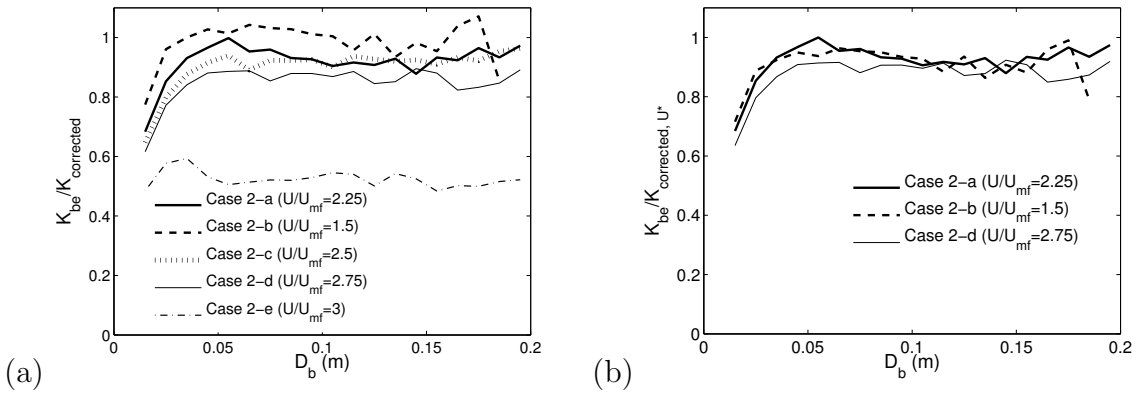

Figure 4.9: Normalized interchange coefficient versus the bubble diameter: a) using $\zeta = 9/4$ for cases 2-a,b,c,d,e; and b) using U^* for cases 2-a,b,d.

As Fig. 4.9a reflects, if bubbles are not very small, all the values of the normalized interchange coefficient are nearly constant and close to the unity despite their different superficial velocity. This demonstrates that the model proposed in Eq. 4.12 is capable of incorporating the increase of the gas interchange coefficient when the superficial gas velocity is augmented. Exception of this is the gas interchange of bubbles in the bed with the highest superficial velocity, case 2-e (Table 4.3). Passing from superficial velocity $2.75U_{mf}$ to $3U_{mf}$ abruptly halves the mean gas interchange coefficient. This can be explained considering that the air excess of case 2-e gives a regime transition from freely bubbling to turbulent fluidization. The regime transition for superficial velocities $U \sim 3U_{mf}$ has been also reported by Makkawi & Wright (2002). Therefore, the proposed model $K_{corrected,2D}$ can be used when the fluidized bed is working in bubbling regime but not in turbulent fluidization.

Despite $K_{corrected,2D}$ shows a very good prediction of the simulation results, it can be slightly improved by calculating more precisely ζ in Eq 4.11. Varying the superficial gas velocity leads to a change in the coefficients Ψ and δ that may affect ζ and $K_{corrected,2D}$ used for the normalization in Fig. 4.9a. Table 4.4 contains the resulting values of δ and Ψ for three different superficial velocities in the simulated bubbling bed (cases 2-a, 2-b and 2-d).

Table 4.4: Values of δ, Ψ and ζ for cases 2-a, 2-b and 2-d

Case	U/U_{mf}	δ	Ψ	ζ
2-a	2.25	1.3	0.3943	2.2463
2-b	1.5	1.45	0.401	2.435
2-d	2.75	1.26	0.385	2.1817

According to Table 4.4, increasing the superficial velocity U of the bed uniformizes the throughflow within the bed area since δ decreases. The simulations also seem to indicate that the increase of U has the additional effect of augmenting the throughflow in a larger extend than the visible flow, which produces a slight decrease on the value of Ψ. The resulting value of ζ decreases with an increase of U as shown in Table 4.4. When the values of ζ in Table 4.4 are incorporated in $K_{corrected,2D}$ (Eq. 4.11) for the normalization of the interchange coefficient, the curves shown in Fig. 4.9b are less sensitive to U/U_{mf} than in Fig. 4.9a. Therefore, the corrected model in Eq. 4.11 is able to retain more precisely the effect of the superficial gas velocity on the interchange coefficient in a bubbling bed. Nevertheless, the observed variation of ζ with U/U_{mf} is not intense and $\zeta = 9/4$ can be considered a good approximation for the 2D bubbling beds studied here.

4.6.4 Bed height effect

The effect of the bed height on the gas interchange between bubbles and emulsion is shown in Fig. 4.10. This figure contains the normalised interchange coefficient defined in the previous section using the proposed model, and the crossflow ratio versus the bubble diameter. Results are depicted for different settled bed heights, H_0, and same superficial gas velocity ($U = 2.25U_{mf}$).

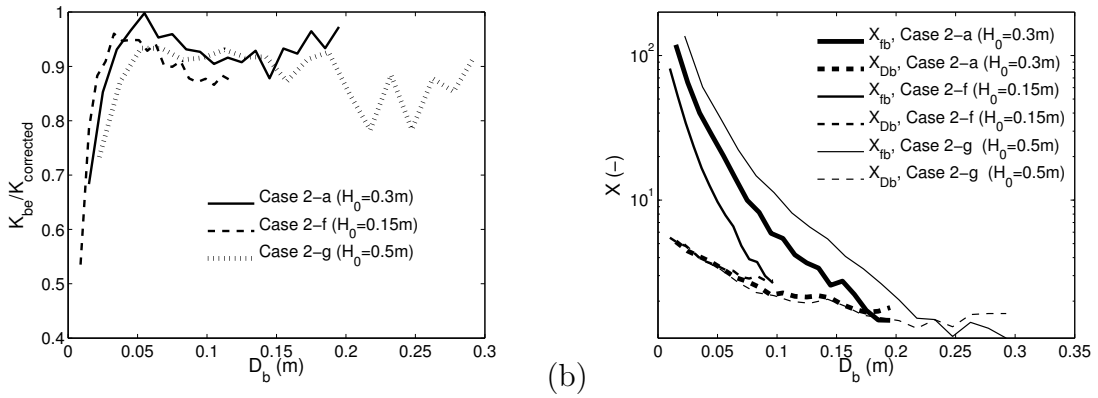

Figure 4.10: Effect of the static bed height on: a) the normalised interchange coefficient; and b) the crossflow ratio, versus the bubble diameter. Cases 2-a,f,g.

It seems from Fig. 4.10a that the gas interchange coefficient of a bubble with a given diameter is not strongly affected by the static bed height when the bubble diameter is greater than 5 cm. Obviously, the crossflow ratio calculated using the distance to the freeboard, Fig. 4.10b, increases with the settled bed height since bubbles require longer times to reach the bed surface. In turn, the crossflow ratio calculated using the bubble diameter, X_{Db}, is not affected by the static bed height, which corroborates the fact that the gas interchange and bubble velocity can be assumed insensitive to the settled bed height for the operating conditions analyzed in this work.

Taking into account the reduced effect of the bed height on the gas interchange, substantial differences in the interchange coefficient are not expected when increasing the bed width while keeping the gas superficial velocity unchanged. However, if the bed width is reduced to values close to the bubble diameter, the bed regime passes from bubbling to slugging and significant changes on the interchange coefficient may occur.

4.6.5 Particle size dependence

In this section the effect of the particle size is studied with the simulation results from case 2-h in Table 4.3. In this case, the particles used are smaller ($d_p = 0.46$ mm) than in case 2-a ($d_p = 0.7$ mm). The static bed height $H_0 = 0.3$ m and the relative superficial gas velocity $U/U_{mf} = 2.25$ was taken the same for the two cases. Note that in case 2-h, the superficial gas velocity $U = 0.4275$ m/s, is different from case 2-a since U_{mf} depends on the particle size. Fig. 4.11 shows the simulated interchange coefficient and crossflow ratio, using $L_c = D_b$, for case 2-h. The results are presented together with the theoretical model by Davidson (Davidson & Harrison, 1963), Eq. 4.2, and the corrected model, Eqs. 4.12 and 4.13, for the case 2-h.

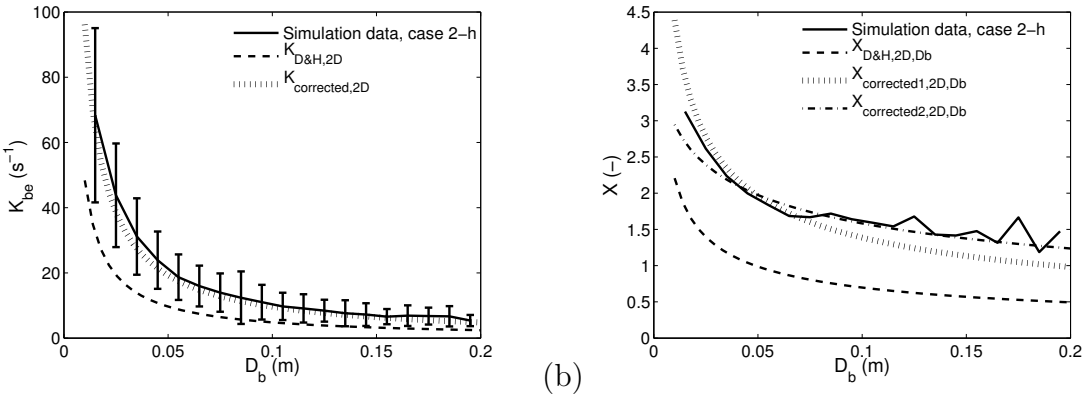

Figure 4.11: Results for particles with $d_p = 0.46$ mm: a) interchange coefficient; and b) crossflow ratio, versus the bubble diameter. Case 2-h.

As reflected in Fig. 4.11, particles with diameter $d_p = 0.46$ mm lead to smaller gas interchange coefficients and crossflow ratios than particles with $d_p = 0.7$ mm (Figs.4.7b and 4.8b). Using smaller particles means that the minimum velocity U_{mf} needed to fluidized the bed is smaller and, therefore, smaller values of the interchange coefficient are obtained. Fig. 4.11a demonstrates that for particles with $d_p = 0.46$ mm the corrected model $K_{corrected,2D}$ (Eq. 4.12), is still able to predict the gas interchange coefficient calculated from the two-fluid 2D simulations of bubbling beds. As in Fig. 4.7b, $K_{D\&H,2D}$ from the potential flow theory for isolated bubbles clearly underpredicts the interchange coefficient given by the simulations.

Concerning the crossflow ratio shown in Fig. 4.11b, the corrected model $X_{corrected1,2D}$ was calculated using Eq. 4.13 with $v_b = v_{b,i}$ and $\phi = 0.7$ as in Fig. 4.8b. $X_{corrected2,2D}$ was obtained employing Eq. 4.13 with $v_b = v_{b,b}$. In this case the bubble velocity, $v_{b,b}$, was computed by fitting Eq. 4.4 to the mean bubble velocity obtained from the simulated case 2-h, leading to $c_1 = 0.82$ and $c_2 = 0.41$. Differences between $X_{corrected1,2D}$ and $X_{corrected2,2D}$ are relatively small and both approaches give acceptable estimations of the simulated crossflow ratio.

4.6.6 Preliminary estimation of the gas interchange in 3D bubbles

In this last section the results from 2D bubbles obtained in the two-fluid simulations are extrapolated to 3D bubbles. This is done by revolving each 2D bubble from the simulation over a vertical axis that crosses the bubble centroid. Note that this procedure is only used to estimate the differences between the 2D and the 3D model. Fully 3D simulations with three dimmensional bubbles should be needed to complete this analysis. The angle of revolution is $\theta_r = \pi$ (180°) since the bubbles may not be symmetrical along the vertical axis, and the whole bubble contour should be considered. Thus, the volume of gas crossing the bubble boundary in each artificially created 3D bubbles is:

$$\dot{V}_{be,3D} \approx \int_{\Omega_b} \alpha_g \theta_r |x - x_c| [-(u_g - u_b)dy + (v_g - v_b)dx] \tag{4.14}$$

where x_c is the horizontal coordinate of the bubble centroid.

Using Eq. 4.14, the results of an isolated bubble were firstly analyzed and are shown in Fig. 4.12a, together with the previous results from the 2D analysis, Eq. 4.7. The Davidson & Harrison's model (Davidson & Harrison, 1963) for spherical voids yields ($\dot{V}_{be} = (3/4)D_b^2 U_{mf}\pi$), so the potential flow expression of the interchange coefficient for isolated bubbles is:

$$K_{D\&H,3D} = \frac{9}{2}\frac{U_{mf}}{D_b} \tag{4.15}$$

In view of Eq. 4.15, the interchange coefficient for 3D bubbles is higher than for 2D bubbles, Eq. 4.2. The simulation results for isolated 2D bubbles and for the same bubbles extrapolated to 3D are included in Fig. 4.12a. Each point in the figure corresponds to an instantaneous value of the interchange coefficient calculated with the simulation results using the volume of gas from Eq. 4.7 or Eq. 4.14. As Fig. 4.12a demonstrates, the interchange coefficient in 3D isolated bubbles extrapolated from 2D simulations is in perfect agreement with $K_{D\&H,3D}$. This means that, for isolated bubbles, the 3D extrapolation methodology given by Eq. 4.14 leads to results that are in harmony with the potential flow theory, Eq. 4.15. Fig. 4.12a includes also an example snapshot of the solids volume fraction of the bed containing one of the analyzed isolated bubbles.

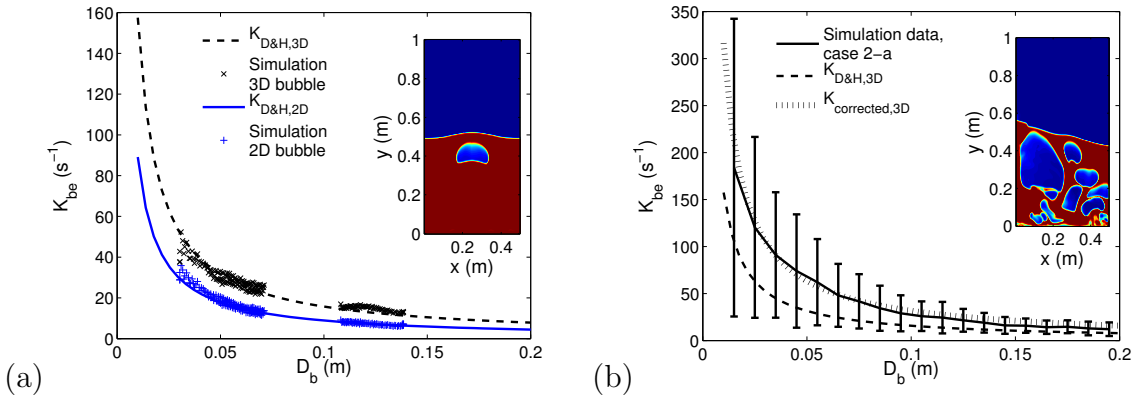

(a) (b)

Figure 4.12: 3D Interchange coefficient versus the bubble diameter for: a) the isolated bubble case 1-b; and b) the bubbling bed case 2-a.

Eq. 4.14 can be used as well to study the bed in the fully bubbling regime (case 2-a). The results for the interchange coefficient obtained from 3D bubbles extrapolated from the simulated 2D bubbles are shown in Fig. 4.12b, which also has a snapshot of the solids volume fraction to clearly identify the bubbling regime of this case. According to Fig. 4.12b the potential flow model for 3D bubbles, $K_{D\&H,3D}$, clearly fails in the prediction of the gas interchange for multiple interacting bubbles in the simulated bed. As for the case of 2D bubbles, the following corrected model is proposed here:

$$K_{corrected,3D} = \frac{9}{2}\frac{U^*}{D_b} = \frac{\zeta_{3D}U}{D_b} \tag{4.16}$$

which is based on the use of the effective velocity U^* instead of the minimum fluidization velocity U_{mf}. Using U^* described in Eq. 4.9, it is easy to find that $\zeta_{3D} =$

$(9/2)\,[\delta(1-\Psi)+(U_{mf}/U)(1-\delta-\delta\Psi)]$ in Eq. 4.16,

As a first approximation, the throughflow concentration parameter, δ, and the visible flow fraction, Ψ, can be assumed close to the values obtained for a 2D bed in section 5.2. Thus $\zeta_{3D} = 3.97 \approx 4$ and,

$$K_{corrected,3D} \approx \frac{4U}{D_b} \tag{4.17}$$

Fig. 4.12b proves that the model proposed in Eq. 4.17 is capable of predicting the gas interchange in multiple interacting 3D bubbles that have been extrapolated from the 2-D simulation of a bubbling bed. According to Eq. 4.11 and Eq. 4.16, the relative increase experienced by the interchange coefficient when passing from 2D bubbles to 3D bubbles is the same for isolated bubbles than for multiple bubbles, that is:

$$\frac{K_{corrected,3D}}{K_{corrected,2D}} = \frac{K_{D\&H,3D}}{K_{D\&H,2D}} \tag{4.18}$$

Though fully 3D simulations have not been used here, the good predictive results of the interchange coefficient model $K_{corrected,3D}$ shown in Fig. 4.12b are remarkable considering the simplicity of Eq. 4.17.

4.7 Conclusions

Two-fluid model simulations were used in this work to characterize the mean gas interchange coefficient, K_{be}, and crossflow ratio, X, of bubbles in a fluidized bed of Geldart group B particles.

Firstly, it has been demonstrated that the simulations are able to reproduce realistically the pressure distribution and the gas flow for isolated bubbles, and the results are in agreement with classical potential flow model by Davidson & Harrison (Davidson & Harrison, 1963).

Secondly, the mean gas interchange coefficient, K_{be}, and crossflow ratio, X, of slow bubbles in two-dimensional fully bubbling beds were characterized for several operating conditions. Both K_{be} and X decrease with the distance to the distributor and the bubble diameter, their values being over two times those predicted by the potential flow theory of isolated bubbles. To improve the prediction of the gas interchange coefficient between the bubble and emulsion phases, the corrected expression, $K_{corrected,2D} \approx 9U/4D_b$, was proposed in the present work for multiple interacting 2D bubbles. This novel expression is able of predicting the gas interchange coefficient and crossflow ratio, even varying the superficial gas velocity, the static bed height and the particle size. A limitation of the model was found when the fluidized bed is working under high

gas velocity rates. In particular, at a velocity of $U \sim 3U_{mf}$, the fluidization regime is transitioning from freely bubbling to turbulent fluidization, and the values predicted by $K_{corrected,2D}$ overestimate those given by the 2D simulation.

Finally, the gas interchange in 3D bubbles has been estimated using an extrapolation from the 2D bubbles obtained in the two-fluid simulations. This extrapolation to 3D was done by revolving the 2D bubbles around their vertical axis. The resulting gas interchange coefficient for isolated 3D bubbles agrees almost perfectly with the potential flow theory for spherical bubbles (Davidson & Harrison, 1963). For multiple interacting 3D bubbles in a fully bubbling bed the potential flow theory is not satisfactory, and the corrected expression of the gas interchange coefficient, $K_{corrected,3D}$, applied to 3D bubbles is the model that follows very closely the extrapolated simulation results. Note that this procedure is only used to estimate the differences between the 2D and the 3D model. Fully 3D simulations with three dimensional bubbles should be needed to complete this analysis.

The corrected expressions proposed in this work accounting for the gas interchange coefficient and crossflow ratio for 2D bubbles, may be of direct application in the development of discrete bubble models (DBM) and other phenomenological tools used for simulating industrial scale fluidized bed gasifiers and combustors, in which the prediction of the gas behaviour is a key factor.

Nomenclature

a	isolated bubble radius (m)
c_1,c_2	coefficients for the bubble velocity (-)
D_b	bubble equivalent diameter (m)
d_p	particle diameter (mm)
H	height (m)
H_0	static bed height (m)
K_{be}	interchange coefficient (s^{-1})
$K_{corrected,2D}$	corrected interchange coefficient for 2D bubbles (s^{-1})
$K_{corrected,3D}$	corrected interchange coefficient for 3D bubbles (s^{-1})
$K_{D\&H,2D}$	potential flow interchange coefficient for 2D bubbles (s^{-1})
$K_{D\&H,3D}$	potential flow interchange coefficient for 3D bubbles (s^{-1})
K_{gs}	gas-solid momentum exchange (-)
U	superficial gas velocity (m/s)
U^*	corrected velocity (m/s)
U_{mf}	minimum fluidization velocity (m/s)

g	gravity vector (m/s^2)
P	pressure (Pa)
ΔP_g	relative pressure of the gas (Pa)
V_b	bubble volume (m^3)
$\dot{V}_{be}$	volumetric gas flow rate (m^3/s)
$\vec{v}_b$	bubble velocity (m/s)
$\vec{v}_g$	gas velocity (m/s)
$\vec{v}_s$	solids velocity (m/s)
$v_{b,b}$	bubble velocity for bubbling beds (m/s)
$v_{b,i}$	bubble velocity for isolated bubbles (m/s)
W	bed width (m)
X	crossflow ratio (-)
$X_{corrected1,2D}$	corrected crossflow ratio using Equation 4.6 (-)
$X_{corrected2,2D}$	corrected crossflow ratio using Equation 4.4 (-)
X_{Db}	crossflow ratio referred to the bubble diameter (-)
X_{fb}	crossflow ratio referred to the surface of the bed (-)
$X_{D\&H,2D}$	potential flow crossflow ratio for 2D bubbles (-)
x	horizontal coordinate (m)
x_c	x referred to the bubble centroid (m)
y	vertical coordinate (m)
y_c	y referred to the bubble centroid (m)
Z	2D bed thickness (m)

Greek letters

α_s	solids volume fraction (-)
α_g	voidage (-)
δ	throughflow concentration parameter (-)
ϕ	coefficient for the bubble velocity (-)
ρ_d	bulk density (kg/m^3)
ρ_s	solids density (kg/m^3)
ρ_g	gas density (kg/m^3)
Ψ	fraction of visible bubble flow (-)
θ_r	angle of revolution $(-)$
ζ	coefficient for the corrected model (-)

Bibliography

Benyahia, S., Syamlal, M., O'Brien, T.J. Summary of MFIX equations 2005-4, 2007.

Busciglio, A., Vella, G., Micale, G., Rizzutia, L. Analysis of the bubbling behaviour of 2D gas solid fluidized beds: Part II. Comparison between experiments and numerical simulations via Digital Image Analysis Technique. *Chem. Eng. J.* 148 (2009) 145-163.

Chiba, T. and Kobayashi, H. Gas Exchange between the Bubble and Emulsion Phases in Gas-Solid Fluidized Beds. *Chem. Eng. Sci.* 25, (1970) 1375-1385.

Collins, R. An extension of Davidson's theory of bubbles in fluidized beds. *Chem. Eng. Sci*, 20, (1965) 747-755.

Development of a novel infrared technique for instantaneous, whole-field, non invasive gas concentration measurements in gas-solid fluidized beds. Dang, T.Y.N., Kolkman, T., Gallucci, F., van Sint Annaland, M. *Chem. Eng J.* 219 (2013) 545-557.

Darton, R.C., La Nauze, R.D., Davidson, J.F., Harrison, D. Bubble growth due to coalescence in fluidised beds. *Trans. IChemE*, 55 (1977) 2411-2437.

Davidson J.F. and Harrison, D. Fluidized Particles, Cambridge University Press, New York, 1963.

Gidaspow, D. Multiphase flow and Fluidization: Continuum and kinetic theory descriptions; Academic Press: San Diego, CA. 1994.

Hernández-Jiménez, F., Sánchez-Delgado, S., Gómez-García, A., Acosta-Iborra, A. Comparison between two-fluid model simulations and particle image analysis & velocimetry (PIV) results for a two-dimensional gas-solid fluidized bed. *Chem. Eng. Sci.* 66 (2011) 3753-3772.

Hernández-Jiménez, F., Third, J.R., Acosta-Iborra, A., Müller, C.R. Comparison of bubble eruption models with two-fluid simulations in a 2D gas-fluidized beds. *Chem. Eng J.* 171 (2011) 328-339.

Johnson, P.C., Jackson, R. Frictional collisional constitutive relations for antigranulocytes materials, with application to plane shearing. *J. of Fluid Mech.* 176 (1987), 67-93.

Kunii, D., Levenspiel, O. Fluidization Engineering: Butterworth-Heinemann: Newton, MA, 1991.

Li, T., Grace, J.R., Bi, X. Study of wall boundary condition in numerical simulations of bubbling fluidized beds. *Powder Technol.* 203 (2010) 447-457.

Makkawi, Y.T., Wright, P.C. Fluidization regimes in a conventional fluidized bed characterized by means of electrical capacitance tomography. *Chem. Eng. Sci.* 57 (2002) 2411-2437.

Patil, D.J., van Sint Annaland, M., Kuipers, J.A.M. Gas dispersion and bubble-to-emulsion phase mass exhange in a gas-solid bubbling fluidized bed: a computational and experimental study. *Int. J. of Chem. Reactor Eng.*, 1 (2003), 1-20.

Pavlin, T., Wang, R., McGorty, R., Rosen, M.S., Cory, D.G., Candela, D., Mair, R.W., Walsworth, R.L. Noninvasive measurements of gas exchange in a three dimensional fluidized bed by hiperpolarized Xe NMR. *Appl. Magn. Reson.*, 32 (2007), 93-122.

Sit, S.P., Grace, J.R. Interphase mass transfer in an aggregative fluidized bed. *Chem. Eng Sci.* 33 (1978) 11115-1122.

Sit, S.P., Grace, J.R. Effect of bubble interaction on interphase mass transfer in gas fluidized beds. *Chem. Eng Sci.* 36 (1981) 327-335.

Solimene, R., Marzocchella, A., Passarelli, G., Salatino, P. Assessment of Gas-Fluidized Beds Mixing and Hydrodynamics by Zirconia Sensors. *AIChE Journal* 52, (2006) 185-198.

Syamlal, M., Rogers, W., O'Brien, T.J. MFIX Documentation: Theory guide, U.S. department of Energy (DOE), Morgantown Energy Technology Center, Morgantown, West Virginia, 1993.

Wu, W. and Agarwal, P.K. The effect of bed temperature on mass transfer between the bubble and emulsion phases in a fluidized beds. *Can. J. Chem. Eng.* 81, (2003) 940-948.

Chapter 5

Euler-Euler and Euler-Lagrangian evaluation of pseudo-2D gas fluidized beds

Contents

5.1 Abstract

This chapter is divided in two main sections. In the first one, the differences between two modelling strategies, namely Euler-Euler and Euler-Lagrangian models, are critically evaluated. The Euler-Euler simulations were performed by the author of this dissertation using the code MFIX, whereas the Euler-Lagrangian simulations were gently provided by Dr. J. R. Third and Dr. C. R. Müller (Müller et al., 2008) from the Laboratory of Energy Science and Technology, ETH Zürich, employing an in house DEM code. A 2D bed of width, height and transverse thickness of respectively, 0.2 m, 0.5 m and 0.01 m, served as a test case. The settled bed height was $H_0 = 0.2$ m. Particles of density $\rho = 1000$ kg/m^3 and diameter $d_p = 1.2$ mm were fluidized with air injected from below. Comparison between the simulation results is based on both instantaneous and time-averaged properties. A particular focus of this study is the influence of the coefficients of restitution and friction on the simulation results.

The comparison between both models indicates that the wall boundary condition for the solid phase is a key factor in the simulations. Therefore, a new partial-slip boundary condition for the solid phase in pseudo two−dimensional (2D) beds is estimated using information from DEM simulations and implemented in the two-fluid model. The high spatial resolution, and real discrimination between solids and gas, of the DEM allow to be obtained the information required for the new boundary condition, viz. the particle interaction with the walls. In addition, the new boundary condition is compared with the classical Johnson and Jackson boundary condition (Johnson and Jackson, 1987), which is commonly employed for the particle phase in two-fluid models. The effect of the coefficients of restitution and friction for particle-particle and particle-wall contacts, as well as the effect of the superficial gas velocity on the values of the parameters of the new boundary condition are studied. In order to develop the new boundary condition, a smaller bed is analysed in section 5.6 in order to reduce the computational cost of the DEM simulations. The new boundary condition is found to be contrary to the Johnson and Jackson (Johnson and Jackson, 1987) at low values of solids concentration. Furthermore, this new boundary condition implemented in the two-fluid model improves the results compared to the Johnson and Jackson boundary condition.

5.2 Introduction

Numerical modelling of fluidized beds has advanced significantly over the last two decades, the most popular modelling approaches being the Euler-Euler and Euler-Lagrangian models. The Euler-Lagrangian approach combines an Eulerian description of the fluid-phase with a Lagrangian particle simulation, in which the trajectory of each particle is calculated based on Newton's second Law. The gas-solids interaction is computed through semi-empirical closure models (Deen et al., 2007). Although very promising, the Euler-Lagrangian approach is very computationally expensive and is, therefore, currently unable to simulate the large number of particles encountered in medium- or large-scale fluidized beds.

In the Euler-Euler approach (Gidaspow, 1994; Van Wachem et al., 1998) the particles and the fluid phase are treated as inter-penetrating continua (two-fluid model). As in the case of the Euler-Lagrangian approach, two-fluid simulations of fluidized beds require closure relationships for the gas-solids interaction. However, since the particle motion is not modelled in detail, the two-fluid model also requires closure relationships for the particle-particle interactions. These closure relationships may be empirical in nature or may be derived from theoretical relations that are linked to the kinetic theory of granular gases (Gidaspow, 1994).

In a bed of small thickness, i.e. a pseudo−2D bed, the front and the rear walls restrict the solids motion, leading to different flow behaviour compared to fully three-dimensional (3D) systems. For beds of small transverse thicknesses, the effect of the front and the rear walls on the particle motion can be significant and should not be neglected.

Li et al. (2010) investigated the influence of the particle-wall boundary condition (BC) by performing 2D and 3D Eulerian-Eulerian simulations of a pseudo-2D fluidized bed and concluded that the wall effects play an important role in CFD simulations. These authors modified the specularity coefficient of the Johnson and Jackson BC (Johnson and Jackson, 1987) in order to fit the experimental data. However, this procedure implicitly assumes that the Johnson and Jackson BC is valid for all the fluidized bed configurations, including pseudo-2D beds. Analogously, in Chapter 2 of the present dissertation (also see Hernández-Jiménez et al. (2011)) a pseudo-2D fluidized bed was studied using 2D Eulerian-Eulerian simulations and PIV measurements. The results of that chapter clearly showed that the pure 2D simulations systematically over-predict the solids velocity while keeping a realistic relationship between bubble size and velocity. Thus, it seems that the effect of the front and rear walls causes the observed discrepancies, though caution should be taken in attributing the origin of this to a

mere specularity coefficient of the particle-wall interaction.

Schneiderbauer et al. (2012a,b) developed, from an analytical point of view, a boundary condition for the solids stresses and the flux of fluctuation energy for collisional granular flows of spheres, considering sliding and non-sliding collisions, based on the Johnson and Jackson BC. They validated it using experimental measurements from a multiple spout pseudo 2D bed and a discharge of particles in a rectangular bin. More recently, Li and Benyahia (2012) revisited the Johnson and Jackson (Johnson and Jackson, 1987) BC for granular flows, theoretically studying the collision between a particle and a flat wall. They suggested an analytical expression for the specularity coefficient, but also concluded that soft-sphere DEM simulations are needed to properly study the particle-wall interaction. From a conceptual point of view, Schneiderbauer et al. (2012a,b) and Li and Benyahia (2012) consider that the Johnson and Jackson BC is still valid for fluidized beds provided the specularity coefficient is correctly calculated as a function of the local bed dynamics. However, it is not clear whether the Johnson and Jackson BC employed in these three references is always valid. This BC assumes that the particles interact with a single surface in an infinite volume, but in fact both the front and rear walls simultaneously affect the particle motion in pseudo-2D beds.

Chapter 2 of this dissertation compared Euler-Euler simulations with experimental results. In the present chapter an additional source on information is introduced, the Euler-Lagrangian approach. Thus, the first aim of this chapter is to compare the Euler-Euler and Euler-Lagrangian approaches for a specific test case, consisting of a pseudo$-$2D gas fluidized bed. In addition, the effect of parameters such as the inter-particle and particle-wall coefficients of friction, and the coefficient of restitution, will be studied for both models.

The second aim of the chapter is to developed a new partial-slip BC for the solid phase in pseudo-2D beds by means of DEM simulations and subsequently to implement this BC in the two-fluid model. In the DEM the spatial resolution and the discrimination between phases are sufficiently high to obtain information regarding the interaction of individual particles with the walls. The new BC is compared with the Johnson and Jackson BC (Johnson and Jackson, 1987), which is commonly employed in two-fluid simulations. The effect of the coefficients of restitution and friction for particle-particle and particle-wall contacts, as well as the effect of the superficial gas velocity on the parameter values of the newly proposed BC are studied.

5.3 DEM Approach

The Discrete Element Model (DEM) is based on the work of Tsuji et al. (1993), which combines the discrete element model of Cundall and Strack (1979) to simulate the particulate phase, with the volume-averaged Navier-Stokes equations for the fluid phase, as derived by Anderson and Jackson (1967). The DEM simulations have been gratefully provided by Dr. James R. Third & Dr. Christoph R. Müller and are post-processed in this chapter. For each particle, the linear and angular momenta are governed by Newtons second law:

$$m_p \frac{d\vec{v}_s}{dt} = -V_p \nabla p + \frac{V_p \beta}{(1-\alpha_g)}(\vec{v}_g - \vec{v}_s) + \vec{F}_c \tag{5.1}$$

$$I_p \frac{d\vec{\omega}_s}{dt} = \vec{T}_p \tag{5.2}$$

where $m_p, \vec{v}_s$, $\vec{\omega}_s$, $V_p \vec{v}_g$, β, $\vec{F}_c$, $\vec{T}_p$ and I_p are the mass, linear and angular velocities of the particle, the particle volume, the velocity of the gas phase, the interphase momentum exchange coefficient, the force and torque resulting from the collision of the particles, and the moment of inertia of the particle, respectively. To model the collision between contacting particles the soft-sphere approach was used, in which the particles are allowed to overlap by a small amount, δ (Cundall and Strack, 1979). For the fluid the volume-averaged continuity and momentum equations are given by Anderson and Jackson (1967):

$$\frac{\partial}{\partial t}(\alpha_g \rho_g) + \nabla \cdot (\alpha_g \rho_g \vec{v}_g) = 0 \tag{5.3}$$

$$\frac{\partial}{\partial t}(\alpha_g \rho_g \vec{v}_g) + \nabla \cdot (\alpha_g \rho_g \vec{v}_g^2) = -\alpha_g \nabla p + \nabla \cdot \overline{\overline{\tau_g}} + \alpha_g \rho_g \vec{g} - \vec{F}_p \tag{5.4}$$

here, $\overline{\overline{\tau_g}}$ is the viscous stress tensor and $\vec{F}_p$ is the rate of exchange of momentum between the particulate and the fluid phases. The fluid was assumed to be Newtonian. The rate of momentum exchange between the particulate and fluid phases was calculated by adding up the fluid forces acting on the N_p individual particles in a fluid cell of volume V_{cell}.

$$\vec{F}_p = \frac{\vec{V}_p}{V_{cell}} \frac{\sum_{N=1}^{N_p} \beta(\vec{v}_g - \vec{v}_s)}{1-\alpha_g} \tag{5.5}$$

This DEM approach has been validated in a practical way using a narrow bed with experimental granular temperature measurements performed with MRI (Müller et al., 2008).

5.4 Two-Fluid Model Approach

The two-fluid model (TFM), based on the conservation equations of mass, momentum and granular temperature, was solved using the MFIX code (Multifluid Flow with Interphase eXchanges) (Syamlal et al., 1993; Benyahia et al., 2007). The kinetic theory of granular gases was used for the closure of the solids pressure stress terms. A second order accurate scheme (Superbee) was used to discretize the convective derivatives in the balance equations. The governing equations as well as the closure models of the two-fluid model can be found in Appendix A.

5.5 Critical evaluation of Euler-Euler and Euler-Lagrangian models.

In this section a comparison between the Euler-Euler and Euler-Lagrangian approaches is performed. It is done for a specific test case, consisting of a pseudo−2D gas fluidized bed. In addition, the effect of parameters such as the inter-particle and particle-wall coefficients of friction, and the coefficient of restitution, will be studied for both models.

5.5.1 Numerical simulations

The gas-fluidized bed studied in this section was of 0.2 m width, 0.01 m transverse thickness and 0.5 m height, filled with spherical particles of density $\rho = 1000$ kg/m^3 and diameter $d_p = 1.2$ mm. The static bed height was $H_0 = 0.2$ m and the gas inlet velocity was $U = 0.6$ m/s, corresponding to $U/U_{mf} = 2$. Several cases were studied to evaluate the effect of the properties of the particles and walls. Tables 5.1 and 5.2 summarise the cases studied in this section.

Table 5.1: Simulation parameters for the TFM simulations

Case	**Restitution coefficient**	**Coeff. of friction between particles**	**Walls boundary condition**
Case 1	0.9	0.57	Partial-slip
Case 2	0.9	0.1	Partial-slip
Case 3	0.9	0.57	Free slip
Case 4	0.5	0.57	Partial-slip

The parameters that are varied are the inter-particle and particle-wall coefficients of friction, and the restitution coefficient. Case 1 is taken to be the base case incorporating commonly used parameters. The inlet has been modelled as a homogeneous velocity inlet and the outlet as a constant pressure outlet for both models. The computational

Table 5.2: Simulation parameters for the DEM simulations

Case	Restitution coefficient	Coeff. of friction between particles	Wall boundary condition
Case 1	0.9	0.57	0.57
Case 2	0.9	0.1	0.1
Case 3	0.9	0.57	0
Case 4	0.5	0.57	0.57

domain for the TFM simulations comprised 57 x 141 x 8 cells in the x- (width), y- (height) and z- (thickness) directions, respectively. This creates a mesh with a 3.5 mm cell size. A standard partial-slip boundary condition was applied at the walls of the fluidized bed, with a specularity coefficient of $\phi = 0.6$ (Johnson and Jackson, 1987). The fluid computational domain for the DEM model comprised 58 x 148 x 3 cells in the x-, y- and z- directions, respectively. The fluidized bed contained 265650 particles. Interactions between particles are modelled using a damped Hertzian spring with an E-modulus of 1.2×10^6 N/m^2.

In this section, the drag law proposed by Benyahia et al. (2006) was selected for the two-fluid model simulations and the drag law proposed by Beetstra et al. (2007) for the DEM simulations. Details about the drag force can be found in Appendix A. For the time-averaged results, 40 seconds are employed for the Euler- Euler model and 28 seconds for the Euler-Lagrangian model.

5.5.2 Results and discussion

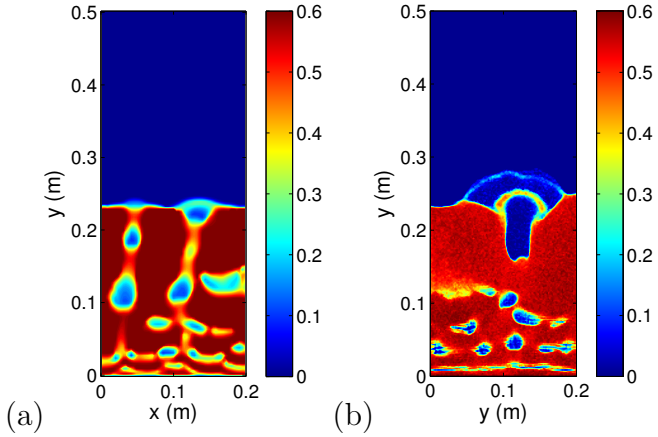

Figure 5.1: Instantaneous snapshot of the bed showing α_s: a) TFM; b) DEM.

Figure 5.1 shows instantaneous snapshots of the solids volume fraction for case 1 simulated using the two models. Both snapshots were taken after the transient

fluidization that occurs during start-up. The snapshots show the characteristic pattern of 2-D beds: small and narrow bubbles appearing in the bottom of the bed, and bigger and less numerous circular bubbles reaching the bed surface. Here bubbles are located where the solids volume fraction reaches a value close to zero. The solids volume fractions presented have been averaged over the entire bed thickness.

Figures 5.2 and 5.3 show the solids volume fraction averaged over the width and thickness of the bed, as a function of time, for the two fluid model and DEM respectively. Both models show the creation of small, slow-moving bubbles close to the distributor and the coalescence and eruption of faster bubbles at distances around $y = 0.1$ m above the distributor.

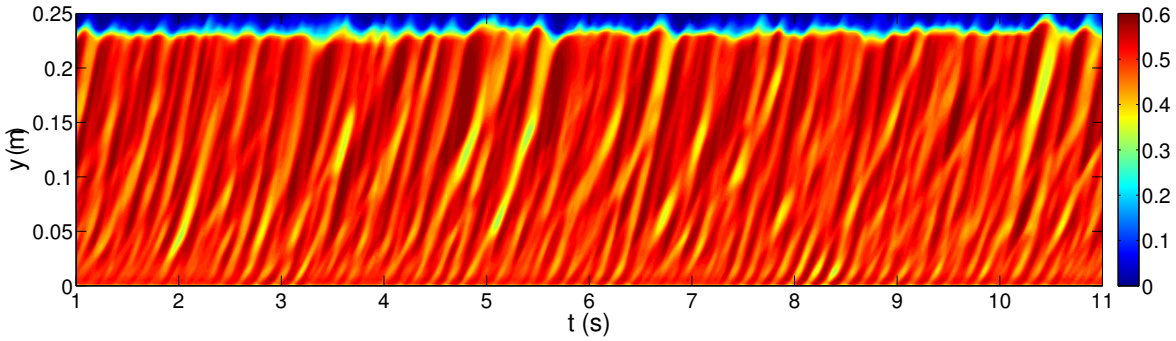

Figure 5.2: XZ-averaged α_s, TFM. Case 1.

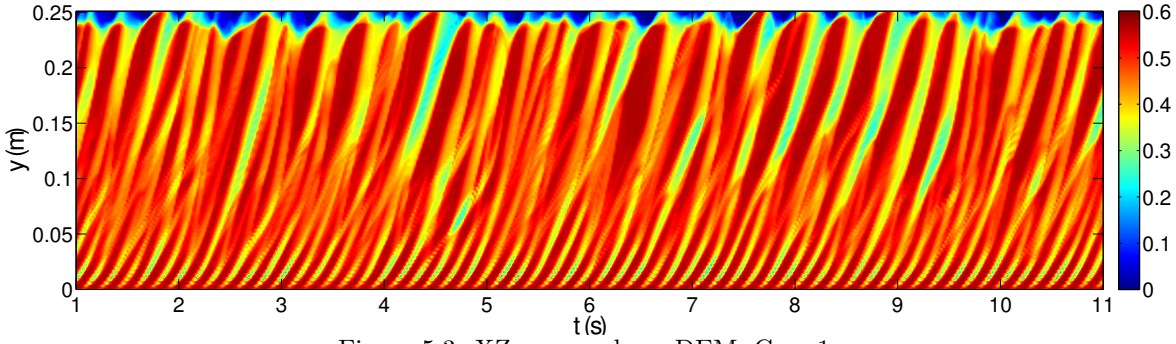

Figure 5.3: XZ-averaged α_s, DEM. Case 1.

Figures 5.4a and 5.4b show the power spectra obtained from the data presented in Figures 5.2 and 5.3 at two different heights, $y = 0.005$ m (close the distributor) and $y = 0.217$ m (close to the top of the bed). For both models the maxima in the power spectra occur at higher frequencies at $y = 0.005$ m than at $y = 0.217$ m. This is expected because bubbles coalesce as they rise through the bed, leading to a reduction in the number of bubbles that cross a horizontal section.

It should be noted, however, that the frequency depicted in Figure 5.4 is a 'bubble coherence frequency' because several bubbles may cross a horizontal section at any

instant of time. Therefore, the frequencies of Figure 5.4 cannot be interpreted as a single bubble frequency unless the size of the bubble is comparable to the bed width, i.e. near the bed surface. The bubble coherence frequency near the distributor defines the principal frequency of bubble formation. This frequency of bubble formation is qualitatively similar in both models, namely $\sim$ 6 Hz. The principal frequencies at $y = 0.217$ m, i.e. the frequency of bubble eruption, are also similar for both simulation strategies. In particular, Figure 5.4 shows that the peak of the power spectrum at $y = 0.217$ m occurs between 2.5 and 3 Hz, which is in agreement with the bed oscillation frequency due to bubble eruption given by Baskakov et al. (1986):

$$f = \frac{\sqrt{g/H_0}}{\pi} \tag{5.6}$$

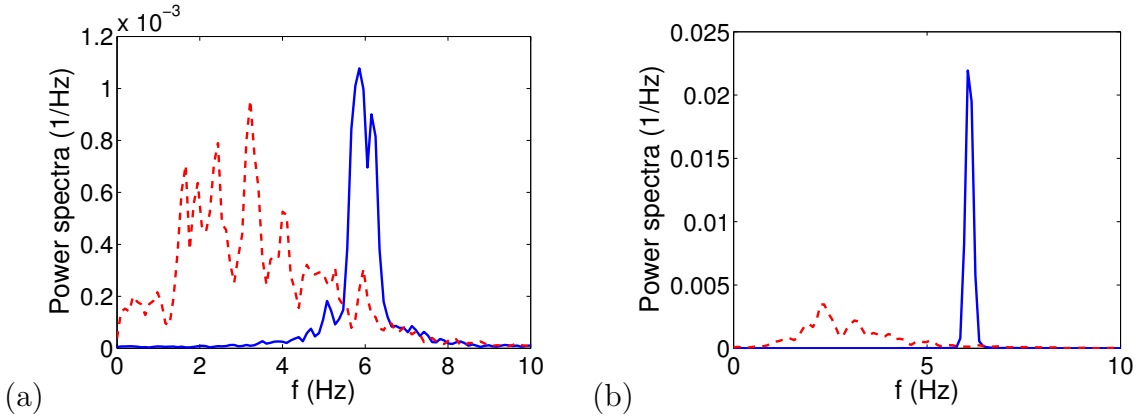

Figure 5.4: Power spectra of XZ-averaged α_s, a) TFM, b) DEM. $y = 0.005$ m (blue solid line); $y = 0.217$ m (red dash line). Case 1.

The average solids volume fraction in an x-z plane located at $y = 0.22$ m is shown in Figure 5.5 for the two fluid model and DEM. This y position is close to the freeboard of the bed. Figure 5.5a reveals that the amplitude of the fluctuations in the solids volume fraction is smaller in the two-fluid simulations when compared with the DEM results. This is expected since the two-fluid approach tends to smear the distinction between the bubble and particulate phases. For the DEM a sharper, and more realistic, transition between the bubble and particulate phase is modeled.

Figure 5.5b plots the dominant frequencies, extracted as the peak-frequency from the power spectra, as a function of vertical position, y. In both simulation strategies, the profiles of peak-frequencies are in good agreement. In particular, high frequencies (around 6 Hz) are observed near the distributor and there is a transition zone in 0.05 m $\leq y \leq$ 0.1 m. Near the freeboard both simulations show a region where the frequency stabilizes due to big bubbles passing at a frequency around 2.5 Hz. Figures 5.2 and 5.3

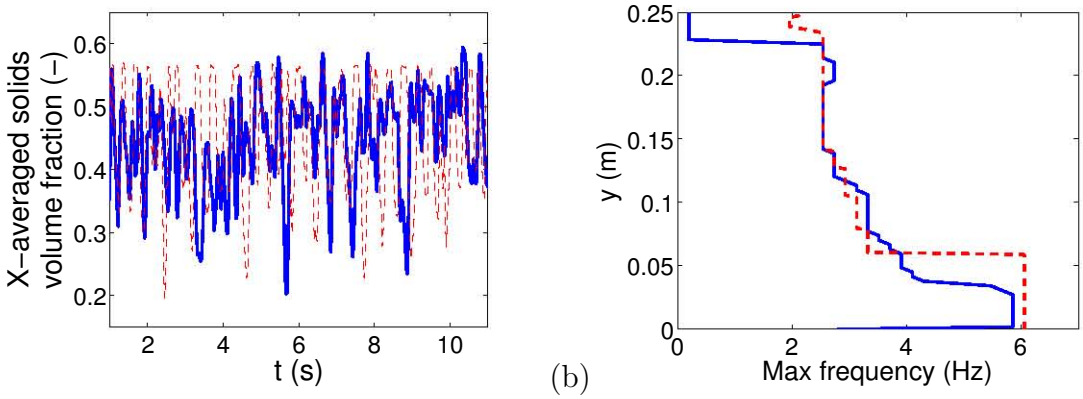

Figure 5.5: a) XZ-averaged α_s at a height of 0.22 m b) Vertical profile of peak frequency for XZ-averaged α_s: TFM (blue solid line); DEM (red dash line). Case 1.

reinforce this observation: both figures indicate a large number of slow-moving bubbles close to the distributor and a smaller number of faster bubbles after the transition zone.

The effect of the wall friction is demonstrated in Figures 5.6a and 5.6b. Here, the solids velocity and solids volume fraction, averaged with respect to time and transversal thickness, z, are presented at a height $y = 0.01$ m for both simulation strategies. In case 1, both models predict very similar magnitudes for the solids velocity, however the bed hydrodynamics revealed by the two simulations are substantially different. In the TFM simulations there are two preferential bubble paths at a distance of ~ 0.05 m away from the lateral walls (low values of α_s in Figure 5.6b). On the other hand in the DEM there is only one path in the middle of the bed. For case 3, which employs a free slip condition at the walls, the time-averaged velocities within the bed are an order of magnitude greater than those obtained for case 1. Furthermore, there are substantial discrepancies between the two-fluid and DEM results obtained for case 3: the TFM predicts velocities that are approximately twice those predicted by the DEM and also predicts higher solids volume fractions, i.e. smaller bed expansion.

Finally, Figure 5.7 compares the solids velocity in both models for cases 1, 2 and 4. For the TFM only small changes in the profile of the solids velocity can be observed for the case that the coefficients of friction and restitution are reduced. However, for the DEM the coefficient of friction plays an important role. Reducing the coefficient of friction in the DEM from 0.57 to 0.1 leads to a substantial increase in the time-averaged solids velocities, as seen in Figure 5.7b. Furthermore, it is observed that for the TFM reducing the coefficient of restitution decreases the gradient along x-direction in the solids velocity profile; only very small variations were observed in the DEM results.

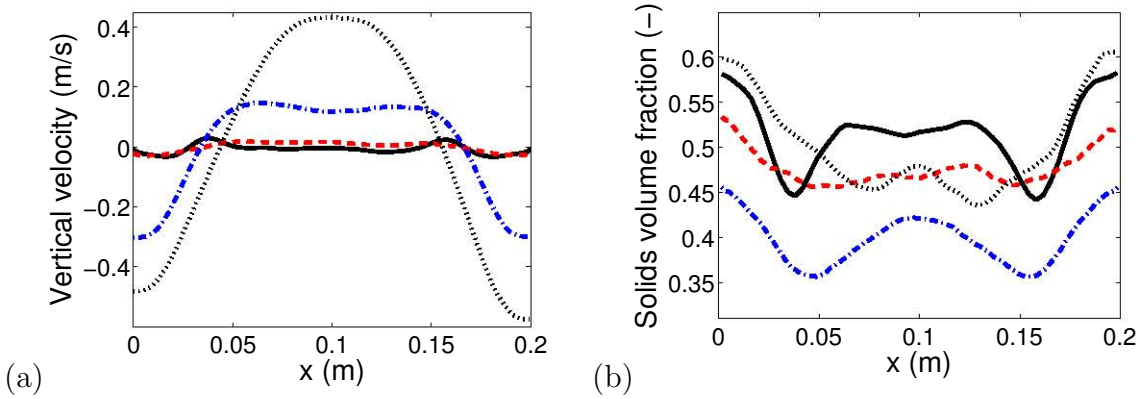

Figure 5.6: Time averaged values of a) solids vertical velocity and b) α_s at a height of 0.1 m: TFM case 1 (black solid line); DEM case 1 (red dash line); TFM case 3 (black dot line); DEM case 3 (blue dash-dot line).

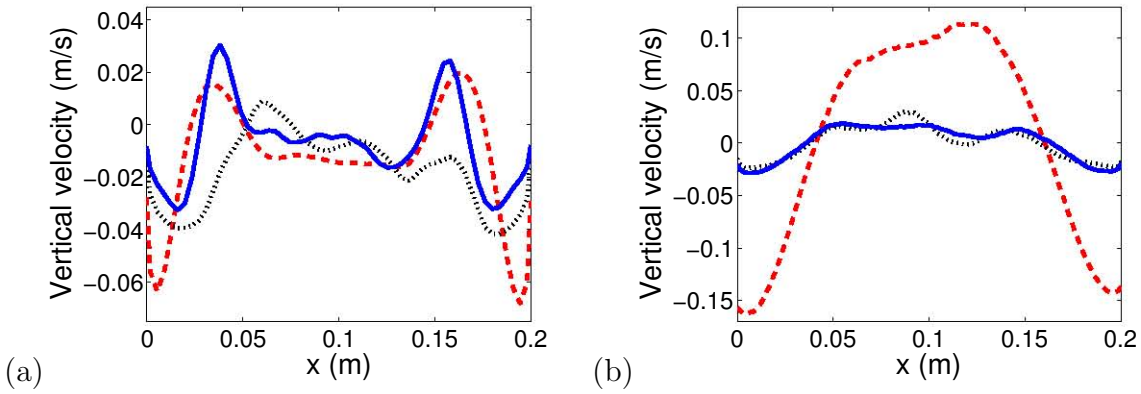

Figure 5.7: Time averaged values of solids vertical velocity at a height of 0.1 m, a) TFM b) DEM: case 1 (blue solid line); case 2 (red dash line); case 4 (black dot line).

5.6 An estimation of the wall boundary condition using DEM

In view of the discrepancies encountered between the DEM and TFM approaches when applied to pseudo-2D beds, the wall boundary condition for the solids phase may be an influential factor in the simulation results. Therefore, in this section a new partial-slip BC for the solid phase in pseudo-2D beds is developed by means of DEM simulations and is subsequently implemented in a TFM. This new BC is compared with the classical Johnson and Jackson BC (Johnson and Jackson, 1987). The effect of the coefficients of restitution and friction for particle-particle and particle-wall contacts, as well as the effect of the superficial gas velocity on the parameter values of the newly proposed BC is studied.

5.6.1 Numerical simulations

A smaller system was chosen for this section in order to reduce the computational cost of the DEM simulations. The gas-fluidized bed studied in this section was of width W = 0.15 m, height H = 0.2 m and thickness Z = 0.01 m, and was partially filled with spherical particles of density $\rho_s = 2500$ kg/m^3 and diameter $d_p = 1.14$ mm. The fluidizing gas was air and was uniformly injected through the base of the bed. The minimum fluidization velocity, U_{mf}, was 0.62 m/s. A fixed pressure BC was chosen at the top of the freeboard. The main simulation parameters are listed in Table 5.3. Several cases, varying the coefficient of restitution, the coefficient of friction between particles (which in DEM is the same as the coefficient of friction between particles and walls) and the gas velocity were studied and are summarized in Table 5.4. Case 1 was selected as the base case.

Table 5.3: General simulation parameters.

Parameter	**Value**
Particle density (kg/m^3), ρ_g	2500
Gas density (kg/m^3), ρ_g	1.2
Gas viscosity (Pa s), μ_g	1.8e-5
Particle diameter (mm), d_p	1.14
Bed width (m), W	0.15
Bed height (m), H	0.2
Bed thickness (m), Z	0.01
Static bed height (m), Z	0.06

Table 5.4: Simulation parameters for the DEM simulations

Case	U/U_{mf}	**Coefficient of restitution (-)**	**Angle of internal friction (°)**
Case 1	2	0.9	30
Case 2	2	0.9	5.71
Case 3	2	0.5	30
Case 4	1.75	0.9	30
Case 5	2.25	0.9	30

A second order accurate scheme was used to discretize the convective derivatives, and the 3D computational domain was discretized using cubic cells of length 3.3 mm for both modelling approaches. For time-averaging the simulation results, 55 seconds of physical time were used for the solids velocity and concentration, and 25 seconds for the bubble properties.

In this section, both modelling approaches (DEM and TFM) employed the drag force correlation proposed by Beetstra et al. (2007) to describe the momentum exchange between the gas and the solid phases. Details about the drag force can be found in Appendix A.

5.6.2 Results: Partial−slip estimated from DEM

The shear force experienced by the bed particles at the wall is related to the gradient of their vertical velocity perpendicular to the wall, $\partial V_y/\partial Z$. As a first approximation, $\partial V_y/\partial Z$ is a function of the physical parameters of the bed (coefficient of restitution, e, coefficient of friction between particles, ϕ), the particle velocity at the wall, $V_{y,wall}$, the thickness of the bed, Z, and the solids concentration, α_s. Thus, dimensional analysis based on the Buckingham π theorem leads to:

$$\left.\frac{\partial V_y}{\partial Z}\right|_{wall} = g(e, \phi, V_{y,wall}, Z, \alpha_s) \longrightarrow \frac{Z}{V_{y,wall}} \left.\frac{\partial V_y}{\partial Z}\right|_{wall} = f(\alpha_s, e, \phi) \tag{5.7}$$

Using Equation 5.7, the spatial derivative of the particle vertical velocity can be expressed as a function of the vertical particle velocity at the wall:

$$\left.\frac{\partial V_y}{\partial Z}\right|_{wall} = h_w V_{y,wall} \tag{5.8}$$

where $h_w = f(\alpha_s, e, \phi)/Z$ is a partial-slip coefficient, which depends on the solids concentration as well as the bed thickness and the coefficients of restitution and friction.

To estimate h_w the thickness of the bed was divided into 6 virtual cells and the two cells closest to a wall in the z-direction were used to estimate the particle velocity at the front and rear walls and the spatial derivative of the velocity at the walls of the bed. In each frame, the instantaneous velocity of the particles was spatially averaged in a cell of size 3.3 x 3.3 x 1.6 mm. The simulation data were recorded at 50 Hz for a simulated time period of 10 s to perform this analysis. The cells near the distributor and near the bed surface were excluded from the analysis in order to avoid the effects of air injection and bubble eruption which may not be representative of the solids motion inside the bulk of the bed.

Figure 5.8 shows a set of scatter plots obtained from DEM simulations. Each point of the scatter plots represents a value of $(\partial V_y/\partial Z)_{wall}$ versus $V_{y,wall}$ in a cell face at the bed wall. Each subfigure plots points within a certain range of α_s. Since the ranges of α_s are small, regression of a line in the scatter plots provides an estimation of the value of h_w in Equation 5.8 for a fixed α_s, represented by the red line. Despite the apparent high scattering in Figure 5.8, the number of points on each subfigure is more

concentrated near the regression line. To demonstrate this, the standard deviation from the regression line for the data points in Figure 5.8 is calculated. On each subfigure the standard deviations for the points above and below the regression line were independently calculated and fitted to a second order polynomial to soften it. These curves are plotted as black lines in Figure 5.8.

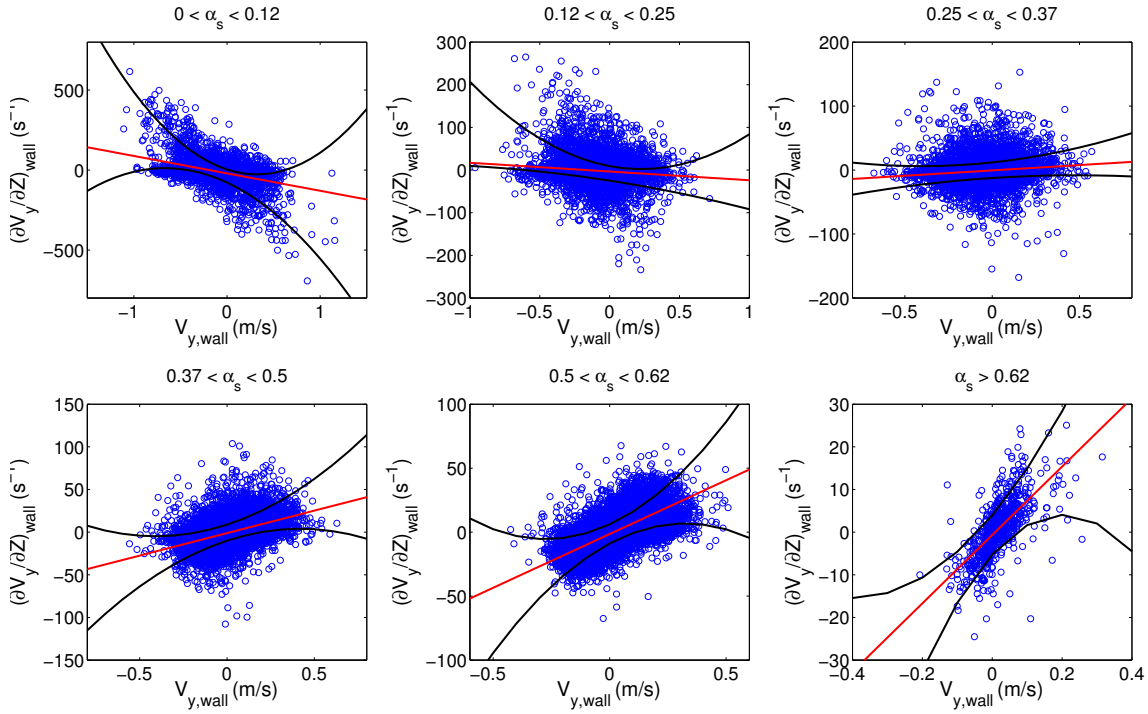

Figure 5.8: Spatial derivative of the particle velocity at the wall, $(\partial V_y/\partial Z)_{wall}$, as a function of the velocity at the wall, $V_{y,wall}$, for different values of solids fraction, α_s, circle blue points; regression line, solid red line; and upper and lower values of the standard deviation, solid black lines. Case 1.

According to Figure 5.8, for values of the solids volume fraction larger than ∼0.25, the regression lines in the scatter plots have a positive slope, as expected. However, for lower values of the solids volume fraction ($\alpha_s \leq 0.25$) the slopes of the regression lines are negative, which means that the magnitude of the vertical velocity increases close to the wall. This is opposite to the trend predicted by Johnson and Jackson (1987), which assumes that the effect of the wall is to retard particle motion. One possible explanation for this behaviour could be that in a pseudo−2D bed particles interact with the gas flow and the walls in such a way that the faster particles tend to drift towards the walls when the solids volume fraction is small.

Using the slope of the lines in Figure 5.8, the values of the normalized partial-slip coefficient $h_w Z = (\partial V_y/\partial Z)_{wall}(Z/V_{y,wall})$ can be plotted as a function of α_s. The best fit to this data was found to be of the form given by Equation 5.9.

$$\left.\frac{\partial V_y}{\partial Z}\right|_{wall} = A\ln(\alpha_s) + B \tag{5.9}$$

Where A and B are obtained by fitting Equation 5.9 to the slopes of the regression lines in Figure 5.8. Equation 5.9 can be easily implemented in the TFM simulations as a partial-slip BC. Several attempts were made to study how other parameters affect this correlation, e.g. the granular temperature or the slip velocity. However none of these parameters were found to influence appreciably the functional form (Equation 5.9) of the correlation proposed.

The results obtained for the new partial-slip BC for quasi-2D beds, Equation 5.9, are shown in Figure 5.9 together with the partial-slip BC proposed by Johnson and Jackson (1987) using the specularity coefficient $\Phi = 0.005$, as recommended by Li et al. (2010). The new partial-slip condition follows a trend markedly different to that of the classical partial-slip BC at low values of α_s. The negative value of the slope indicates that the magnitude of the particle velocity at the wall is typically greater than the velocity in the centre of the bed when the solids volume fraction is smaller than 0.25.

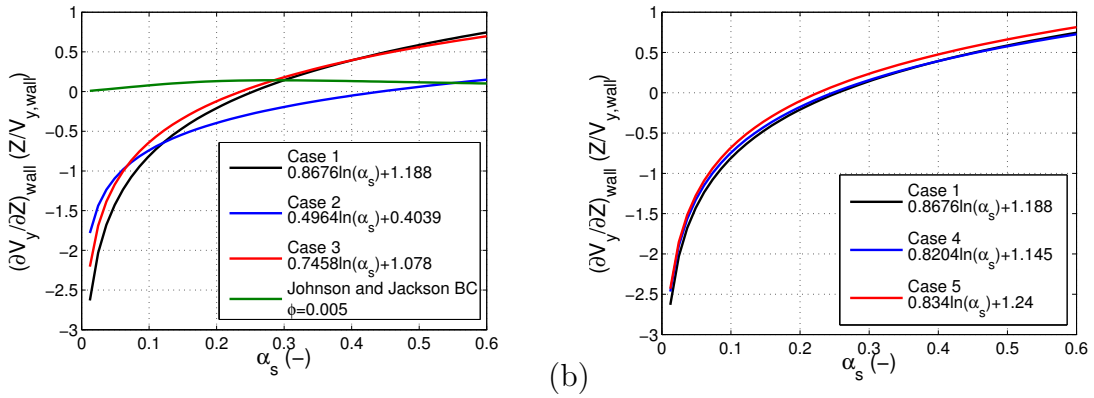

(a) (b)

Figure 5.9: Logarithmic fit to the normalized partial-slip coefficient versus the solids volume fraction: a) effect of the coefficients of restitution and friction and b) effect of the superficial gas velocity.

Furthermore, it can be observed in Figure 5.9a that the coefficient of restitution has a smaller effect on the normalized partial-slip coefficient than the coefficient of friction. The small friction coefficient used in case 2 resulted in relatively small values of the partial-slip coefficient for most solids concentrations. For this case the partial-slip coefficient is only positive for high solids concentrations (0.5-0.6). Paying attention to the effect of the superficial gas velocity (Figure 5.9b), very similar curves are obtained for varying gas velocities, implying that the partial-slip coefficient in quasi-2D beds is relatively insensitive to U/U_{mf}.

Figure 5.10 shows the variation of the coefficients A and B as a function of the coefficients of restitution and friction (Figure 5.10a) and the gas velocity (Figure 5.10b). It can be seen that the coefficient of friction has a stronger influence on the values of A and B than the coefficient of restitution. Both coefficients remain roughly constant over the range of gas velocities studied.

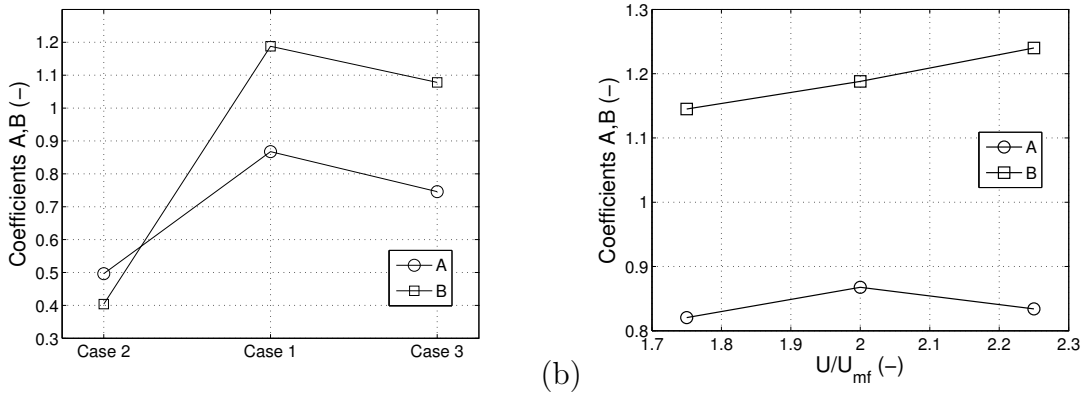

Figure 5.10: Coefficients A and B of Equation 5.9 obtained from the logarithmic fit shown in Figure 5.9.

5.6.3 Results: Comparison with the TFM

The new partial-slip BC coefficient obtained from the DEM was implemented in the TFM. Figure 5.11 shows the solids volume fraction contour maps overlaid by the solids velocity vectors obtained from the DEM (Figure 5.11a), TFM simulation with the new BC (Figure 5.11b) and TFM simulation with the Johnson and Jackson BC (Figure 5.11c), of Case 1. The bed behaviour was found to be similar in the DEM and TFM with the new BC simulations. Concerning the solids motion, downflow close to the lateral walls and upflow in the middle of the bed can be observed in Figure 5.11a,b. Regarding the time-averaged values of the solids fraction, the DEM and TFM with the new BC simulations have similar patterns, i.e. a high solids concentration close to the lateral walls and uniform concentration in the middle of the bed, which is indicative of good solid mixing. In contrast, the TFM with the Johnson and Jackson BC shows a completely different flow behaviour.

The solids hold-up along the bed height and the vertical velocity of the solids at a height of 5.5 cm is shown in Figure 5.12 for the base case. Three different simulations are compared in the figure: the DEM simulation, the TFM with the new partial-slip BC, Equation 5.9, and the TFM using the Johnson and Jackson (1987) BC. Figure 5.12a shows that the bed expansions obtained in the DEM and the TFM with the

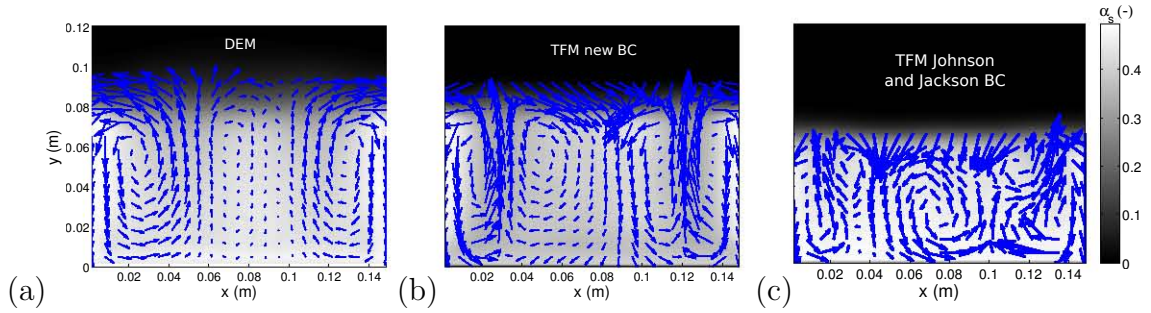

Figure 5.11: Solids volume fraction contour map overlaid with the solids velocity vectors: a) DEM simulation, b) TFM simulation with the new BC and c) TFM simulation with the Johnson and Jackson BC, Case 1.

new BC simulations are similar, whereas the TFM with the Johnson and Jackson BC underestimates the trends of the DEM simulations. Regarding the solids velocity, Figure 5.12b confirms that the TFM simulations with the Johnson and Jackson BC predicts values of the same order of magnitude as the DEM simulations but the bed behaviour is different, showing 4 convection cells instead of the 2 cells observed in the DEM and the TFM with the new partial-slip BC.

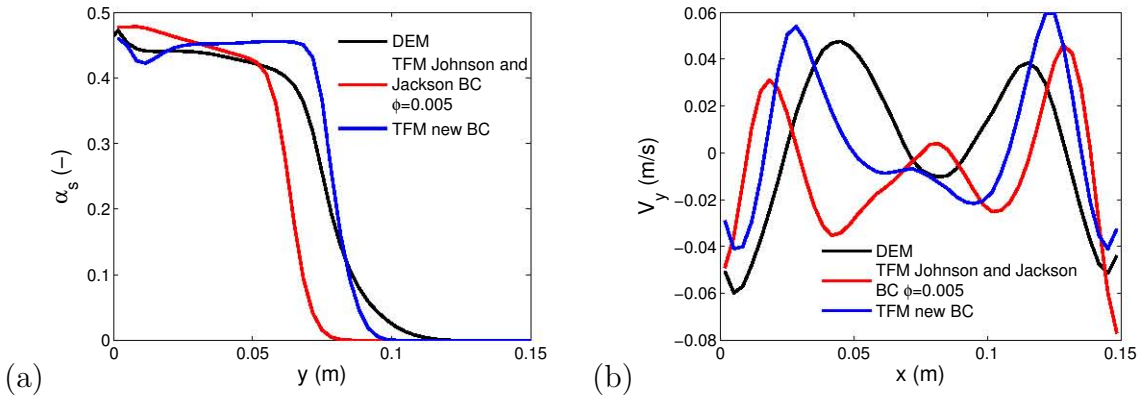

Figure 5.12: a) Solids hold-up along the bed height, and b) vertical solids velocity at a height of 5.5 cm above the distributor using the DEM, TFM with the new BC and TFM with the Johnson and Jackson BC. Case 1.

Further important features in fluidized beds are the bubble characteristics and dynamics. In order to study the bubble motion, it is necessary to distinguish between the bubbles and the emulsion phase. This was done by setting a cutoff value for the solids volume fraction equal to $\alpha_s = 0.3$ (Hernández-Jiménez et al., 2011), which is the arithmetic mean of the maximum and minimum solids volume fractions in the simulated bed. Any region in which the solids volume fraction was less than 0.3 was defined as a bubble. Figure 5.13 shows the mean bubble diameter versus the vertical position in the bed and the mean bubble velocity as a function of the bubble diameter.

The standard deviations in these measurements are plotted as errorbars for the DEM and the TFM with the new BC simulations.

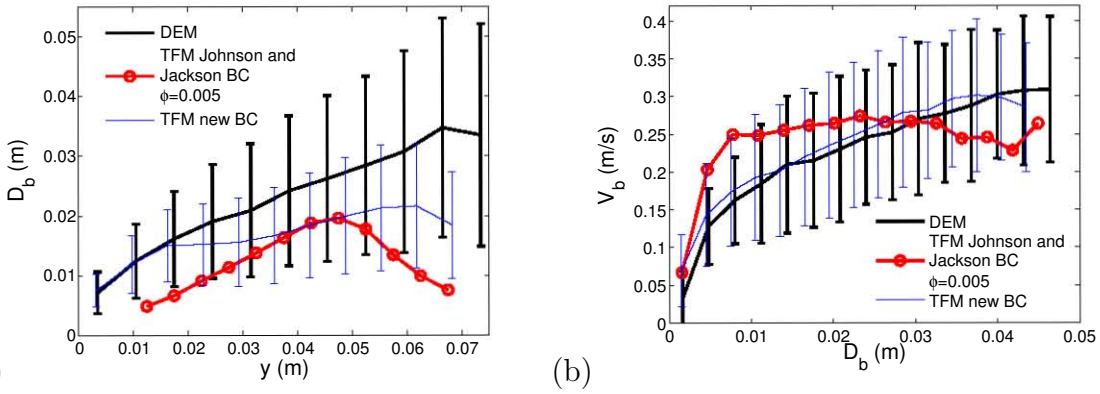

Figure 5.13: a) Bubble diameter versus vertical position, and b) bubble velocity in the vertical direction versus bubble diameter, for the DEM simulation and the TFM with the new BC and TFM with the Johnson and Jackson BC simulations, Case 1.

Figure 5.13a shows that the TFM with the new BC slightly underpredicts the bubble diameter compared to the DEM, but shows better results than those obtained with the TFM using Johnson and Jacksons BC. Regarding the bubble velocity (Figure 5.13b), both the DEM and the TFM with the new BC follow the same trend, whereas the bubble velocity predicted by the TFM with the Johnson and Jackson BC is almost independent of the bubble diameter.

5.7 Conclusions

In the first part of this chapter, DEM and TFM simulations of 2D bubbling fluidized beds have been compared. For the base case, in which the coefficient of friction was set to 0.57, both simulation strategies yield time-averaged velocities with similar magnitudes, however the agreement of the characteristics of the velocity profiles is disappointing, especially for the case using zero friction for the particle-wall contact. The TFM predicts that the highest velocities within the bed are located at a distance of ~ 0.05 m away from the side wall, whereas the DEM predicts that the highest velocities are located at the centre of the bed. For both simulation techniques, the time-averaged solids volume fractions show minima that are coincident with the maxima in the velocity profiles. This is consistent with the hypothesis that bubbles preferentially pass through these locations.

The behaviour of bubbles has been examined by averaging the solids volume fraction over horizontal cross sections of the bed. Both the two-fluid and DEM simulations

predict a coherence bubble frequency of 6 Hz close to the distributor and a frequency close to 2.5 Hz near the surface of the bed.

Furthermore, the influence of the coefficients of friction and restitution on the simulation results has been investigated. The time averaged solids velocity and solids volume fraction profiles suggest that, within the range examined here, the behaviour of the bed, using TFM and DEM, is relatively insensitive to the particle-particle coefficient of friction and, for the DEM results, to the coefficient of restitution. However, setting the particle-wall coefficient of friction to zero was found to have a pronounced effect on the particle motion within the bed. Under these conditions both models were found to give time-averaged solids velocities an order of magnitude larger than those predicted for simulations with particle-wall friction.

The fact that the velocity of the TFM and the DEM simulations is very sensitive to the particle-wall friction coefficient indicates that the particle-wall BC is a key factor in the simulation. The disagreement encountered between the mean velocity distribution of the TFM and the DEM can be caused by the way the particle wall BC is implemented in the TFM. Thus, in the second part of the chapter a new boundary condition for the solid phase in pseudo-2D fluidized beds has been developed. This new BC was based on a partial-slip equation fitted to DEM simulation data. Several particle parameters were tested to study their effect on the parameters of the new partial-slip BC. The friction coefficient for particle-wall contacts was found to be the most important parameter. At low values of the solids volume fraction, the partial-slip coefficient was found to be negative and, thus, contrary to the Johnson and Jackson (1987) BC. The new BC was implemented in a TFM and was shown to give more favourable results for pseudo-2D beds than the classical Johnson and Jackson BC.

Nomenclature

A, B	coefficients (-) in Equation 5.9
D_b	bubble equivalent diameter (m)
e	coefficient of restitution (-)
$\vec{F}_c$	force resulting from the collision of the particles (N)
$\vec{F}_p$	rate of exchange of momentum between the solid and the fluid phases (kg/m^2)
I_p	moment of inertia of the particle (kg m^2)
m_p	mass of the particle (kg)
N_p	number of particle $(-)$
$\vec{T}_p$	torque resulting from the collision of the particles (N m)

U	superficial gas velocity (m/s)
U_{mf}	minimum fluidization velocity (m/s)
V_b	bubble velocity (m/s)
$\vec{v}_g$	gas velocity (m/s)
$\vec{v}_s$	solids velocity (m/s)
V_{cell}	volume of fluid cell (m^3)
V_p	particle volume (m^3)
V_x	solids horizontal velocity (m/s)
V_y	solids vertical velocity (m/s)
V_{wall}	solids velocity at the wall (m/s)

Greek letters

α_g	gas volume fraction ()
α_s	solids volume fraction ()
β	interphase momentum exchange coefficient ($-$)
$\vec{\omega}_s$	angular velocity of the particle (m/s)
ρ_s	solids density (kg/m^3)
$\overline{\overline{\tau_g}}$	viscous stress tensor (Pa)
ϕ	coefficient of friction (-)

Bibliography

Anderson, T.B., Jackson, R. A fluid mechanical description of fluidized beds. *Ind. Eng. Chem. Fund* 6 (1967) 527-539.

Baskakov, A.P., Tuponogov, V.G., Filippovski, N.F. A study of pressure fluctuations in a bubbling fluidized bed. *Powder Technol.* 45 (1986) 113-117.

Beetstra, R., van der Hoef, M.A., Kuipers, J.A.M. Drag Force of Intermediate Reynolds Number Flow Past Mono- and Bidisperse Arrays of Spheres. *AIChE J.* 53 (2007) 489-501.

Benyahia, S., Syamlal, M., O'Brien, T.J. Extension of Hill-Koch-Ladd drag correlation over all ranges of Reynolds number and solids volume fraction. *Powder Technol.* 162 (2006) 166-174.

Benyahia, S., Syamlal, M., O'Brien, T.J. Summary of MFIX equations 2005-4, 2007.

Cundall, P.A., Strack, C.D.L. A discrete numerical-model for granular assemblies. *Geotechnique* 29 (1979) 47-65.

Deen, N.G., van Sint Annaland, M., van der Hoef, M.A., Kuipers, J.A.M. Review of discrete particle modelling of fluidized beds *Chem. Eng. Sci.*, 62 (2007), pp. 28-44

Gidaspow, D. Multiphase flow and Fluidization: Continuum and kinetic theory descriptions; Academic Press: San Diego, CA. 1994.

Grace, J.R., Taghipour, F. Verification and validation of CFD models and dynamic similarity for fluidized beds. *Powder Technol.* 139 (2004) 99-110

Hernández-Jiménez, F., Sánchez-Delgado, S., Gómez-García, A., Acosta-Iborra, A. Comparison between two-fluid model simulations and particle image analysis & velocimetry (PIV) results for a two-dimensional gas-solid fluidized bed. *Chem. Eng. Sci.* 66 (2011) 3753-3772.

Johnson, P.C., Jackson, R. Frictional collisional constitutive relations for granular materials, with application to plane shearing. *J. of F. Mech.*, 176(1987), 6793.

Kunii, D., Levenspiel, O. Fluidization Engineering: Butterworth-Heinemann: Newton, MA, 1991.

Li, T., Benyahia, S. Revisiting Johnson and Jackson boundary condition for granular flows. *AIChE J.* 58 (2012) 2058-2068.

Li, T., Grace, J.R., Bi, X. Study of wall boundary condition in numerical simulations of bubbling fluidized beds. *Powder Technol.* 203 (2010) 447-457.

Müller, C.R., Holland, D.J., Sederman, A.J., Scott, S.A., Dennis, J.S., Gladden, L.F. Granular temperature: Comparison of Magnetic Resonance measurements with Discrete Element Model simulations. *Powder Technol.* 203 (2008) 241-253.

Schneiderbauer, S., Schellander, D., Löderer, A., Pirker, S. Non-steady state boundary conditions for collisional granular flows at flat frictional moving walls. *Int. J. Multiphase Flow* 43 (2012) 149-156.

Schneiderbauer, S., Aigner, A., Pirker, S. A comprehensive frictional-kinetic model for gasparticle flows: Analysis off fluidized and moving bed regimes. *Chem. Eng. Sci.* 80 (2012) 279-292.

Syamlal, M., Rogers, W., O'Brien, T.J. MFIX Documentation: Theory guide , U.S. department of Energy (DOE), Morgantown Energy Technology Center, Morgantown, West Virginia, 1993.

Tsuji, Y., Kawaguchi, T., Yanaka, T. Discrete particle simulations of 2-dimensional fluidized-beds. *Powder Technol.* 77 (1993) 79-87.

Van Wachem, B.G.M., Schouten, J.C., Krishna, R., van den Bleek, C.M. Eulerian simulations of bubbling behaviour in gas-solid fluidised beds. *Computers Chem. Eng.*, 22 (1998), pp. S299-S306

Chapter 6

Experimental quantification of the particle-wall frictional forces in pseudo-2D gas fluidized beds

Contents

6.1 Abstract

In this chapter a novel measurement technique for pseudo-2D fluidized beds is developed. The objective is to give an estimation of the overall frictional force between the solids and the front and rear walls of the bed. For doing this, the measured pressure signal in the bed is processed in combination with the solids distribution (i.e. centre of mass position, velocity and acceleration) obtained from digital image analysis of the optically accessible front view of the bed. This is performed by acquiring the pressure signal in the bed simultaneously to the digital images. Both the pressure and the digital images are connected through a simple force balance in the bed, and a particle-wall interaction coefficient is obtained assuming that the overall frictional force is proportional to the centre of mass velocity. The particle-wall interaction coefficient found using this technique is of the order of 40 to 120 kg/m^{2}s in the bed tested, and the standard deviation of the frictional forces reaches more than 70% of the weight of the bed. Therefore, the results indicate that the contribution of the particle-to-wall friction on the fluctuation of the pressure drop in a pseudo-2D bed is not negligible.

6.2 Introduction

Pseudo two−dimensional (2D) beds have been crucial for the understanding of the dynamics of gas−particle systems. In this regard, pseudo−2D fluidized bed systems typically have a transparent wall in order to allow optical access to the system, and possess a small thickness to ensure that the visualization is representative of the whole system. In this type of systems, Digital Image Analysis (DIA) or Particle Image Velocimetry (PIV) can be applied to characterize the bubble phase and the solids motion, respectively. Such studies have been proved to be a valuable tool for the understanding of fluidized bed systems, see for example Shen et al. (2004); Santana et al. (2005); Almendros-Ibáñez et al. (2006); Müller et al. (2007); Laverman et al. (2008); Busciglio et al. (2008); Sánchez-Delgado et al. (2010); Hernández-Jiménez et al. (2011a,b); Soria-Verdugo et al. (2011a,b); Sánchez-Delgado et al. (2013).

Alternatively, pressure signal analysis is widely used in the literature to characterize the dynamics of fluidized bed systems. Many works have been done in this field and nowadays the pressure signal is routinely employed to obtain a large amount of information concerning the dynamics of a fluidized bed, e.g. van Ommen et al. (2011).

Computational Fluid Dynamics (CFD) can be a very effective complementary tool to the experiments for achieving a detailed analysis of hydrodynamics in complex gas-solids flows. Note that, in these pseudo-2D beds, the front and the rear walls restrict

the solids motion, leading to a different flow behaviour compared to fully three− dimensional (3D) systems. Pseudo−2D, the effects of the front and the rear wall on the particle motion can be significant and should not be neglected in numerical simulations of pseudo−2D beds (Li et al., 2010; Hernández-Jiménez et al., 2011a). However, there is a lack of experimental quantification of the wall frictional forces in pseudo−2D beds. Knowledge of the wall frictional forces in real thin beds can be useful in the understanding of fluidized beds and will facilitate the development of particle− wall interaction models and the validation of the different simulation approaches, such as two−fluid models.

The gas pressure in the bed can be inferred from the solids distribution since these two parameters are inextricably linked to each other in bubbling fluidization (Davidson and Harrison, 1963; Baskakov et al., 1986; van Ommen et al., 2011). This was verified by Croxford and Gilbertson (2011), who estimated the spatial distribution of the pressure in a pseudo 2D bubbling bed by numerically solving the Davidson and Harrison (1963) quasi-steady potential flow equations of the gas phase. They used, as an input for the equations, the bubbles size and location experimentally measured with a digital camera. Their simulation successfully reproduced the pressure field when the bubbles over a wide region of the bed were considered.

The previous chapters of this PhD report have presented results of 2D and 3D two−fluid models simulations of fluidized beds, showing that in this type of modelling the effects of the front and rear walls are not negligible. Also, in the previous chapter, a set of DEM simulations was used to improve the existing wall boundary conditions for the solids velocity in pseudo-2D beds. It was shown that the solids velocity boundary condition was linked to the particle-wall frictional forces.

In the present chapter an experimental procedure is employed to estimate the particle-wall frictional forces and complete the vision of the effects of walls in pseudo-2D beds. For doing this, as a novelty, a new methodology is proposed for coupling the pressure signal analysis with the digital image acquisition of a real fluidized pseudo−2D bed in order to give an estimation of the frictional forces exerted by the front and rear walls on the bed particles. Using a force balance, the frictional force between the bed and the walls is estimated here as a function of the instantaneous pressure drop in the bed, the bed weight, and the velocity and acceleration of the centre of mass of the bed. Additionally, results from a 2D simulation, i.e. without incorporating the front and rear walls, have been included to show that in the absence of the front and rear walls the pressure and the acceleration of the centre of mass of the bed are perfectly correlated.

6.3 Experimental setup

The experimental facility employed in this work is a pseudo-2D cold fluidized bed of dimensions 0.3 m x 1 m x 0.01 m (width W, height H, and thickness Z). The bed was filled with ballotini glass particles of 2500 kg/m^3 density. The experiments were carried out for three different particle sizes: Geldart's classification type B of 0.4−0.6 mm diameter, type B−D particles of 0.6−0.8 mm diameter, and type D particles of 1−1.3 mm diameter. The air distributor consists of a perforated plate with two rows of 30 holes of 1 mm diameter arranged in a triangular configuration with 1 cm pitch. The front and rear walls of the bed were made of glass and the rear wall was painted in black to increase contrast in the front images. A sum up of the experimental parameters is included in Table 6.1.

Two pressure probes were used during the measurements. One of the probes was placed in the plenum chamber and the other in the bed axis at 5 cm above the distributor plate. The pressure fluctuations in the plenum chamber were measured with a LUCAS (SN924-063Y) differential pressure transducer and the pressure fluctuations in the bed were measured with an ELLISON (PR 3110) differential pressure transducer. Both transducers were connected to the probes by means of a silicon tube with a total length of 50 cm and an internal diameter of 4 mm. According to van Ommen et al. (2004) pressure waves in a bubbling bed at $2U_{mf}$ can be detected at radial distances up to 0.3 m from their origin. Also, Croxford et al. (2005) reported that for a small-scale fluidized bed one probe is sufficient, in principle, to characterize the bed hydrodynamics. Therefore, only the pressure probe at 5 cm above the distributor will be used in the bed studied here. In addition, two spotlights were used to get a uniform illumination of the front of the bed. A digital camera, Basler A640, took images of the front view of the fluidized bed at 100 frames per second and, simultaneously, the pressure transducers recorded the pressure signals at 2000 Hz. Figure 6.1 shows a scheme of the facility and an example of a greyscale image acquired with the digital camera.

The measurement error committed in the experimental setup is related to the devices employed. Regarding the pressure transducers, the measurement error is 1% of the full span, which is 3.5 mbar for the LUCAS transducer (range 0-350 mbar) and 2 mbar for the ELLISON transducer (range 0-200 mbar). In the digital images acquired, the error in the discrimination of the bubble and dense phases is directly related to the spatial resolution of the image, i.e. the size of a pixel, which is 1 mm.

Table 6.1: Experimental setup.

Parameter		Value
Bed height, H (m)		1
Bed width, W (m)		0.3
Bed thickness, Z (m)		0.01
Aspect ratio, h_0/W $(-)$		0.75, 1, 1.25
Particles density, ρ_s (kg/m^3)		2500
Small particles	d_p (mm)	0.4−0.6
	U_{mf} (m/s)	0.27
Medium particles	d_p (mm)	0.6−0.8
	U_{mf} (m/s)	0.44
Big particles	d_p (mm)	1−1.3
	U_{mf} (m/s)	0.67

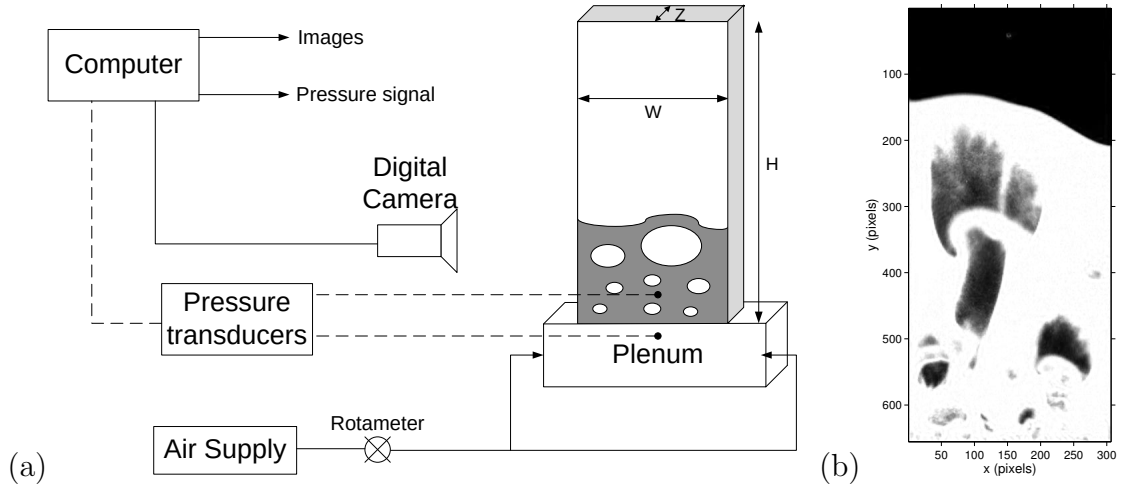

Figure 6.1: a) Sketch of the experimental facility and b) example of a front view image of the fluidized bed.

6.4 Theory

A simple balance of vertical forces in a control volume comprising the gas and particles in a fluidized bed is shown in Figure 6.2. The balance indicates that the force exerted by the pressure drop in the bed, ΔP, just over the area $A_T = WZ$ of the distributor, i.e. $F_{\Delta P} = A_T \Delta P$, must compensate the inertia force due to the acceleration of the centre of mass of the bed, F_a, plus the force due to the weight of the bed, F_g, (i.e. hydrostatic pressure) and the frictional force of the bed walls on the gas and solids phases, F_{fric}:

$$F_{\Delta P} = F_a + F_g + F_{fric} = m\frac{d^2 y_{cm}}{dt^2} + mg + F_{fric} \tag{6.1}$$

where $m = A_T(1-\epsilon_0)\rho_s h_0$ is the mass of the bed particles, y_{cm} is the vertical position of the centre of mass of the bed, and d^2y_{cm}/dt^2 is the acceleration of the centre of mass.

In Equation 6.1 the inertia and weight of the gas have been neglected since the gas density is much smaller than the particle density. Also, the contribution of the gas phase to the frictional force F_{fric} is expected to be very reduced compared to the frictional force between particles and wall. Note that $F_{\Delta P}$ is equivalent to the force produced by the gas on all the bed particles.

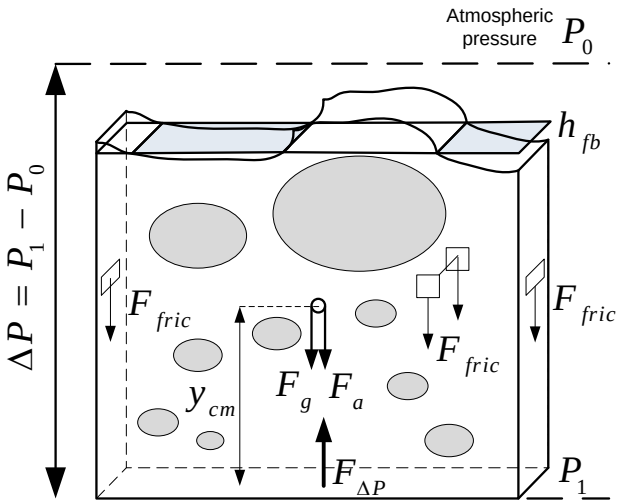

Figure 6.2: Balance of forces acting on the bed material. Arrows indicate the direction of the forces when their value is positive in Equation 6.1.

In general, the frictional force is equal to the shear stress, τ, times the surface area of the lateral walls in contact with the bed, $A_L = (2W + 2Z)h_{fb} \approx 2Wh_{fb}$, where h_{fb} is the time−averaged height of the fluidized bed. Following the classical Coulomb's friction model, it will be assumed that the force due to the shear stress is proportional to the normal force times the Coulomb coefficient of friction, $F_{fric} \sim \mu F_N$.

According to the kinetic theory of granular flows, the normal force is a function of the granular temperature of the particles, $F_N \sim f(\Theta)$, and the granular temperature is proportional to the gradient of the particle velocity in perpendicular to the wall $\partial v/\partial n$, (Johnson and Jackson, 1987). The velocity gradient depends on the bed dynamics of the particles in the bed.

In the present work, it is postulated that, as a first approximation, the velocity gradient is proportional to the local value of either the velocity of the particles, the acceleration of the particles, the kinetic energy of the particles near the wall, or a cosntant independent of the particle movement. Integrating τ all over the area of the bed walls A_L:

$$F_{fric} = \int_{A_L} \tau dA \approx cA_L\Omega \tag{6.2}$$

where the frictional form, Ω, can be the instantaneous velocity, dy_{cm}/dt, the acceleration, $|d^2y_{cm}/dt^2|\xi$, or the squared velocity, $(dy_{cm}/dt)^2\xi$, of the centre of mass of the bed. Frictional forces oppose the direction of the centre of mass velocity, which is mathematically expressed in Ω with $\xi = \text{sign}(dy_{cm}/dy)$. If the frictional force is considered constant (i.e. independent of the bed dynamics), then $\Omega = \xi$. In Equation 6.2, c is a proportionality constant that can be interpreted as a new particle-wall interaction coefficient that multiplies $A_L\Omega$ instead of F_N.

The whole balance of forces in Equation 6.1 can be divided by the transversal area A_T of the bed in order to work with pressures instead of forces:

$$\begin{gathered}\Delta P = \Delta P_a + \Delta P_g + \Delta P_{fric} = \\ (1-\epsilon_0)\rho_s h_0 \left(\frac{d^2y_{cm}}{dt^2} + g\right) + c\frac{A_L}{A_T}\Omega\end{gathered} \tag{6.3}$$

Note that the term $(1-\epsilon_0)\rho_s h_0 g$ in Equation 6.3 corresponds to the mass of solids in the bed. This term is kept constant in the calculations.

6.5 Data processing

6.5.1 Initial processing

Pressure signals and front−view digital images of the pseudo−2D bed were acquired simultaneously, at 2000 Hz and 100 Hz respectively, during $T = 300$ seconds using the software LabView®. The pressure signals were resampled to 100 Hz to make its temporal resolution equal to the digital images. All the processing described in this section was programmed using the software MATLAB®.

The procedure employed to measure the pressure drop in the bed, ΔP_{meas}, is to use the pressure acquired at $y_P = 5$ cm over the distributor, ΔP_P, and scale it using the averaged weight of the column of particles within this measurement point and the distributor.

$$\Delta P_{meas} \approx \Delta P_P + \rho_s(1-\epsilon_{mf})gy_P \tag{6.4}$$

In Equation 6.4 ϵ_{mf} is employed because the number of bubbles close to the distributor is very reduced and, according to the two fluid theory, the void fraction in the dense phase takes the value for the minimum fluidization conditions.

Owing to the relatively large pressure drop caused by the distributor orifices, the fluctuations of the pressure in the plenum are soften. It is not trivial how to correct this pressure signal in the plenum to calculate ΔP_{meas}, and the attempts performed to connect the plenum pressure were unsuccessful.

DIA was applied to the acquired images of the bed in order to distinguish between bubbles and dense phase. This allowed for the calculation of the vertical position of the centre of mass of the bed, y_{cm}, at each time instant. The centre of mass is calculated with the grey scale images recorded by the camera using the grey level of each pixel. In the bubbles $\alpha_s = 0$, and the grey level pixels of the image is minimum (≈ 0). Also, in the emulsion phase $\alpha_s \approx \alpha_{mf}$ and the grey level of the pixels is close to the maximum (≈ 255). Following Almendros-Ibáñez et al. (2010), a linear relationship between grey levels and solids volume fraction is assumed. Therefore:

$$y_{cm} = \frac{\int \alpha_s y dA}{\int \alpha_s dA} \approx \frac{\sum_{i=1}^{N} y_i GL_i}{\sum_{i=1}^{N} GL_i} \tag{6.5}$$

where y is the vertical distance relative to the distributor, i is the pixel number, N is the total number of pixels in the image and GL is the grey level of each pixel in the images.

6.5.2 Estimation of the particle-wall interaction coefficient

The force balance presented previously can be employed to make an estimation of the particle-wall interaction coefficient c. Two methods are proposed here depending on the way Equation 6.3 is processed.

Derivation method

The result of applying Equation 6.5 at each time instant is a discrete time series of y_{cm} that is numerically differentiated, using second order finite differences, to obtain the time series of the centre of mass velocity, dy_{cm}/dt, and acceleration, d^2y_{cm}/dt^2.

The particle-wall interaction coefficient is obtained by comparing the time evolution of the pressure drop in the bed, ΔP_{meas} (Equation 6.4), with the right hand side of Equation 6.3 representing the pressure drop calculated only with the vertical position of the centre of mass of the bed, y_{cm}, in Equation 6.5. Therefore, the most probable value of c is estimated by performing the following least square minimization over the total time period of measurement (T):

$$\min_{c} \left[\int_0^T \left(\Delta P_{meas} - \Delta P_{calculated} \right)^2 dt \right] \tag{6.6}$$

where $\Delta P_{calculated}$ is expressed according to Equation 6.3 as a function of y_{cm} and Ω.

$$\Delta P_{calculated} = (1-\epsilon_0)\rho_s h_0 \left[\frac{d^2 y_{cm}}{dt^2} + g\right] + c\frac{A_L}{A_T}\Omega \tag{6.7}$$

The algorithm used to calculate c is described in Figure 6.3. The calculus starts with an estimation of c that is used to obtain the pressure drop calculated, $\Delta P_{calculated}$ (Equation 6.7). Despite the images and the pressure were acquired simultaneously, their synchronization is not initially perfect because of a hardware delay produced by differences in the response time of activation of the pressure and the digital image measurement systems. This hardware delay, $t_d = d\Delta t$, is estimated with the maximum of the cross−correlation of the two signals, ΔP_{meas} and $\Delta P_{calculated}$. The delay, lower than 10 time points, may be different every time the systems are activated so it has to be calculated for each measurement data set. After adjusting the delay between the two signals, the particle-wall interaction coefficient, c, is obtained from Equation 6.6, whose integral is computed using a summation extended over all the signal terms.

$$\min_c \left[\sum_{i=1}^{N-d} \left(\Delta P_{meas,i} - \Delta P_{calculated,i}\right)^2 \Delta t\right] \tag{6.8}$$

The whole procedure is repeated starting with the obtained value for c until convergence, which requires over 10 iterations.

Integration method

The algorithm presented in the previous section resorted to the force balance in its differential form, Equation 6.3. However this form can be affected by the measurement noise amplified during the differentiation of y_{cm}. To solve this problem, the force balance can be introduced in the algorithm in an integrated form. Integration is an operation less sensitive to noise than differentiation. In such form, instead of derive twice y_{cm} to obtain the centre of mass acceleration, Equation 6.3 has to be integrated twice.

$$\int_{t=0}^{T}\int_{t'=0}^{t} \Delta P dt' dt = (1-\epsilon_0)\rho_s h_0 \left(y_{cm} + g\frac{T^2}{2}\right) + c\frac{A_L}{A_T}\int_{t=0}^{T}\int_{t'=0}^{t} \Omega dt' dt \tag{6.9}$$

The algorithm used in the integration method to determine the particle-wall interaction coefficient c is similar than the one proposed for the derivation method excepting that Equation 6.9 is used instead of Equation 6.8. The complete algorithm for the integral form is described in Figure 6.4.

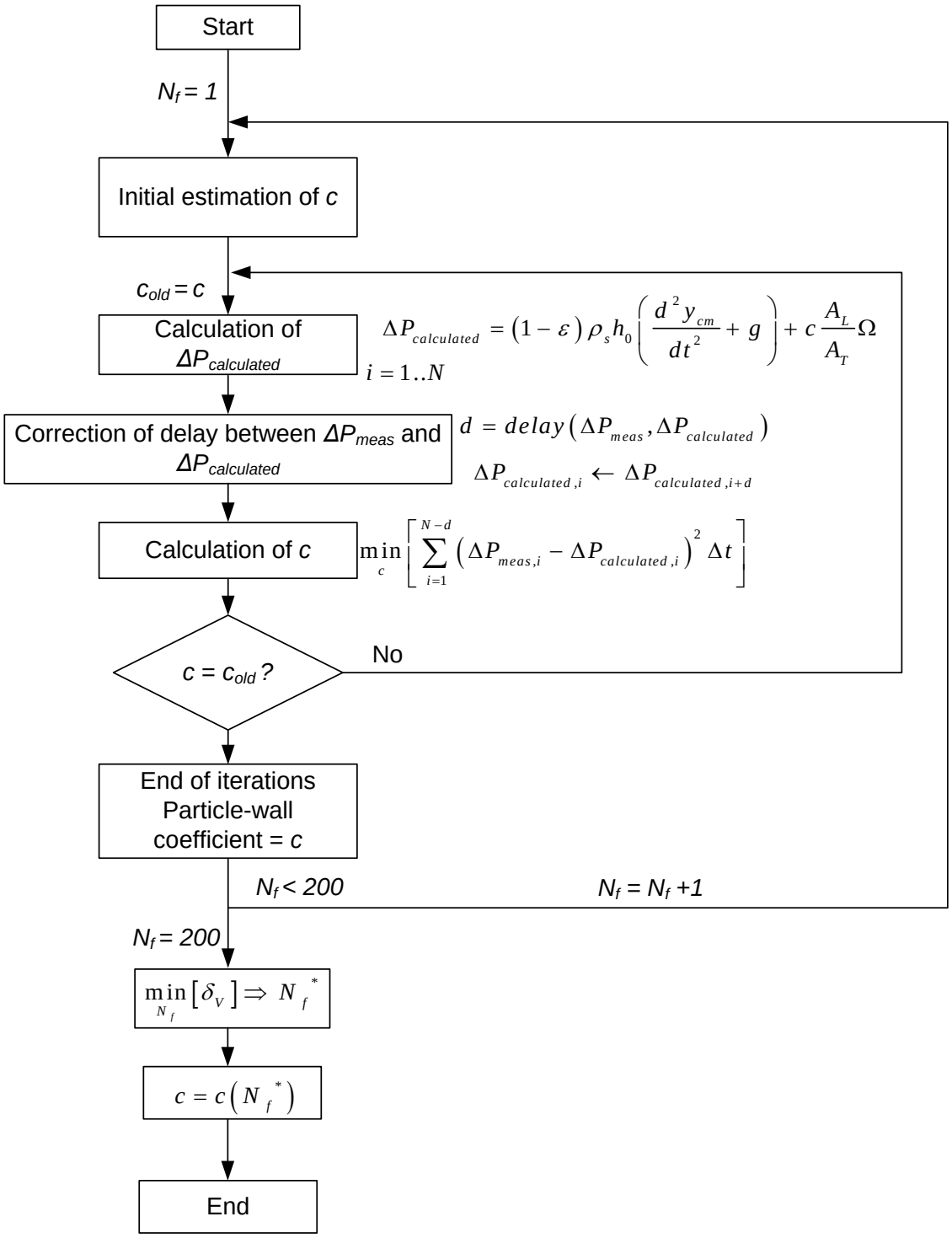

Figure 6.3: Iterative loop for the calculation of the particle-wall interaction coefficient, c, as a function of N_f. Derivation method.

Besides, a moving average filter was applied to y_{cm} in order to reduce the spurious high frequencies created by the measurement noise that can be amplified during the differentiation of y_{cm}. Also spurious low frequencies can be amplified during the

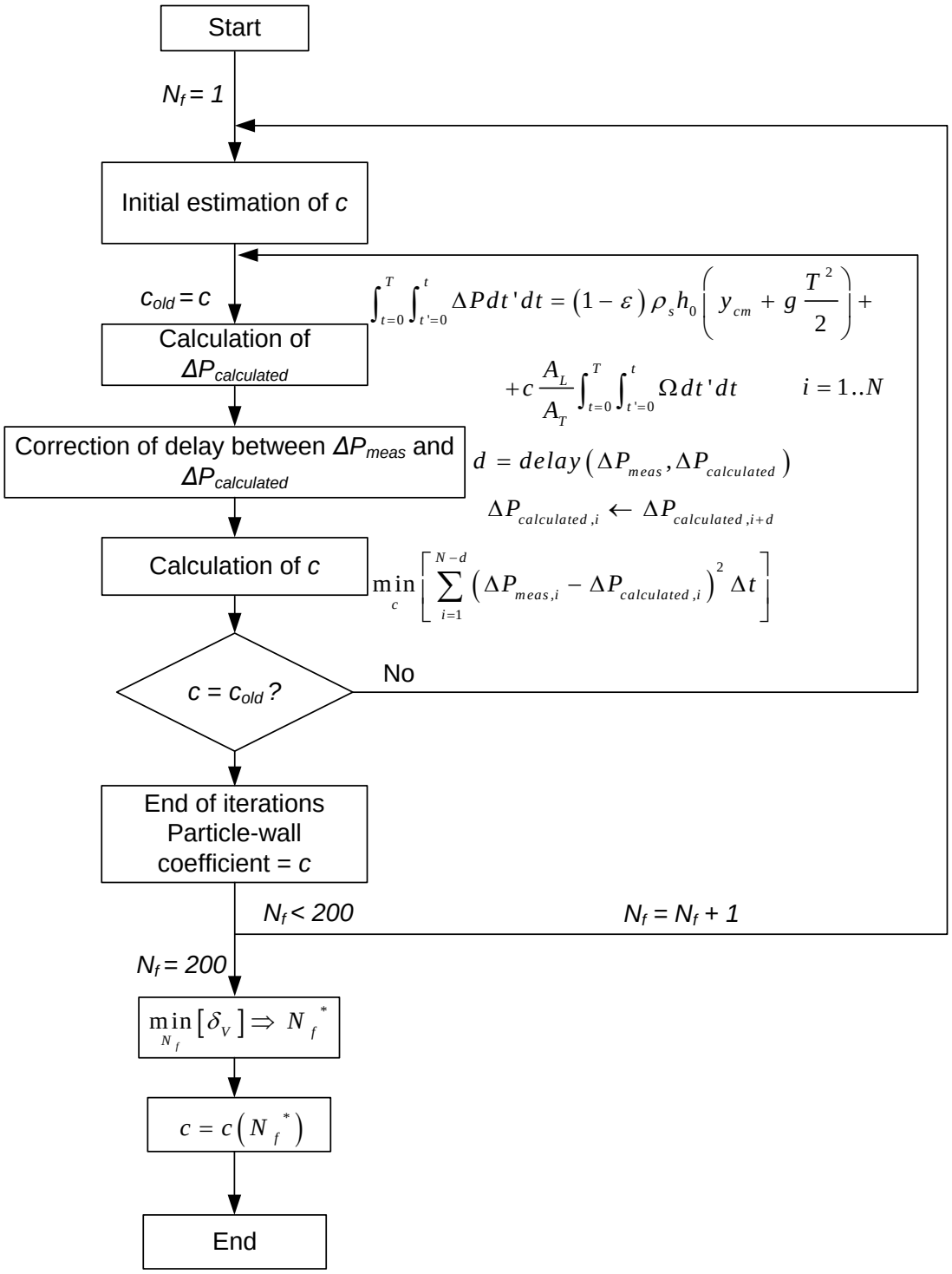

Figure 6.4: Iterative loop for the calculation of the particle-wall interaction coefficient, c, as a function of N_f. Integration method.

integration of the signals. These low frequencies are eliminated here by filtering the integrated signal with a wide span (i.e. N_f large) moving average filter and subtracting this filtered integrated signal to the unfiltered one. As the moving average smooths

the signals, it must be applied not only to y_{cm} but also to ΔP_{meas} on each calculation. However, the resulting coefficient c is sensitive to the number of points chosen for the moving average filter, N_f. Alternative filtering strategies were studied (e.g. Butterworth filtering, etc.) and the results were still sensitive to other parameters present in the filters. To solve this issue, c is estimated here for a value of N_f not larger than 200 that minimizes the error between the signal measured and the signal calculated, $\Delta P_{calculated,i}$.

6.5.3 Discrepancy factors

The functional form of the friction force, Ω in Equation 6.2, will be chosen on the basis of a discrepancy factor, δ, that accounts for the differences between the pressure measured, ΔP_{meas}, and the pressure calculated, $\Delta P_{calculated}$. Figure 6.5 shows an illustration of the pressure measured and calculated, and the distance between a point on one signal and the other signal. Depending on the way the distance is calculated, two ways of defining the discrepancy factor arise. The vertical discrepancy, δ_V, is a function of d_V which considers only the vertical distance between both signals. The total discrepancy, δ_T, is function of d_T which considers the minimum distance between both signals through any possible direction (see Figure 6.5).

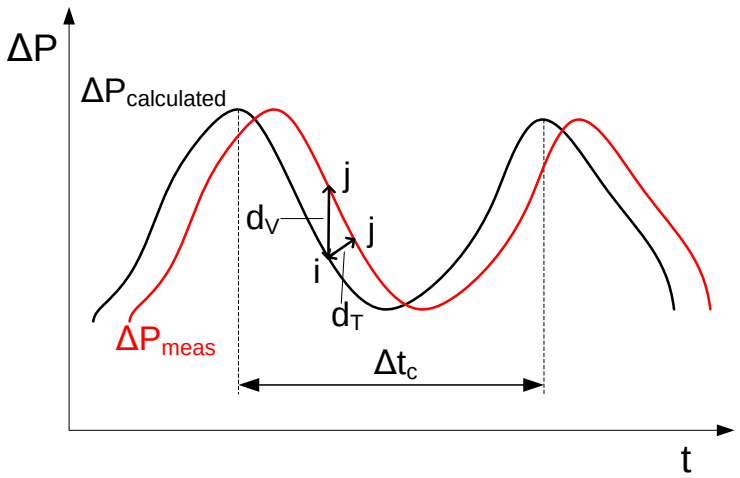

Figure 6.5: Illustration of the discrepancy factor calculation.

$$\delta_V = \sqrt{\frac{1}{N-d}\sum_{i=1}^{N-d}\frac{d_{V,i}^2}{\sigma_{\Delta P_{meas}}^2}} \tag{6.10}$$

$$\delta_T = \sqrt{\frac{1}{N-d}\sum_{i=1}^{N-d}\frac{d_{T,i}^2}{\sigma_{\delta P_{meas}}^2}} \tag{6.11}$$

where $\sigma_{\Delta P_{meas}}$ is the standard deviation of ΔP_{meas} and d_V and d_T have been calculated as follows:

$$d_{V,i} = \Delta P_{meas,i} - \Delta P_{calculated,i}$$

$$d_{T,i}^2 = \min_j d_{i,j}^2$$

$$d_{i,j}^2 = (\Delta P_{meas,i} - \Delta P_{calculated,j})^2 + \left(\frac{\sigma_{\Delta P_{meas}}}{\Delta t_c}\right)^2 ((i-j)/f)^2$$

$$\Delta t_c \approx \frac{1}{f_0} = \frac{\pi}{\sqrt{g/h_0}}$$

where f is the acquisition frequency, 100 Hz, f_0 is the characteristic frequency of the bed oscillation as determined by Baskakov (Baskakov et al., 1986), and i, j are data points for ΔP_{meas} and $\Delta P_{calculated}$, respectively, (see Figure 6.5).

As mentioned previously, δ_T has two contributions: the vertical and the horizontal discrepancies. The quadratic vertical contribution of the discrepancy is given in Equation 6.11 in relative form by dividing it with the square of a characteristic value that ranges the pressure oscillations (i.e. the square of the standard deviation of the pressure oscillations $\sigma_{\Delta P}^2$). The quadratic horizontal contribution of the discrepancy is normalized with the square of period of the oscillation, Δt_c^2, which is the characteristic value that ranges an oscillation along the horizontal axis (i.e. the time). Since Equation 6.11 has only $\sigma_{\Delta P}^2$ in the denominator, the scaling factor $(\sigma_{\Delta P}/\Delta t_c)^2$ is multiplying the quadratic horizontal contribution instead of $(1/\Delta t_c)^2$.

Also, it has to be noticed that the estimation of c (Equation 6.8) considers only the vertical displacements, δ_V, otherwise the comparison between ΔP_{meas} and $\Delta P_{calculated}$ in Equation 6.8 would be insensitive to the delay between both signals and could not be correctly calculated in the iterative algorithm described in Figure 6.3.

6.6 Results

6.6.1 Dependence of the frictional forces

The first part of the results focuses on the dependence form of the frictional forces. The aim of this section is to find the best choice for Ω in Equation 6.2. Recall that the functional form Ω considered are the velocity of the centre of mass, dy_{cm}/dt, the square of the velocity of the centre of mass, $(dy_{cm}/dt)^2\xi$, the acceleration of the centre of mass, $|d^2y_{cm}/dt^2|\xi$, or the unity, ξ, if the frictional forces are considered to be constant.

Figure 6.6 shows the discrepancy factors, δ_V and δ_T, versus the number of points used in the moving average filter, N_f, for the derivation and integration method and for the different choices of the functional form, Ω. Only one configuration of the experiments was represented but analogous results were found for the rest of configurations.

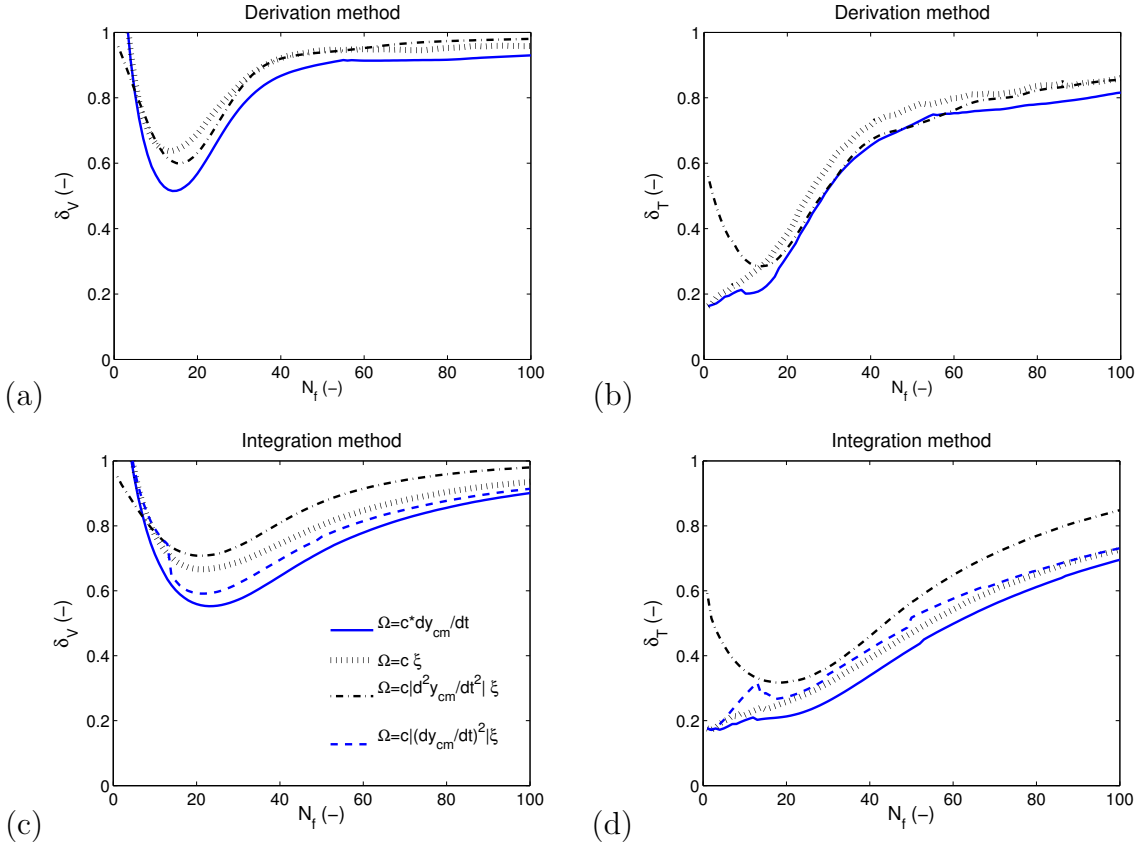

Figure 6.6: Discrepancy factor, δ, versus N_f for the different forms of Ω, a) Derivation method, δ_V, b) Derivation method, δ_T, c) Integration method, δ_V and d) Integration method, δ_T. Experimental data for $U/U_{mf} = 2.5$, $h_0/W = 1$ and $d_p = 0.4 - 0.6$ mm.

Figures 6.6a and 6.6b do not include the results for the functional form $\Omega = (dy_{cm}/dt)^2\xi$ because the algorithm used did not converge for the derivation method using this functional form.

According to Figure 6.6, values of δ_V in the range 50-100% are obtained depending on the functional form, Ω, and the method selected. It may seem that the signals ΔP_{meas} and $\Delta P_{calculated}$ are very different since the values found for δ_V are large. However, a small relative displacement of the curves along the horizontal axis (i.e time in Figure 6.5) can substantially increase δ_V even if these signals are identical. To avoid this problem, a better quantification of the discrepancy is the total discrepancy, δ_T, defined in Equation 6.11, which takes into account the local difference of the signals in both axes of Figure 6.5. Using δ_T, the observed discrepancy between ΔP_{meas} and $\Delta P_{calculated}$ is reduced to the range 20-85%.

From Figure 6.6 it can be seen that the best functional form of the friction forces is considering that Ω is proportional to dy_{cm}/dt, since this leads to the smallest discrepancy factor, δ_V and δ_T, in both the derivation and integration methods. Therefore, the force balance that will be considered hereafter is:

$$\Delta P = (1-\epsilon_0)\rho_s h_0 \left(\frac{d^2 y_{cm}}{dt^2} + g \right) + c \frac{A_L}{A_T} \frac{dy_{cm}}{dt} \tag{6.12}$$

It is important to note that the fact that the best functional form Ω resulted proportional to the velocity can be seen as an indicative of the fluid like character of the emulsion phase. In a real fluid, the frictional pressure drop when the fluid is moving through a channel is given by:

$$\Delta P_{fric} = \frac{1}{2} v^2 \rho_s \frac{L}{D_n} f \tag{6.13}$$

where f is the friction coefficient. In laminar flows and beginning of turbulence (i.e. not very high velocities or very viscous flows), f is inversely proportional to the Reynolds number, therefore, $f \sim a/v$. Thus:

$$\Delta P_{fric} \sim \frac{1}{2} v^2 \rho_s \frac{L}{D_n} \frac{a}{v} \sim bv \tag{6.14}$$

where a and b are constants.

Equation 6.14 indicates that the frictional pressure drop in a fluid is proportional to the velocity, an outcome that is found in Figure 6.6 for the solids phase in the bubbling bed.

6.6.2 Simulation evidence

This part shows the results obtained from 2D and 3D two−fluid model simulations of the fluidized bed employed in the experiments. The simulation results are used to check the consistency of the force balance and the algorithms proposed in section 4. In

the simulation, the two−fluid model equations based on the conservation of mass and momentum, together with the balance of granular temperature, were solved using the MFIX code (Multifluid Flow with Interphase eXchanges). The governing equations as well as the closure models of the two-fluid model can be found in Appendix A.

A second order accurate scheme was selected to discretize the convective derivatives of the governing equations, and the computational domain was meshed using square cells of length 5 mm for the 2D simulation. The distributor was modelled as a uniform velocity inlet and a fixed pressure boundary condition was chosen at the top of the freeboard. The particle−wall interaction on the lateral walls of the bed was modelled as partial−slip boundary condition, with specularity coefficient equal to 0.6, using the Johnson and Jackson boundary condition for solids (Johnson and Jackson, 1987). The drag model employed for the particle−air interactions was the one proposed by Gidaspow (Gidaspow, 1994). Details about the drag force can be found in Appendix A.

The simulation considered particles of 0.5 mm diameter, which corresponds to the average diameter of the particles within the range 0.4−0.6 mm tested in the experiments (Table 6.1). The superficial gas velocity was $2U_{mf}$. It has to be noted that the front and rear walls are not presented in the simulation since the numerical domain is 2D, which is equivalent to having front and rear walls with null friction.

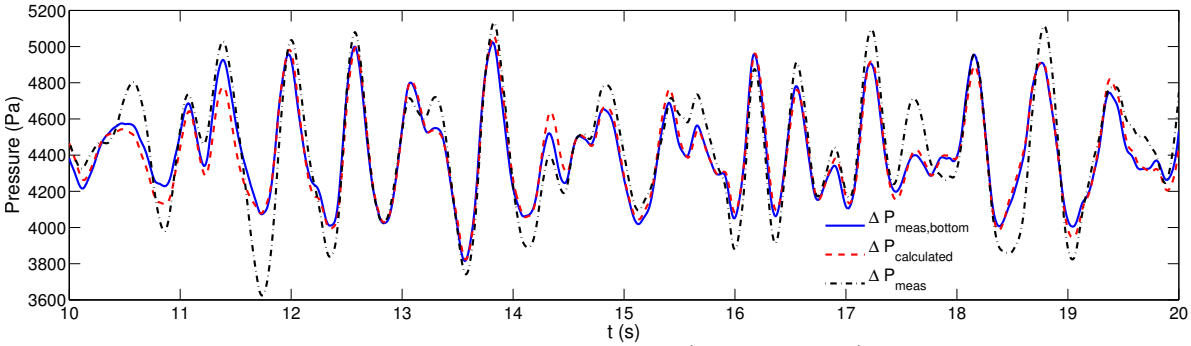

Figure 6.7: Pressure signals at the bottom of the bed ($\Delta P_{meas,bottom}$) and extrapolated from 5 cm above the distributor (ΔP_{meas}), and pressure calculated using the centre of mass of the bed ($\Delta P_{calculated}$). Simulation 2D results for $U/U_{mf} = 2.0$, $h_0/W = 1$, $d_p = 0.5$ mm.

Figure 6.7 shows the simulation results concerning i) the instantaneous pressure of the gas, spatially−averaged along the width W, at the bottom of the bed ($\Delta P_{meas,bottom}$), ii) the pressure calculated ($\Delta P_{calculated}$), and iii) the pressure measured by a virtual probe at 5 cm above the distributor and extrapolated to the bottom of the bed as explained in section 6.5.1 (ΔP_{meas}). $\Delta P_{calculated}$ is obtained using the same procedure as for the digital images, but using the solids volume fraction instead of the grey level of the image. It can be clearly seen that both signals, ΔP_{meas} and $\Delta P_{calculated}$, are very

well correlated. The particle-wall interaction coefficient estimated is negligible due to absence of the front and rear walls and the fact that c is referred per unit area A_L. The little differences between the pressure curves in Figure 6.7 can be attributed to the moving average filter employed to soft the acceleration signal and the small friction produced by the lateral walls of the simulated bed.

In a experiment $\Delta P_{meas,bottom}$ is quite difficult to measure due to the local variation of pressure created by the jet effect of the orifices of the distributor. However, as the simulation shows in Figure 6.7 the pressure extrapolated from a point at 5 cm above the distributor, ΔP_{meas}, also represents fairly well the fluctuations of the pressure at the bottom and can be used as a substitute of $\Delta P_{meas,bottom}$. Discrepancies between $\Delta P_{meas,bottom}$ and ΔP_{meas} are due to the pressure perturbation produced by the passing of small bubbles through the sampling point. Note also that in the simulation results the correction of the delay of the signals is not needed since they are perfectly synchronized, and the position of the centre of mass is calculated from the instantaneous snapshots of the void fraction, α_s, instead of the gray level (Equation 6.7).

Therefore, on view of the similitude between ΔP_{meas} and $\Delta P_{calculated}$, the simulation indicates that the force exerted by the pressure drop in the bed is directly linked with the force due to the acceleration of the mass centre of a pure 2D bed (i.e. null front and rear wall friction forces). The simulations also shows that the use of the local pressure measured at 5 cm is a good alternative for estimating the pressure drop in the bed.

Besides, two 3D simulations of the pseudo-2D bed were performed to check the effects of the front and rear walls on the simulations. These 3D simulations consider particles of 0.7 mm (average diameter of the particle within the range $0.6 - 0.8$ mm tested in the experiments, Table 6.1), with a superficial gas velocity of $2.5U_{mf}$, aspect ratio unity and the thickness of the bed $Z = 1$ cm. The particle size and superficial gas velocity of the 3D simulation were intentionally selected different to the 2D simulation to demonstrate that equivalent results are obtained. The 3D domain was discretized with the same cell size as the 2D simulation, but considering 4 nodes in the transversal direction. In one of the 3D simulations, a free-slip boundary condition for the solid phase is employed at the four walls, Figure 6.8. In the other 3D simulation, the same wall boundary condition for the solids phase as in the 2D simulation is chosen for the four walls, that is, the standard partial-slip boundary condition, Figure 6.9.

Figures 6.8 and 6.9 show the pressure extrapolated from a point at 5 cm above the distributor (ΔP_{meas}), the pressure calculated without considering the frictional forces ($\Delta P_a + \Delta P_g$), and considering them ($\Delta P_{calculated}$). In particular, in the 3D simulation with null friction at the walls (i.e., free-slip boundary condition), $\Delta P_a + \Delta P_g$ is similar to $\Delta P_{calculated}$ and both signals are practically equal to ΔP_{meas} (Figure 6.8).

From Figure 6.9 it can be seen the effects of the front and rear walls. What Figure 6.9 shows is that the pressure calculated without considering the frictional forces, $\Delta P_a + \Delta P_g$, cannot reproduce the extrapolated pressure, ΔP_{meas}, when there is wall friction (e.g. partial-slip boundary condition for the solid phase). Also, this prediction is clearly improved when the frictional forces are considered, $\Delta P_{calculated}$. This indicates that the wall frictional forces are the cause of the different behaviour of $\Delta P_a + \Delta P_g$ and ΔP_{meas}.

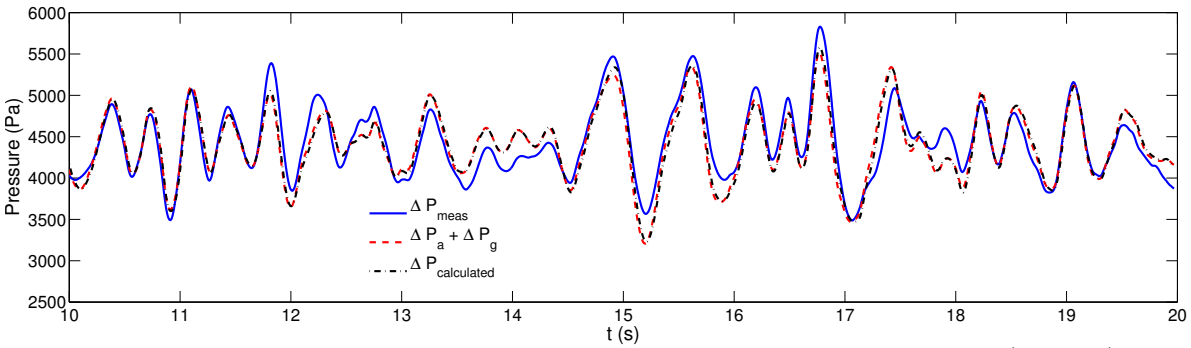

Figure 6.8: Pressure signal extrapolated from a point at 5 cm above the distributor (ΔP_{meas}), calculated without considering the frictional forces ($\Delta P_a + \Delta P_g$), and considering them ($\Delta P_{calculated}$). Simulation 3D results for $U/U_{mf} = 2.5$, $h_0/W = 1$, $d_p = 0.7$ mm. Free-slip boundary condition.

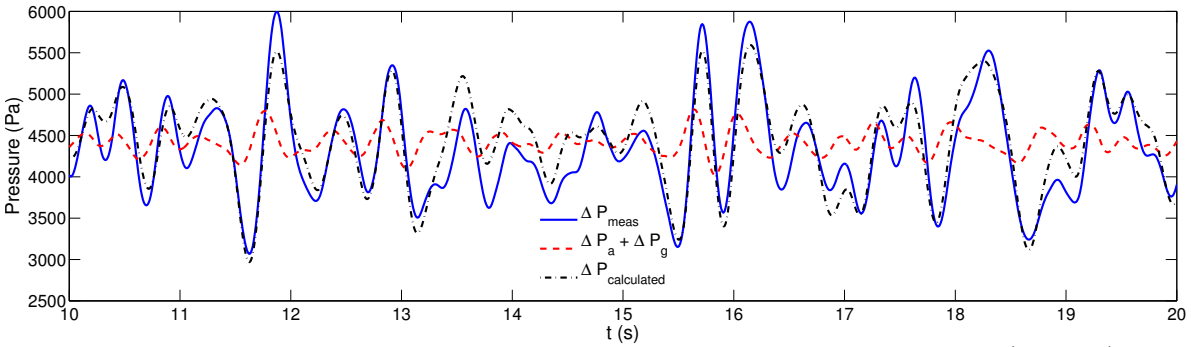

Figure 6.9: Pressure signal extrapolated from a point at 5 cm above the distributor (ΔP_{meas}), calculated without considering the frictional forces ($\Delta P_a + \Delta P_g$), and considering them ($\Delta P_{calculated}$). Simulation 3D results for $U/U_{mf} = 2.5$, $h_0/W = 1$, $d_p = 0.7$ mm. Partial-slip boundary condition.

In summary, it is demonstrated in this section, by means of 2D and 3D simulations, that the front and rear walls in a pseudo-2D bed tend to reduce the amplitude of the pressure fluctuations, and this reduction is attributed to the particle-wall frictional forces.

6.6.3 Experimental quantification of the particle-wall interaction coefficient

Turning now to the experimental results, Figure 6.10 shows, as an illustrative example, the time evolution of the pressure drop measured in the experimental pseudo−2D bed at 5 cm above the distributor (extrapolated using Equation 6.4), ΔP_{meas}, and the pressure drop calculated with DIA, without considering the frictional forces, $\Delta P_a + \Delta P_g$, and considering it, $\Delta P_{calculated}$. For $\Delta P_{calculated}$ the particle-wall interaction coefficient, c, is estimated with the algorithm proposed in Figure 6.3 based on the derivation method, c_D. Clearly, the calculation of the pressure drop in the bed with DIA is able to reproduce reasonably well most of the oscillations experienced by the pressure measured in the experiment. Also, the estimation of the pressure measured is clearly improved if the frictional forces are considered. Very similar results were found for the integrated pressure using the integration method, and for the other operating conditions studied.

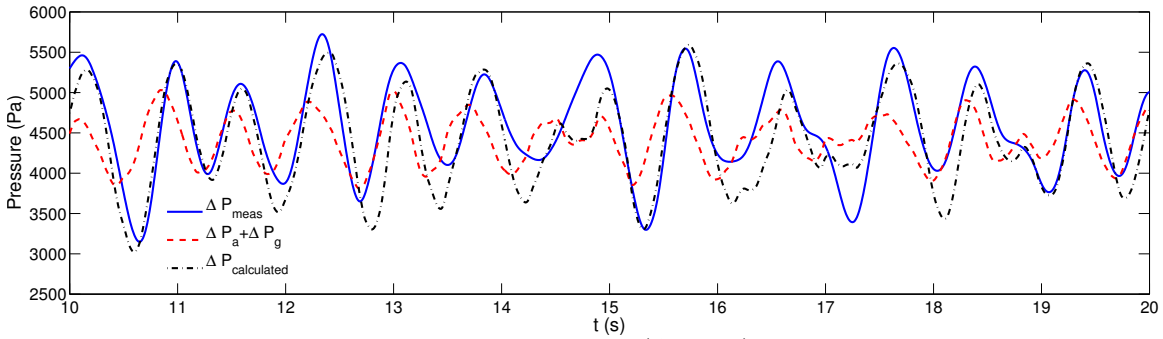

Figure 6.10: Pressure signals measured with a probe (ΔP_{meas}) and calculated with DIA, without considering the frictional forces ($\Delta P_a + \Delta P_g$), and considering them ($\Delta P_{calculated}$). Experimental results for $U/U_{mf} = 2.5$, $h_0/W = 1$, $d_p = 0.6 - 0.8$ mm.

The particle-wall interaction coefficient, c, can be estimated under the different operative conditions presented in Table 6.1. For that purpose a set of experiments were done for a range of superficial gas velocities (U/U_{mf}= 1.5, 2, 2.5 and 3), static bed aspect ratii (h_0/W = 0.75, 1 and 1.25) and particle sizes, d_p = 0.4−0.6 mm, 0.6−0.8 mm and 1−1.3 mm. The values of the particle-wall interaction coefficient, c, resulting from these experiments are presented in Figures 6.11, 6.12 and 6.13, for the two different calculation procedures described in section 4: c_D refers to the derivation method and c_I to the integration method.

Figure 6.11 contains the results for the smaller particles ($d_p = 0.4-0.6$ mm) studied in the experiment. The values of the particle-wall interaction coefficient estimated with the derivation method, c_D, are very similar to the ones estimated with the integration method, c_I. It can be seen a small increment of c with the superficial gas velocity

for $U > 2U_{mf}$. Also, Figure 6.11 shows that the particle-wall interaction coefficient, c, is almost insensitive to the bed aspect ratio. In both alternatives, the cases with low velocity ($U = 1.5U_{mf}$) are more disperse and deviate from the latter tendency, specially in the derivation method.

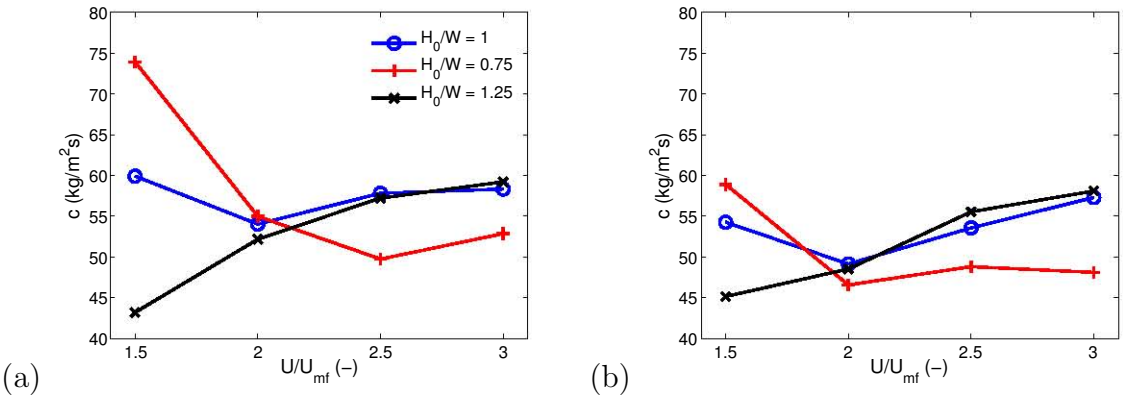

Figure 6.11: Experimental particle-wall interaction coefficient, c, versus U/U_{mf} for $d_p = 0.4 - 0.6$ mm and the three different aspect ratios studied, a) c_D and b) c_I.

Figure 6.12 shows the particle-wall interaction coefficient for the medium size particles ($d_p = 0.6 - 0.8$ mm). As with the smaller particles, c_D and c_I are very similar. In the medium size particles, the small sensitivity to the aspect ratio is observed again, except the results for the high gas velocity ($U = 3U_{mf}$), which may be attributed to a change in the fluidization regime.

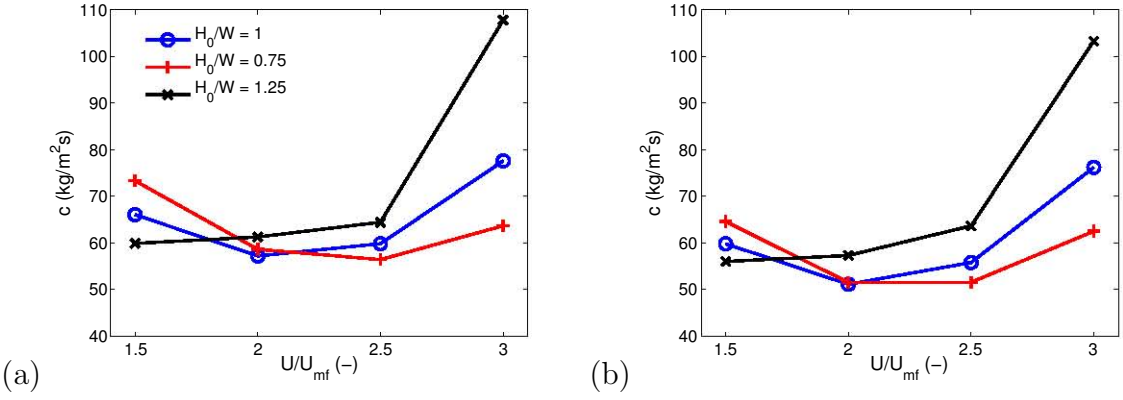

Figure 6.12: Experimental particle-wall interaction coefficient, c, versus U/U_{mf} for $d_p = 0.6 - 0.8$ mm and the three different aspect ratios studied, a) c_D and b) c_I.

The particle-wall interaction coefficient estimated for the biggest particle size studied in the experiments ($d_p = 1 - 1.3$ mm) is shown in Figure 6.13. As for the previous particles, the results for the biggest particles are relatively insensitive to the bed aspect ratio and limitedly sensitive to the superficial gas velocity. Nevertheless, the case for

the higher aspect ratio seems to slightly deviate from the tendency of the other two aspect ratios tested.

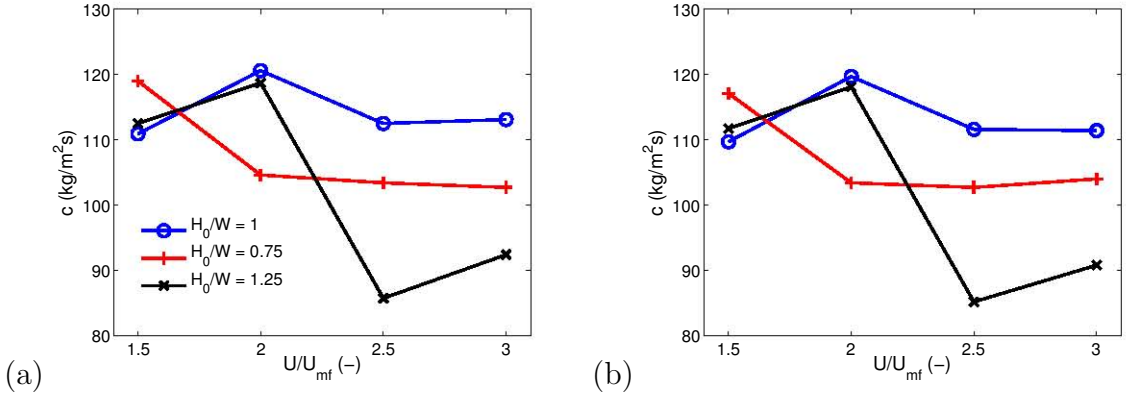

Figure 6.13: Experimental particle-wall interaction coefficient, c, versus U/U_{mf} for $d_p = 1 - 1.3$ mm and the three different aspect ratios studied, a) c_D and b) c_I.

The previous results suggest that the particle-wall interaction coefficient, c, is weakly affected by the aspect ratio of the bed. Exception of this is, perhaps, the data dispersion observed at low or high superficial velocities. Therefore a robust estimation of the particle-wall interaction coefficient can be made by averaging the particle-wall interaction coefficient obtained for the three aspect ratios, keeping constant U/U_{mf} and d_p. Figure 6.14 shows the results of this mean particle-wall interaction coefficient, $\overline{c}$.

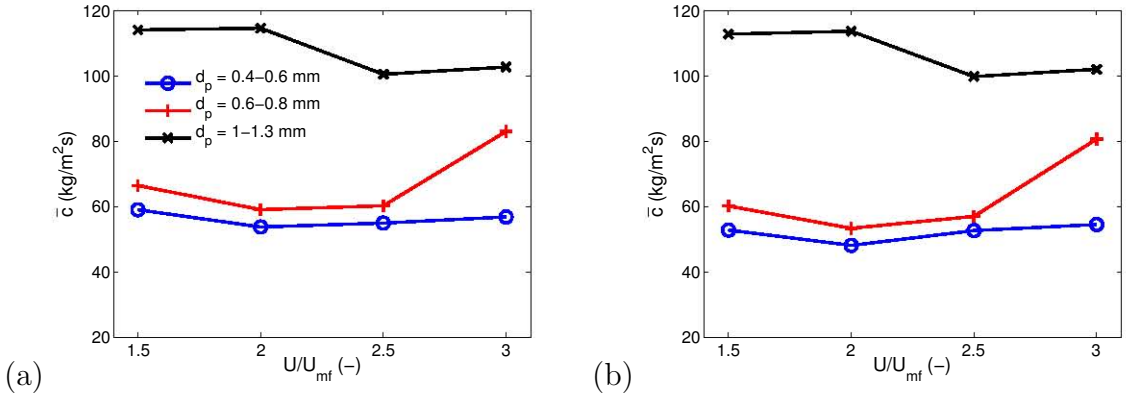

Figure 6.14: Comparison of the experimental mean particle-wall interaction coefficient, $\overline{c}$, versus U/U_{mf} for different particle sizes studied, a) c_D and b) c_I.

In general, the particle-wall interaction coefficient, $\overline{c}$, for the particles of $d_p = 1-1.3$ mm is almost the double than for the other particles. The medium size particles ($d_p = 0.6-0.8$ mm) give values of the mean particle-wall interaction coefficient slightly higher than for the small particles ($d_p = 0.4 - 0.6$ mm).

Therefore, the experiments indicate that the particle-wall interaction coefficient defined as Equation 6.2, with $\Omega = dy_{cm}/dt$, increases substantially with the particle size. The growth of the particle-wall interaction coefficient with the size of the particles may be attributed to the enhancement of the wall effects produced when the number of particles that can be allocated along the transversal direction, Z, of the bed is reduced. In contrast, the variation of $\overline{c}$ with the superficial gas velocity in Figure 6.14 is comparatively small and without a defined trend.

Taking into account all the results presented previously, very similar values of the coefficient $\overline{c}$ are obtained for the two methodologies developed in this work, integration and derivation. This outcome was expected since the derivation and integration methods are conceptually equivalent and the inequalities are due to the different sources of numerical inaccuracies and noise frequencies amplified. The resemblance between c_D and c_I also makes the result more trust worthy.

Considering that the mean particle-wall interaction coefficient, $\overline{c}$, in Figure 6.14 is relatively insensitive to both the aspect ratio and the superficial gas velocity, a simple dependence in terms of the particle diameter can be retained, i.e. $\overline{c} = f(d_p)$, in this first experimental characterization of the value of $\overline{c}$. Figure 6.15 plots the mean particle-wall interaction coefficient versus the particle diameter. This Figure is constructed by averaging the values of $\overline{c}$ of Figure 6.14 for each particle diameter. Taking into account that the derivation method gives very similar results to the integration method, the mean particle-wall interaction coefficient obtained with both methods are used in Figure 6.15 to fit a function that models $\overline{c}$ versus d_p. In view of Figure 6.15, it seems that $\overline{c}$ does not depend linearly on d_p but rather quadratically. Thus, based on the trend found for the present results, a second order polynomial of the form $a_2 d_p^2 + a_1 d_p + a_0$, is selected as a simple example of model function.

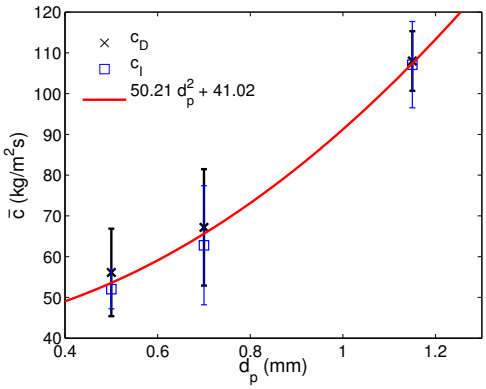

Figure 6.15: Experimental mean particle-wall interaction coefficient, $\overline{c}$, versus d_p for: c_D, c_I and fitting curve. The vertical bars denote the standard deviation of the experimental data from the mean.

According to the constitutive relations for granular materials by Johnson and Jackson (1987), the particle-wall frictional force is not a strong function of the particle diameter. These authors developed their theory considering that the particles were immersed in a very large volume compared to the particle size and that the walls are not close to each other. For the pseudo−2D fluidized bed studied here, the frictional forces clearly depend on the particle diameter. This can be explained considering that in the pseudo−2D bed the volume is not very large since the thickness is in the order of 10 times d_p. Making d_p much smaller than Z, the bed thickness will be seen by a particle as infinitely large. Thus, in order to make the quadratic function model more consistent with the Johnson and Jackson friction constitutive relations, the derivative of $\overline{c}$ with regard d_p must vanish when d_p/Z tends to zero (i.e. $2a_2 d_p + a_1 \to 0$ when $d_p \to 0$). By this way $\overline{c}$ approaches asymptotically to a constant value. This implies that the coefficient $a_1 = 0$ and the polynomial to be fitted is $a_2 d_p^2 + a_0$. The result of the least square regression of this quadratic function to the frictional force data in Figure 6.15 is:

$$\overline{c} = 50.21\ (d_p[\text{mm}])^2 + 41.02 \tag{6.15}$$

Note that in Equation 6.15, the particle diameter, d_p, must be introduced in [mm].

It has to be said that the results presented here were performed for a pseudo-2D bed of a fixed thickness $Z = 1$ cm, which means that the proposed correlation may be valid only for beds of such thickness. The root mean square difference between Equation 6.15 and all of the individual experimental data in Figures 6.11, 6.12 and 6.13 gives a regression error of Equation 6.15 equal to 10.7 kg/m^{2}s, which is a 19% of $\overline{c}$ in the most unfavourable case (smallest value of $\overline{c}$), and 9% in the most favourable case, with an average value of 14%. Nevertheless, a dimensionless analysis can be performed to envision how the effect of the bed thickness could be included in Equation 6.15. The particle-wall interaction coefficient, c, is a function of d_p, ρ_s, U/U_{mf}, Z, h_0, W, g, μ and other parameters related to the geometrical and elasticity characteristics of the particles (e.g. maximum packing limit, sphericity, rugosity and restitution coefficient of the particles). That is:

$$c = f(d_p, \rho_s, U/U_{mf}, Z, H, W, g, \mu, \text{geometry-elasticity}) \tag{6.16}$$

Using the Buckingham pi theorem, the dimensionless particle-wall interaction coefficient can be expressed as follows:

$$\frac{c}{\rho_s Z^{1/2} g^{1/2}} = f'\left(\frac{d_p}{Z}, \frac{U}{U_{mf}}, \frac{h_o}{W}, \frac{W}{Z}, \mu, \text{geometry-elasticity}\right) \tag{6.17}$$

Hence, the dimensionless mean particle-wall interaction coefficient is basically a function of d_p/Z, μ and the geometrical and elasticity characteristic of the particles:

$$\frac{c}{\rho_s Z^{1/2} g^{1/2}} = f''\left(\frac{d_p}{Z}, \mu, \text{geometry-elasticity}\right) \tag{6.18}$$

Note that Equation 6.15 was obtained for the conditions $Z = 1$ cm, $g = 9.81$ m/s^2, $\rho_s = 2500$ kg/m^3. Thus, comparing Equation 6.15 with Equation 6.18 the following tentative dependence of the particle-wall interaction coefficient on the thickness Z arises:

$$\frac{c}{\rho_s Z^{1/2} g^{1/2}} = \frac{50.21 \cdot 10^6 \left(\frac{d_p}{Z}\right)^2 0.01^2 + 41.02}{2500 \cdot 0.01^{1/2} \cdot 9.81^{1/2}} = 6.41 \left(\frac{d_p}{Z}\right)^2 + 5.24 \cdot 10^{-2} \tag{6.19}$$

All the variables in Equation 6.19 are now expressed in SI units (e.g. metres [m] for d_p and Z).

Finally, what Equation 6.19 suggests is that the particle-wall interaction coefficient increases when the thickness of the bed tends to small values, since:

$$c = 6.41 \frac{d_p^2 \rho_s g^{1/2}}{Z^{3/2}} + 5.24 \cdot 10^{-2} \rho_s Z^{1/2} g^{1/2} \tag{6.20}$$

Note that Equation 6.20 increseases with large values of Z. Nevertheless, this behaviour is an artifact caused by the quadratic function used to fit the experimental data and weakly affects the value of c if the ratio dp/Z is small.

The last part of this section focuses on the quantification of the frictional forces relative to the other forces in the bed. Figure 6.16 compares the standard deviation of the pressure signals in the bed, $\Delta P_{calculated}$, ΔP_a and ΔP_{fric}, normalized with the mean pressure drop in the bed due its weight, $\rho_s g h_0 (1 - \epsilon_0)$. The results correspond to the medium size particles and aspect ratio equal to unity. Similar trends were found for the other particles and aspect ratios. As expected, the measured and the calculated pressure drop depend linearly on the superficial gas velocity as a result of the growth the bubbles that produce the pressure fluctuations of the bed. Also, Figure 6.16 shows that the frictional force is not negligible in the force balance, increasing its relative contribution when the gas velocity is augmented.

Figure 6.16 can be complemented with a percentage quantification of the force fluctuations in the bed. Table 6.2 shows the relative fluctuation of each force in the bed, which is calculated dividing the standard deviation of each pressure contribution by the standard deviation of the pressure measured, ΔP_{meas}. It is clear from Table 6.2

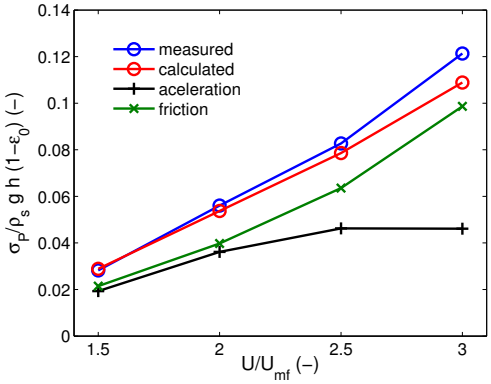

Figure 6.16: Normalized standard deviation of the pressure terms versus U/U_{mf}. Experimental data for $h_0/W = 1$, $d_p = 0.7$ mm, c_I.

that the fluctuations of $\Delta P_{calculated}$ are very similar to that of ΔP_{meas}, which reflects the compliance with the force balance proposed in the theory section. Also, Table 6.2 shows that the frictional forces accounts for more than the 70% of the overall fluctuations in the bed. This important impact of the frictional force in the pressure drop oscillations becomes even greater than the contribution of the force due to the acceleration of the centre of mass at high superficial gas velocities.

Table 6.2: Forces acting in the bed, $h_0/W = 1$, $d_p = 0.7$ mm, c_I.

$\sigma_P/\sigma_{\Delta P_{meas}}$	U/U_{mf}			
	1.5	2.0	2.5	3.0
calculated	100.24%	95.92%	95.01%	89.76%
acceleration	68.41%	64.55%	55.90%	38.02%
friction	76.13%	70.94%	76.83%	81.31%

6.7 Conclusions

In this work, the frictional forces exerted by the front and rear walls on the solids of a pseudo−2D fluidized bed were experimentally characterized. This was done by linking the pressure drop measured in the bed with the acceleration and velocity of its centre of mass obtained from digital image measurements of the solids distribution. The frictional forces were assumed to be a function of the bed dynamics and it was found that the best choice is to consider the friction proportional to the solids velocity through a particle-wall interaction coefficient, c. This resulting coefficient was in the range of 40 to 120 kg/m^{2}s for the operative conditions studied in the present work. Two different methods to estimate the particle-wall interaction coefficient were presented, and the two methods gave very similar results. In general the particle-wall interaction

coefficient, c, was found to be very sensitive to the particle diameter, less affected by the superficial gas velocity and weakly affected by the bed aspect ratio. The contribution of the frictional forces on the fluctuations of the pressure drop in the bed (i.e. the standard deviation of the pressure drop) results to be even larger than the pressure fluctuation induced by the acceleration of the bulk of the bed. These empirical findings evidence that the friction of particles with the walls plays an important role in the dynamics of pseudo−2D beds.

Nomenclature

A_L	lateral area (m^2)
A_T	transversal area (m^2)
c	interaction constant in the force balance (kg/m^2s)
d	delay points (−)
d_p	particle diameter (mm)
f	acquisition frequency (Hz)
f_0	characteristic pressure frequency (Hz)
$F_{\Delta P}$	force due to the pressure drop in the bed (N)
F_a	force due to the acceleration of the centre of mass of the bed (N)
F_g	force due to the bed weight (N)
F_{fric}	frictional forces (N)
F_N	normal force (N)
GL	grey level of the pixels (−)
g	gravity (m/s^2)
H	bed height (m)
h_{fb}	mean freeboard height (m)
h_0	static bed height (m)
m	mass of the bed (kg)
N	number of pixels (-)
N_f	number of points of the moving average filter (-)
n	normal direction to the wall (-)
ΔP	pressure drop in the bed (Pa)
ΔP_{meas}	pressure drop measured (Pa)
$\Delta P_{calculated}$	pressure drop calculated (Pa)
ΔP_p	pressure drop at 5 cm over the distributor (Pa)
T	total measurement time (s)
t_d	time delay (s)

Δt	sampling time interval (s)
U	superficial gas velocity (m/s)
U_{mf}	minimum fluidization velocity (m/s)
v	solids velocity (m/s)
y_{cm}	vertical position of the centre of mass of the bed (m)
y_p	vertical position of the pressure probe (cm)
W	bed width (m)
Z	bed thickness (m)

Greek letters

α_s	solids volume fraction (−)
α_{mf}	solids volume fraction at minimum fluidization conditions(−)
δ	discrepancy factor (−)
δ_v	vertical discrepancy factor (−)
δ_T	total discrepancy factor (−)
ϵ_0	static bed void fraction (−)
ϵ_{mf}	bed void fraction at minimum fluidization conditions (−)
μ	Coulomb coefficient of friction (−)
Ω	functional of the frictional force (−)
ρ_s	solids density (kg/m^3)
τ	shear stress (N/m^2)
θ	granular temperature (J/kg)
$\sigma_{\Delta P}$	standard deviation of the pressure (Pa)
ξ	direction of the centre of mass velocity

Bibliography

Almendros-Ibáñez, J.A., Sobrino, C., de Vega, M., Santana, D., A new model for ejected particle velocity from erupting bubbles in 2-D fluidized beds. *Chem. Eng. Sci.* 61 (2006) 5981-5990.

Almendros-Ibáñez, J.A., Pallarès, D., Johnsson, F., Santana, D., Voidage distribution around bubbles in a fluidized bed: Influence on throughflow. *Powder Technol.* 197 (2010) 73-82.

Baskakov, A.P., Tuponogov, V.G., Filippovski, N.F.. A study of pressure fluctuations in a bubbling fluidized bed. *Powder Technol.* 45 (1986) 113-117.

Busciglio, A., Vella, G., Micale, G., Rizzuti, L. Analysis of the bubbling behaviour of 2D gas solid fluidized beds: Part I. Digital image analysis technique. *Chem. Eng. J.* 140 (2008) 398-413.

Croxford, A.J., Harrison, A.J.L., Gilbertson, M.A. The optimisation of pressure measurements for the control of bubbling fluidised beds *Int. J. Chem. Reactor Eng.* 3 (2005) p.A39.

Croxford, A.J., Gilbertson, M.A. Pressure fluctuations in bubbling gas-fluidized beds. *Chem. Eng. Sci.* 16 (2011) 3569-3578.

Davidson J.F., Harrison, D. Fluidised Particles, Cambridge University Press, Cambridge, 1963.

Gidaspow, D., Multiphase flow and Fluidization: Continuum and kinetic theory descriptions; Academic Press: San Diego, CA. 1994.

Hernández-Jiménez, F., Sánchez-Delgado, S., Gómez-García, A., Acosta-Iborra, A., Comparison between two-fluid model simulations and particle image analysis & velocimetry (PIV) results for a two-dimensional gas-solid fluidized bed. *Chem. Eng. Sci.* 66 (2011) 3753-3772.

Hernández-Jiménez, F., Third, J.R., Acosta-Iborra, A., Müller C.R. Comparison of bubble eruption models with two-fluid simulations in a 2D gas-fluidized bed. *Chem. Eng. J.* 171 (2011) 328-339.

Johnson, P.C., Jackson, R., Frictional collisional constitutive relations for granular materials, with application to plane shearing. *J. Fluid Mech.*, 176 (1987), 6793.

Kunii, D., Levenspiel, O., Fluidization Engineering: Butterworth-Heinemann: Newton, MA, 1991.

Laverman, J.A., Roghair, I., van Sint Annaland, M., Kuipers, H. Investigation into the hydrodynamics of gas-solid fluidized beds using particle image velocimetry coupled with digital image analysis. *Can. J. Chem. Eng.*, 86 (2008), pp. 523-535

Li, T., Grace, J.R., Bi, X., Study of wall boundary condition in numerical simulations of bubbling fluidized beds. *Powder Technol.* 203 (2010) 447-457.

Müller, C.R., Davidson, J.F., Dennis, J.S., Hayhurst, A.N., A study of the motion and eruption of a bubble at the surface of a two-dimensional fluidized bed using particle image velocimetry (PIV). *Ind. Eng. Chem. Res.* 46 (2007) 1642-1652.

Sánchez-Delgado, S., Marugán-Cruz, C., Acosta-Iborra, A., Santana, D. Dense-phase velocity fluctuation in a 2-D fluidized bed. *Powder Technol.* 200 (2010), pp. 37-45

Sánchez-Delgado, S., Marugán-Cruz, C., Soria-Verdugo, A., Santana, D. Estimation and experimental validation of the circulation time in a 2D gassolid fluidized beds. *Powder Technol.* 235 (2013) 669-676

Santana, D., Nauri, S., Acosta, A., Garcia, N., Macias-Machin, A., Initial particle velocity spatial distribution from 2-D erupting bubbles in fluidized bed. *Powder Technol.* 150 (2005) 1-8.

Shen, L., Johnsson, F., Leckner, B.. Digital image analysis of hydrodynamics two-dimensional bubbling fluidized beds. *Chem. Eng. Sci.* 59 (2004) 2607-2617.

Soria-Verdugo, A., García-Gutíerrez, L.M., Sánchez-Delgado, S., Ruiz-Rivas, U. Circulation of an object immersed in a bubbling fluidized bed. *Chem. Eng. Sci.* 66, (2011) 78-87.

Soria-Verdugo, A., García-Gutiérrez, L.M., García-Hernando, N., Ruiz-Rivas, U. Buoyancy effects on objects moving in a bubbling fluidized bed. *Chem. Eng. Sci.* 66, (2011) 2833-2841.

van Ommen, van der Schaaf, J., Schouten, J.C., van Wachem, B.G.M., Coppens, M.O., van der Bleek, C.M. Optimal placement of probes for dynamic pressure measurements in large-scale fluidized beds. *Powder Tehcnol.* 139 (2004) 264-276.

van Ommen, R. J., Sasic, S., van der Schaaf, J., Gheorghiu, S., Johnsson, F., Coppens, M.O. Time-series analysis of pressure fluctuations in gassolid fluidized beds - A review. *Int. J. Multiphase Flow* 37 (2011) 403-428.

Chapter 7

Conclusions

7.1 General conclusions

Pseudo-2D fluidized beds are commonly used in the characterisation of the behaviour of fluidized beds. The relatively small thickness of these systems allows for the visualisation of the bed interior if one of the walls is optically accessible. However, a correct interpretation of the physics in the bed is crucial for its understanding and extrapolation to fully 3D systems. Additionally, the observations of pseudo-2D beds can be used to validate numerical codes that will eventually permit the simulation of more complex fluidized bed systems.

In this dissertation, numerical and experimental investigations on pseudo-2D fluidized beds were performed to gain knowledge about the behaviour of pseudo-2D systems. The main conclusions presented in Chapters 2 to 6 are summarised in the following lines.

As a first step in the study, a comparison between two-fluid model simulations and experimental results in a pseudo-2D gas fluidized bed was performed in Chapter 2. Apart from the bubble behaviour usually examined in this type of work,, the time-averaged dense phase velocity, the air throughflow and the instantaneous interactions between the bubbles and dense phase of the simulations were compared with experimental observations. The two-fluid model simulations employed two different well known drag models (Gidaspow and Syamlal - O'Brien) and the governing equations were solved in a pure 2D domain. The experimental data were obtained using a combination of non-intrusive techniques (i.e., PIV and DIA). The simulation results showed fairly good agreement with the experimental results with regard to the bubble growth and velocity, as well as the bubble probability distribution. The present work proves that the dense phase probability experimentally obtained by DIA can be used as a good approximation of the time-averaged particle volume fraction in a bubbling bed.

Nevertheless, the results also indicate that the time-averaged velocities of the particle phase in the simulated 2D bed are nearly one order of magnitude larger than the velocities obtained from the PIV experiments. This significant result occurs for the two well-known drag models tested, indicating that in Eulerian-Eulerian 2D two-fluid simulations the bubble behaviour is relatively weakly affected by the streaming generated by the dense phase. This result is surprising because bubbles are the main mechanism of the movement of solids. Furthermore, the differences in the visible bubble flow between the simulation and the experimental results are not as high as the increment of the velocity of the solids in the results comparison. Therefore, the discrepancies found for the velocity of the solids cannot be attributed solely to the high number of bubbles in the simulated bed, but in fact, these differences can be attributed to the absence of the front and rear walls and their associated effect in pure 2D simulations.

The discrepancies found between the experiments and simulations regarding the mean velocity of the solids may be caused by several factors. To rule out some of these factors the motion of particles around bubbles from two-fluid model simulations were compared in Chapter 3 of the thesis with classical models from the literature (Davidson and Harrison, 1963). The bed was simulated in a pure 2D domain (e.g., without considering the front and rear walls). For isolated bubbles that are far from the freeboard, the simulated particle motion around the bubbles is found to be described well by the potential flow theory, a finding that is in agreement with experimental evidence (Davidson and Harrison, 1963). For erupting bubbles, good agreement is found between the simulated velocity profiles and the PIV data reported by Müller et al. (2007).

Another way of verifying the validity of the simulation results concerning the bubble behaviour is the analysis of the gas phase. Thus, the velocity of the gas crossing the bubbles was calculated from the simulation results and compared with the potential flow theory of Davidson (Davidson and Harrison, 1963). The results in Chapter 4 demonstrated that the 2D simulations are can realistically reproduce the pressure distribution and the gas flow for isolated bubbles, and the results are in good agreement with the classical potential flow model of Davidson (Davidson and Harrison, 1963).

Because both the interchange coefficient and the crossflow ratio are difficult parameters to measure in experimental facilities, the simulation results presented in Chapter 4 served an additional aim: the characterisation of the gas interchange in 2D beds under bubbling conditions. The simulations revealed that both coefficients decrease with the distance to the distributor and the particle diameter, their values being two times those predicted by the potential flow theory. To facilitate the prediction of the gas interchange, a new model was proposed for 2D interacting bubbles. In this model, the

gas interchange coefficient is not only a function of the minimum fluidization velocity (as for isolated bubbles) but also depends on the superficial velocity of the bed and the throughflow parameter.

Because that the 2D two-fluid model simulations are able to correctly predict the bubble behaviour observed in pseudo-2D beds, there is strong evidence to suggest that the effect of the front and rear walls of the bed may be the cause of the discrepancies between the pure 2D simulations and the pseudo-2D measurements. As a result, fully 3D simulations of pseudo-2D beds considering the classical particle-wall boundary conditions are presented in Chapter 5. The usage of the classical boundary condition (originally developed for a wall affecting a semi-infinite volume of particles) was proved to be unsuccessful for reproducing the expected behaviour of pseudo-2D beds, even after adjusting the empirical coefficients, such as the specularity coefficient. A plausible explanation of this is that in a real pseudo-2D bed, the front and rear walls simultaneously affect the motion of the particles. This was corroborated in Chapter 5 by the DEM simulation data from which the micro-structure of the particle-wall interaction was extracted and proposed in a novel form describing the boundary condition of the particles in a pseudo-2D bed. It was shown that at low values of the solids volume fraction, the partial-slip coefficient can be negative and, thus, contrary to the behaviour yielded by the Johnson and Jackson (1987) boundary condition. The new boundary condition developed in Chapter 5 was also implemented in the two-fluid model and was shown to give more favourable results for pseudo-2D fluidized beds than the classical boundary condition from Johnson and Jackson (1987).

A different way to investigate the effects of the walls in the bed was followed in Chapter 6. In particular, an experimental quantification of the frictional forces due to the walls on the solids phase of a pseudo-2D fluidized bed was performed. This was performed by linking the pressure drop measured in the bed with the acceleration and velocity of its centre of mass obtained from the digital image measurements of the solids distribution. The frictional forces were assumed to be a function of the bed dynamics. The best choice is to consider the friction equal to the solids velocity times a friction constant, which manifests the fluid-like behaviour of the dense phase. The friction constant was found to be very sensitive to the particle diameter, less affected by the superficial gas velocity and weakly affected by the bed aspect ratio. The contribution of the frictional forces on the fluctuations of the pressure drop in the bed was to be even larger than the pressure fluctuation induced by the acceleration of the bulk of the bed.

Overall, the results of this dissertation indicate that the numerical and experimental observations of pseudo-2D beds should be interpreted with caution. Despite the good

harmony seen between experimental pseudo-2D beds, pure 2D simulations, and 2D classical models with regards to the behaviour of isolated bubbles (bubble diameter and velocity, solids motion around bubbles and gas interchange), the physics occurring in pseudo-2D beds is substantially affected by the presence of the front and rear walls of the bed. This is evidenced by the disagreement between experiments and simulations concerning the magnitude of the mean particle motion. Furthermore, the thesis has revealed, numerically and experimentally, that the effects exerted by the bed walls on the particles are not negligible and can affect the motion of the dense phase, as well as the pressure fluctuations in the bed. Therefore, validation of the codes and models by merely checking the bubble phase should be avoided due to the apparent uncoupling between the bubble behaviour and the mean solids motion. Hence, to correctly extrapolate the experimental results from pseudo-2D beds to other systems, or to validate the numerical codes with the pseudo-2D observations, it is essential to resort to specific particle-wall interaction models capable of describing the combined effect of all the bed walls in these types of beds of small thickness.

7.2 Future work

The numerical and experimental investigations conducted in the present thesis have clarified some facts concerning pseudo-2D beds, but additional questions have been opened. The following points suggest some possible future work to continue with the research started in this thesis.

Future works regarding numerical investigations:

- The new proposed boundary condition developed using the DEM simulations was implemented in the two-fluid model for a specific base case because the initial motivation was to show that the standard particle-wall boundary conditions may not be valid for pseudo-2D beds. Nevertheless, to generalise the new developed boundary condition, a natural extension of this work is to study the effect of the thickness of the bed and the particle diameter on the particle-wall interactions in fluidized beds.

- The gas interchange between the bubble and emulsion phases in bubbling beds was characterised numerically in Chapter 4. Recent experimental techniques, such as the infrared technique developed by Dang et al. (2013), could allow for non-intrusive measurement of the gas transport in beds with multiple bubbles (bubbling regime). Direct or indirect experimental results of the gas interchange

for the bubbling regime would be of great interest to compare them with the model proposed in this thesis. These results will show, among other information, whether the pure 2D simulations are able to reproduce the gas interchange in a real pseudo-2D bed.

- Objects immersed in fluidized beds are mainly driven by the motion of particles, which in sum are conveyed by the rise of bubbles in the bed. Recent works have studied the motion of objects in fluidized beds using experimental pseudo-2D beds and 2D and 1D simulations (García-Gutiérrez et al., 2013; Soria-Verdugo et al., 2011a; Farzaneh et al., 2013). The comparison of the 2D numerical simulations and pseudo-2D experimental results (as performed in Chapters 2 and 6) could be used as a tool to clarify whether the front and rear walls of a pseudo-2D bed have a net effect on the motion of objects in the bed.

Future works regarding experimental investigations:

- The effect of the thickness of the pseudo-2D beds on the wall friction has been postulated in Chapter 6 on the grounds of dimensional analysis because only a bed of fixed thickness was experimentally studied. Therefore, future studies varying this thickness should be performed to verify experimentally the findings shown in the present thesis.

- Previous works have shown the importance of the bed wall distances in pseudo-2D beds, such as the variation of the minimum fluidization velocity with the thickness of the bed performed by Sánchez-Delgado et al. (2010). The frictional forces experimentally estimated in the pseudo-2D bed of Chapter 6 may be related to such variation of the minimum fluidization velocity, and further work may be needed to properly study their link.

Bibliography

Acosta-Iborra, A., Sobrino, C., Hernández-Jiménez, F., de Vega, M. Experimental and computational study on the bubble behavior in a 3-D fluidized bed. *Chem. Eng. Sci.* 66 (2011) 3499-3512.

Acosta-Iborra, A., Hernández-Jiménez, F., de Vega, M., Briongos, J.V. A novel methodology for simulating vibrated fluidized beds using two-fluid models. *Chem. Eng. J.* 198-199 (2012) 261-274.

Ahuja, G.H., Patwardhan, A.W., CFD and experimental studies hold-up distribution and circulation patterns in gas-solid fluidized beds *Chem. Eng. J.*, 143 (2008), pp. 147-160

Almendros-Ibáez, J.A., Sobrino, C., de Vega, M., Santana, D., A new model for ejected particle velocity from erupting bubbles in 2-D fluidized beds *Chem. Eng. Sci.*, 61 (2006), pp. 5981-5990

Almendros-Ibáñez, J.A., Pallarés, D., Johnsson, F., Santana, D. Novel approach to characterize fluidized bed dynamics combining particle image velocimetry and finite element method. *Ind. Eng. Chem. Res* 48 (2009) 5010-5023.

Almendros-Ibáñez, J.A., Pallarès, D., Johnsson, F., Santana, D., Voidage distribution around bubbles in a fluidized bed: Influence on throughflow. *Powder Technol.* 197 (2010) 73-82.

Anderson, T.B., Jackson, R. A fluid mechanical description of fluidized beds. *Ing. Eng. Chem. Fund.* 6 (1967) 527-539.

Baskakov, A.P., Tuponogov, V.G., Filippovski, N.F. A study of pressure fluctuations in a bubbling fluidized bed. *Powder Technol.* 45 (1986) 113-117.

Basu, P. Combustion and Gasification in Fluidized Beds CRC, Taylor & Francis, Boca Raton (2006)

Beetstra, R., van der Hoef, M.A., Kuipers, J.A.M. Drag Force of Intermediate Reynolds Number Flow Past Mono- and Bidisperse Arrays of Spheres. *AIChE J.*. 53 (2007) 489-501.

Benyahia, S., Syamlal, M., O'Brien, T.J. Extension of Hill-Koch-Ladd drag correlation over all ranges of Reynolds number and solids volume fraction. *Powder Technol.* 162 (2006) 166-174.

Benyahia, S., Syamlal, M., O'Brien, T.J. Summary of MFIX equations 2005-4, 2007.

Boemer, A., Qi, H., Renz, U., Verification of Eulerian simulation of spontaneous bubble formation in a fluidized bed *Chem. Eng. Sci.*, 53 (1998), pp. 1835-1846

Bokkers, G.A.,Laverman, J.A., van Sint Annaland, M., Kuipers, J.A.M., Modelling of large-scale dense gas-solid bubbling fluidised beds using a novel discrete bubble model *Chem. Eng. Sci.*, 61 (2006), pp. 5590-5602

Bokkers, G.A., van Sint Annaland, M., Kuipers, J.A.M., Mixing and segregation in a bidisperse gas-solid fluidised bed: a numerical and experimental study *Powder Technol.*, 140 (2004), pp. 176-186

Briongos, J. V., Sánchez-Delgado, S., Acosta-Iborra, A., Santana, D. A novel approach for modeling bubbling gas-solid fluidized beds. *AIChE Journal.* 57, 7, (2011) 1733-1750.

Busciglio, A., Vella, G., Micale, G., Rizzuti, L. Analysis of the bubbling behaviour of 2D gas solid fluidized beds: Part I. Digital image analysis technique. *Chem. Eng. J.* 140 (2008) 398-413.

Busciglio, A., Vella, G., Micale, G., Rizzuti, L., Analysis of the bubbling behaviour of 2D gas-solid fluidized beds. Part II. Comparison between experiments and numerical simulations via Digital Image Analysis Technique *Chem. Eng. J.*, 148 (2009), pp. 145-163

Caicedo, G.R., Prieto Marqus, J.J., Garca Ruz, M., Guardiola Soler,J. A study on the behaviour of bubbles of a 2D gas-solid fluidized bed using digital image analysis *Chem. Eng. and Proc.*, 42 (2003), pp. 9-14

Chiba, T. and Kobayashi, H. Gas Exchange between the Bubble and Emulsion Phases in Gas-Solid Fluidized Beds. *Chem. Eng. Sci.* 25, (1970) 1375-1385.

Collins, R. An extension of Davidson's theory of bubbles in fluidized beds. *Chem. Eng. Sci*, 20, (1965) 747-755.

Croxford, A.J., Harrison, A.J.L., Gilbertson, M.A. The optimisation of pressure measurements for the control of bubbling fluidised beds *Int. J. Chem. Reactor Eng.* 3 (2005) p.A39.

Croxford, A.J., Gilbertson, M.A. Pressure fluctuations in bubbling gas-fluidized beds. *Chem. Eng. Sci.* 16 (2011) 3569-3578.

Cundall, P.A., Strack, C.D.L. A discrete numerical-model for granular assemblies. *Geotechnique* 29 (1979) 47-65.

Dan, S., Jianzhi, W., Huilin, L., Yunhua, Z., Juhui, C., Gidaspow, D., Ming, C., Numerical simulation of gas-particle flow with a second-order moment method in bubbling fluidized beds *Powder Technol.*, 199 (2010), pp. 213-225

Dang, T.Y.N., Kolkman, T., Gallucci, F., van Sint Annaland, M. Development of a novel infrared technique for instantaneous, whole-field, non invasive gas concentration measurements in gas-solid fluidized beds. *Chem. Eng J.* 219 (2013) 545-557.

Darton, R.C., LaNauze R.D., Davidson, J.F., Harrison, D., Bubble growth due to coalescence in fluidized beds *Trans. of the Institute Chem. Eng.*, 55 (1977), pp. 274-280

Davidson, J. R., Harrison, D., Fluidized Particles Cambridge University Press (1963)

Davidson, J. R., Harrison, D., Fluidization Academic Press, New York (1971)

Deen, N.G., van Sint Annaland, M., van der Hoef, M.A., Kuipers, J.A.M., Review of discrete particle modelling of fluidized beds *Chem. Eng. Sci.*, 62 (2007), pp. 28-44

Deen, N.G., Kriebitzsch S.H.L., van der Hoef, M.A., Kuipers, J.A.M., Direct numerical simulation of flow and heat transfer in dense fluid?particle systems *Chem. Eng. Sci.*, 81 (2012), pp. 329-344

Deza , M., Franka, N. P., Heindel, T. J., Battaglia, F., CFD modelling and X-ray imaging of biomass in a fluidized bed *J. of Fluids Eng.* (2009), p. 131

Do, H.T., Grace, J.R., Clift, R. Particle ejection and entrainment from fluidized beds. *Powder Technol.* 6 (1972) 195.

Farzaneh, M., Almstedt, A.E., Johnsson, F., Pallarès, D. Simulation of fuel mixing in fluidized bed using a combined tracking technique. *Proceedigns of FLUIDIZATION XIV Conference*, Paper no. 186 (2013).

Fluent, 2006. Fluent 6.3 Documentation. FLUENT Inc. http://fluent.com/.

Fung, A.S., Hamdullahpur, F.A. A gas and particle flow model in the freeboard of a fluidized bed based on bubble coalescence. *Powder Technol.* 74 (1994) 121.

Simulation of object motion in a bubbling fluidized bed using a Monte Carlo method. García-Gutiérrez L.M., Soria-Verdugo A., García-Hernando N., Ruiz-Rivas U. *Chem. Eng. Sci.*, 96 (2013) 26?32.

Geldart, D. Types of gas fluidization *Powder Technol.*, 7 (1973), pp. 285-292

George, S.E., Grace, J.R. Entrainment of particles from aggregative fluidized beds. *AIChE Symp. Ser.* 74 (1978) 67.

Gidaspow, D. Multiphase Flow and Fluidization: Continuum and Kinetic Theory Descriptions Academic Press, San Diego (1994)

Gidaspow, D., Jung, J., Singh, R.K. Hydrodynamics of fluidization using kinetic theory: an emerging paradigm: 2002 Flour-Daniel lecture. *Powder Technol.*, 148 (2004), pp. 123-141.

Goldschmidt, M. J. V., Kuipers, J. A., van Swaaij, W. P. M., Hydrodynamic modelling of dense gas-fluidised beds using the kinetic theory of granular flow: effect of coefficient of restitution on bed dynamics *Chem. Eng. Sci.*, 56 (2001), pp. 571-578

Grace, J.R., Taghipour, F., Verification and validation of CFD models and dynamic similarity for fluidized beds *Powder Technol.* 139 (2004), pp. 99-110

Hartung, G., Müller, C.R., Hult, J., Kaminski, C.F, Dennis, J.S. Laser diagnostic investigation of the bubble eruption patterns in the free board of fluidized beds. Part 1: Optimized Acetone PLIF measurements, *Industrial & Engineering Chemistry Research* 47, 5686-5697, 2008.

Hatano, H., Ishida, M. The entrainment of solids particles from a gas-solid fluidized bed. *J. Chem. Eng. Jpn.* 14 (1981) 306.

Hernández-Jiménez, F., Sánchez-Delgado, S., Gómez-García, A., Acosta-Iborra, A. Comparison between two-fluid model simulations and particle image analysis & velocimetry (PIV) results for a two-dimensional gas-solid fluidized bed. *Chem. Eng. Sci.* 66 (2011) 3753-3772.

Hernández-Jiménez, F., Third, J.R., Acosta-Iborra, A., Müller, C.R. Comparison of bubble eruption models with two-fluid simulations in a 2D gas-fluidized beds. *Chem. Eng J.* 171 (2011) 328-339.

Hill, R.J., Koch, D.L., Lad, A.J.C. The first effects of fluid inertia on flows in ordered and random arrays of spheres. *J. Fluid Mech.* 448 (2001) 213-241.

Hill, R.J., Koch, D.L., Lad, A.J.C. Moderate Reynolds number flows in ordered and random arrays of spheres. *J. Fluid Mech.* 448 (2001) 243-278.

Hilligardt, K., Werther, J., Local bubble gas hold-up and expansion of gas/solid fluidized beds *German Chem. Eng.*, 9 (1986), pp. 215-221

Hosseini, S.H., Ahmadi, G., Rahimi, R., Zivdar, M., Esfahany, M.N., CFD studies of solids hold-up distribution and circulation patterns in gas-solid fluidized beds *Powder Technol.*, 200 (2010), pp. 202-215

Johnsson, F., Andersson, S., Leckner, B., Expansion of a freely bubbling fluidized bed *Powder Technol.*, 68 (1991), pp. 117-123

Johnsson, F., Zijerveld, R.C., Schouten, J.C., van den Bleek, C.M., Leckner, B. Characterization of fluidization regimes by time-series analysis of pressure fluctuations. *Int. J. Multiphase Flow.*, 26 (2000), pp. 663-715

Johnson, P.C., Jackson, R. Frictional collisional constitutive relations for antigranulocytes materials, with application to plane shearing. *J. of Fluid Mech.* 176 (1987), 67-93.

Jung, J., Gidaspow, D., Gamwo, I.K., Measurement of two kinds of granular temperatures, stresses and dispersion in bubbling beds *Industrial & Engineering Chemistry Research*, 44 (2005), pp. 1329-1341

Jung, J., Gidaspow, D., Bubble computation, granular temperatures, and Reynolds Stresses *Chem. Eng. Communications*, 193 (2006), pp. 946-975

Köhl, M.H., Lu, G., Third, J.R., Häberlin, M., Kasper, L., Prüssmann, K.P., Müller, C.R. Magnetic resonance imaging (MRI) study of jet formation in packed beds *Chem. Eng. Sci.* 97 (2013) 406-412.

Kriebitzch, S.H.L., van der Hoef, M.A., Kuipers, J.A.M. Fully resolved simulation of a gas-fluidized bed: A critical test of DEM models *Chem. Eng. Sci.* 91 (2013) 1-4.

Kuipers, J.A.M., Van Duin, K.J., Van Beckum, F.P.H., Van Swaaij, W.P.M. A numerical model of gas-fluidized beds *Chem. Eng. Sci.* 47 (1992) 1913-1924.

Kunii, D., Levenspiel, O., 1991. Fluidization Engineering. Butterworth-Heinemann Series in Chemical Engineering.

Ladd, A.J.C., Verberg, R., Lattice-Boltzmann simulations of particle fluid suspensions *J. of Statistical Physics*, 104 (2001), pp. 1191-1251

Laverman, J.A., Roghair, I., van Sint Annaland, M., Kuipers, H., Investigation into the hydrodynamics of gas-solid fluidized beds using particle image velocimetry coupled with digital image analysis *Can. J. Chem. Eng.*, 86 (2008), pp. 523-535

Levy, E.K., Caram, H.S., Dille, J.C.,Edelstein, S. Mechanism for solid ejections from gas-solid fluidized beds. *AIChE J.* 29 (1983) 383.

Li, T., Benyahia, S. Revisiting Johnson and Jackson boundary condition for granular flows. *AIChE J.* 58 (2012) 2058-2068.

Li, T., Grace, J., Bi, X. Study of wall boundary condition in numerical simulations of bubbling fluidized beds *Powder Technol.*, 203 (2010), pp. 447-457

Lin, J.S., Chen, M.M., Chao, B.T., A novel radioactive particle tracking facility for measurement of solids motion in gas fluidized beds *AIChE J.*, 31 (1985), pp. 465-473

Lun, C. K. K., Savage, S. B., Jeffrey, D. J. and Chepurniy, N. Kinetic theories for granular flow: inelastic particles in Couette flow and slightly inelastic particles in a general flow field *J. of Fluid Mech.*, 140 (1984), pp. 223-256

Lindborg, H., Lysberg, M., Jakobsen, H.A., Practical validation of the two-fluid model applied to dense gas-solid flows in fluidized beds *Chem. Eng. Sci.*, 62 (2007), pp. 5854-5869

Liu, Z., Zheng, Y., Jia, L., Zhang, Q., Study of bubble induced flow structure using PIV *Chem. Eng. Sci.*, 60 (2005), pp. 3537-3552

Mathiesen, V., Solberg, T., Hjertager, B.H. An experimental and computational study of multiphase flow behavior in a circulating fluidized bed *Int. J. Multiphase Flow* 26 (2000) 387-419.

Makkawi, Y.T., Wright, P.C. Fluidization regimes in a conventional fluidized bed characterized by means of electrical capacitance tomography. *Chem. Eng. Sci.* 57 (2002) 2411-2437.

McKeen, T., Pugsley, T., Simulation and experimental validation of a freely bubbling bed of FCC catalyst *Powder Technol.*, 129 (2003), pp. 139-152

Min, J., Drake, J. B., Heindel, T. J., Fox, R. O., Experimental validation of CFD simulations of a lab-scale fluidized-bed reactor with and without side-gas infection *AIChE J.*, 56 (2010), pp. 1434-1446

Müller, C.R., Davidson, J.F., Dennis, J.S., Hayhurst, A.N. A study of the motion and eruption of a bubble at the surface of a two-dimensional fluidized bed using particle image velocimetry (PIV). *Ind. Eng. Chem. Res* 46 (2007) 1642-1652.

Müller, C.R., Holland, D.J., Sederman, A.J., Scott, S.A., Dennis, J.S., Gladden, L.F. Granular temperature: Comparison of Magnetic Resonance measurements with Discrete Element Model simulations. *Powder Technol.* 203 (2008) 241-253.

Müller, C.R., Hartung, G., Davidson, J.F., Hult, J., Kaminski, C.F., Dennis, J.S. Laser diagnostic investigation of the bubble eruption patterns in the free board of fluidized beds. Part 2: Simultaneous acetone PLIF and stereoscopic PIV measurements, *AIChE Journal* 55, 1369-1382, 2009.

Nedderman, R.M., Laohakul, C. The thickness of the shear zone of flowing granular materials *Powder Technol.*, 25 (1980), pp. 91-100

Otsu, N. A threshold selection method from gray-level histograms IEEE Transactions on Systems, Man, and Cybernetics, 9 (1979), pp. 62-66

Patil, D.J., van Sint Annaland, M., Kuipers, J.A.M. Gas dispersion and bubble-to-emulsion phase mass exhange in a gas-solid bubbling fluidized bed: a computational and experimental study. *Int. J. of Chem. Reactor Eng.*, 1 (2003), 1-20.

Patil, D.J., van Sint Annaland, M., Kuipers, J.A.M., Critical comparison of hydrodynamic models for gas-solid fluidized beds-Part I: bubbling gas-solid fluidized beds operated with a jet *Chem. Eng. Sci.*, 60 (2005), pp. 57-72

Pavlin, T., Wang, R., McGorty, R., Rosen, M.S., Cory, D.G., Candela, D., Mair, R.W., Walsworth, R.L. Noninvasive measurements of gas exchange in a three dimensional fluidized bed by hiperpolarized Xe NMR. *Appl. Magn. Reson.*, 32 (2007), 93-122.

Peirano, E., Delloume, V., Leckner, B., Two- or three-dimensional simulations of turbulent gas-solid flows applied to fluidization *Chem. Eng. Sci.*, 56 (2001), pp. 4787-4799

Pemberton, S.T., Davidson, J.F. Elutriation from fluidized beds - I. Particle ejection from the dense phase into the freeboard. *Chem. Eng. Sci.* 41 (1986) 243.

Raffel, M., Willert, C., Kompenhans, J. Particle Image Velocimetry, A Practical Guide Springer, Berlin (2007)

Reddy, R.K., Sathe, M.J., Joshi, J.B., Nandakumar, K., Evans, G.M. Recent developments in experimental (PIV) and numerical (DNS) investigation of solid-liquid fluidized beds *Chem. Eng. Sci.* 92 (2003) 1-12.

Sánchez-Delgado, S., Marugán-Cruz, C., Acosta-Iborra, A., Santana, D., Dense-phase velocity fluctuation in a 2-D fluidized bed *Powder Technol.*, 200 (2010), pp. 37-45

Sánchez-Delgado, S., Marugán-Cruz, C., Soria-Verdugo, A., Santana, D. Estimation and experimental validation of the circulation time in a 2D gas-solid fluidized beds. *Powder Technol.* 235 (2013) 669-676

Santana, D., Nauri, S., Acosta, A., Garca, N., Macas-Machn, A., Initial particle velocity spatial distribution from 2-D erupting bubbles in fluidized bed *Powder Technol.*, 150 (2005), pp. 1-8

Saxena, S.C., Mathur, A. On the origin of solids projected from the surface of a gas-fluidized beds. *Chem. Eng. Sci.* 39 (1984) 917.

Schaeffer, D.G., Instability in the evolution equations describing incompressible granular flow *J. of Diff. Equations*, 66 (1987), pp. 19-50

Parametric effects of particle size and gas velocity on cluster characteristics in fast fluidized beds Sharma, A.K., Tuzla, K., Matsen, J., Chen, J.C. *Powder Technol.* 111 (2000) 114-122.

Shen, L., Johnsson, F., Leckner, B., Digital image analysis of hydrodynamics two-dimensional bubbling fluidized beds *Chem. Eng Sci.*, 59 (2004), pp. 2607-2617

Sit, S.P., Grace, J.R. Interphase mass transfer in an aggregative fluidized bed. *Chem. Eng Sci.* 33 (1978) 11115-1122.

Sit, S.P., Grace, J.R. Effect of bubble interaction on interphase mass transfer in gas fluidized beds. *Chem. Eng Sci.* 36 (1981) 327-335.

Sobrino, C., Almendros-Ibáñez, J.A., Santana, D., Vázquez, C., de Vega, M. Maximum entropy estimation of the bubble size distribution in fluidized beds *Chem. Eng Sci.* 64 (2009) 2307-2319.

Sobrino, C., Acosta-Iborra, A., Santana, D., de Vega, M. Bubble characteristics in a bubbling fluidized bed with a rotating distributor *Int. J. Multiphase Flow* 35 (2009) 970-976.

Solimene, R., Marzocchella, A., Passarelli, G., Salatino, P. Assessment of Gas-Fluidized Beds Mixing and Hydrodynamics by Zirconia Sensors. *AIChE Journal* 52, (2006) 185-198.

Solimene, R., Marzocchella, A., Ragucci, R., Salatino, P. Laser diagnostics of hydrodynamics and gas-mixing induced by bubble bursting at the surface of gas-fluidized beds *Chem. Eng. Sci.* 62, (2007) 94-108.

Soria-Verdugo, A., García-Gutíerrez, L.M., Sánchez-Delgado, S., Ruiz-Rivas, U. Circulation of an object immersed in a bubbling fluidized bed. *Chem. Eng. Sci.* 66, (2011) 78-87.

Soria-Verdugo, A., García-Gutiérrez, L.M., García-Hernando, N., Ruiz-Rivas, U. Buoyancy effects on objects moving in a bubbling fluidized bed. *Chem. Eng. Sci.* 66, (2011) 2833-2841.

Sveen J.K., 1998-2007. MATPIV. http://www.math.uio.no/jks/matpiv/.

Syamlal, M., O'Brien, T.J., 1987. Derivation of a drag coefficient from velocity-voidage correlation. U.S. Department of Energy, Office of Fossil; Energy, National Energy Technology Laboratory, Morgantown, WV. Unpublished Report. Syamlal and O'Brien, 1989

Syamlal, M., Rogers, W., O'Brien T.J., MFIX Documentation: Theory guide , U.S. department of Energy (DOE), Morgantown Energy Technology Center, Morgantown, West Virginia, 1993.

Taghipour, F., Ellis, N., Wong, C., Experimental and computational study of gas-solid fluidized bed hydrodynamics *Chem. Eng Sci.*, 60 (2005), pp. 6857-6867

J. R. Third and C. R. Müller Coupled LBM-DEM simulations of gas fluidised beds. *Proceedings of FLUIDIZATION XIV Conference*, Paper no. 130 (2013).

Toei, R., Matsumo, R., The Coalescence of Bubbles in the Gas-Solid Fluidized Bed Kyoto University, Japan (1967)

Y. Tsuji, T. Kawaguchi, T. Yanaka, Discrete particle simulations of 2-dimensional fluidized-beds *Powder Technol.* 77 (1993) 79-87.

Van der Hoef, M.A., van Sint Annaland, M., Kuipers, J.A.M., Computational fluid dynamics for dense gas-solid fluidized beds: a multiscale modeling strategy *China Particuology.*, 3 (2005), pp. 69-77.

van Ommen, van der Schaaf, J., Schouten, J.C., van Wachem, B.G.M., Coppens, M.O., van der Bleek, C.M. Optimal placement of probes for dynamic pressure measurements in large-scale fluidized beds. *Powder Tehcnol.* 139 (2004) 264-276.

Measuring the Gas-Solids Distribution in Fluidized Beds - A Review van Ommen, J.R., Mudde, R.F. *Int. J. of Chem. R. Eng.*, 6 (2008) R3.

van Ommen, R. J., Sasic, S., van der Schaaf, J., Gheorghiu, S., Johnsson, F., Coppens, M.O. Time-series analysis of pressure fluctuations in gas?solid fluidized beds - A review. *Int. J. Multiphase Flow*, 37 (2011) 403-428.

Van Wachem, B.G.M., Almstedt, A.E., Methods for multiphase computational fluid dynamics *Chem. Eng. J.*, 96 (2003), pp. 81-98

Van Wachem, B.G.M., Schouten, J.C., Krishna, R., van den Bleek, C.M., *Chem. Eng. Sci.*, 22 (1998), pp. S299-S306

Vejahati, F., Mahinpey, N., Ellis, N., Nikoo, M.B., CFD simulation of gas-solid bubbling fluidized bed: a new method for adjusting drag law *Can. J. Chem. Eng.*, 87 (2009), pp. 19-30

Vun, S., Naser, J., Witt, P.J., Yang, W. Measurements and numerical predictions of gas vortices formed by single bubble eruptions in the freeboard of a fluidised bed. *Chem. Eng. Sci.* 65 (2010) 5808-5820.

Wang., J., Liu, Y., EMMS-based Eulerian simulation on the hydrodynamics of a bubbling fluidized bed with FCC particles *Powder Technol.*, 197 (2010), pp. 241-246

Werther, J. Measurement techniques in fluidized beds *Powder Technol.* 102 (1999) 15-36.

Wu, W. and Agarwal, P.K. The effect of bed temperature on mass transfer between the bubble and emulsion phases in a fluidized beds. *Can. J. Chem. Eng.* 81, (2003) 940-948.

Yang, W.-C., Handbook of Fluidization and Fluid-Particle Systems Marcel Dekker, New York (2003)

Appendix A

Summary of equations of the two-fluid model

A.1 Governing equations

Mass conservation of gas (g) and solid (s) phases:

$$\frac{\partial}{\partial t}(\alpha_g \cdot \rho_g) + \bigtriangledown \cdot (\alpha_g \cdot \rho_g \cdot \overrightarrow{v_g}) = 0 \tag{A.1}$$

$$\frac{\partial}{\partial t}(\alpha_s \cdot \rho_s) + \bigtriangledown \cdot (\alpha_s \cdot \rho_s \cdot \overrightarrow{v_s}) = 0 \tag{A.2}$$

Momentum conservation equations of gas and solid phases:

$$\begin{aligned} \frac{\partial}{\partial t}(\alpha_g \rho_g \vec{v_g}) + \nabla(\alpha_g \rho_g \vec{v_g}^2) = \\ -\alpha_g \nabla p + \nabla \overline{\overline{\tau_g}} + \alpha_g \rho_g \vec{g} - K_{gs}(\vec{v_g} - \vec{v_s}) \end{aligned} \tag{A.3}$$

$$\begin{aligned} \frac{\partial}{\partial t}(\alpha_s \rho_s \vec{v_s}) + \nabla(\alpha_s \rho_s \vec{v_s}^2) = \\ -\alpha_s \nabla p - \nabla P_s + \nabla \overline{\overline{\tau_s}} + \alpha_s \rho_s \vec{g} + K_{gs}(\vec{v_g} - \vec{v_s}) \end{aligned} \tag{A.4}$$

Granular temperature conservation-like equation:

$$\begin{aligned} \frac{3}{2}\left(\frac{\partial}{\partial t}(\rho_s \alpha_s \Theta) + \nabla(\rho_s \alpha_s \vec{v_s} \Theta)\right) = \\ (-P_s \overline{\overline{I}} + \overline{\overline{\tau_s}}) : \nabla \vec{v_s} + \nabla(k_{\Theta,s} \nabla \Theta) - \gamma_\Theta - 3K_{gs}\Theta \end{aligned} \tag{A.5}$$

Where $(-P_s \overline{\overline{I}} + \overline{\overline{\tau_s}}) : \bigtriangledown \overrightarrow{v_s}^2$ is the generation of Θ by the solids stress tensor, $k_{\Theta,s} \cdot \bigtriangledown \Theta$ is the diffusion of Θ energy and γ_Θ is the collisional dissipation of Θ. In mass and

momentum conservation, the code solves the equation for one phase, and calculates the other assuming that $\alpha_g = 1 - \alpha_s$.

A.2 Drag models

A.2.1 Gidaspow

Gidaspow's drag function:

$$K_{gs} = \begin{cases} \frac{3}{4} C_D \frac{\rho_g \alpha_g \alpha_s |\vec{u}_g - \vec{u}_s|}{d_s} \varepsilon_g^{-2.65} & \alpha_g \geq 0.8 \\ \\ 150 \frac{\alpha_s^2 \mu_g}{\alpha_g d_s^2} + 1.75 \frac{\alpha_s \rho_g |\vec{u}_g - \vec{u}_s|}{d_s} & \alpha_g < 0.8 \end{cases} \tag{A.6}$$

where the drag coefficient is defined as

$$C_D = \begin{cases} \frac{24}{Re}(1 + 0.15 Re^{0.687}) & Re < 1000 \\ \\ 0.44 & Re \geq 1000 \end{cases} \tag{A.7}$$

and

$$Re = \frac{\rho_g \alpha_g |\vec{u}_g - \vec{u}_s| d_s}{\mu_g} \tag{A.8}$$

A.2.2 Syamlal - O'Brien

Syamlal - O'Brien's drag function:

$$K_{gs} = \frac{3 \cdot \alpha_s \cdot \alpha_g \cdot \rho_g}{4 \cdot v_{r,s}^2 \cdot d_s} C_D \left(\frac{Re_s}{v_{r,s}} \right) |\overrightarrow{v_s} - \overrightarrow{v_g}| \tag{A.9}$$

Where the drag coefficient is defined as:

$$C_D = \left(0.63 + \frac{4.8}{\sqrt{Re_s / v_{r,s}}} \right) \tag{A.10}$$

with $Re_s = \frac{\rho_g \cdot d_s \cdot |\overrightarrow{v_s} - \overrightarrow{v_g}|}{\mu_g}$

Where:

$$v_{r,s} = 0.5(A - 0.06Re_s + \sqrt{(0.06Re_s)^2 + 0.12Re_s(2B - a) + A^2}) \tag{A.11}$$

with $A = \alpha_g^{4.14}$

and for $\alpha_g \leq 0.85 \rightarrow B = 0.8\alpha_g^{1.28}$

and for $\alpha_g > 0.85 \rightarrow B = \alpha_g^{2.65}$

A.2.3 Hill - Koch - Ladd

Hill and Koch drag law, proposed by Benyahia *et al.*.

$$K_{gs} = 18\mu_g(1 - \alpha_s)^2\alpha_s\frac{F}{d_s^2} \tag{A.12}$$

where μ_g is the gas viscosity, α_s is the solids volume fraction, d_s is the particle diameter, and F is the dimensionless drag force, which is expressed as a function of the particle Reynolds number $Re = (\rho_g(1-\alpha_s)|v_g - v_s|d_p)/(2\mu_g)$, and a set of parameters as follows:

$$F = 1 + 3/8Re \quad \alpha_s \leq 0.01 \ , \ Re \leq \frac{(F_2 - 1)}{(3/8 - F_3)}$$

$$F = F_0 + F_1Re^2 \quad \alpha_s > 0.01 \ , \ Re \leq \frac{F_3 + \sqrt{F_3^2 - 4F_1(F_0 - F_2)}}{2F_1}$$

$$F = F_2 + F_3Re \begin{cases} \alpha_s \leq 0.01 \ , & Re > \frac{F_2 - 1}{3/8 - 8F_3} \\ \alpha_s > 0.01 \ , & Re > \frac{F_3 + \sqrt{F_3^2 - 4F_1(F_0 - F_2)}}{2F_1} \end{cases}$$

$$F_0 = \begin{cases} (1 - w)a + wb & 0.01 < \alpha_s < 0.4 \\ b & \alpha_s \geq 0.4 \end{cases}$$

$$F_1 = \begin{cases} \sqrt{\frac{2}{\alpha_s}}/40 & 0.01 < \alpha_s \leq 0.1 \\ 0.11 + 0.00051\exp(11.6\alpha_s) & \alpha_s > 0.1 \end{cases}$$

$$F_2 = \begin{Bmatrix} (1-w)c + wb & \alpha_s < 0.4 \\ b & \alpha_s \geq 0.4 \end{Bmatrix}$$

$$F_3 = \begin{Bmatrix} 0.9351\alpha_s + 0.03667 & \alpha_s < 0.0953 \\ 0.0673 + 0.212\alpha_s + 0.0232/(1-\alpha_s)^5 & \alpha_s \geq 0.0953 \end{Bmatrix}$$

$$a = \left[\frac{1 + 3\sqrt{\alpha_s/2} + (135/64)\alpha_s ln(\alpha_s) + 17.14\alpha_s}{1 + 0.681\alpha_s - 8.48\alpha_s^2 + 8.16\alpha_s^3} \right]$$

$$b = \left[10\frac{\alpha_s}{(1-\alpha_s)^3} \right]$$

$$c = \left[\frac{1 + 3\sqrt{\alpha_s/2} + (135/64)\alpha_s ln(\alpha_s) + 17.89\alpha_s}{1 + 0.681\alpha_s - 11.03\alpha_s^2 + 15.41\alpha_s^3} \right]$$

$$w = e^{(-10(0.4-\alpha_s)/\alpha_s)}$$

A.2.4 Beetstra

Beetstra drag function:

$$K_{gs} = 18F\frac{\mu_g(1-\alpha_g)\alpha_g}{d_s^2} \tag{A.13}$$

where:

$$\begin{aligned} F = 10\frac{1-\alpha_g}{\alpha_g^2} + \alpha_g^2(1 + 1.5\sqrt{1-\alpha_g}) \\ + \frac{0.413\mathrm{Re}}{24\alpha_g^2}\left(\frac{\alpha_g^{-1} + 3\alpha_g(1-\alpha_g) + 8.4\mathrm{Re}^{-0.343}}{1 + 10^{3\alpha_{s,max}}\mathrm{Re}^{-0.5-2\alpha_{s,max}}} \right. \end{aligned} \tag{A.14}$$

$$\mathrm{Re} = \frac{\rho_g(1-\alpha_{s,max})ud_s}{\mu_g} \tag{A.15}$$

A.3 Kinetic theory implemented in ANSYS Fluent

The Solids pressure can be expressed as a function of the particle granular temperature:

$$P_s = \alpha_s \cdot \rho_s \cdot \theta + 2 \cdot \rho_s \cdot (1 + e_{ss} \cdot \alpha_s^2) \cdot g_{0,ss} \cdot \theta \tag{A.16}$$

The solid-phase stress tensor is defined as:

$$\overline{\overline{\tau_s}} = \alpha_s \cdot \mu_s \cdot (\nabla \overrightarrow{v_s} + \nabla \overrightarrow{v_s}^T) + \alpha_s \cdot (\lambda_s - \frac{2}{3}\mu_s)\nabla \cdot \overrightarrow{v_s} \cdot \overline{\overline{I}} \tag{A.17}$$

Where solid shear viscosity is:

$$\mu_s = \mu_{s,col} + \mu_{s,fr} + \mu_{s,kin} \tag{A.18}$$

The model of Gidaspow for the diffusion coefficient of granular temperature:

$$\begin{aligned} k_{\Theta,s} = & \frac{150 \cdot \rho_s \cdot d_s \cdot \sqrt{\theta \cdot \pi}}{384 \cdot (1 + e_{ss}) g_{0,ss}} \left[1 + \frac{6}{5}\alpha_s \cdot g_{0,ss} \cdot (1 + e_{ss})\right]^2 \\ & + 2 \cdot \rho_s \cdot d_s \cdot \alpha_s^2 \cdot g_{0,ss} \cdot (1 + e_{ss}) \cdot \sqrt{\frac{\theta}{\pi}} \end{aligned} \tag{A.19}$$

The model of Syamlal - O'Brien for the diffusion coefficient of granular temperature:

$$\begin{aligned} k_{\Theta,s} = & \frac{15 \cdot \rho_s \cdot d_s \cdot \alpha_s \cdot \sqrt{\theta \cdot \pi}}{4 \cdot (41 - 33\eta)} \left[1 + \frac{12}{5}\eta^2 \cdot (4\eta - 3)\alpha_s \cdot g_{0,ss} \right. \\ & \left. + \frac{16}{15\pi}(41 - 33\eta) \cdot \eta \cdot \alpha_s \cdot g_{0,ss}\right] \end{aligned} \tag{A.20}$$

with $\eta = \frac{1}{2}(1 + e_{ss})$

The model of Gidaspow for the kinetic viscosity:

$$\mu_{s,kin} = \frac{10 \cdot \rho_s \cdot d_s \cdot \sqrt{\theta \cdot \pi}}{96 \cdot \alpha_s \cdot (1 + e_{ss}) g_{0,ss}} \left[1 + \frac{4}{5}\alpha_s \cdot g_{0,ss} \cdot (1 + e_{ss})\right]^2 \tag{A.21}$$

The model of Syamlal - O'Brien for the kinetic viscosity:

$$\mu_{s,kin} = \frac{\alpha_s \cdot \rho_s \cdot d_s \cdot \sqrt{\theta \cdot \pi}}{6 + \cdot(3 - e_{ss})} \left[1 + \frac{2}{5}\alpha_s \cdot g_{0,ss} \cdot (1 + e_{ss}) \cdot (3 \cdot e_{ss} - 1)\right] \tag{A.22}$$

The collisional viscosity is defined with:

$$\mu_{s,col} = \frac{4}{5}\alpha_s \cdot \rho_s \cdot d_s \cdot g_{0,ss} \cdot (1 + e_{ss}) \left(\frac{\theta}{\pi}\right)^2 \tag{A.23}$$

And the frictional viscosity:

$$\mu_{s,fr} = \frac{P_s \cdot \sin\theta}{2\sqrt{I_{2D}}} \tag{A.24}$$

Where ϕ is the angle of internal friction, and I_{2D} is the second invariant of the deviatory stress tensor.

Finally, the collisional dissipation of energy is modelled as:

$$\gamma_\theta = \frac{12 \cdot (1 - e_{ss}^2) \cdot g_{0,ss}}{d_s\sqrt{\pi}} \rho_s \cdot \alpha_s \cdot \theta^{3/2} \tag{A.25}$$

A.4 Kinetic theory implemented in MFIX

Einstein summation convention implied only on subscripts i and j.

Gas momentum equation stresses.

$$\tau_{g,ij} = 2\mu_{g,t} S_{g,ij} \tag{A.26}$$

$$S_{g,ij} = \frac{1}{2}\left(\frac{\partial u_{g,i}}{\partial x_j} + \frac{\partial u_{g,j}}{\partial x_i}\right) - \frac{1}{3}\frac{\partial u_{g,i}}{\partial x_i} \tag{A.27}$$

$$\mu_{g,t} = min(\mu_{max}, \mu_g + \mu_e) \tag{A.28}$$

$$\mu_e = 2 l_p^2 \alpha_g \rho_g \sqrt{I_{2Dg}} \tag{A.29}$$

$$\begin{aligned} I_{2Dg} =& \frac{1}{6}\left[(D_{g,11} - D_{g,22})^2 + (D_{g,22} - D_{g,33})^2 + (D_{g,33} - D_{g,11})^2\right] + \\ &+ D_{g,12}^2 + D_{g,23}^2 + D_{g,31}^2 \end{aligned} \tag{A.30}$$

Solids stresses:

$$\tau_p = \left(-P_s + \eta\mu_b \frac{\partial u_{s,i}}{\partial x_i}\right)\delta_{ij} + 2_p S_{s,ij} \tag{A.31}$$

where

$$S_{s,ij} = \frac{1}{2}\left(\frac{\partial u_{s,i}}{\partial x_j} + \frac{\partial u_{s,j}}{\partial x_i}\right) - \frac{1}{3}\frac{\partial u_{s,i}}{\partial x_i} \tag{A.32}$$

Radial distribution function at contact:

$$g_0 = \frac{1}{1 + \left(\frac{\alpha_s}{\alpha_{s,max}}\right)^{\frac{1}{3}}} \tag{A.33}$$

Solids pressure:

$$P_s = \alpha_s \rho_s \Theta_s \left[1 + 4\eta \alpha_s g_{0,ss}\right] \tag{A.34}$$

Solids viscosity:

$$\mu_s = \left(\frac{2+\alpha}{3}\right)\left[\frac{\mu_s^*}{g_{0,ss}\eta(2-\eta)}\right. \\ \left.\left(1 + \frac{8}{5}\eta\alpha_s g_{0,ss}\right)\left(1 + \frac{8}{5}\eta(3\eta-2)\alpha_s g_{0,ss}\right) + \frac{3}{5}\eta\mu_b\right] \tag{A.35}$$

with

$$\mu_s^* = \frac{\rho_s \alpha_s g_{0,pp} \Theta_p \mu}{\rho_s \alpha_s g_{0,ss} \Theta_s + \left(\frac{2K_{gs}\mu}{\rho_s \alpha_s}\right)} \tag{A.36}$$

$$\mu = \frac{5}{96}\rho_s d_s \sqrt{\pi \Theta_s} \tag{A.37}$$

$$\mu_b = \frac{256}{5\pi}\mu\alpha_s^2 g_{0,ss} \tag{A.38}$$

Solids conductivity:

$$\kappa_s = \left(\frac{\kappa_s^*}{g_{0,ss}}\right)\left[\left(1 + \frac{12}{5}\eta\alpha_s g_{0,ss}\right)\left(1 + \frac{12}{5}\eta^2(4\eta-3)\alpha_s g_{0,ss}\right) + \right. \\ \left. + \frac{64}{25\pi}(41-33\eta)\eta^2(\alpha_s g_{0,ss})^2\right] \tag{A.39}$$

with

$$\kappa_s^* = \frac{\rho_s \alpha_s g_{0,ss} \Theta_s \kappa}{\rho_s \alpha_S g_{0,ss} \Theta_s + \frac{6K_{gp}\kappa}{5\rho_s\alpha_s}} \tag{A.40}$$

$$\kappa = \frac{75\rho_s d_s \sqrt{\pi\Theta_s}}{48\eta(41-33\eta)} \tag{A.41}$$

Collisional dissipation:

$$J_m = \frac{48}{\sqrt{\pi}}\eta(1-\eta)\frac{\alpha_s g_{0,ss}}{d_s}\Theta_s^{3/2} \tag{A.42}$$

$$\eta = \frac{1+e}{2} \tag{A.43}$$

Exchange terms:

$$\Pi_s = -3K_{gs}\Theta_s + \frac{81\alpha_s\mu_g^2|\vec{u}_g - \vec{u}_s|^2}{g_{0,ss}d_p^3\rho_s\sqrt{\pi\Theta_s}} \tag{A.44}$$

A.5 Frictional stress

Shaeffer's model is considered for both codes, ANSYS Fluent and MFIX. This model is used at the critical state when the solids volume fraction exceeds the maximum packing limit α^*.

$$P_c = \begin{cases} 10^{24}(\alpha^* - \alpha_g)^{10} & \alpha_g < \alpha^* \\ 0 & \alpha_g \geq \alpha^* \end{cases} \tag{A.45}$$

$$\mu_f = \begin{cases} min\left(\frac{P_c \sin(\phi)}{\sqrt{4I_{2D}}}, \mu_s^{max}\right) & \alpha_g < \alpha^* \\ 0 & \alpha_g \geq \alpha^* \end{cases} \tag{A.46}$$

$$\mu_s^{max} = 100 \tag{A.47}$$

$$\mu_b = 0 \tag{A.48}$$

$$\begin{aligned} I_{2D} =& \frac{1}{6}\left[(D_{s,11} - D_{s,22})^2 + (D_{s,22} - D_{s,33})^2 + (D_{s,33} - D_{s,11})^2\right] + \\ &+ D_{s,12}^2 + D_{s,23}^2 + D_{s,31}^2 \end{aligned} \tag{A.49}$$

$$D_{s,ij} = \frac{1}{2}\left(\frac{\partial u_{s,i}}{\partial x_j} + \frac{\partial u_{s,j}}{\partial x_i}\right) \tag{A.50}$$

A.6 Solution procedure

Two-fluid hydrodynamic models, also referred as Eulerian-Eulerian models, treat the fluid and solids as two continuous and fully interpenetrating phases. This approach

results in mass, momentum, and energy balance equations for both the gas and solids phases. Two different codes were used in the realization of this PhD, ANSYS Fluent and MFIX (Multiphase Flow with Interphase eXchanges).

ANSYS Fluent software contains the broad physical modelling capabilities needed to model flow, turbulence, heat transfer, and reactions for industrial applications ranging from air flow over an aircraft wing to combustion in a furnace, from bubble columns to oil platforms, from blood flow to semiconductor manufacturing, and from clean room design to waste water treatment plants.

MFIX is a general purpose hydrodynamic model for describing chemical reactions and heat transfer in dense or dilute fluid-solids flows, which typically occur in energy conversion and chemical processing reactors.

In both ANSYS Fluent and MFIX codes, the governing equations are solved on a computational domain with a finite number of cells or control volumes. Second order accurate schemes for discretizing the convection terms were used in both codes.

In particular, the MFIX code uses an extension of the SIMPLE method, using a volume fraction correction equation in an iterative procedure to adjust the velocities in order to satisfy conservation of mass in both phases. That equation also incorporates the effect of solids pressure. The nodal points are located at cell centres where scalars are saved. Velocities are defined at cell faces by using a staggered grid. The finite volume method integrates the equations over each cell. Also, its numerical technique was replaced with a semi-implicit scheme that uses automatic time-step adjustment to speed up the code.

The time step chosen for ANSYS Fluent was a fixed time step with a conservative number of iterations per time step to ensure its convergence. For the Gidaspow drag model, a time step of 5e-4 seconds, with 75 iterations per time step, was chosen in order to ensure the convergence of the problem, with a numerical criterion of 5e-4 for the continuity equation, which is the most critical due to the convergence. The criterion chosen of 75 iterations per time step to ensure that the residuals of all the equations, including the continuity one, are completely stabilized (i.e the residuals do not vary in time). Therefore, once all of the residuals are stabilized there is no sense in continuing iterating in a given time step. In other words, in our simulation using FLUENT code, and taking into account that the time step is very reduced (5e-4 s), 75 iterations per time steps is actually a very conservative figure that ensures, by far, that in each time step the obtained solution is converged, and do not change if more time steps were added. The Syamlal - O'Brien drag function was solved with the same time step, but 100 iterations per time step were needed in order to ensure its convergence.

Nomenclature

C_D	drag coefficient, (−)
d_s	diameter, m
e_{ss}	restitution coefficient, (−)
F	dimensionless drag force, (−)
$g_{0,ss}$	radial distribution coefficient, (−)
K_{gs}	gas/solid momentum exchange, (−)
P_s	solids pressure, Pa
$\vec{g}$	aceleration due to gravity, 9,8 m/s^2
$k_{\Theta,s}$	diffusion coefficient for granular energy, kg/s m
Re	Reynolds number, (−)
v_i	velocity, m/s
$\vec{v_i}$	velocity vector, m/s
t	time, s

Greek letters

α_i	volume fraction, (−)
Θ_i	granular temperature, m^2/s^2
μ_i	shear viscosity, kg/s m
ρ_i	density, kg/m^3
$\overline{\overline{\tau_i}}$	stress tensor, Pa
Θ	granular temperature, (J/kg)

Subscripts

g	gas
i	general index
s	solids

Appendix B

Streamlines computation

B.1 Streamlines computation

Given that the particulate phase, outside bubbles, in fluidized beds behaves like an incompressible fluid (Davidson and Harrison, 1963) it is possible to use a Poisson equation for the computation of the streamlines of the particulate phase in a two dimensional flow. This procedure is described in the following lines. Precaution in the interpretation of the streamlines should be taken for regions of the bed where the void fraction of particles varies greatly, such in the bubble interphase and bed surface, and can depart from the incompressibility condition. This can be easily deduced from the Eulerian equations of the particulate phase (2, 4). However, these regions are narrow in size and the dissipative nature of the Poisson equation yields smooth streamlines, avoiding unrealistic oscillations or abrupt changes in the streamlines direction. For the same reason, the method is especially suitable for extracting the streamlines when the velocity field is affected by measurement noise. In a two-dimensional incompressible flow, the stream function is related to the horizontal and vertical components of the velocity, u and v respectively:

$$\frac{\partial \psi}{\partial y} = u \tag{B.1}$$

$$\frac{\partial \psi}{\partial x} = -v \tag{B.2}$$

Introducing equations B.1 and B.2 into the vorticity definition,

$$\zeta = \frac{\partial v}{\partial x} - \frac{\partial u}{\partial y} \tag{B.3}$$

the next Poisson equation for the stream function appears

$$\frac{\partial^2\psi}{\partial x^2} - \frac{\partial^2\psi}{\partial y^2} = -\zeta \tag{B.4}$$

With the appropriate boundary conditions for ψ, equation B.4 can be solved and the streamlines computed from the isovalue lines of the stream function. In the present work, centred finite differences have been used for the discretization of the spatial derivatives in a rectangular mesh not necessarily homogeneous:

$$\zeta_{i,j} \approx \frac{v_{i+1,j} - v_{i-1,j}}{\triangle x_i + \triangle x_{i-1}} - \frac{u_{i,j+1} - u_{i,j-1}}{\triangle y_j + \triangle y_{j-1}} \tag{B.5}$$

$$\left.\frac{\partial^2\psi}{\partial x^2}\right|_{i,j} \approx \frac{2}{\triangle x_{i-1} + \triangle x_i}\left(\left.\frac{\partial\psi}{\partial x}\right|_{i+\frac{1}{2},j} - \left.\frac{\partial\psi}{\partial x}\right|_{i-\frac{1}{2},j}\right) \tag{B.6}$$

$$\left.\frac{\partial^2\psi}{\partial y^2}\right|_{i,j} \approx \frac{2}{\triangle y_{j-1} + \triangle y_j}\left(\left.\frac{\partial\psi}{\partial y}\right|_{i,j+\frac{1}{2}} - \left.\frac{\partial\psi}{\partial y}\right|_{i,j-\frac{1}{2}}\right) \tag{B.7}$$

Where the indices (i, j) refer to the position (x_i, y_j) of a node in the computational mesh, and $(i + 1/2, j)$, $(i - 1/2, j)$, and so on, account for discretizations placed in intermediate positions between nodes; for example:

$$\left.\frac{\partial\psi}{\partial x}\right|_{i+\frac{1}{2},j} \approx \frac{\psi_{i+1,j} - \psi_{i,j}}{\triangle x_i} \tag{B.8}$$

$$\left.\frac{\partial\psi}{\partial y}\right|_{i,j+\frac{1}{2}} \approx \frac{\psi_{i,j+1} - \psi_{i,j}}{\triangle y_j} \tag{B.9}$$

Notice that $\triangle x_i = x_{i+1} - x_i$, $\triangle x_{i-1} = x_i - x_{i-1}$, $\triangle y_j = y_{j+1} - y_j$ and $\triangle y_{j-1} = y_j - y_{j-1}$ are the horizontal and vertical separation of consecutive nodes. In a homogeneous mesh $\triangle x_i$ and $\triangle y_j$ are constant regardless the node position and the discretization becomes second order accurate. It is assumed that the dense phase does not penetrate the walls and the distributor. Therefore, these boundaries are defined by a single value of ψ, which is arbitrarily assigned to zero. The value of ψ at the upper part of the bed, i.e. the free board, can be readily calculated integrating equation B.2 (or its discretized version as in B.5 along horizontal direction. With the described discretization of spatial

derivatives, equation B.4 can be expressed as:

$$(a+b+c+d)\cdot\psi_{i,j} - a\psi_{i+1,j} - b\psi_{i-1,j} - c\psi_{i,j+1} - d\psi_{i,j-1} = \zeta_{i,j} \tag{B.10}$$

Where,

$a = \frac{2}{\triangle x_i + \triangle x_{i-1}} \cdot \frac{1}{\triangle x_i}$, $b = \frac{2}{\triangle x_i + \triangle x_{i-1}} \cdot \frac{1}{\triangle x_{i-1}}$, $c = \frac{2}{\triangle y_i + \triangle y_{i-1}} \cdot \frac{1}{\triangle y_i}$, $d = \frac{2}{\triangle y_i + \triangle y_{i-1}} \cdot \frac{1}{\triangle y_{i-1}}$.

The expression B.10 conforms a system of equations, each one accounting for a node point (i, j), that can be solved with a standard matrix inversion procedure such as Gauss Seidel or SOR methods. The above simple approximations of derivatives are not computationally demanding and provide satisfactory results for the fluidized beds tested. Obviously more precise and sophisticated techniques can be used for the solution of equation B.4.